Resonantly excited quantum dots in micropillars: an efficient source of indistinguishable single photons interfaced with fibre

Thesis submitted to

Cardiff University

for the degree of

Doctor of Philosophy

Matthew Jordan

Cardiff University, School of Engineering

30 Sep 2024

Summary

The research presented in this thesis examines a popular solid state solution for the generation of indistinguishable single photons for quantum computing: self-assembled quantum dots embedded in semiconductor pillar microcavities. Coupling to the cavity modes of these structures increases the spontaneous emission rate of the dots via Purcell enhancement, while also directing the output light in such a way to be efficiently collected into an optical fibre. This makes them a strong choice of source for photonics-based quantum applications, including computation, metrology, and secure communications.

Two designs of micropillar, configured for a low- or high-quality factor, are studied both computationally, using finite-difference time-domain (FDTD) methods, and experimentally. The high-aspect ratio pillars used in lab work were produced using a novel direct-write lithography-based fabrication process capable of deep sidewall etches with smoothness (53 ± 10) pm, matching the state of the art, as determined using photoluminescence and reflectivity based spectroscopic characterisation. The two-level single photon source properties are confirmed by observing Rabi oscillations in power dependence data, a low $\tau = 0$ second-order correlation count of 0.027 ± 0.004, and Hong-Ou-Mandel interference visibility (99.0 ± 1.0) %.

By exciting a pillar with emitters at different heights within the cavity electric field, the HE_{11} mode can be supressed, revealing a background spectrum of 'leaky' non-cavity modes. The Zeeman effect then allows single transitions to be magnetically detuned across the cavity resonance, using pulsed laser excitation lifetimes to extract device Purcell factors. Along with further studies simulating a pillar without distributed Bragg reflectors (DBRs), which reproduces the broad non-cavity mode emission spectrum, this offers new insights into the pillar shape's influence on its optical properties, which can inform the design of more efficient cavity devices.

Contents

List of publications

Journal papers

Direct-write projection photolithography of quantum dot micropillar single photon sources
Androvitsaneas, P., Clark, R.N., Jordan, M., Alvarez Perez, M., Peach, T., Thomas, S., Shabbir, S., Sobiesierski, A.D., Trapalis, A., Farrer, I.A. Langbein, W. and Bennett, A.J. 2023. *Applied Physics Letters* 123(9).

Probing Purcell enhancement and photon collection efficiency of InAs quantum dots at nodes of the cavity electric field
Jordan, M., Androvitsaneas, P., Clark, R.N., Trapalis, A., Farrer, I., Langbein, W., and Bennett, A.J. 2024. *Physical Review Research* 6(2), p. L022004.

Modelling non-cavity modes using a micropillar without Bragg reflectors
Jordan, M., Langbein, W., and Bennett, A. J. 2025. (Under preperation)

Conference papers

Quantum dot micropillar cavities with SiO_2 hard mask microlenses
Jordan, M., Androvitsaneas, P., Clark, R. N., Trapalis, A., Farrer, I., Langbein, W. and Bennett, A. J. 2024. In: Proceedings of SPIE: Photonic and Phononic Properties of Engineered Nanostructures XIV. San Francisco, 27 January - 1 Februrary, 2024.

List of symbols

General quantities

x, y, z	Cartesian coordinates
r	Radial coordinate
θ	Polar angle
ϕ	Azimuthal angle
A	Area
V	Volume
t	Time
τ	Time difference
λ	Wavelength
f	Frequency
ω	Angular frequency
A_0, A_1 ...	Amplitude
E	Energy
P	Power
I	Intensity
p	Momentum

Universal constants

a_0	Bohr radius
c	Speed of light in a vacuum
e	Elementary charge
h	Planck constant
$\hbar$	Reduced Planck constant
μ_B	Bohr magneton

Qubit states

N_q	Number of qubits
c_1, $c_2 \dots c_n$	Complex probability amplitudes
ψ	Wavefunction

Field vector operators

$\vec{\boldsymbol{E}}$	Electric field
$\vec{\boldsymbol{E}}_{\mathrm{vac}}$	Vacuum electric field amplitude operator
$\vec{\boldsymbol{B}}$	Magnetic flux density
$\vec{\boldsymbol{H}}$	Magnetic field strength
$\vec{\boldsymbol{P}}$	Poynting vector
$\vec{\boldsymbol{S}}$	Surface normal vector
$\vec{\boldsymbol{d}}$	Electric dipole amplitude operator

Microcavity and mode properties

d	Micropillar diameter
d_{a} / d_{b}	Major / minor axis diameter of an elliptical micropillar
d_{eff}	Effective diameter of an elliptical micropillar
E_{c}	Cavity mode energy
E_0	Design / resonance energy of a microcavity
ΔE	Uncertainty in energy
λ_{c}	Cavity mode wavelength
λ_0	Design / resonance wavelength of a microcavity
$\Delta\lambda$	Mode width (full-width-half-maximum)
f_0	Design / resonance frequency of a microcavity
f_{c}	Cavity mode frequency
Δf	Linewidth

K_{cav}	Wavelength number thickness of cavity spacer layer
M_{eff}	Effective number of DBR mirror pairs
M_{DBR}, M_{u}, M_{l}	Number of DBR mirror pairs in each stack
M_{A}, M_{G}	Number of DBR mirrors of $Al_{0.95}Ga_{0.05}As$ and GaAs.
R_{DBR}, R_{u}, R_{l}	Reflectivity coefficients of DBR stacks
L_{cav}	Cavity spacer layer thickness
L_{DBR}	Electric field penetration depth into DBR layers
L_{eff}	Effective cavity length
$L_{\mathrm{A}}, L_{\mathrm{G}}$	Thickness of DBR material layers
Q	Quality factor
Q_0	Quality factor of a planar microcavity
Q_{s}	Quality factor loss coefficient due to sidewall scattering
Q_{abs}	Quality factor loss coefficient due to photon absorption
κ_{s}	Sidewall roughness coefficient
k_{t}	Transverse wavevector
k_0	Longitudinal wavevector
V_{m}	Mode volume
$\beta_{\mathrm{HE}_{11}}$	Mode propagation constant
J_0	Bessel function of the first kind of zeroth order
X_{φ,N_0}	N_0^{th} zero of the Bessel function of order φ
k_{A}	Mode azimuthal wavenumber
k_{R}	Mode radial wavenumber

Particle and quasi-particle properties

X	Exciton
X^0	Neutral exciton
X^-	Negative trion / charged exciton
X^+	Positive trion / charged exciton

X_{b}	Bright exciton
X_{b}	Dark exciton
XX / X_2	Biexciton
m_{e}	Rest mass of an electron
m_{e}^*	Effective mass of an electron
m_{h}^*	Effective mass of a hole
m_{X}^*	Effective mass of an exciton
s_{e}	Electron spin
s_{h}	Hole angular momentum
s_{X}	Total electron-hole angular momentum
a_{X}	Characteristic radius of an exciton
d_{X}	Characteristic diameter of an exciton
λ_{dB}	de Broglie wavelength

<u>Photon states and statistics</u>

N_{p}	Photon number
$\overline{N}_{\mathrm{p}}$	Mean photon number
$P(N_{\mathrm{p}})$	Photon number probability distribution
$\lvert\alpha_{\mathrm{p}}\rangle$	Coherent photon state
ρ	Density of states
T_1	Radiative lifetime
ΔT_1	Uncertainty in radiative lifetime
T_2	Dephasing time
w	Sinusoidal beat time period
φ	Sinusoidal beat phase offset

k_{damp}	Additional beat damping parameter
γ_{SE}	Spontaneous emission rate
τ_{re}	System recycling time
$g^{(2)}$	Second order correlation
$R_{\mathrm{f}}(\tau)$	$g^{(2)}$ normalisation factor
N_{e}	Number of emitters
N_{∞}	QD population under power broadening
Ω	Rabi frequency
Θ	Pulse area
E_p	Pulse envelope
M_{S}	Intrinsic two-photon indistinguishability
V_{HOM}	Hong-Ou-Mandel visibility
V_{raw}	Raw measured Hong-Ou-Mandel visibility value
V_{corr}	Hong-Ou-Mandel visbility corrected for interferometer visibility
$\hat{a}^{\dagger}$, $\hat{b}^{\dagger}$	Photon creation operators
$\hat{c}^{\dagger}$, $\hat{d}^{\dagger}$	Photon output operators
S_1, S_2, S_3	Stokes parameters
2Ψ	Polarisation ellipticity
2χ	Polarisation azimuth
δ_p	Polarisation degree
E_{shift}	Shift in energy due to quadratic Zeeman effect
ΔE_{med}	Bandgap of medium surrounding a quantum dot
ΔE_{QD}	Bandgap of quantum dot material
E_{CB}	Conduction band energy
E_{VB}	Valence band energy

ΔE_{Z}	Energy splitting via the Zeeman effect
σ	Diamagnetic shift coefficient
g_{QD}	Effective g-factor of quantum dot

<u>Material properties</u>

n	Real refractive index
$\underline{n}$	Complex refractive index
n_{i}	Imaginary part of refractive index
n_{eff}	Effective refractive index
ε	Absolute permittivity
ε_{r}	Dielectric constant / relative permittivity
$\varepsilon_{\mathrm{r,eff}}$	Effective dielectric constant / relative permittivity
μ	Magnetic permeability
α_{M}	Material absorption coefficient
n_{above}	Refractive index of medium above upper DBR stack
n_{below}	Refractive index of medium below lower DBR stack
n_{cav}	Refractive index in the cavity spacer layer
n_{DBR}, n_1, n_2	Refractive index of DBR materials

<u>Device emission rates and efficiencies</u>

Γ	Decay rate
Γ_{L}	Decay rate via “lossy” non-cavity modes
Γ_0	Decay rate in a homogenous medium
Γ_{C}	Decay rate via cavity modes
$\Gamma_{\mathrm{C_0}}$	Maximum decay rate via cavity modes
Γ_{up}	Decay rate in the upward direction
Γ_{down}	Decay rate in the downward direction
Γ_{out}	Decay rate of upward emissions via the cavity mode
Γ_{tot}	Total decay rate

T	Normalised transmission through a surface
β	Spontaneous emission coupling factor
η	Cavity directionality
ξ	Outcoupling efficiency
F_{P}	Purcell factor
ϵ_{s}	Photon source efficiency

<u>Experimental apparatus properties</u>

ϵ_{d}	Detector efficiency
f_{O}	Objective lens focal length
f_{S}	Stage lens focal length

List of abbreviations

ALD – Atomic Layer Deposition

APD – Avalanche Photodiode

CCD – Charge-Coupled Device

CW – Continuous Wave

DBR – Distributed Bragg Reflector

DFG – Difference-Frequency Generation

DOS – Density of States

ECR – Electron Cyclotron Resonance

FDTD – Finite-Difference Time Domain

FEM – Finite-Element Method

FIB – Focused Ion Beam

FSS – Fine Structure Splitting

FWHM – Full-Width Half-Maximum

HBT – Hanbury Brown and Twiss (Effect/Experiment)

HOM – Hong-Ou-Mandel (Effect/Experiment)

ICP - Inductively Coupled Plasma

KLM – Knill-Laflamme-Milburn (Scheme)

LA – Longitudinal Accoustic (Phonons)

LDH – Laser Diode Head

LDOS – Local Density of States

LED – Light Emitting Diode

LPCVD – Low Pressure Chemical Vapour Deposition

MBE – Molecular Beam Epitaxy

MFD – Mode Field Diameter

NA – Numerical Aperture

ND – Neutral Density (Filter)

NIR – Near Infrared

PBC – Periodic Boundary Condition

PBS – Polarised Beam Splitter

PL – Photoluminescence

PECVD – Plasma-Enhanced Chemical Vapour Deposition

PMF – Polarisation Maintaining Fibre

PML - Perfectly Matched Layer (Boundary Conditions)

PPLN – Periodically Poled Lithium Niobate (Waveguide)

QD – Quantum Dot

QFC – Quantum Frequency Conversion

QKD – Quantum Key Distribution

QPM – Quasi-Phase-Matched

RF – Radio Frequency

RIE – Reactive Ion Etching

RMS – Root Mean Square (Error)

RRS – Resonant Rayleigh Scattering

SE – Spontaneous Emissions

SEM – Scanning Electron Microscope (Image)

SFG – Sum-Frequency Generation

SHG – Second-Harmonic Generation

SNSPD – Superconducting Nanowire Single Photon Detector

SPDC – Spontaneous Parametric Down Conversion

UHV – Ultra High Vacuum

WL – White Light (Reflectivity)

Acknowledgements

First, I'd of course like to take this opportunity to express my thanks to both Prof. Anthony J. Bennett and Prof. Wolfgang Langbein for their supervision throughout my PhD programme. I'd equally very much like to thank my frequent lab partner Dr. Petros Androvitsaneas, whose experiment designs, laboratory work, and support have been curcial throughout my project.

I also extend my gratitude to the other members of the Bennett Lab who aided me over the project, in particular Dr. Rachel Clark, Dr. John Hadden, and Dr. Sam Bishop. Rachel was involved in preparing our samples alongside Petros and the staff of the cleanroom of the European Regional Development Fund (ERDF) funded Institue for Compound Semiconductors (ICS) at Cardiff Univeristy. Meanwhile, the latter two provided a lot of help with the programming of Labview virtual instruments for experimental work and, in the case of Dr. Hadden, provided a great starting point for the simulation work I've partaken in across the last few years.

Outside of Cardiff University, I also owe thanks to Prof. Ian Farrer and our other collaborators at the University of Sheffield and the National Epitaxy Facility, who manufactured our samples. Thank you also to Dr. Alex Davis and Dr. Josh Nunn of the University of Bath, who collaborated with us on frequency conversion.

My PhD studentship and research was financially supported by the Engineering and Physical Sciences Research Council (EPSRC) via Grant No. EP/T017813/1 and EP/T001062/1, under Cardiff University's School of Engineering and the Quantum Computing and Simulation (QCS) Hub at the University of Oxford.

Finally, I thank my mum and dad, Harriet and Wayne Jordan, who have been with me every step of the way.

Chapter 1
Introduction and motivation

1.1 Quantum technologies

Broadly speaking, the primary aim of quantum technologies is to use the unique features of quantum mechanical systems to achieve performance significantly superior to systems solely based upon classical physics (Zhang et al. 2001; Dowling and Milburn 2003).

One way this is achieved is via the description and manipulation of information not using classical bits, but quantum bits, or “qubits”. Whereas a classical bit used in computing today may only take on one of two binary values (|0⟩ and |1⟩), a qubit can exist in a superposition of both, represented:

$$|\psi\rangle = c_1|0\rangle + c_2|1\rangle \tag{1.1}$$

In which are c_1 and c_2 are complex probability amplitudes, whose squares give the probability of the system being in either state totalling 1 (Nielsen and Chuang 2010). These permitted states form a two-dimensional complex vector space, or “Hilbert Space” (Prugovecki 1982).

In the context of quantum physics, a qubit is defined as a two-level system, such as the two states of an electron, up (|↑⟩) or down (|↓⟩) (Schumacher 1995), or the polarisation of light, horizontal ((|h⟩) or vertical ((|v⟩) (O'Brien et al. 2009).

Most quantum algorithms require the control of millions of qubits, which must be connected to logical gates with minimal introduction of decoherence, a major challenge in the development of such systems (LaPierre 2021). Any number of qubits

N_{q} may be combined by entanglement to form a larger Hilbert space of $2^{N_{\mathrm{q}}}$ dimensions (DiVincenzo 2000).

A wide range of qubit implementations and algorithms have been applied to the development of technologies including quantum computing (DiVincenzo and Loss 1999) and simulation (Johnson et al. 2014), cryptography (Zhang et al. 2001), and sensing (Degen et al. 2017).

1.1.1 Quantum computing and simulation

Numerical simulations are extremely important to developing understanding of natural phenomena, however many systems (e.g. superconducting materials) are described with models too complex to solve accurately with classical computers but may be solvable with quantum computers (Johnson et al. 2014). These include research areas such as high-energy (Jordan et al. 2012) and condensed matter physics (Lewenstein et al. 2012). In particular, they are ideal for simulating systems containing quantum effects themselves (Gershenfeld and Chuang 1997).

Only very small general quantum systems can be simulated on a classical computer. This is because the Hilbert space, as mentioned, scales exponentially with the system size. For example, describing the fully general state of just 37 qubits would require about 1 TB of memory in a classical computer, as each added qubit doubles the required memory (Brown et al. 2010). By contrast, a quantum computer would be able to efficiently encode and store the Hilbert space of a quantum system's state using its own natural superpositions (Feynman 1982), allowing calculation in a time scaling at a much slower rate with the number of simulated qubits (Lloyd 1996).

Quantum computers show great potential in other areas as well, such as optimisation and machine-learning, with the potential to offer major improvements over classical "brute force" algorithms in a wide range of domains (Abbas et al. 2023; Brooks 2023).

1.1.2 Quantum cryptography

Modern methods of public-key cryptography use the computational difficulty involved in solving particular problems, such as finding prime factors of large numbers. However, in truth these aren't necessarily difficult, and become 'easy' when quantum computation is in play (Shor 1994). By contrast, quantum cryptography is generally accepted to allow communications to be completely secure, even when eavesdropped on by a third party.

For example, quantum key distribution (QKD) supplements classical communication with a quantum channel. Due to quantum behaviour, any attempt to listen in on this channel disturbs the transmission. There are many protocols for QKD, including the Bennett-Brassard 1984 protocol (Bennett and Brassard 1984) and the Cabello protocol (Cabello 2000), using different behaviour to secure channels (Zhang et al. 2001).

1.1.3 Quantum sensing

Another major use-case for quantum mechanical systems is quantum sensing, taking advantage of the sensitivity of such systems to their surroundings and other quantum properties in order to perform measurements with a precision and performance greater than their classical counterparts (Degen et al. 2017).

One example of this is using squeezed states of light, in which a state's quantum uncertainty is reduced without violating Heisenberg's uncertainty principle (Walls 1983), to reduce noise in measurements (Li et al. 2016; Lawrie et al. 2019). This has notably been applied in the LIGO-Virgo-KAGRA gravitational wave observatories, to increase detection rates (Acernese et al. 2019).

Where a long roadmap remains for some other quantum technologies, advanced quantum sensors taking advantage of entanglement and other effects (Braunstein and Van Loock 2005; Degen et al. 2017) are already seeing deployment in some sectors.

This includes use in biomedical applications (Aslam et al. 2023), energy (Crawford et al. 2021), and climate science (Strangfeld et al. 2023).

1.2 Di Vincenzo’s five criteria for implementing quantum computation

DiVincenzo (2000) defined five simple criteria necessary for quantum computing technologies, which have served as a guide for researchers over the following decades since his publication (Georgescu 2020). These are:

1.2.1 Scalability with well-characterised qubits

A physical system with a collection of well-characterised qubits is needed. To be well-characterised, it is required that the system has a well-defined Hamiltonian and almost always remains in the subspace of the two levels of the qubit. While qubits may be formed using systems with a third or fourth state, the apparatus should be designed to minimise the probability of entering these states, confining it to this part of the Hilbert space (DiVincenzo and Loss 1998).

The system should also be scalable, a key challenge, as larger and larger experimental systems are often required to hold more qubits, and may be more difficult to characterise and control (DiVincenzo 2000), without introducing dissipation or decoherence (LaPierre 2021).

1.2.2 The state of qubits can be initialised to a simple fiducial state

Computation requires performing operations on qubit states and then measuring and reporting a result. This is dependent on the initial state of the system.

In many cases, initialisation is achieved by annealing the system to the ground state (DiVincenzo 2000), typically rendered $|0\rangle$. A system of spin qubits may be initialised by cooling it such that they relax to their ground state, prepared for further computations. Qubits may also be actively initialised, circumventing their relaxation time, using methods such as optical pumping (LaPierre 2021).

This is also a requirement of quantum error correction, which requires a consistent supply of qubits in the initial, low-entropy state. Thus, either the qubits need to be initialised in a time approximately equal to or less than the gate operation time, or a “conveyer belt” scheme may be required to prevent qubits from interacting with computations while they are re-initialised (DiVincenzo 2000).

1.2.3 Relevant decoherence times significantly longer than the logical gate operation time

Decoherence times describe how long it may take a qubit to be destroyed by decoherence due to contact with its environment, which on a computing level may introduce errors and loss of data. A long decoherence time is desired to allow multiple quantum gate operations (DiVincenzo 2000; LaPierre 2021).

However, remaining decoherence events may be countered using error correction (Shor 1995,1996; Steane 1996; Aharonov and Ben-Or 1997) or dynamical decoupling (DiVincenzo 2000) - averaging unwanted system-environment coupling to zero (Viola and Lloyd 1998). This prevents the decoherence time becoming a limiting factor for long-duration computations and has led to the development of error correction algorithms becoming a dominant strategy for extended operations in recent years (Bravyi et al. 2024; Klimov et al. 2024).

Quantum error correction can be made completely fault-tolerant, but this requires that the rate of errors can be kept sufficiently small to minimise them occurring during the correction process – requiring a decoherence times 10^4-10^5 times longer than the time to execute a single gate operation, or the computer “clock time” (DiVincenzo 2000).

1.2.4 A universal set of quantum gates

It must be possible to set qubits to superpositions of their two states (LaPierre 2021). While computable algorithms are restricted by the number of implementable gates, a universal quantum computer can be constructed using a small set of one and two qubit gates (DiVincenzo 2000).

A “universal” set of logical gates, in both classical and quantum computing, is able to approximate (or in the case of exact universality, reproduce exactly) the operation of any other configuration of gates (Brylinski and Brylinski 2002). In the case of classical computers, this can famously be achieved simply using “NAND” operators, which return a false output only when both their inputs are true (Sheffer 1913), and “NOR” operators, which return true only when both inputs are false (Peirce 1880).

In the case of quantum computers, a set of gates must be able to influence the total energy (i.e. the Hamiltonian) of the system to be universal (DiVincenzo 2000).

1.2.5 A qubit-specific measurement capability

For a computation result to be output, it is necessary to be able to measure the state of specific qubits to extract information. It is useful for qubits to have a high quantum efficiency, as this means measurements made are more reliable. To be efficient, a qubit must be readable to outcomes with probabilities independent of any other system parameters, including other qubits, and must not affect their state in turn (DiVincenzo 2000).

While unity quantum efficiency would be ideal, computation can be achieved at lower percentages, albeit requiring other resources. Repeated measurements can be used to produce reliable results from inefficient qubits (DiVincenzo 2000), with even efficiencies below 1% being technically feasible for ‘bulk’ calculations in some schemes (Gershenfeld and Chuang 1997). Quicker measurements, on the order of 10^{-4} times the decoherence time are ideal for simplifying error correction, as otherwise more quantum gates may be required (DiVincenzo 2000).

To give some examples of measurement methods, an atomic spin state may be read out using a Stern-Gerlach apparatus, spin-dependent fluorescence, or spin-to-spin conversion, the latter two methods being more practical (LaPierre 2021).

1.2.6 Supplementary criteria

Along with his five main criteria, DiVincenzo suggests two more linked features which are important for quantum information processing tasks beyond ‘basic’ computations such as quantum communication: “the ability to interconvert stationary and flying qubits” and to “faithfully transmit flying qubits between specified locations” (DiVincenzo 2000).

The terminology “flying qubit” (Turchette et al. 1995) is used to emphasise that qubits that are optimal for transmitting over long distances and qubits optimally used in computation (“standing qubits”) may not be encoded in the same form. In particular, flying qubits need to be transmittable over longer distances and travel times without risk of decoherence. Combined with the previous point, it thus also becomes necessary to be able to convert a qubit from one type to another.

Other than some discussions suggesting the use of electrons transmitted through solids (DiVincenzo and Loss 1999), photons were popularly seen as the ideal choice for long distance transmission of qubits at the time of publication, given the already well-established use of optical fibres (DiVincenzo 2000), and have remained so since (LaPierre 2021), being seen as only reliable option for flying qubits (Zeuner et al. 2021).

1.3 Photons as a hardware layer for quantum computing

Many different physical systems serve as possible bases for quantum computers. These include atom (Weiss and Saffman 2017) and ion traps (Bruzewicz et al. 2019), nuclear magnetic resonance (Vandersypen and Chuang 2004), superconductors, and linear quantum optics (Kok et al. 2007).

Photons (Huang et al. 2020) are ideal carriers of classical and quantum communication, quickly fulfilling several of the criteria laid out by DiVincenzo (2000). They can be transmitted over large distances and only suffer decoherence when absorbed (Hecht 2015). Linear optics-based quantum computers can also be easily scaled up to use larger numbers of photons and to have higher sampling rates. This lays the path towards performance competing with classical computers (Wang et al. 2017).

Qubits can also be encoded on to several fundamental photon degrees of freedom, including orbital angular momentum, time-bin, frequency and path (Cozzolino et al. 2019). While it is more difficult to make photonic qubits interact, as photons don't deterministically interact with each other, there are other methods that can be used, like quantum dot solid state systems that use electron spin to demonstrate single-photon switching (Sun et al. 2018).

There are several possible photonic implementations for quantum computing, but few of them are scalable, or if they are they often require challenging components like extremely efficient single-photon sources. For example, nonlinear crystals have been developed that can probabilistically produce entangled photon pairs, but this precludes deterministic operation with single-photon states. It is desirable to create a single-photon nonlinearity for optical quantum information processing (Ourjoumtsev et al. 2006).

Indeed, with photons being a viable hardware layer for qubits, single-photon sources play a crucial role in a number of quantum applications, including quantum metrology (Magnitskii et al. 2017), secure quantum communications (Kołodyński et al. 2020), quantum simulation for instance boson sampling (Wang et al. 2017; Brod et al. 2019), and scalable optical quantum computing (Raussendorf and Harrington 2007; Rudolph 2017).

There are various types of single photon source. Progress has been made in generating single photons using spontaneous parametric down-conversion (SPDC), however the brightness of SPDC sources is fundamentally limited by their Poissonian emission behaviour (Yang et al. 2020).

Semiconductor quantum dots, or ‘artificial atoms’ (Silbey et al. 2022), are one example of a promising technology that has the potential to be scaled up for the architecture of a quantum computer with continued research and development (Delbecq et al. 2014; Arakawa and Holmes 2020). The emission rates of these sources can be enhanced by taking advantage of the Purcell effect, placing the emitter inside a resonant cavity structure (Purcell 1946). This scheme is the focus of this thesis.

To be an optimal base for qubits, single photon sources need to be simultaneously pure (having a low probability of multiphoton emissions), indistinguishable (producing identical results from all parameter measurements), and efficient (Ding et al. 2016).

1.3.1 Efficiency and scalability of sources

As discussed in section 1.2.1, implementing quantum computing requires scalable qubit systems, to ensure it can be controlled and characterised as the number of qubits in the processor increases (DiVincenzo 2000) and such that information can be exchanged between stationary and flying qubits with high fidelity (Uppu et al. 2021), also one of DiVincenzo’s supplementary criteria (DiVincenzo 2000). Optical quantum applications like Boson sampling scale in efficiency exponentially over classical computation with the number of photons, so a source capable of producing many indistinguishable single-photons is desired (Tomm et al. 2021).

For example, Knill et al. (2001) produced the Knill-Laflamme-Milburn (KLM) scheme, which allows universal quantum communication using linear optics (as opposed to non-linear optics, where light interacting with matter can output beams of different wavelengths (Abramczyk 2005)) by ‘transferring’ non-linearities in photo-detectors to bosonic qubits (Knill et al. 2000; Knill et al. 2001). However, while the KLM scheme can be scaled up in-principal (Kok et al. 2007), the large resource overhead required makes this challenging (O'Brien et al. 2009).

Varnava et al. (2008) found that efficient linear optical quantum computation is possible if the product of the photon source efficiency ϵ_d and detector efficiency ϵ_s is greater than 2/3, provided the sources are perfectly pure and indistinguishable. This threshold may be reduced to >1/2 if using polarisation-entangled photon-pair sources (Gong et al. 2010). Another study, taking a source with a multi-photon component, suggests that implementing basic entanglement gates would require detector and source efficiencies of ~0.9, and single photon purities greater than 0.93 (Jennewein et al. 2011). Maximising the internal and outcoupling efficiencies of single-photon sources thus remains a vital task for quantum computing implementations, though this does not preclude use of less efficient sources in other discussed quantum applications.

1.3.2 Single photon purity

For use in quantum applications, the light from a source ideally needs to consist of only single photons per emission event. However, most light sources are designed to emit numbers of photons orders of magnitude larger.

It is possible to attenuate sources, to decrease their intensity. Take the case of a 1 mW light emitting diode (LED) pulsing at 100 MHz, which emits approximately 10^8 photons per pulse. Seemingly, one could attempt to attenuate the emission rate by using an ND8 filter to reduce its intensity down eight orders of magnitude (Macleod 2017). However, in truth, the number of photons detected per pulse is random, here following Poissonian statistics (Fox 2006b).

For a coherent state of light, the photon number probability distribution can be classically expressed as:

$$P(N_{\mathrm{p}}) = \frac{\bar{N}_{\mathrm{p}}{}^{N_{\mathrm{p}}}}{N_{\mathrm{p}}!} e^{-\bar{N}_{\mathrm{p}}} \tag{1.2}$$

Where N_{p} is the number of photons detected, while $\bar{N}_{\mathrm{p}}$ is the mean photon number (Xiao et al. 2004). Alternatively, the coherent state $|\alpha_{\mathrm{p}}\rangle$ may be described not as a statistical mix of N_{p}, but rather as a superposition of photon number (Fock) states for the pulse:

$$|\alpha_\mathrm{p}\rangle = \sum_{N_\mathrm{p}=0}^{\infty} \alpha_\mathrm{p}^{N_\mathrm{p}} \frac{e^{-|\alpha_\mathrm{p}|^2/2}}{\sqrt{N_\mathrm{p}!}} |N_\mathrm{p}\rangle \tag{1.3}$$

From this, the photon number probability distribution, i.e. the probability of the state being collapsed to a particular photon number N_p, may be expressed:

$$P(N_\mathrm{p}) = \frac{\langle N_\mathrm{p}\rangle^{N_\mathrm{p}}}{N_\mathrm{p}!} e^{-\langle N_\mathrm{p}\rangle} \tag{1.4}$$

With $\langle N_\mathrm{p}\rangle = |\alpha_\mathrm{p}|^2$ corresponding to the mean photon number (Glauber 1963; Paschotta 2019). This prevents the orderly emitting of a photon per pulse. Instead, any one pulse could contain any number of photons, with the probability of each quantity depending on the mean photon number. Fig. 1.1 shows how the probability distribution varies for a range of values for $\overline{N}_\mathrm{p}$.

As can be seen, it is not possible to produce regular single-photon emissions by using a neutral density filter. Even with a mean photon number of 1, a single photon is produced in less than 40% of emission events. It is instead necessary to develop a specialised source that can consistently produce single photons. This may be achieved using a two-level system, such as an atom.

While one may critically point out that the photon number distribution of an inefficient single photon source (e.g. of 1 % efficiency) and a Poissonian source with a low mean photon number (e.g. $\overline{N}_\mathrm{p}$ = 0.01) are similar, no amount of attenuation of the prior will eliminate the probability of multi-photon emission events.

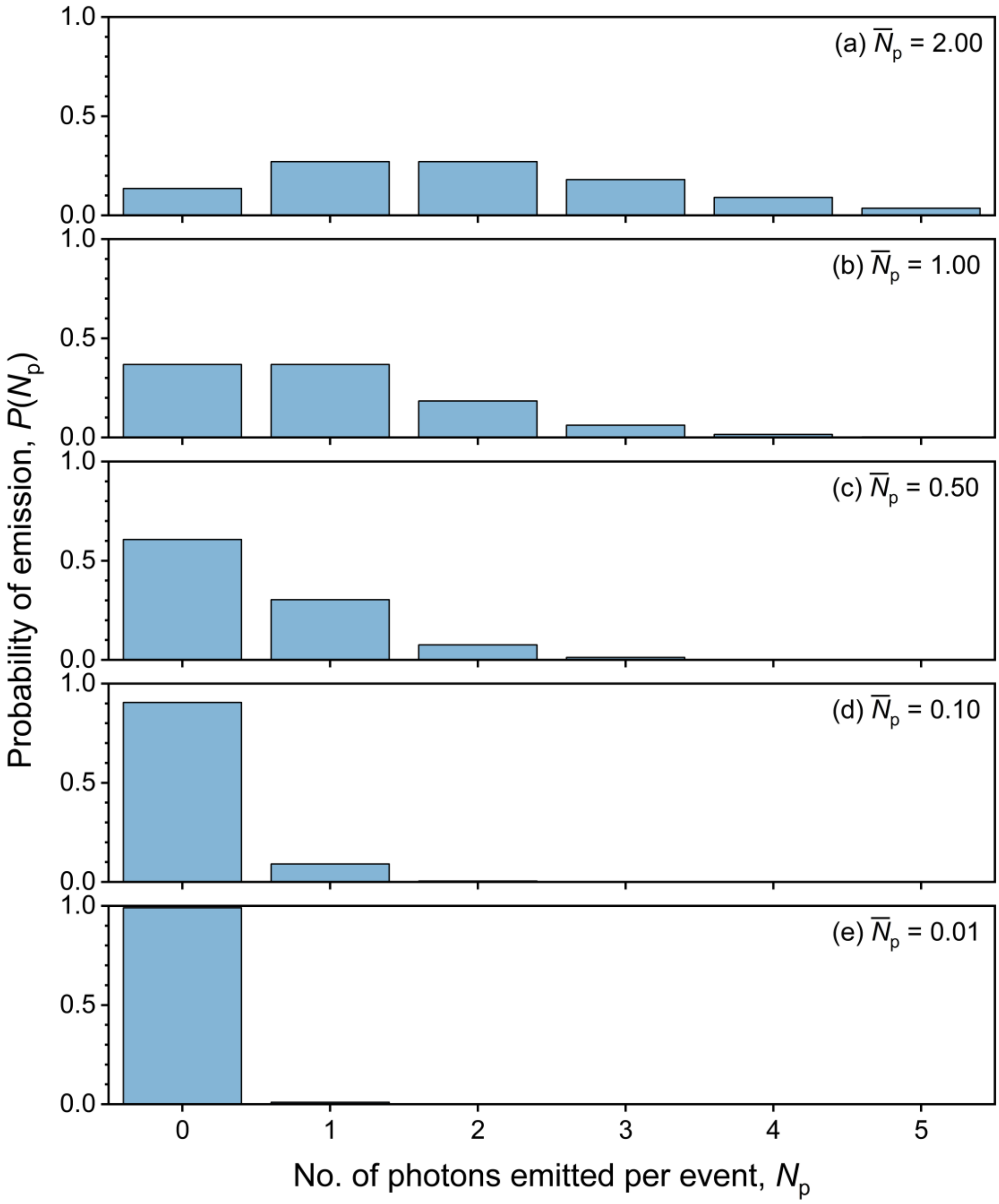

Fig. 1.1 – Probability distributions of the number of photons being emitted at any time, with various mean photon numbers $\overline{N}_\mathrm{p}$. These values were calculated using (1.2).

If a two-level atom emits a photon at a time of $t = 0$, it will be in the ground state, making it impossible to immediately emit another photon. Instead, it can only be emitted after a waiting time, which is determined by the spontaneous emission (SE) time and the re-excitation time. This results in a finite time delay between photon-emissions (Anderson 1987). Under pulsed excitation, this means that only one photon will be emitted per pulse, provided that the pulse length is much shorter than the lifetime of the system. This is called photon antibunching, measurable using a second-order correlation measurement $g^{(2)}(\tau)$, using a Hanbury Brown and Twiss (HBT) experiment (Brown and Twiss 1956), something which is discussed further in Chapter 4 and used in Chapter 6. By comparison, a Poissonian source will not show antibunching, but rather consistent spacing between subsequent photon detections. Meanwhile, a source following super-Poissonian statistics, such as a thermal source, would show bunching, in which photon detections are clustered together (Loudon 1976; Sparavigna 2021).

Increasing the number of atoms obscures this effect. Thus, strong photon antibunching can be used to show that the source of the radiation field is a single anharmonic quantum system (e.g. two-level) – when photons of a particular energy are filtered out, such as through a diffraction grating spectrometer, they are seen to be produced by a single transition. If the emitter spectrum is harmonic, or there are multiple anharmonic emitters, the detection of a photon at $t = 0$ doesn't guarantee the system is in its ground state immediately after (Michler et al. 2000a).

1.3.3 Photon indistinguishability

Applications such as linear-optical quantum computing require identical wave packets in consecutive photons, for use in implementations such as quantum gates. It is therefore important to maintain indistinguishable spectra across photons, excited deterministically with minimal dephasing (Reitzenstein and Forchel 2010). In a broad sense, two photons are considered to be identical when they cannot be discerned based on their properties, such as frequencies, momenta and polarisation (Lal et al. 2022).

The indistinguishability of a single photon source may be tested using a two-photon interference visibility measurement, or a Hong-Ou-Mandel experiment. This also offers a method for extracting the dephasing time T_2 (Hong et al. 1987; Santori et al. 2002). This method is also discussed in greater detail in Chapter 4 and utilised in Chapter 6.

Given the reliance on photon packets overlapping, the Hong-Ou-Mandel effect can be used to measure bandwidth, path lengths and timing, serving as one of the underlying physical mechanisms for logic gates in linear optical quantum computations (Knill et al. 2001). This technique has been able to measure time-intervals at an extremely small scale, with Hong et al. originally measuring to 50 fs (Hong et al. 1987). This has been demonstrated at a range of photon frequencies, including those corresponding to optical, telecom and microwave wavelengths (Lang et al. 2013). Indistinguishability in the Hong-Ou-Mandel experiment has also been observed in laser-cooled Rb atoms (Kaufman 2015).

1.4 Thesis overview

This thesis explores the design, fabrication, and performance of self-assembled InAs quantum dots embedded in GaAs-$Al_{0.95}Ga_{0.05}As$ semiconductor microcavities etched into cylindrical micropillars, for use as sources of single photons.

Chapter 2 provides some background on the requirements of a single photon source, before discussing the theory behind the generation of single photons using quantum dots and Purcell-enhancing microcavities, including micropillars. Chapter 3 provides a description of the finite-difference time-domain (FDTD) simulation techniques in this thesis. Chapter 4 similarly explains some of the experiments used in the research presented, including wavelength- and time-resolved photoluminescence, second-order correlations, and Hong-Ou-Mandel interference visibility measurements.

Chapter 5 introduces the designs of micropillar used in this thesis and simulates their properties. The fabrication process for the physical samples is outlined and the resulting etch quality is characterised. Chapter 6 continues examining the devices produced, confirming and quantifying their single photon emitter properties. Further work studies the power-dependence of some of these quantities.

Next, Chapters 7 and 8 computationally and experimentally study the non-cavity “leaky” modes of such devices, and their influence on key characteristics such as the Purcell factor, introducing new techniques to allow their study. This includes suppressing cavity modes by placing emitters in an electric field node in the cavity spacer layer and reproducing the spectrum of non-cavity modes using a micropillar uniformly consisting of a material with a refractive index averaging that of GaAs and $Al_{0.95}Ga_{0.05}As$.

Finally, some concluding remarks and suggestions for future research on quantum dots in micropillar cavities are made in Chapter 9.

Chapter 2
Background and theory

This chapter lays out the basic principles and requirements of a single-photon source for use in quantum applications, before focusing on semiconductor quantum dots and their embedding in cavity structures such as micropillars.

2.1 Semiconductor quantum dots

Quantum dots (QDs), sometimes known as ‘artificial atoms’ (Ashoori 1996), are nanoscale semiconductor particles that confine electrons and holes in all three directions. They typically have diameters on the order of tens of nm (Alivisatos 1996b) and consist of just hundreds to thousands of atoms (Fölsch et al. 2014). As their nickname implies, they exhibit atom-like symmetries and feature discrete energy levels (Banin et al. 1999), offering strong absorption and narrowband emission in both visible and infrared wavelengths (García de Arquer et al. 2021). They have also emerged as a promising source of single photons for use in quantum applications (Senellart et al. 2017).

2.1.1 Fabrication of quantum dots and self-assembly

Self-assembled quantum dots may be produced through molecular beam epitaxy (MBE). In this epitaxial growth process, atomic monolayers of the quantum dot material are deposited onto a substrate by thermal molecular beams under ultra high vacuum (UHV) conditions. At a critical thickness, dependent on the lattice parameters and surface energies of the materials, strain makes it energetically favourable for the deposited atoms to assemble into small randomly distributed nanoscale ‘islands’, producing the quantum dots (Arthur 2002). The structures used in this thesis consist of InAs dots grown on GaAs with a (100) crystal orientation. In the case of these materials, this key “lattice mismatch” is ~7% , resulting in Stranski-Krastanov growth (Gerard 1991; Khandekar et al. 2005). Under this growth method (Fig. 2.1), some atoms remain distributed over the substrate surface, forming a “wetting layer” (Stranski and Krastanow 1938; Parker 1985).

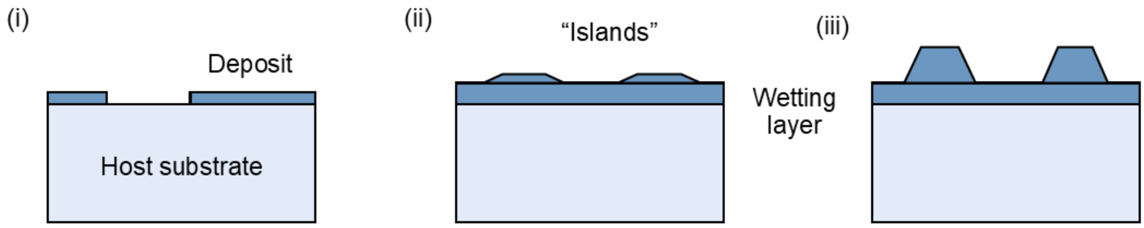

Fig. 2.1 – The Stranski-Krastanov growth method. (i) Atomic monolayers are gradually deposited. (ii) At a critical thickness, these assemble into small islands. (iii) These islands build up, forming quantum dots on a wetting layer.

Techniques are also available which can deterministically place QDs in a sample. For example, the substrate may be pre-patterned to introduce divets, which the deposits with fill preferentially (Schneider et al. 2012), or one can use “buried stressors”, in which an oxide aperture serves as a central nucleation site for islands (Große et al. 2020). Alternatively QDs may be fabricated in position using a “top-down” approach, as opposed to the “bottom-up” approach of growing quantum dots, utilising lithography-based methods to “cut” a small confining volume with dimensions down to 30 nm from an existing semiconductor layer (Bera et al. 2010; García de Arquer et al. 2021), using techniques like E-beam lithography (Dieleman et al. 2020) and focused ion beams (FIB) (Chason et al. 1997).

2.1.2 Excitonic structure of a quantum dot and its atom-like behaviour

Quantum dots are “zero-dimensional” point-like semiconductor nanostructures, as opposed to one-dimensional devices like nanowires, two-dimensional quantum wells, and three-dimensional bulk structures, with charge carriers being confined to a region around or smaller than the exciton de Broglie wavelength, $\lambda_{\mathrm{dB}} = h/p$ (De Broglie 1924), in all three spatial dimensions due to a discontinuous bandgap between the dot material and that surrounding it. This width is the characteristic diameter of the exciton, d_{X}, which may be calculated:

$$d_{\mathrm{X}} = 2a_{\mathrm{X}} = \frac{2\varepsilon_{\mathrm{r}}(\infty)m_{\mathrm{e}}}{m_{\mathrm{X}}^{*}}a_0 \tag{2.1}$$

Where a_{X} is the radius of the exciton, $\varepsilon_{\mathrm{r}}(\infty)$ is the high frequency dielectric constant, a_0 is the Bohr radius, m_{e} is the rest mass of the electron, and m_{X}^{*} is the effective mass of the exciton, given by:

$$m_{\mathrm{X}}^{*} = \frac{m_{\mathrm{h}}^{*}m_{\mathrm{e}}^{*}}{m_{\mathrm{h}}^{*} + m_{\mathrm{e}}^{*}} \tag{2.2}$$

Where m_{h}^{*} is the effective mass of a hole and m_{e}^{*} is the effective mass of the electron in the valence and conduction bands (Brus 1986; Edvinsson 2018). In most semiconductor materials, this distance ranges from about 2 to 50 nm (Alivisatos 1996a), though values around 70 nm have been reported for InAs (Puangmali et al. 2010; Reiss et al. 2016).

This confinement modifies the electronic density of states (DOS), with the function varying significantly for different levels of confinement. This is sketched for each device in Fig. 2.2 (Alivisatos 1996b; Rabouw and de Mello Donega 2017).

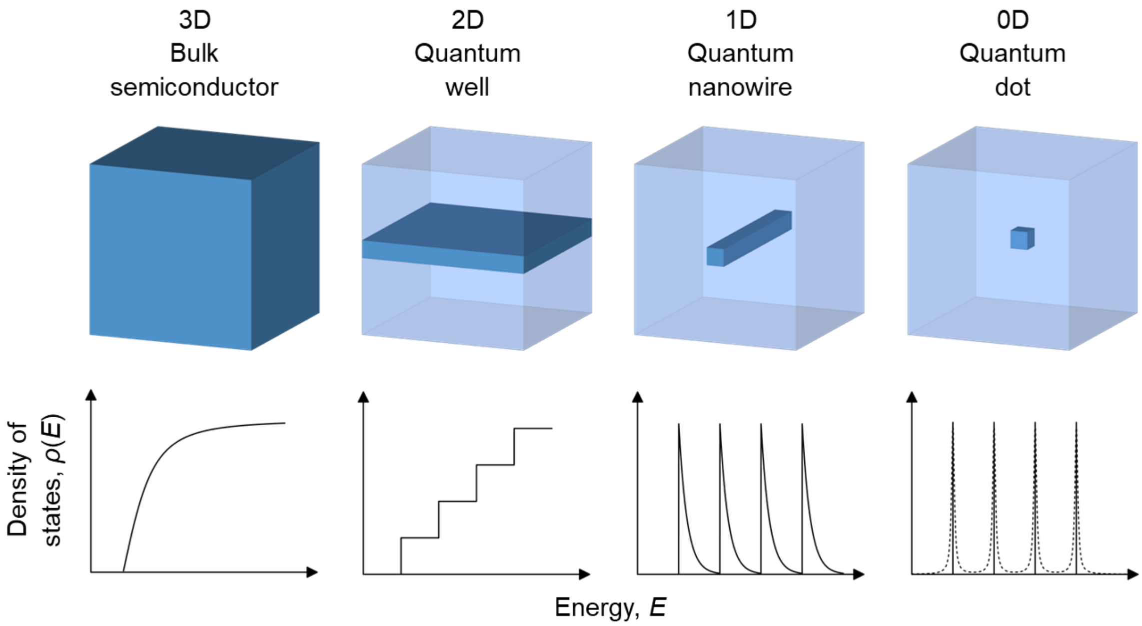

Fig. 2.2 – Different semiconductor nanostructures, with an increasing number of spatially confined dimensions. Top visualises the heterostructure geometries. Bottom shows sketches of their corresponding exitonic density of state functions.

Theoretically, the density of states in quantum dots, where all three dimensions are confined, would consist of a series of delta functions corresponding to discrete energy levels (Reed et al. 1988; Smith III et al. 1988; Kira and Koch 2011). In reality, each peak forms a Lorentzian of finite width (illustrated with a dashed line in Fig. 2.2) as the energy levels are broadened due to the lifetime of the transition. This arises from the energy-time form of Heisenberg's uncertainty principle $\Delta E \Delta T_1 \geq \hbar$ (Busch 2002), with the uncertainty in lifetime ΔT_1 and energy ΔE being related. Additional effects, such as interactions with phonons, increasing with temperature, will cause further broadening, adding a Gaussian component (Berkovits 1995).

There are four main types of quantum dots: type I, inverse type I, type II, and inverse type II. The type of a quantum dot depends on the energy gap between the valence and conduction bands of the semiconductor. A type I (inverse type I) QD has a larger (smaller) band gap than its surroundings. Type II (inverse type II) QDs have a valence (conduction) band within the bandgap of their surroundings, such that their energy gaps overlap (Bera et al. 2010; Vasudevan et al. 2015), as shown in Fig. 2.3. In type I QDs, electrons and holes are both confined within the quantum dot layer. In type II, one is confined in the QD and one outside, but remain electrically bound due to Coulomb attraction between them (Iikawa et al. 2004; Jacak et al. 2013). For example, InAs QDs in GaAs are type I.

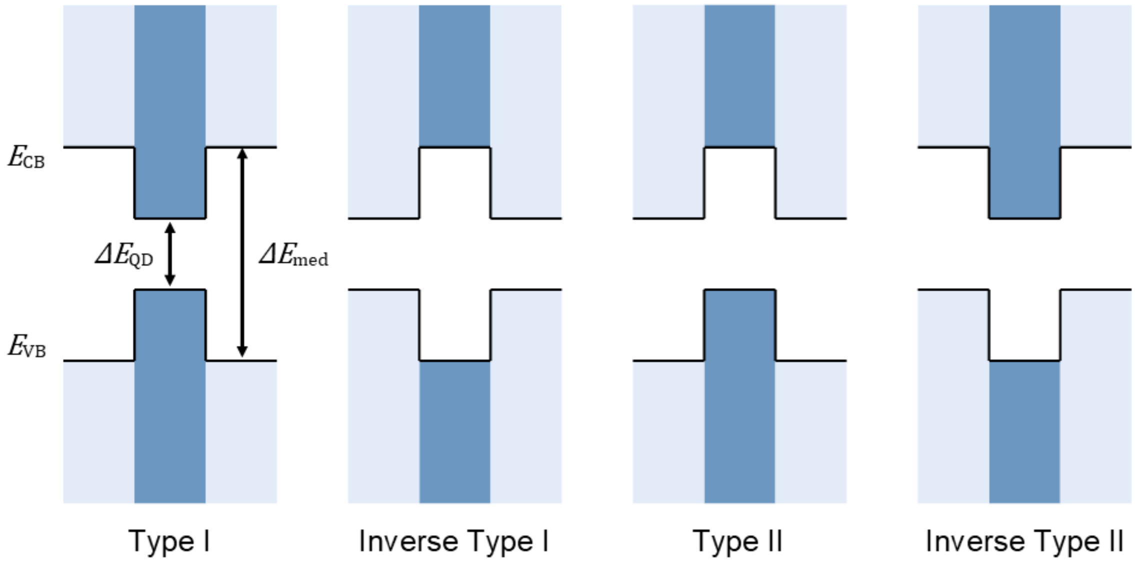

Fig. 2.3 – Band potentials for different types of quantum dot. The top energy, E_{CB}, is for the conduction band and the bottom, E_{VB}, for the valence band. The bandgaps of the quantum dot material (red), ΔE_{QD} and the surrounding medium (grey), ΔE_{med}, are indicated.

The QD may be excited resonantly, using photons with an energy equal to their resonant energy. This scheme will directly create charge carriers inside the quantum dot without delayed trapping effects which increase timing jitter anywhere between 100 ps to a few ns, reducing the emission linewidth and allowing the observation of non-classical effects like Rabi oscillations (Muller et al. 2007). They can also be excited non-resonantly, using photons with energies greater than the bandgap of the surrounding material, which will generally produce a free electron and hole in the region surrounding the QD. If repeated enough, some of these will relax into the QD, the system's lowest energy potential well (Shan et al. 2014), via mechanisms such as phonon emission (Heitz et al. 1996) and Auger processes (Paskov et al. 2000). Between the two schemes, there is also quasi-resonant excitation using photons in between the bandgaps of the QD and surrounding medium, exciting higher QD states such as a *p* and *d*-states, which then, upon relaxation into the *s*-shell, is also capable of delivering single photons (Shan et al. 2014)

Quasi-particles such as excitons and biexcitons are formed when free electrons and holes are captured by the quantum dot's potential, with up to two electrons or holes of opposite spins occupying each energy level, following the Pauli Exclusion Principle (Pauli 1925). A neutral exciton (X^0) is formed by a single electron-hole pair, forming a dipole. This is formed when an electron is excited from the valence band to the conduction band via photoexcitation, or by electrical injection (Yuan et al. 2002), leaving a hole in the prior. Two pairs form a biexciton (XX or X_2). Uneven numbers of electrons and holes form charged excitons, "trions" if there are three electrons and holes total, either positive (with one negative electron and two positive holes, X^+) or negative (with two electrons and one hole, X^-) (Safwan and El–Meshed 2015; Mermillod et al. 2016). A plot of these configurations in a type 1 InAs QD in GaAs, which have room temperature direct bandgap energies of 0.36 eV (Bouarissa and Boucenna 2008) and 1.42 eV (Hjort et al. 2013), is shown in Fig. 2.4.

As the electron returns to the valence band and recombines with a hole, they spontaneously emit a photon corresponding to the transition energy. The quantisation of these transitions results in the discrete transition lines of a QD. In the case of a biexciton, the decay occurs in a two-step cascading process, with one electron-hole pair combining first, leaving an exciton, which then decays itself. The subsequent biexciton and exciton decay energies vary typically by a few meV (Ikezawa et al. 2006; Vonk et al. 2021) despite occupying the same energy level, due to contributions from the Coulomb interaction between the carriers in the prior . This notably can be used to generate polarisation-entangled photons (Salter et al. 2010).

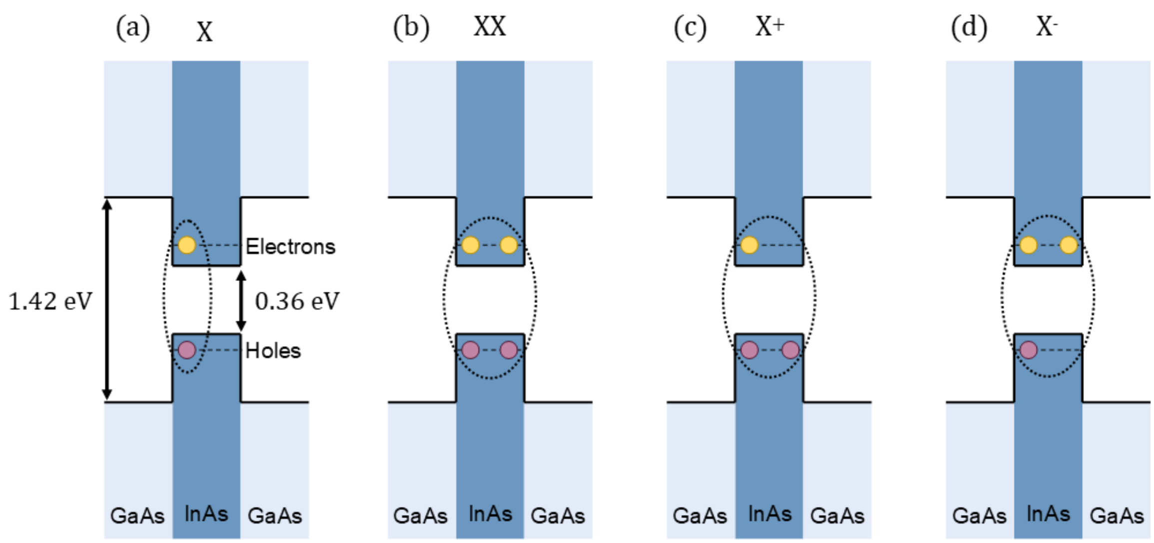

Fig. 2.4 – Electron-hole configurations in the potential of a type I InAs QD in GaAs. (a) A neutral exciton, X^0, (b) a biexciton, XX, (c) a positively charged exciton / trion, X^+, (d) a negatively charged exciton / trion, X^-.

Within an electron-hole pair, the hole has a total angular momentum of $s_\mathrm{h} = \pm 3/2$ and the electron, as mentioned previously, has a spin $s_\mathrm{e} = \pm 1/2$ (Van Kesteren et al. 1990), for four possible total z-axis angular momentums of $s_\mathrm{X} = -2, -1, +1, +2$.

When the interaction between s_e and s_h are negligible, the exciton state is four-fold degenerate. However, in the case of strong spin-orbit coupling, or in spin-dependent effects, this becomes split into two degenerate state pairs through electronic interactions dominated by the exchange interaction, along the lines of $s_\mathrm{X} = \pm 2$ and $s_\mathrm{X} \pm 1$, with the latter having a lower energy than prior. This is due to the electron spin and hole angular momentum being aligned in the case of $s_\mathrm{X} = \pm 2$, for which the exchange interaction lowers the energy. The prior form a "bright" exciton X_b, which can decay to the ground state by emitting a single photon, and the latter a "dark" exciton X_d, for which this is forbidden (Van Venrooij et al. 2024). By contrast, a biexciton has total angular momentum $s_\mathrm{X} = 0$, as it will always consist of a pair of electrons and a pair of holes each with opposite spins (de-Leon and Laikhtman 2002). In the case of trions, either the total electron or hole angular momentum will be zero, and thus the exchange interaction energy will be zero and the degeneracy is unbroken without an external field (Tischler et al. 2002).

Any elongation or strain in self-assembled QDs will further reduce the symmetry and break the degeneracy of excitons further, introducing fine-structure splitting (FSS) in the previously doubly-degenerate exciton states (Van Venrooij et al. 2024). As a result, transitions from the bright state become linearly polarised along the major and minor axes of the QD elongation, rather than circularly polarised (Seguin et al. 2005).

The excitonic spontaneous emission (SE) rate of a QD, γ_{SE}, is described by Fermi's golden rule:

$$\gamma_{\mathrm{SE}} = \frac{1}{T_1} = \frac{4\pi}{\hbar} \langle \left| \vec{\boldsymbol{d}} \cdot \vec{\boldsymbol{E}}_{\mathrm{vac}}{}^2 \right| \rangle \, \rho(\omega) \tag{2.3}$$

Where $\vec{\boldsymbol{d}}$ and $\vec{\boldsymbol{E}}_{vac}$ are the electric dipole and vacuum electric field amplitude operators respectively, and $\rho(\omega)$ is the density of states as a function of angular frequency (Fermi 1950; Reitzenstein and Forchel 2010). In a bulk volume, V, of real refractive index, n, the latter is given by (Haus 2016):

$$\rho(\omega) = \frac{V n^3 \omega^2}{\pi^2 c^3} \tag{2.4}$$

For the emission of photons from InAs QDs in bulk GaAs, the SE rate is typically on the order of 1 GHz, with the radiative lifetime around 1 ns (Heitz et al. 1997; Colocci et al. 1999). The resulting time delay between spontaneous emissions means that only single photons will be emitted at a time, resulting in anti-bunching (Michler et al. 2000a), as discussed in the previous section.

Through this, QDs are useful as a source of single photons for quantum applications, with new research producing QD systems approaching ideal single-photon source behaviour (Senellart et al. 2017). Indeed, scattering resonant, coherent light from quantum emitters to imprint quantum correlations is one of the most promising methods to obtain substantial nonlinear effects at a single-photon level (Konthasinghe et al. 2012; Wang et al. 2017). For example, the potential ability to use spin to entangle photons sequentially emitted from a QD provides options for the generation of cluster states and other multi-photonic states (Lee et al. 2019; Appel et al. 2022). It has also been observed that the nonlinearity of a transition will sort photons, modifying the counting statistics of a beam. This can be used to create strong correlations between detections and to create polarisation-correlated photons from an uncorrelated stream (Bennett et al. 2016a).

2.2 Microresonators, microcavities and micropillars

In solid state devices, it is possible to structure the local photonic environment to promote the efficient collection of photons into a lens. This can be achieved by suppressing emission into unwanted directions, such as in a photonic crystal (Englund et al. 2005; Sapienza et al. 2010), or by promoting emission into a single mode coupling well to far-field optics, such as with a nano-antenna (Claudon et al. 2010; Curto et al. 2010).

One popular wavelength-scale 3D cavity design embeds semiconductor quantum dots into a monolithic microresonator called a micropillar (Gerard et al. 1996; Vahala 2003; Reitzenstein and Forchel 2010).

2.2.1 Introduction to microcavities and micropillars

A microcavity is a three-dimensional structure consisting of a spacer layer between distributed Bragg reflectors (DBRs). The spacer layer, of refractive index n_{cav}, has thickness $K_{\mathrm{cav}}\lambda_0/n_{\mathrm{cav}}$, where K_{cav} is some multiple of ½, most commonly equal to 1, such that the spacer is one wavelength thick ($\lambda_0/n_{\mathrm{cav}}$). The DBRs consist of repeated, alternating quarter-wavelength ($\lambda_0/4n_{\mathrm{DBR}}$) thick layers of low and high refractive indices, n_1 and n_2. Light within the cavity is partially reflected at the layer boundaries, interfering to form cavity modes within the highly reflective stopband of the DBRs at the design wavelength λ_0, with an electric field maximum (anti-node) in the spacer layer. The stopband becomes more reflective with increasing DBR periods, though this may come with a downside of increased scattering and absorption.

A low density layer of QDs is typically positioned at the anti-node in the cavity field to maximise coupling to the fundamental HE_{11} cavity mode, i.e. the hybrid mode HE $_{k_A k_R}$ of azimuthal and radial wavenumbers $k_A = k_R = 1$ (Connor 1972; Reitzenstein and Forchel 2010), discussed further in Section 2.2.2.

A pillar microcavity, or "micropillar", is formed by etching a planar microcavity down to a cylindrical shape to confine the lateral modes of the structure. An example of a GaAs/AlAs micropillar with InGaAs QDs is presented below in Fig. 2.5.

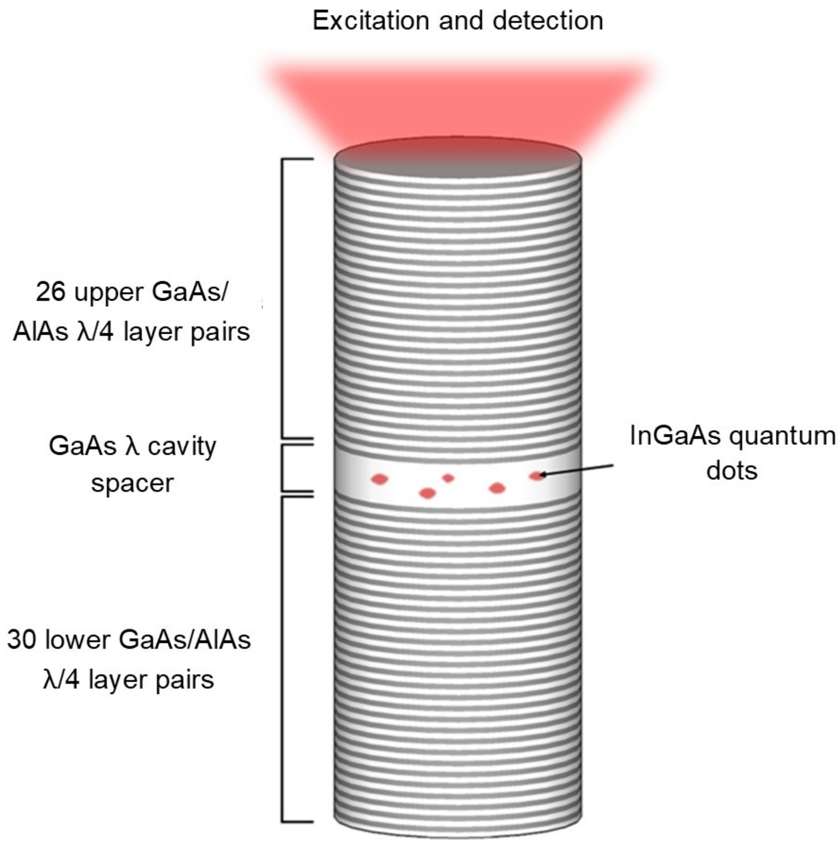

Fig. 2.5 – Sketch of a micropillar structure with light coupled through the top facet, consisting of many InGaAs quantum dots embedded in a GaAs wavelength-size cavity, with 26 upper and 30 lower GaAs/AlAs pairs of quarter-wavelength DBR layers .

In this case, and in those examined in this thesis, the micropillar is driven using laser light coupled in through the top of the micropillar. It is also via the pillar top that most of cavity mode-coupled light is emitted.

Various processing methods exist to pattern planar microcavity samples for etching pillar structures, which may in turn be achieved using techniques like inductively coupled plasma (ICP) etching (Pearton et al. 2000; Booker et al. 2020). The most popular of these options is electron-beam lithography. Another option, developed and discussed within this thesis, is maskless direct-write lithography (Androvitsaneas et al. 2023).

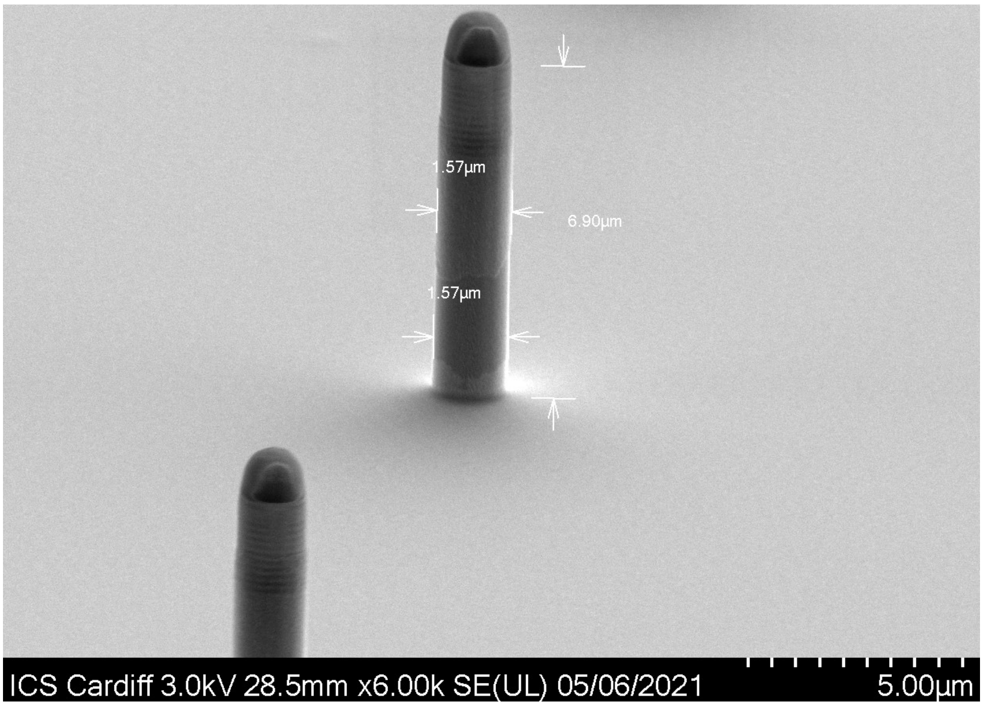

Fig. 2.6 – Scanning electron microscopy (SEM) image of a micropillar cavity processed in Cardiff in May 2021 by Dr Petros Androvitsaneas and Dr Rachel Clark, using a direct-write lithography-based method. The dark, rounded material on the top of the pillar is Silicon Oxide, to be removed in later processing steps.

Recent years have seen steady progress towards unity efficiency, single-photon purity and indistinguishability for a number of different etched designs, including Bragg gratings and micropillars (Bennett et al. 2016b; Ding et al. 2016; Wang et al. 2019a; Wang et al. 2020a; Tomm et al. 2021) driven by advances in processing (Ding et al. 2016), in-situ lithography (Dousse et al. 2010), and coherent excitation (Muller et al. 2007; Nick Vamivakas et al. 2009).

For example, in one study, an open tuneable, microcavity containing gated quantum dots was found to ensure low noise during operation and position emission frequency. Highly coherent single-photons were detected with a probability of 57%, with a repetition rate in the GHz (Tomm et al. 2021), a particularly impressive result given that many other authors exclude detection efficiencies from their reported values. In another experiment, pulsed resonant excitation of a Purcell-enhanced QD-micropillar system generated resonance fluorescence single-photons, combining high purity (99.1%), efficiency (66% - inferred into the first lens, but with a far lower detection efficiency) and indistinguishability (98.5%) (Ding et al. 2016). This, and similar results, are included in Table 2.1 below.

For the sake of clarity amid differences in reporting, efficiencies are noted with their corresponding used definitions: “first lens” referring to the number of polarised photons extracted from the bulk semiconductor and collected per pulse at the first lens, “end-to-end” referring to the full source to detector efficiency, the latter being much harder to optimise.

Table 2.1 – Recent single-photon source designs and results, presented chronologically by publication date.

Author	Experimental setup	Efficiencies	Purity $(1-g^{(2)}(0))$	Indistingu-ishability
Ding et al. (2016)	Purcell-enhanced QD-micropillar system, of 2.5 μm diameter with a GaAs cavity sandwiched between 25.5 lower and 15 upper $\lambda/4$ Bragg reflector pairs. Excited with 897.44nm laser pulses.	33.0 % (first lens) 4.6 % (end-to-end)	99.1 %	98.5 %

Somaschi et al. (2016)	In(Ga)As QD embedded in a GaAs micropillar cavity sandwiched between 30 lower and 20 upper GaAs and $Al_{0.9}Ga_{0.1}As$ Bragg reflector layers. Doped, and an electrical bias is applied.	16 % (first lens)	99.4 %	99.6 %
Wang et al. (2017)	InAs/GaAs QD coupled to a 2 μm diameter λ thick micropillar cavity, between 25.5 lower and 15 $\lambda/4$ AlAs/GaAs Bragg reflector pairs. Excited with 893.2 nm laser pulses.	28.4 % (end-to-end)	97.3 %	93.9 %
He et al. (2018)	λ thick elliptical micropillar with major/minor axes of 2.1/1.4 μm with a InAs/GaAs QD sandwiched between 25.5 lower and 15 upper $\lambda/4$ AlAs/GaAs Bragg reflector pairs. Excited with 874.13 nm laser pulses.	15.0 % (end-to-end)	99.5 %	97.6 %
Wang et al. (2019a)	Narrow-band elliptical micropillar with major/minor axes of 2.1/1.4 μm with a GaAs/InAs QD sandwiched between 25.5 lower and 15 upper $\lambda/4$ AlAs Bragg reflector pairs.	60 % (first lens) 24 % (end-to-end)	97.5%	97.5 %
	Broad-band elliptical Bragg grating, with a central disk of major/minor axes 770/775 nm surrounded by an elliptical grating with periods 380/372 nm and fully etched 100 nm wide trenches.	56 % (first lens)	99.1 %	95.1 %
Tomm et al. (2021)	Gated QDs in an open tuneable Fabry-Perot microcavity. Used a wavelength of 920 nm.	57.0 % (end-to-end)	97.9 %	96.7 %
Ginés et al. (2022)	In(Ga)As QD embedded in a 2.02 μm diameter GaAs micropillar cavity sandwiched between 18 lower and 5 upper GaAs and AlAs Bragg reflector layers.	69.4 % (first lens)	98.4 % (exciton) 99.1 % (biexciton)	47 % (biexciton)

2.2.2 Modes of a micropillar

When a micropillar is etched, the sidewalls laterally confine the field, splitting it into many modes at increasing levels of blueshift from the design energy. For a micropillar, these hybrid modes are designated HE $_{k_\mathrm{A}k_\mathrm{R}}$ or EH $_{k_\mathrm{A}k_\mathrm{R}}$, depending on whether the magnetic or electric fields are dominant respectively, where k_A = 0, 1, 2… is the azimuthal wavenumber, and k_R = 1, 2, 3… is the radial wavenumber (Connor 1972; Reitzenstein and Forchel 2010).

Each of these modes will have differing transverse electric field distributions. The electric field x-y amplitude profiles and vector field directions are sketched for the first six modes in Fig. 2.7 below. Note only HE_{11} of these has a non-zero component at the centre of the cavity.

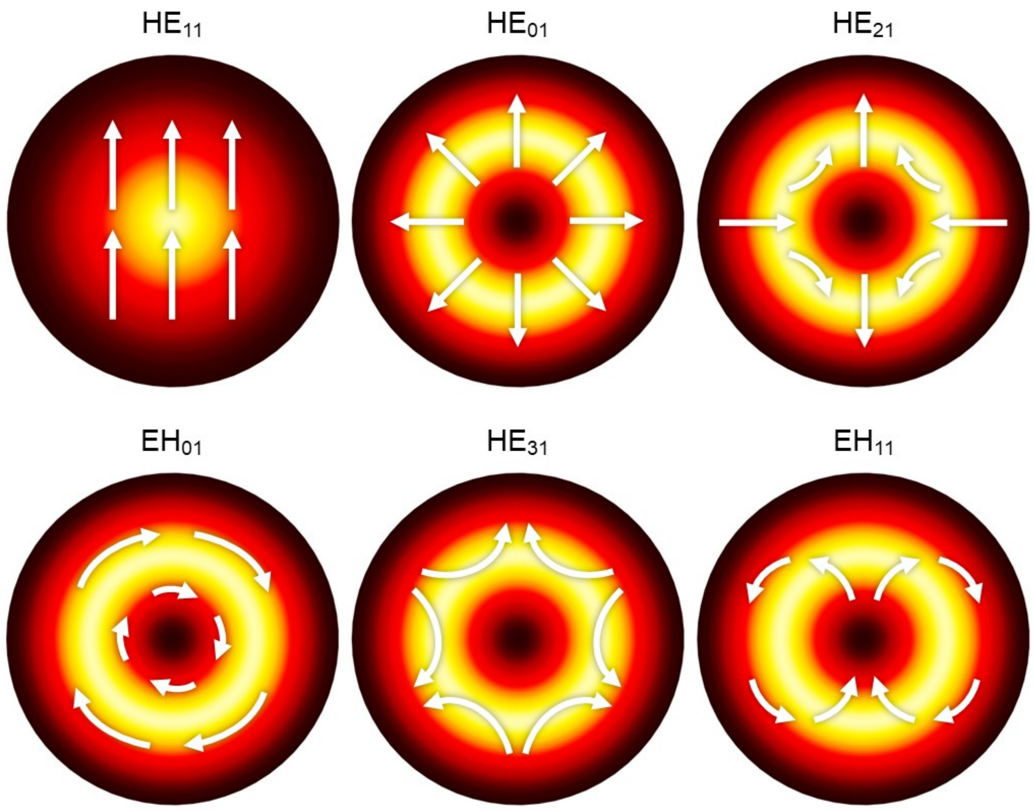

Fig. 2.7 – Sketched $\vec{\boldsymbol{E}}$-field amplitudes and vector field patterns for the first six cavity modes, from HE_{11} to EH_{11}.

Each mode which isn't circularly symmetrical (HE_{11}, HE_{21}, HE_{31}, EH_{11}...) will have even and odd polarised vector field solutions. This allows the HE_{11} mode to be divided into two linearly polarised components of phase difference $\frac{\pi}{2}$. Ideally, these are degenerate, but any amount of ellipticity in the microstructure will result this degeneracy being lifted, forming two linearly polarised modes orthogonal to one another, oriented along the major and minor axis of the elliptical cross-section (Gayral et al. 1998; Wang et al. 2019a; Zhang et al. 2021). These modes' energies will be split approximately proportional to the ellipticity, and the pillar may be described using an effective diameter $d_{\mathrm{eff}} = 2\sqrt{d_{\mathrm{a}} d_{\mathrm{b}}}$, where d_{a} and d_{b} are the long and short axes of the ellipse (Gayral et al. 1998).

The blueshifted energies of each mode may be obtained from the equation:

$$E_{\mathrm{c}} = \sqrt{E_0^2 + \frac{\hbar^2 c^2}{\varepsilon_{\mathrm{r,eff}}} \frac{4X_{\varphi,N_0}^2}{d^2}} \tag{2.5}$$

Where E_0 is the resonance energy of the microcavity, $\varepsilon_{\mathrm{r,eff}}$ is the effective dielectric constant of the micropillar, d is its diameter, and X_{φ,N_0} is the N_0^{th} zero of the Bessel function of order φ, using parameters corresponding to each mode(s) (Heuser et al. 2018). This may be rewritten in terms of wavelength:

$$\frac{1}{\lambda_{\mathrm{c}}^2} = \frac{1}{\lambda_0^2} + \frac{X_{\varphi,N_0}^2}{\varepsilon_{\mathrm{r,eff}} \pi^2 d^2} \tag{2.6}$$

To provide an example of these relationships, Fig. 2.8 shows the wavelengths of modes from HE_{11} to EH_{21} and over diameters 1.5 to 4.7 μm collected over various FDTD simulations of GaAs/$Al_{0.95}Ga_{0.05}As$ micropillars with 7 (26) upper (lower) DBR pairs, using methods discussed in Chapter 3. As some modes have zero components at the centre of the spacer, not all would be visible by simply exciting with an electric dipole source at that position. Instead, several sources were distributed randomly and cylindrically asymmetrically throughout the layer with various in-plane orientations.

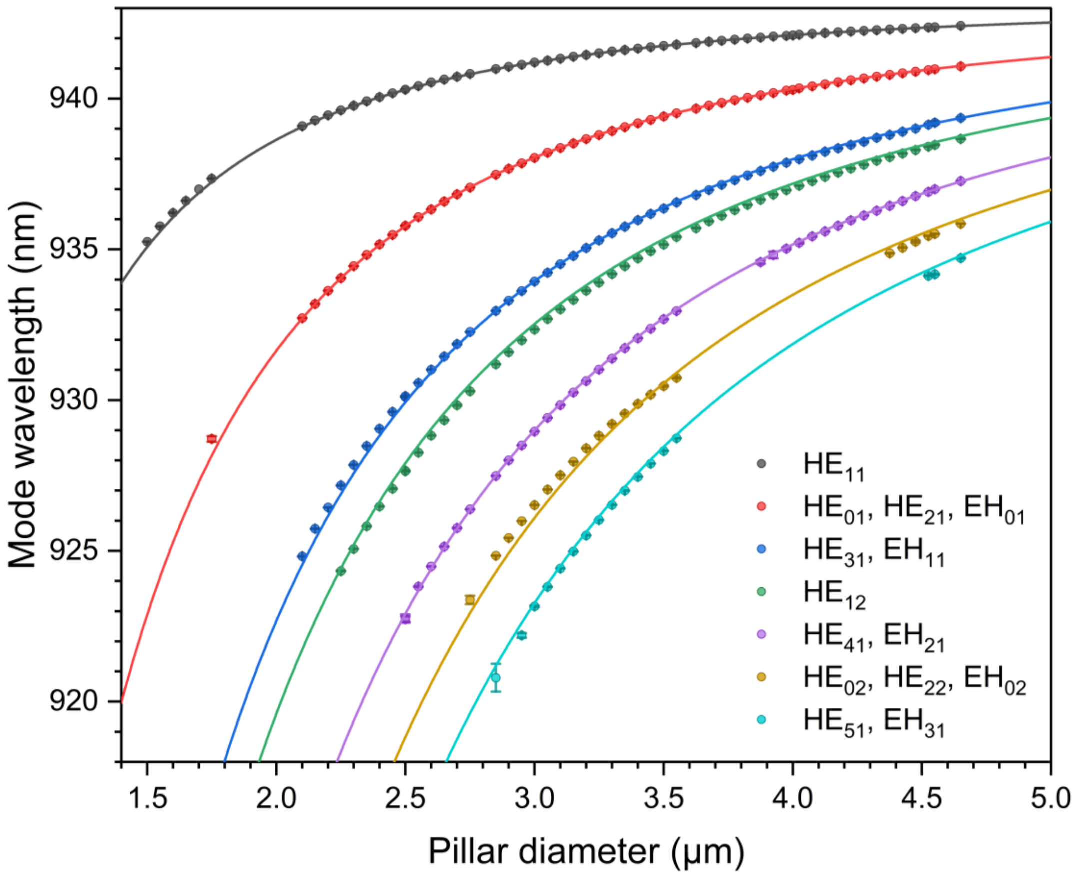

Fig. 2.8 – Fitted mode wavelengths, including higher order modes, of a GaAs/$Al_{0.95}Ga_{0.05}As$ micropillar with 7 (26) upper (lower) DBR pairs as a function of diameter, as simulated in Lumerical FDTD.

As may be seen, the modes approach the design wavelength as the diameter increases. Each mode peak has been fitted with (2.6), using global values for the planar wavelength and effective dielectric constant. As different modes are being fitted, however, the value of x_{φ,N_0} must be specialised in each case. The values calculated and used for each of these are specified in Table 2.2.

Table 2.2 – Micropillar modes and their corresponding Bessel function zero parameters and results, as used in globally fitting modes with wavelength using (2.5) (Kowalski et al. 2010; Le Kien et al. 2017).

Mode	Order, φ	Ordinal Number, N_0	Corresponding Bessel Function Zero, X_{φ,N_0}
HE_{11}	0	1	2.40483
HE_{01}, HE_{21}, EH_{01}	1	1	3.83171
HE_{31}, EH_{11}	2	1	5.13562
HE_{12}	0	2	5.52008
HE_{41}, EH_{21}	3	1	6.38016
HE_{02}, HE_{22}, EH_{02}	1	2	7.01559
HE_{51}, EH_{31}	4	1	7.58834

Fitting all the modes globally allows an accurate determination of fit parameters for the effective dielectric constant and design (planar) wavelength of $\varepsilon_{\mathrm{r,eff}}$ = 13.17 ± 0.01 and λ_0 = (943.269 ± 0.004) nm respectively.

Note that several of the modes are degenerate. While these can diverge from each other due to ellipticity of the micropillar, they are still clustered around Bessel function numbers used. In these simulations, they cannot be distinguished and are thus fitted as a single mode group. Some of the non-degenerate modes also overlap with each other due to the micropillar's low Q factor, as well as with the structure's non-cavity modes, and thus ambiguous fitting may contribute quite significantly to inaccuracies in the data points plotted. As can be seen, while the placement of data points broadly follows the fitted curves.

Regardless, in this thesis we are primarily concerned with the HE_{11} mode, which shows the smallest blueshift from the design wavelength and has the smallest mode volume. In the x, y plane, this mode follows a transverse electric field distribution $\vec{\boldsymbol{E}} \propto J_0(k_{\mathrm{t}} r)$, with J_0 being the Bessel function of the first kind of zeroth order, k_{t} being the transverse wavevector, and r being the radial displacement from the central axis. This property is utilised for determining the losses via etched sidewalls and the effect on the device's quality factor in the next section. This distribution is approximately Gaussian, making it a good choice for optimal coupling into an output fibre (Rivera et al. 1999; Reitzenstein and Forchel 2010).

Meanwhile, Fig. 2.9 shows an example of the longitudinal electric field distribution, plotting the normalised absolute electric field as a function of height in 2.00 μm diameter GaAs/$Al_{0.95}Ga_{0.05}As$ micropillar with 17 (26) upper (lower) DBR pairs, as measured on the central axis (at $x = y = 0$). As may be seen, the field oscillates through subsequent nodes and anti-nodes with height, centred on a maximum anti-node at $z = 0$, where the emitter(s) are placed. This is thus the optimal height at which a QD layer can be grown to maximise coupling to the cavity.

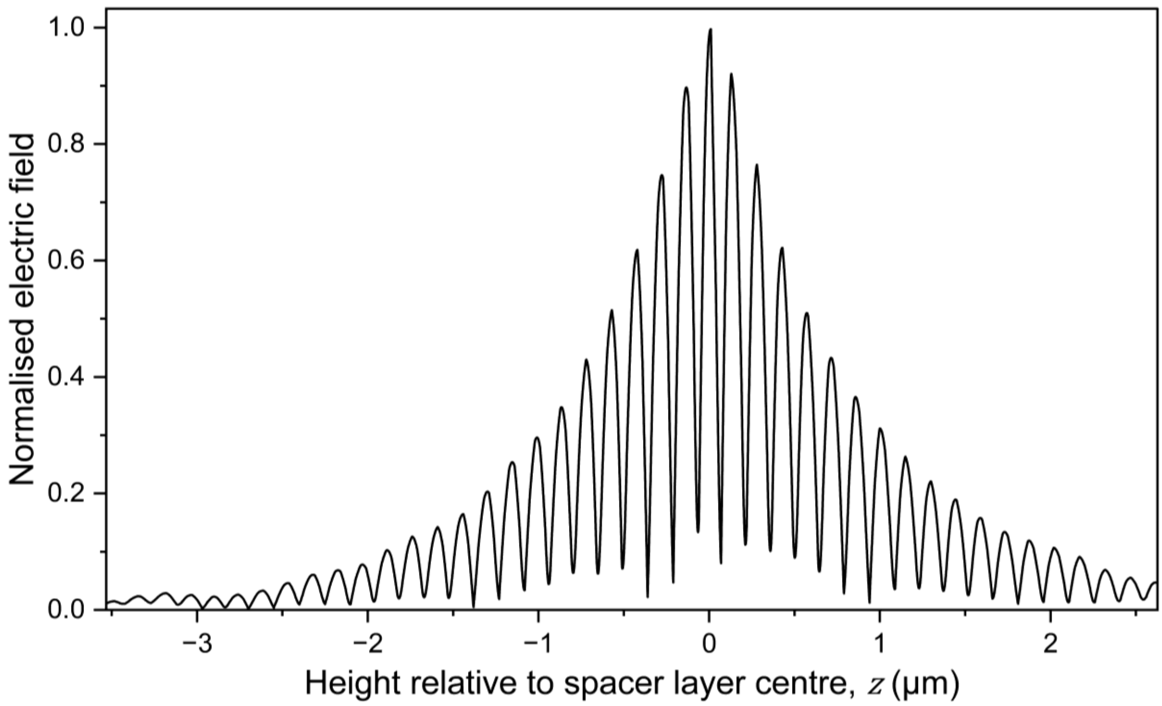

Fig. 2.9 – Normalised electric field amplitude as a function of height relative to the centre of the GaAs spacer layer, where a dipole is placed, in a 2.00 μm diameter GaAs/$Al_{0.95}Ga_{0.05}As$ micropillar with 17 (26) upper (lower) DBR pairs.

2.2.3 Quality factor

The damping of a resonator is described by its quality factor, Q: a unitless parameter defined either as the amount of energy lost per radian of the oscillation or as the ratio of a resonance mode's wavelength, λ_c, to its full-width-half-maximum, $\Delta\lambda$, (or conversely its centre frequency, f_c, to its linewidth, Δf):

$$Q = \frac{\lambda_\mathrm{c}}{\Delta\lambda} = \frac{f_\mathrm{c}}{\Delta f} \tag{2.7}$$

The quality factor of a planar microcavity, Q_0, of design wavelength, λ_0, may be written (Schubert 2018; Jackson 2021):

$$Q_0 = \frac{2n_\mathrm{cav}L_\mathrm{eff}}{\lambda_0}\frac{\pi}{1 - R_\mathrm{l}R_\mathrm{u}} \tag{2.8}$$

L_eff is the effective cavity length, the length of an ideal planar mirror cavity equivalent to the Bragg cavity. This can be approximated using the cavity spacer layer's thickness and the 'penetration depth' L_DBR:

$$L_\mathrm{eff} \approx L_\mathrm{cav} + 2L_\mathrm{DBR} \tag{2.9}$$

L_DBR describes the extent to which the electric field extends into the DBRs, itself dependent on the thicknesses of the λ/4 DBR layers, L_1 and L_2, and the effective number of mirror pairs, M_eff:

$$\mathrm{L_{DBR}} = \frac{1}{2}M_\mathrm{eff}(L_1 + L_2) \tag{2.10}$$

$$M_\mathrm{eff} \approx \frac{1}{2}\frac{n_1 + n_2}{n_1 - n_2} \tag{2.11}$$

Finally, R_u and R_l are, respectively, the reflectivity coefficients of the upper and lower stacks of DBRs. These are generally calculated for a DBR stack of M_DBR mirror pairs between external mediums of refractive index n_above and n_below (Reitzenstein and Forchel 2010; Born and Wolf 2013; Schubert 2018):

$$R_{\mathrm{DBR}} = \frac{1 - \frac{n_{\mathrm{above}}}{n_{\mathrm{below}}} \times \left(\frac{n_1}{n_2}\right)^{2M_{\mathrm{DBR}}}}{1 + \frac{n_{\mathrm{above}}}{n_{\mathrm{below}}} \times \left(\frac{n_1}{n_2}\right)^{2M_{\mathrm{DBR}}}} \tag{2.12}$$

For a GaAs/$Al_{0.95}Ga_{0.05}As$ micropillar on a GaAs substrate, with a GaAs-air top interface, this is thus written for each stack:

$$R_{\mathrm{u}} = \frac{1 - \frac{n_{\mathrm{air}}}{n_{\mathrm{GaAs}}} \times \left(\frac{n_{\mathrm{Al_{0.95}Ga_{0.05}As}}}{n_{\mathrm{GaAs}}}\right)^{2M_{\mathrm{u}}}}{1 + \frac{n_{\mathrm{air}}}{n_{\mathrm{GaAs}}} \times \left(\frac{\mathrm{n}_{Al_{0.95}Ga_{0.05}\mathrm{As}}}{n_{\mathrm{GaAs}}}\right)^{2M_{\mathrm{u}}}} \tag{2.13}$$

$$R_{\mathrm{l}} = \frac{1 - \frac{n_{\mathrm{GaAs}}}{n_{\mathrm{GaAs}}} \times \left(\frac{n_{\mathrm{Al_{0.95}Ga_{0.05}As}}}{n_{\mathrm{GaAs}}}\right)^{2M_{\mathrm{l}}}}{1 + \frac{n_{\mathrm{GaAs}}}{n_{\mathrm{GaAs}}} \times \left(\frac{\mathrm{n}_{Al_{0.95}Ga_{0.05}\mathrm{As}}}{n_{\mathrm{GaAs}}}\right)^{2M_{\mathrm{l}}}} \tag{2.14}$$

Where M_{u} and M_{l} are the numbers of mirror pairs in the upper and lower stack respectively. Together these terms allow one to predict the quality factor of a planar microcavity, albeit neglecting absorption effects. This and another term, $1/Q_{\mathrm{s}}$, may be integrated into a more complete equation, to calculate the quality factor of a cylindrical micropillar (Slusher et al. 1993):

$$\frac{1}{Q} = \frac{1}{Q_0} + \frac{1}{Q_{\mathrm{s}}} + \frac{1}{Q_{\mathrm{abs}}} \tag{2.15}$$

Here, the denominator of the first term, Q_0, is the intrinsic quality factor of the micropillar independent of diameter. This is identical to the quality factor of a planar microcavity with the same layer structure, as given by (2.8).

The second denominator, Q_{s}, is the sidewall component, dependent on the light scattered through the pillar edges due to roughness which acts as an alternative emission channel, degrading the cavity Q factor. As the radius of the pillar is increased, the surface area of the micropillar increases and the proportional roughness relative to the pillar size decreases. This relationship thus gives the diameter dependent component of the Q factor (Barnes et al. 2002):

$$\frac{1}{Q_{\mathrm{s}}} = \kappa_{\mathrm{s}} \frac{2J_0^2(k_{\mathrm{t}}d/2)}{d} \tag{2.16}$$

where κ_{s} is a loss coefficient representing the roughness of the pillar sidewalls, k_{t} is the transverse wavevector, and d is the diameter of the micropillar. The Bessel function of the first kind J_0 describes the electric field distribution of the fundamental mode, such that the component $J_0^2(k_{\mathrm{t}}d/2)$ describes the intensity at the pillar edge (Rivera et al. 1999; Reitzenstein and Forchel 2010). The transverse wavevector may be calculated $k_{\mathrm{t}} = \sqrt{n_{\mathrm{eff}}^2 k_0^2 - \beta_{\mathrm{HE}_{11}}^2}$, where $\beta_{\mathrm{HE}_{11}}$ is the HE_{11} mode propagation constant and k_0 is the longitudinal mode wavevector (Rivera et al. 1999; Huber et al. 2020; Wang et al. 2020a).

Finally, there is also the component describing the losses due to absorption in a material:

$$\frac{1}{Q_{\mathrm{abs}}} = \frac{\lambda \alpha_{\mathrm{M}}}{2\pi n} \tag{2.17}$$

where α_{M} is the diameter independent absorption coefficient and n is the real refractive index of the material (Asano et al. 2006). This absorption arises from a materials extinction coefficient n_{i}, i.e. the imaginary part of the materials complex refractive index $\underline{n}$, which is related to the absorption coefficient (Hecht 2002):

$$\alpha_{\mathrm{M}}(\lambda) = \frac{4\pi n_{\mathrm{i}}}{\lambda} \tag{2.18}$$

In practise, this component is typically negligible in micropillars with quality factors below magnitudes ~ 10^5 (Wang et al. 2020a), with sidewall losses instead being the dominating loss channel in small diameter pillars (Reitzenstein and Forchel 2010; Al-Jashaam 2020). However, absorption is typically increased in doped structures, being proportional to the dopant concentration and the light field strength (Reitzenstein and Forchel 2010).

A typical value of the low temperature absorption coefficient in undoped GaAs around our target wavelength is around 1 cm^{-1}. AlAs meanwhile has absorption coefficient orders of magnitude smaller (Karl et al. 2009). Given that the micropillars studied in this thesis are composed approximately half of GaAs and half AlAs, the effective absorption coefficient may thus be approximated to α_{M} ~ 0.5 cm^{-1}. This, combined with an effective refractive index of n_{eff} ~ 3.7, based on an effective dielectric constant obtained from fitting experimental data in Chapter 5, then returns an absorption loss component of Q_{abs} = 4.95 × 10^6. For a high Q micropillar of intrinsic quality factor Q_0 = 22,500, this would only reduce Q to around 21,500. The reduction due to absorption is even smaller if scattering losses are included. With all this considered, this loss channel will be neglected throughout this thesis.

2.2.4 Purcell enhancement and mode coupling

In the “weak coupling” regime, where the coupling strength is well below the cavity mode or emitter linewidth, a transition’s emission rate is increased on resonance via Purcell enhancement (Moreau et al. 2001; Vahala 2003), resulting in reduced emission into non-cavity modes (Androvitsaneas et al. 2016). The coupling between a single transition and the cavity mode at zero detuning is quantified by the Purcell factor F_{P}, typically defined as the ratio of the radiative decay rate inside the cavity, given by the sum of the decay into the localised cavity mode Γ_{C} and the decay into the non-cavity, leaky modes Γ_{L} (Fox 2006a), relative to the radiative decay rate in a uniform homogenous medium Γ_0. In the case where Γ_{C} >> Γ_{L} the Purcell factor can also be approximated analytically using the mode volume V_{m}, quality factor Q, and effective refractive index n_{eff} (Purcell 1946):

$$F_{\mathrm{P}} = \frac{\Gamma_{\mathrm{C}}+\Gamma_{\mathrm{L}}}{\Gamma_0} \approx \frac{3Q\lambda^3}{4\pi^2 V_{\mathrm{m}} n_{\mathrm{eff}}^3} \tag{2.19}$$

A rigorous derivation and definition of the mode volume and the Purcell effect is given by Muljarov and Langbein (2016).

Multiple methods exist for experimentally determining F_{P} (Munsch et al. 2009), but the most direct is to measure the decay of the emission intensity in time. In solid state systems, it is not always possible to make a comparable measurement of the decay Γ_0 for the same source, and therefore authors estimate Γ_0 from an emitter assumed to be comparable in another sample (Gérard et al. 1998). Alternatively, the transition-mode detuning can be varied by temperature (Munsch et al. 2009; Engel et al. 2023), deposition (Hennessy et al. 2006), static electric (Nowak et al. 2014) or magnetic (Jenkins and Segre 1939) fields. Besides the fact that these control parameters may lead to a change in Γ_0 and Q to some extent, there is an implicit assumption that a decay rate detuned from a mode, Γ_{L}, is comparable to that in a homogenous medium, Γ_0. However, this is generally not the case because the inhomogeneous dielectric environment and its influence on the local photon density of states (LDOS) remains. It should be noted, however, that the notion of emission into individual modes is approximate as this LDOS should be expressed as a sum over all modes of the system and interference occurs between modes (Muljarov and Langbein 2016), some of which effectively contribute negative emission rates.

The fraction of photons emitted into the cavity mode is called the spontaneous emission coupling factor, or β factor (Björk et al. 1993). It is thus related to the Purcell factor by:

$$\beta = \frac{\Gamma_{\mathrm{C}}}{\Gamma_{\mathrm{C}} + \Gamma_{\mathrm{L}}} = \frac{F_{\mathrm{P}}}{F_{\mathrm{P}} + 1} \tag{2.20}$$

The direction of emission can be quantified using a ‘cavity directionality’ parameter , often referred to as the ‘coupling efficiency’. While definitions vary among authors (Liu et al. 2017; Androvitsaneas et al. 2019; Wang et al. 2020a), here it is defined as a simple measure of the proportion of the cavity emissions, approximated based on the total emissions directed upwards or downwards, that is directed to the top of the pillar where a collection optic would be placed:

$$\eta = \frac{\Gamma_{\mathrm{up}}}{\Gamma_{\mathrm{up}} + \Gamma_{\mathrm{down}}} \tag{2.21}$$

This effectively quantifies the “one-sidedness” of the pillar’s cavity mode emissions. To optimise collection efficiency, it is thus desired to maximise this value (Androvitsaneas et al. 2019).

These figures of merit may be combined, defining a more precise outcoupling efficiency parameter ξ as the fraction of the total power integrated over all directions $\Gamma_{\mathrm{C}} + \Gamma_{\mathrm{L}}$ that is directed towards the top of the micropillar specifically via the cavity mode Γ_{out}:

$$\xi = \frac{\Gamma_{\mathrm{out}}}{\Gamma_{\mathrm{C}} + \Gamma_{\mathrm{L}}} \tag{2.22}$$

2.2.5 Phonon-assisted coupling

Along with Purcell-enhancement, the emission behaviour of a QD-micropillar system will also be affected by vibrational states such as phonons. These are quasi-particles, representing a collective excited state in the vibrational modes of a particle lattice, effectively a quantum of vibration (and thus sound or heat) in the same way that a photon is a quantum of the electromagnetic field (Dyson and Derbes 2011; Girvin and Yang 2019), hence the name.

Phonons play a significant role in the relaxation of QD charge carriers. As mentioned previously, it is interactions with phonons in the embedding medium that result in transition zero-phonon lines broadening into a Gaussian shape rather than the delta function theoretically predicted by the 3D confinement of the density of states. This is referred to as phonon-induced dephasing (Muljarov et al. 2005; Denning et al. 2019; Morreau and Muljarov 2019). As phonons represent a vibrational state, their intensity will increase with temperature, further broadening the transition peak (Berkovits 1995), hence why most measurements are performed at cryogenic temperatures.

One related process is phonon-assisted coupling into cavity modes, in which QD transitions detuned from the cavity modes can still couple to it. Effectively, the energy associated with the emission or absorption of a phonon compensates for the difference between that of the exciton and the cavity mode (Hohenester 2010a). This is commonly the main mechanism for small detunings (~2 meV) (Michler et al. 2000b; Roy and Hughes 2011) while larger energy gaps may require more complex interactions involving multi-excitonic states or scattering via the QD wetting layer (Chauvin et al. 2009; Steinhoff et al. 2012; Florian et al. 2013). One benefit of this process is that it allows cavity modes to be driven with a non-resonant laser, producing a peak in the photoluminescent spectrum without exciting on-resonant photons themselves - a useful mechanism for characterising the quality factor of the mode.

2.3 The Zeeman effect and diamagnetic shift

When a weak magnetic field is applied along the epitaxial growth direction of a quantum dot, the bright exciton transition lines are modified by what is referred to as magnetic hyperfine splitting or the Zeeman effect, named for discover Pieter Zeeman, an effect of the magnetic dipole moment interacting with the field (Jenkins and Segre 1939; Kox 1997). This can be broken down into two effects, linearly and quadratically related to the magnetic flux density.

One is the linear splitting of energy levels based on the non-zero spin of the exciton states (Walck and Reinecke 1998). As the field $\vec{\boldsymbol{B}}$ is applied, the transition lines become non-degenerate, splitting by an energy difference of:

$$\Delta E_{\mathrm{Z}} = g_{\mathrm{QD}} \mu_{\mathrm{B}} |\vec{\boldsymbol{B}}| \tag{2.23}$$

Where μ_{B} is the Bohr magneton and g_{QD} is the dot's effective g-factor (Morrison 2020).

The second effect cause the lines to experience a parabolic diamagnetic shift towards higher energies, sometimes referred to discretely as the “quadratic Zeeman effect” (Jenkins and Segre 1939; Schiff and Snyder 1939; Edmonds 1970), which can be described as:

$$E_{\text{shift}} = \sigma\left|\vec{\boldsymbol{B}}\right|^2 \tag{2.24}$$

Where σ is the diamagnetic shift coefficient (Walck and Reinecke 1998; Stier et al. 2016). The diamagnetic shift coefficient can be used in the evaluation of confinement effects, with σ representing the lateral size of the excitons in the structure (Someya et al. 1995), being equal to $\langle e^2(A_{\text{X}})/8m_{\text{X}}^*\rangle$, where e is the elementary charge, A_{X} is the effective area of the excitons perpendicular to the magnetic field and m_{X}^* is the effective reduced mass of electrons and holes in an exciton (Akimoto and Hasegawa 1967). Though once dismissed as a small correction to the linear energy splitting, in solid state physics, the influence of the quadratic element can be significant even at low magnetic fields (Jenkins and Segre 1939; Edmonds 1970).

These effects have been exploited in past studies into semiconductor nanostructures in various ways, ranging from characterising trions in quantum dots (Rudno-Rudziński et al. 2021) to finding evidence of laterally confined excitons in quantum wires (Someya et al. 1995). The Zeeman effect may also be used to modify a transition line towards or away from a cavity mode, providing a method of examining the effects of the latter on the transition’s lifetime (Jordan et al. 2024a), as in a study reported in Chapter 7 of this thesis.

Chapter 3
Finite-difference time-domain simulation method

The Finite-Difference Time-Domain (FDTD) method, or “Yee’s method”, is a numerical technique commonly used for analysing electromagnetic fields in a range of complex geometries. It allows the efficient approximation of Maxwell's curl equations for such structures, achieved by dividing the space of the system into a grid of coordinates and applying finite difference operators for each electromagnetic vector field component to evolve the fields in time (Yee 1966; Schneider 2010; Teixeira et al. 2023), making it most useful for time-dependent solutions, whereas the finite element method (FEM) is more suitably for time-stationary solutions.

This technique is extremely versatile, applicable from microscopic to astronomical scales and useful in a number of difference disciplines, including optics and photonics (Taflove et al. 2013), metamaterials (Foteinopoulou et al. 2003), biophysics and life sciences (McCoy et al. 2021), geophysics (Simpson 2009; Warren et al. 2016), and more.

The simulations described in this text were performed using ANSYS’s Lumerical FDTD solver, which provides a useful design environment for such work, including scripting capabilities. This chapter provides an overview of the FDTD method in general, before expanding on the tools and methods used in the simulations throughout the research in this thesis.

3.1 Basics of the FDTD method

While finite difference schemes had been applied to time-dependent partial differential equations in the past (VonNeumann and Richtmyer 1950), it was Kane Yee (1966) who first proposed the finite-difference time-domain method, as it's now known (Taflove 1980). Uniquely, his paper proposed the staggering on a grid each component of Maxwell's curl equations in such a way that tangential components vanish, satisfying the boundary condition for a perfectly conducting surface (Yee 1966).

3.1.1 Solving Maxwell's curl equations

In non-magnetic materials, Maxwell's curl equations describing the electric field and magnetic field strength $\vec{\boldsymbol{E}}$ and $\vec{\boldsymbol{H}}$ respectively can be written:

$$\frac{\partial \vec{\boldsymbol{H}}}{\partial t} = -\frac{1}{\mu} \nabla \times \vec{\boldsymbol{E}} \tag{3.1}$$

$$\frac{\partial \vec{\boldsymbol{E}}}{\partial t} = \frac{1}{\varepsilon} \nabla \times \vec{\boldsymbol{H}} \tag{3.2}$$

where ε is the absolute permittivity, and μ is the magnetic permeability (Maxwell 1865; Sullivan 2013). Using these vector equations, the six coupled dimensional components of $\vec{\boldsymbol{E}}$ and $\vec{\boldsymbol{H}}$ in cartesian coordinates can then be written (Taflove et al. 2005):

$$\frac{\partial \vec{H}_x}{\partial t} = \frac{1}{\mu}\left[\frac{\partial \vec{E}_y}{\partial z} - \frac{\partial \vec{E}_z}{\partial y}\right] \tag{3.3}$$

$$\frac{\partial \vec{H}_y}{\partial t} = \frac{1}{\mu}\left[\frac{\partial \vec{E}_z}{\partial x} - \frac{\partial \vec{E}_x}{\partial z}\right] \tag{3.4}$$

$$\frac{\partial \vec{H}_z}{\partial t} = \frac{1}{\mu}\left[\frac{\partial \vec{E}_x}{\partial y} - \frac{\partial \vec{E}_y}{\partial x}\right] \tag{3.5}$$

$$\frac{\partial \vec{E}_x}{\partial t} = \frac{1}{\varepsilon}\left[\frac{\partial \vec{H}_z}{\partial y} - \frac{\partial \vec{H}_y}{\partial z}\right] \tag{3.6}$$

$$\frac{\partial \vec{E}_y}{\partial t} = \frac{1}{\varepsilon}\left[\frac{\partial \vec{H}_x}{\partial z} - \frac{\partial \vec{H}_z}{\partial x}\right] \tag{3.7}$$

$$\frac{\partial \vec{E}_z}{\partial t} = \frac{1}{\varepsilon}\left[\frac{\partial \vec{H}_y}{\partial x} - \frac{\partial \vec{H}_x}{\partial y}\right] \tag{3.8}$$

In the FDTD method, the modelled volume is divided into cells within a grid, each containing these dimensional electric and magnetic field components staggered spatially such that each $\vec{\boldsymbol{E}}$-field vector component is located directly in-between a pair of $\vec{\boldsymbol{H}}$-field components, and vice versa (Yee 1966). Fig. 3.1 shows one of these 'Yee cells'.

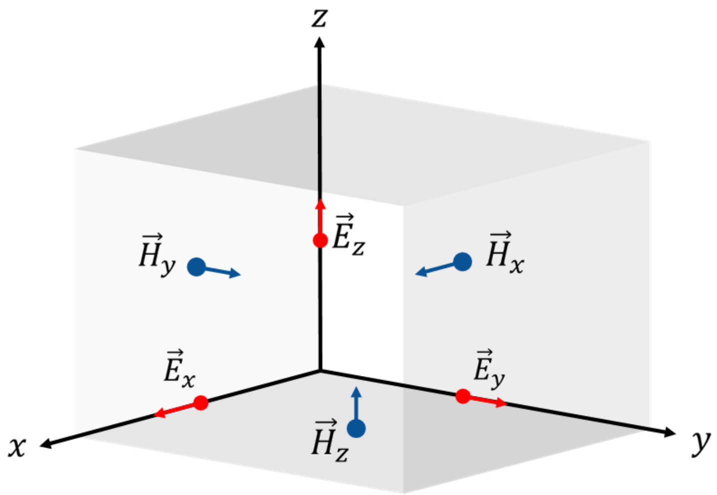

Fig. 3.1 – A single 'Yee cell' of a mesh, showing the positions at which the electric field (red) and magnetic field (blue) vector components are calculated.

In the case of Lumerical FDTD, the data obtained from the solver is automatically integrated to a consistent position at the origin of each grid point (ANSYS 2019b).

The solver automatically generates the simulation grid mesh by default. As a finer mesh will increase the accuracy of the model, albeit with significantly increased time and memory requirements, the mesh may be reduced near material structures where the fields will differ significantly with position. The mesh resolution can also be increased further manually, by specifying a smaller mesh layer over a specific volume within the model (ANSYS 2019b). In the work within this thesis, the mesh fineness is manually increased within a box around the micropillar, changing the step size to 10 nm in all dimensions, unless otherwise noted.

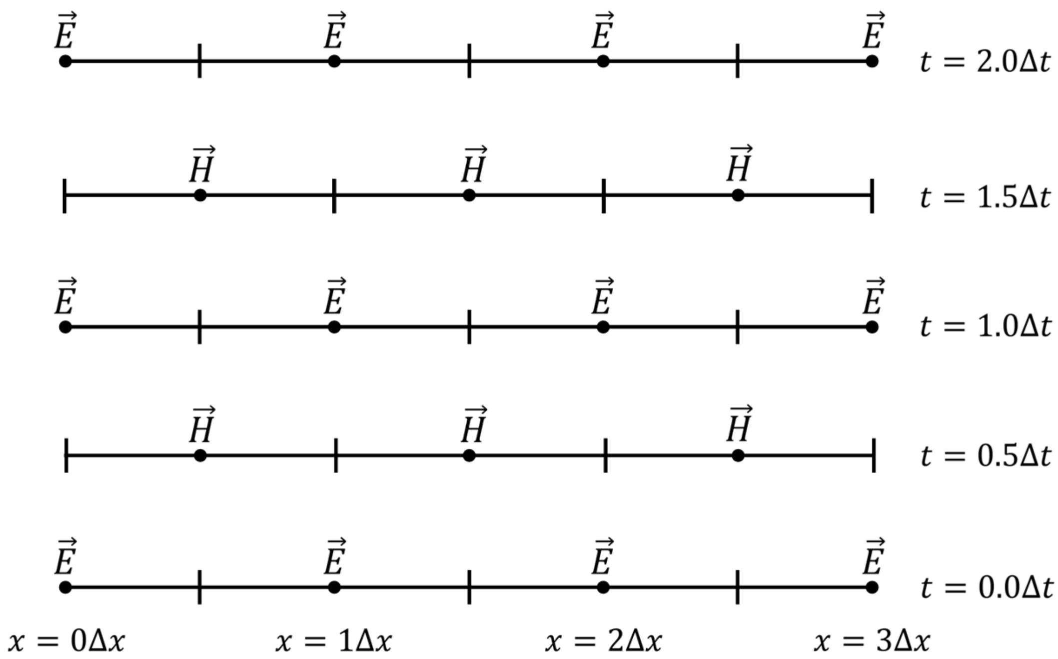

Fig. 3.2 – Illustration showing how a 1D FDTD simulation steps its calculations of the electric and magnetic field in an interleaving ‘leapfrog’ pattern in both space and time.

This collection of partial derivatives allows each component of the electric field partial differential to be calculated from the magnetic field, and vice versa. Typically, FDTD solvers use a 'leapfrog' method to iterate the system in time and space. For example, taking the magnetic field at time $t = N$, then calculating the resulting electric field at time $t = N + \frac{1}{2}$, which it then uses to calculate the magnetic field at time $t = N + 1$, and so on (Sullivan 2013). An illustration of this method being used for a 1D FDTD simulation is shown in Fig. 3.2

This is achieved using central-difference approximations, obtaining a corresponding set of six finite-difference equations, accurate to the second order in both space and time (Yee 1966; Buchanan 1996; Taflove et al. 2005; Teixeira et al. 2023):

$$\frac{\vec{H}^{n+\frac{1}{2}}_{x\,i,j,k} - \vec{H}^{n-\frac{1}{2}}_{x\,i,j,k}}{\partial t} = \frac{1}{\mu}\left[\frac{\vec{E}^{n}_{y\,i,j,k} - \vec{E}^{n}_{y\,i,j,k-1}}{\partial z} - \frac{\vec{E}^{n}_{z\,i,j,k} - \vec{E}^{n}_{z\,i,j-1,k}}{\partial y}\right] \tag{3.9}$$

$$\frac{\vec{H}^{n+\frac{1}{2}}_{y\,i,j,k} - \vec{H}^{n-\frac{1}{2}}_{y\,i,j,k}}{\partial t} = \frac{1}{\mu}\left[\frac{\vec{E}^{n}_{z\,i,j,k} - \vec{E}^{n}_{z\,i-1,j,k}}{\partial x} - \frac{\vec{E}^{n}_{x\,i,j,k} - \vec{E}^{n}_{x\,i,j,k-1}}{\partial z}\right] \tag{3.10}$$

$$\frac{\vec{H}^{n+\frac{1}{2}}_{z\,i,j,k} - \vec{H}^{n-\frac{1}{2}}_{z\,i,j,k}}{\partial t} = \frac{1}{\mu}\left[\frac{\vec{E}^{n}_{x\,i,j,k} - \vec{E}^{n}_{x\,i,j-1,k}}{\partial y} - \frac{\vec{E}^{n}_{y\,i,j,k} - \vec{E}^{n}_{y\,i-1,j,k}}{\partial x}\right] \tag{3.11}$$

$$\frac{\vec{E}^{n+1}_{x\,i,j,k} - \vec{E}^{n}_{x\,i,j,k}}{\partial t} = \frac{1}{\varepsilon}\left[\frac{\vec{H}^{n+\frac{1}{2}}_{z\,i,j+1,k} - \vec{H}^{n+\frac{1}{2}}_{z\,i,j,k}}{\partial y} - \frac{\vec{H}^{n+\frac{1}{2}}_{y\,i,j,k+1} - \vec{H}^{n+\frac{1}{2}}_{y\,i,j,k}}{\partial z}\right] \tag{3.12}$$

$$\frac{\vec{E}^{n+1}_{y\,i,j,k} - \vec{E}^{n}_{y\,i,j,k}}{\partial t} = \frac{1}{\varepsilon}\left[\frac{\vec{H}^{n+\frac{1}{2}}_{x\,i,j,k+1} - \vec{H}^{n+\frac{1}{2}}_{x\,i,j,k}}{\partial z} - \frac{\vec{H}^{n+\frac{1}{2}}_{z\,i+1,j,k} - \vec{H}^{n+\frac{1}{2}}_{z\,i,j,k}}{\partial x}\right] \tag{3.13}$$

$$\frac{\vec{E}^{n+1}_{z\,i,j,k} - \vec{E}^{n}_{z\,i,j,k}}{\partial t} = \frac{1}{\varepsilon}\left[\frac{\vec{H}^{n+\frac{1}{2}}_{y\,i+1,j,k} - \vec{H}^{n+\frac{1}{2}}_{y\,i,j,k}}{\partial x} - \frac{\vec{H}^{n+\frac{1}{2}}_{x\,i,j+1,k} - \vec{H}^{n+\frac{1}{2}}_{x\,i,j,k}}{\partial y}\right] \tag{3.14}$$

These may then be rewritten into an iteritive form:

$$\vec{H}^{n+\frac{1}{2}}_{x\,i,j,k} = \vec{H}^{n-\frac{1}{2}}_{x\,i,j,k} + \frac{\partial t}{\mu}\left[\frac{\vec{E}^{n}_{y\,i,j,k} - \vec{E}^{n}_{y\,i,j,k-1}}{\partial z} - \frac{\vec{E}^{n}_{z\,i,j,k} - \vec{E}^{n}_{z\,i,j-1,k}}{\partial y}\right] \tag{3.15}$$

$$\vec{H}^{n+\frac{1}{2}}_{y\,i,j,k} = \vec{H}^{n-\frac{1}{2}}_{y\,i,j,k} + \frac{\partial t}{\mu}\left[\frac{\vec{E}^{n}_{z\,i,j,k} - \vec{E}^{n}_{z\,i-1,j,k}}{\partial x} - \frac{\vec{E}^{n}_{x\,i,j,k} - \vec{E}^{n}_{x\,i,j,k-1}}{\partial z}\right] \tag{3.16}$$

$$\vec{H}^{n+\frac{1}{2}}_{z\,i,j,k} = \vec{H}^{n-\frac{1}{2}}_{z\,i,j,k} + \frac{\partial t}{\mu}\left[\frac{\vec{E}^{n}_{x\,i,j,k} - \vec{E}^{n}_{x\,i,j-1,k}}{\partial y} - \frac{\vec{E}^{n}_{y\,i,j,k} - \vec{E}^{n}_{y\,i-1,j,k}}{\partial x}\right] \tag{3.17}$$

$$\vec{E}^{n+1}_{x\,i,j,k} = \vec{E}^{n}_{x\,i,j,k} + \frac{\partial t}{\varepsilon}\left[\frac{\vec{H}^{n+\frac{1}{2}}_{z\,i,j+1,k} - \vec{H}^{n+\frac{1}{2}}_{z\,i,j,k}}{\partial y} - \frac{\vec{H}^{n+\frac{1}{2}}_{y\,i,j,k+1} - \vec{H}^{n+\frac{1}{2}}_{y\,i,j,k}}{\partial z}\right] \tag{3.18}$$

$$\vec{E}^{n+1}_{y\,i,j,k} = \vec{E}^{n}_{y\,i,j,k} + \frac{\partial t}{\varepsilon}\left[\frac{\vec{H}^{n+\frac{1}{2}}_{x\,i,j,k+1} - \vec{H}^{n+\frac{1}{2}}_{x\,i,j,k}}{\partial z} - \frac{\vec{H}^{n+\frac{1}{2}}_{z\,i+1,j,k} - \vec{H}^{n+\frac{1}{2}}_{z\,i,j,k}}{\partial x}\right] \tag{3.19}$$

$$\vec{E}^{n+1}_{z\,i,j,k} = \vec{E}^{n}_{z\,i,j,k} + \frac{\partial t}{\varepsilon}\left[\frac{\vec{H}^{n+\frac{1}{2}}_{y\,i+1,j,k} - \vec{H}^{n+\frac{1}{2}}_{y\,i,j,k}}{\partial x} - \frac{\vec{H}^{n+\frac{1}{2}}_{x\,i,j+1,k} - \vec{H}^{n+\frac{1}{2}}_{x\,i,j,k}}{\partial y}\right] \tag{3.20}$$

3.1.2 Simulation boundary conditions

For open systems, it is generally necessary to define absorbing boundary conditions on the edges of the mesh of an FDTD simulation to prevent any outgoing electromagnetic waves being reflected back into the simulation space. The effectiveness of these walls is important in maintaining the accuracy of the FDTD analysis, and in minimising the computational volume and, thus, the resources and time required for the simulation (Prescott 1997).

The most popular absorbing boundary condition is the perfectly matched layer (PML) (Berenger 1994), which is particularly flexible, efficient, and effective (Teixeira et al. 2023). PMLs effectively consist of an absorbing layer around simulation volume, matched in impedance to the neighbouring medium to minimise reflections (Berenger 1994). A number of different implementations of PMLs exist (Chew and Weedon 1994; Roden and Gedney 2000), with one, and the default used in Lumerical FDTD (ANSYS 2019e), being stretched coordinate PML (Gedney and Zhao 2009).

The PML parameters may be customised, such as by changing the number of layers in the PML region and their absorption properties. Lumerical FDTD also offers three default profiles, "standard", offering high absorption with a small number of layers, "stabilised", preventing numerical instabilities where material surfaces cut through the PML region, at the cost of using additional layers, which can increase the computation cost of the simulation, and "steep angle", providing increased absorption of light travelling at shallow angles to the PML plane (ANSYS 2019e).

There are also other options for specialised environments, such as periodic boundary conditions (PBCs) (Kogon and Sarris 2020), which effectively connect opposite sides of the grid to each other. As the name implies, these are ideal when modelling a periodic structures such as photonic crystals (Mekis et al. 1999). PBCs can be achieved using a wide range of algorithms, including the 'constant wavenumber method' (Yang et al. 2007), the 'order-N method' (Chan et al. 1995), the 'spatially looped' algorithm (Celuch-Marcysiak and Gwarek 1995), and others (Cangellaris et al. 1993; Harms et al. 1994; Turner and Christodoulou 1999; Aminian and Rahmat-Samii 2006; Zhou et al. 2011).

Finally, it is also possible to impose symmetric and antisymmetric boundary conditions across symmetrical simulation environments (Huang 2021). These allow the simulation space, and thus the required resources, to be reduced by a factor of 2 for each orthogonal plane of symmetry. The orientation of these planes is dependent on the orientation of the source components and the symmetries of the resulting electric and magnetic fields. Fig. 3.3 shows the required orientations for symmetric and anti-symmetric boundary conditions applied to electric and magnetic components, as well as an example of both symmetry and anti-symmetry conditions applied to dipoles in models symmetric in both x and y directions (ANSYS 2019g).

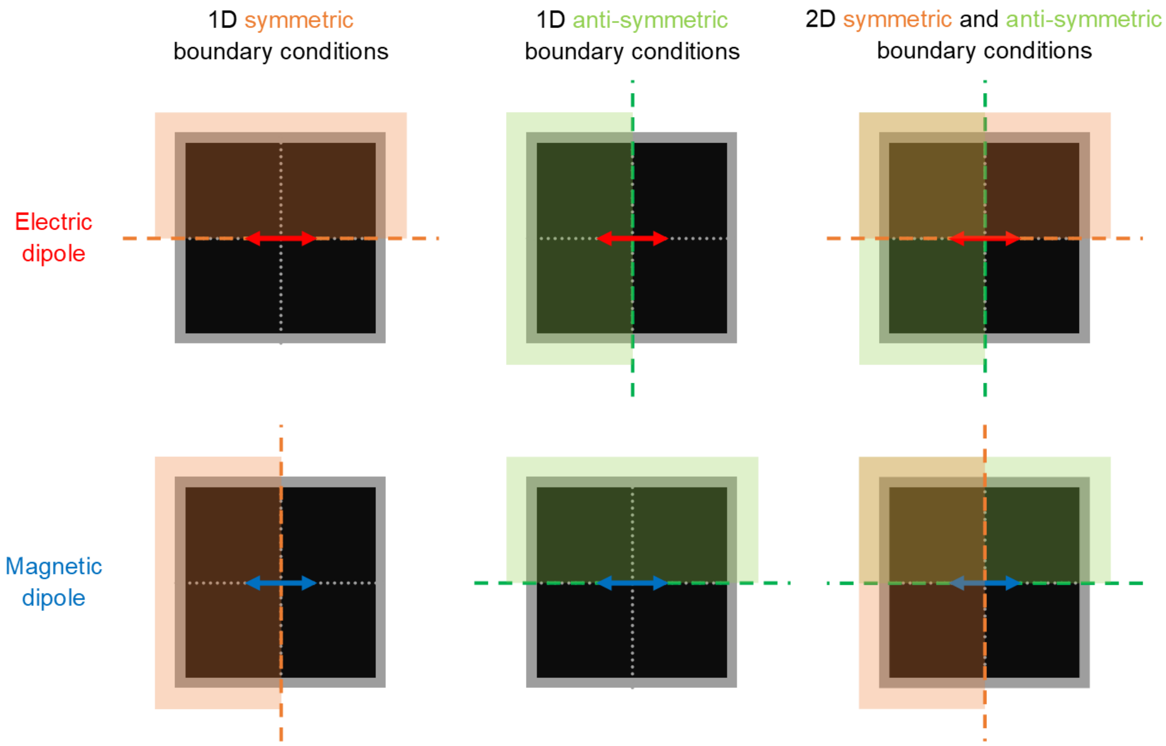

Fig. 3.3 – Reflection symmetry rules for electric and magnetic directional source components.

3.1.3 Sources

Multiple source options are available for exciting a simulated system, including plane waves (Tan and Potter 2010), resistive voltage and current sources (Buechler et al. 1995), and dipole pulses, both electric (Rizvi and Vetri 1994) and magnetic (Özakın and Aksoy 2017).

In FDTD implementations, a source may be either ‘hard’ or ‘soft’. A source is hard when it features field components set at a point. While this is the simplest option, it will have the effect of reflecting any propagating pulses, similar to a metal wall. By comparison, a source is soft when the value is added to the field component at a certain point, which will not block propagation (Brench and Ramahi 1998; Costen et al. 2009; Sullivan 2013). Within the Lumerical FDTD solver, all sources are soft (ANSYS 2019f).

3.1.4 Material properties

To define a structure within an FDTD simulation, one can define a volume and apply material properties to it. Specifically, to simulate propagation in a dielectric medium, one simply needs to change the value of the refractive index, and thus the dielectric constant ε_{r}, for the Yee cells bounded by the structure (Sullivan 2013).

By using a frequency-dependent complex refractive index $\underline{n}$, FDTD solvers can model both dispersion and absorption of light passing through materials (Tan et al. 2006). The complex refractive index takes the form:

$$\underline{n} = n + in_{\mathrm{i}} \tag{3.21}$$

Where n is the real refractive index and n_{i} is the extinction coefficient, a measure of absorption in the material (Dresselhaus 2001; Moller 2007). These may be defined using experimental data or parametrised models (ANSYS 2019d). In particular, the materials used in the simulations in this thesis (SiO_2, GaAs, and $Al_{0.95}Ga_{0.05}As$) are based on experimental data reported by Palik (1998).

3.1.5 Data output

As the name implies, FDTD simulations by default produce results in the time-domain. In particular, the calculated electromagnetic fields are useful for producing animations of field behaviour with time (Teixeira et al. 2023).

These results, however, can be converted into spectral or frequency-domain results by using the Fourier transform (Gray and Goodman 2012):

$$F(\omega) = \int_{-\infty}^{\infty} f(t) e^{-2\pi i \omega t} \, dt \tag{3.22}$$

$$f(t) = \int_{-\infty}^{\infty} F(\omega) e^{2\pi i \omega t} \, d\omega \tag{3.23}$$

3.2 Simulation models used in this thesis

ANSYS Lumerical FDTD is the chosen finite-difference time-domain solver used for the work in this thesis.

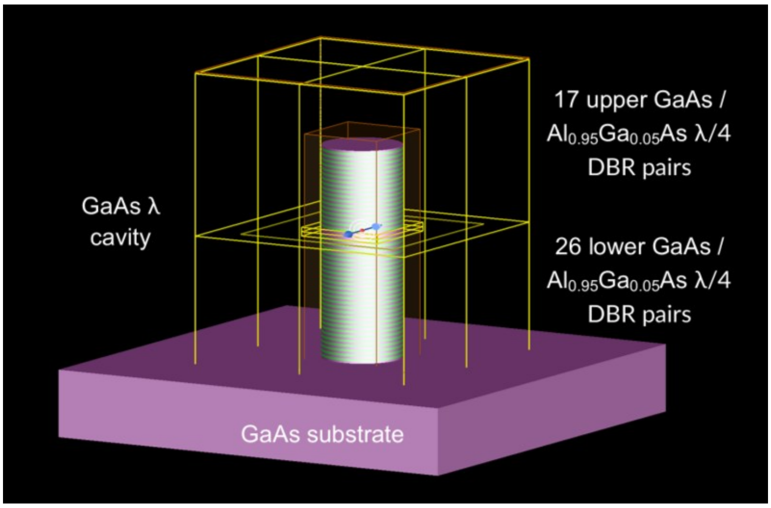

Fig. 3.4 – A screenshot from Lumerical FDTD, showing a "high Q factor" micropillar consisting of 17 (26) upper (lower) Bragg mirrors. The pillar is excited by an electric dipole, marked blue. The red volume shows the simulation region, with the overlapping yellow shapes indicating planar frequency-domain monitors. The orange volume shows a region where the mesh density is manually increased.

This work uses a small 3D simulation volume around the structure being studied, such that the boundaries are $> \lambda$ in distance from the surface of the surfaces of the micropillar, which includes the GaAs substrate layer at the bottom of the space, overlapping with the bottom boundary. Around the simulation space, stretched coordinate PML boundary conditions are used to minimise reflections, using Lumerical FDTD's standard profile, which consists of a minimum of 8 layers. To reduce computation times and required resources, symmetric and anti-symmetric boundary conditions were used for cases where the micropillar is driven by a centred dipole to decrease the simulation volume.

In general, the simulations in this thesis study circularly cylindrical GaAs-$Al_{0.95}Ga_{0.05}As$ micropillars of various diameters, designed for a wavelength of 940 nm. Each one consists of a 267.9 nm GaAs λ cavity spacer layer, with either 7 (low Q design) or 17 (high Q design) $\lambda/4$ alternating GaAs and $Al_{0.95}Ga_{0.05}As$ pairs above and 26 pairs below the spacer, all standing on a planar GaAs substrate. The materials used are modelled with frequency-dependent refractive indices, including dispersion, with zero absorption. The mesh around the pillar is manually increased in density so as to more accurately model its circular sidewalls.

To simulate the spectral response of the device, it is excited by an x-oriented electric dipole embedded in the cavity where a quantum dot would be placed, driven over a broad spectral range from 840 nm to 1070 nm with a Gaussian pulse of 5.6 fs full width at half maximum (FWHM), injecting a total spectral average power of 3.79 fW.

Most simulations in this thesis place the dipole source at a high symmetry point in the centre of the cavity, but it should be noted that this only excites some of the higher order cavity modes of the pillar structure as many of them have nodes of the electric field at the cavity centre. However, as we primarily concern ourselves with the HE_{11} mode and the range of wavelengths immediately surrounding it, this is of limited consequence and helps reduce the time it takes for simulations to run, as symmetric and antisymmetric boundary conditions may be used, as discussed previously.

The outer surfaces of the simulation volume are covered by planar frequency-domain field monitors, which record the electric field and directional transmission of power through the plane, automatically transforming the results into the frequency-domain. Having monitors in all directions is important for calculating the SE coupling and collection efficiencies, as well as other important numbers like the numerical aperture NA and mode field diameter MFD. Additional planar field monitors normal to each dimension x, y, and z intersect at the pillar's centre at the origin.

Simulations are allowed to run until the total energy drops beneath a set threshold, at which point they stop. The threshold used is usually 4.5×10^{-5} times the initial energy, which testing found is required to accurately model high Q factor micropillar modes, except when examining non-cavity modes, at which point a threshold of 10^{-6} is used. If the threshold is too high, the electric fields may not have sufficiently decayed by the time the simulation ends. An example of this comparing the upwards emission of a 2 μm diameter micropillar with 17 (26) upper (lower) DBR pairs that's been allowed to ringdown to either 1×10^{-3} or 4.5×10^{-5} of the initial system energy is shown below in Fig. 3.5.

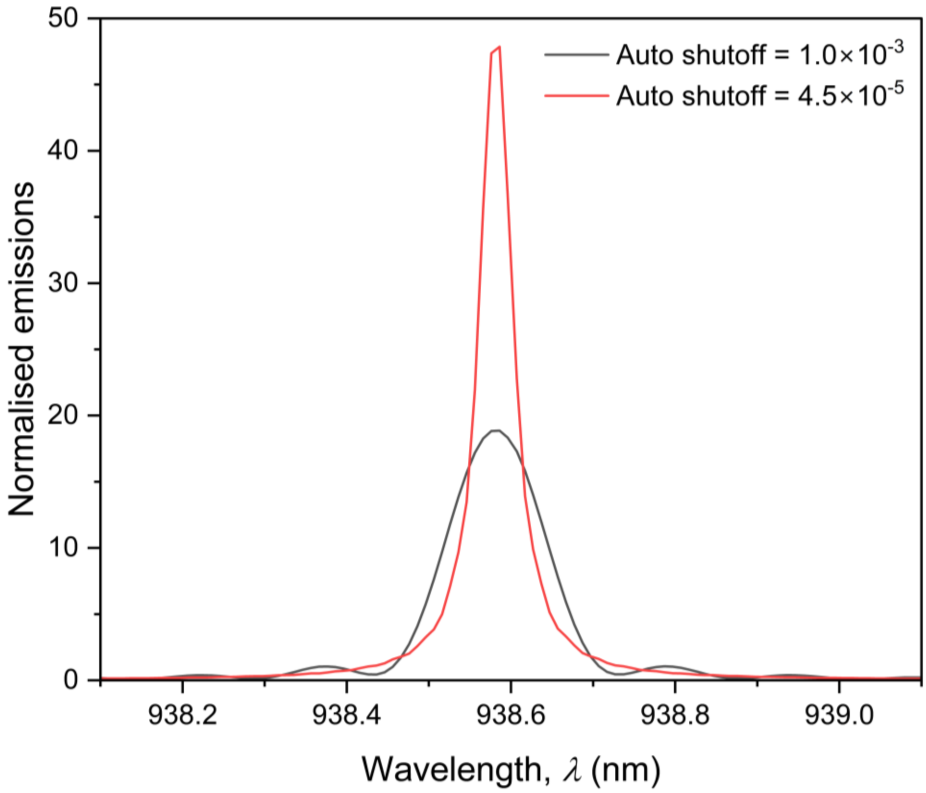

Fig. 3.5 – Transmission spectra recorded for a simulated 2.00 μm diameter micropillar with 17 (26) upper (lower) DBR pairs for emission through the top simulation planar monitor, normalised based on the dipole source power in a homogenous medium. This is accomplished using auto shutoff energy settings of 1×10^{-3} (black) and 4.5×10^{-5} (red) of the initial system energy.

Multiple differences can be seen between the two sets of results. In particular, the peak intensity is reduced by more than a factor of 2, which would dramatically affect not just the calculated efficiencies of the device, but also the total emission intensity and thus the predicted Purcell factor. The peak is broader, resulting in the Q factor obtained from fitting with a Lorentzian being reduced by a factor of ~2.4, from 20831 ± 54, around the hypothetical Q factor of a planar structure with the same DBR composition, to 8741 ± 143. The uncertainty in Q is also increased, due to the data being less accurately modelled with a Lorentzian. When Fourier transformed to obtain transmission spectra, energy remaining in the electric field at the end of the simulation is truncated, effectively multiplying the decay by a square function. This convolves the expected Lorentzian with the Fourier transformed square, producing a sinc function, with damped interference-like peaks on either side of modes, polluting what should be a Lorentzian shape and making results less accurate.

3.3 Results obtained from FDTD simulations in this thesis

In this section, some regular results obtained from simulations in this work are defined.

3.3.1 Emission spectra

The emissions of the device can be studied by recording the power transmitted through the frequency-domain planar monitors surrounding it. This transmission is automatically normalised to the dipole source power. As the emission rate is proportional to the local density of states (LDOS), which is itself proportional to the power emitted by the source, measuring the normalised transmission power returns an equivalent result to recording the emission rate through the corresponding monitor.

A sketch of these monitors and a set of labels to define the transmission through each one is presented below in Fig. 3.6.

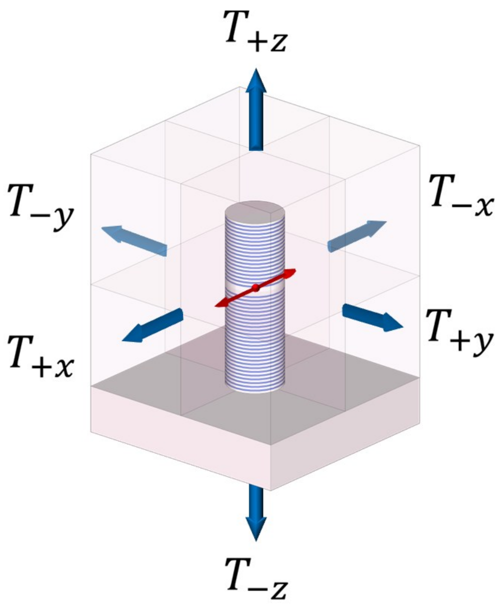

Fig. 3.6 – Sketch showing a micropillar with 17 (26) upper (lower) DBR pairs on a GaAs substrate excited by a dipole oriented in the x direction. Surrounded is a box of six outer planar frequency-domain monitors, with the emissions transmitted through each monitor labelled based on the normal to the monitor surface. Also visible are the three planar monitors providing cross-sections of the micropillar centre

While this is achieved using default commands in Lumerical FDTD, the function can be broken down into the following equation:

$$T(f) = \frac{\frac{1}{2}\int_{\text{monitor}} Re(\vec{\boldsymbol{P}}(f)) \cdot d\vec{\boldsymbol{S}}}{P_{\text{source}}(f)} \tag{3.24}$$

Where $T(f)$ is the normalised transmission as a function of frequency, $\vec{\boldsymbol{P}}(f)$ is the Poynting vector, $d\vec{\boldsymbol{S}}$ is the surface normal and $P_{\text{source}}(f)$ is the power inserted into the system by the source (ANSYS 2019h). The Poynting vector describes the directional energy flux of an electromagnetic field, calculated by the cross product $\vec{\boldsymbol{P}} = \vec{\boldsymbol{E}} \times \vec{\boldsymbol{H}}$ (Poynting 1884).

Given that the light emitted from a real device will be collected to an optic above the pillar, we are primarily concerned with the transmission through the top planar monitor T_{+z}, which the micropillar cavity is designed to emit into most strongly. Cavity modes may then be fitted with Lorentzian peaks to obtain their wavelengths and Q factors, as discussed in Section 2.2, an analogue to analysis of experimental photoluminescence results.

3.3.2 Efficiencies and Purcell factor

By recording transmission spectra through other monitors, device parameters including the Purcell factor, SE coupling efficiency β, cavity directionality η, and the outcoupling efficiency ξ can be determined.

The first property is simplest to calculate. Given that all transmission data is already normalised to the dipole source power, the total transmission through a box enclosing the device will be equal to its Purcell factor, thus all that is required is to sum the emission from all surrounding planar monitors, such that:

$$F_{\mathrm{P}} = T_{\mathrm{total}} = T_{+x} + T_{-x} + T_{+y} + T_{-y} + T_{+z} + T_{-z} \tag{3.25}$$

β is equal to the ratio of cavity mode emissions to the total emissions of a cavity device (Björk et al. 1993). Some papers (Androvitsaneas et al. 2016; Ginés et al. 2022) make the assumption that the cavity mode emissions can be quantified based on the proportion of light emitted in the vertical directions (and indeed it is true that this is the primary emission channel of the mode, with non-cavity modes proportionally emitting more via pillar sidewalls). This can be achieved by directly summing the transmission spectra from planar monitors above and below the simulated pillar. In this research work, this is instead accomplished by directly fitting the cavity mode peak in the total emission spectrum with a Lorentzian and a constant offset, extracting the Lorentzian peak height, excluding background. This not only allows cavity mode emissions through other monitors to be included in efficiency calculations, but also allows non-cavity mode emissions through the top and bottom of the micropillar, to be considered in studies presented in this thesis

$$\beta = \frac{T_{\mathrm{total,cav}}}{T_{\mathrm{total}}} \tag{3.26}$$

η and ξ, by comparison, do still take direction into account. In the prior case, this is directly calculated from the light transmitted through the top monitor divided by the summed light emitted in the vertical direction:

$$\eta = \frac{T_{+z}}{T_{+z}+T_{-z}} \tag{3.27}$$

Meanwhile, ξ combines the methods used to obtain β and η. It describes the proportion of the total emission that is emitted via the cavity mode towards the theoretical placement of a collection optic above the sample. This is similar to β, but only the upwards emission is fitted to extract cavity emissions.

$$\xi = \frac{T_{+z,\mathrm{cav}}}{T_{\mathrm{total}}} \tag{3.28}$$

For each of these calculations, it may be noted that the calculation can be simplified if the system is cylindrically symmetrical, which will be the case for most simulations in this thesis given the benefit of reducing computation time. In these cases, $T_{+x} = T_{-x}$ and $T_{+y} = T_{-y}$, meaning only one set of data is required for each horizontal dimension.

3.3.3 Electric field profiles and mode field diameter (MFD)

The absolute electric field over each planar monitor at the HE_{11} mode can be exported and plotted as a colourmap. This is primarily used in this thesis to examine the electric field profile of cross-sections through the pillar.

This is also used to obtain the mode field diameter. This is an ill-defined property for most micro-cavity structures, as opposed to its usual use in describing optical fibres (Artiglia et al. 1989), but is here defined by default as the diameter at which the electric field intensity at the top of the structure decreased to $1/e^2$ of the maximum value. This data is obtained from the two x-z and y-z cross-sectional monitors, obtaining the mean of the electric field intensities at the HE_{11} wavelength at a z value equal to the top layer boundary of the micropillar. This mean $\vec{\boldsymbol{E}}$-field intensity is then fit with a Gaussian to approximate this diameter, though as is shown later in Section 5.2.4, near-field effects mean that the electric field intensity distribution may not always be described well by this function. Nonetheless, it serves well as an approximate measure of the MFD.

3.3.4 Far-field numerical aperture (NA)

From electric field data recorded at a planar monitor, it is also possible to project the emissions into the far-field (Barth et al. 1992; Gonzalez Garcia et al. 2000; Taflove et al. 2005). This can then be used to calculate results such as the numerical aperture of a device.

Here, this is accomplished by integrating emissions projected into the far field (by default over 1 metre (ANSYS 2019a)) over a collection cone, producing a plot of the transmitted power at the mode wavelength as a function of the sine of the cone half-angle θ, and thus the numerical aperture in air, from 0 to 1. A diagram of the projected cone and the angles described are shown in Fig. 3.7.

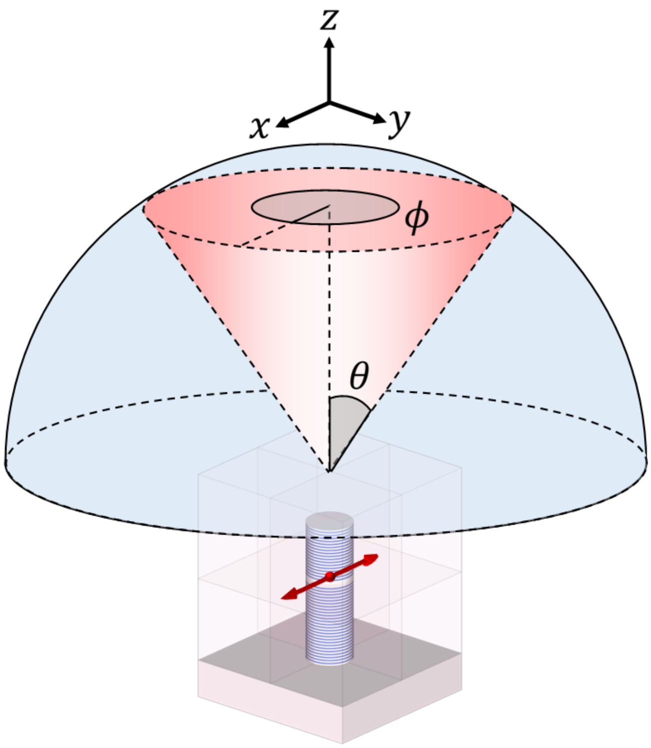

Fig. 3.7 – Sketch of the light transmitted through the top monitor above a pillar projected into the far field, integrated over a collection cone of half-angle θ, integrated fully over 0 to 360° in ϕ.

First, the $\vec{\boldsymbol{E}}$-field intensity over half-angle θ is obtained by integrating:

$$I_{\text{cone}}(\theta, f) = \int_{0^\circ}^{360^\circ} \int_{0^\circ}^{\theta} |\vec{\boldsymbol{E}}|^2(ux, uy, f) \sin(\theta)\, d\theta\, d\phi \tag{3.29}$$

Thus, similarly, over the whole hemisphere:

$$I_{\text{hemisphere}}(\theta, f) = \int_{0^\circ}^{360^\circ} \int_{0^\circ}^{90} |\vec{\boldsymbol{E}}|^2(ux, uy, f) \sin(\theta)\, d\theta\, d\phi \tag{3.30}$$

The ratio of these results, describing the proportion of the far field $\vec{\boldsymbol{E}}$-field intensity within the cone of half angle θ, is then multiplied by transmission through the monitor in the near field (ANSYS 2019c):

$$P(\theta, f) = \frac{I_{\mathrm{cone}}(\theta, f)}{I_{\mathrm{total}}(f)} * T(f) \tag{3.31}$$

An example of this result at the HE_{11} cavity mode of a 2.00 µm diameter micropillar with 17 (26) upper (lower) DBRs is shown in Fig. 3.8 below. The NA reported is then that at which the total power transmitted through the cone is $1 - 1/e^2$ times the maximum value, marked on the plot using a red dashed line.

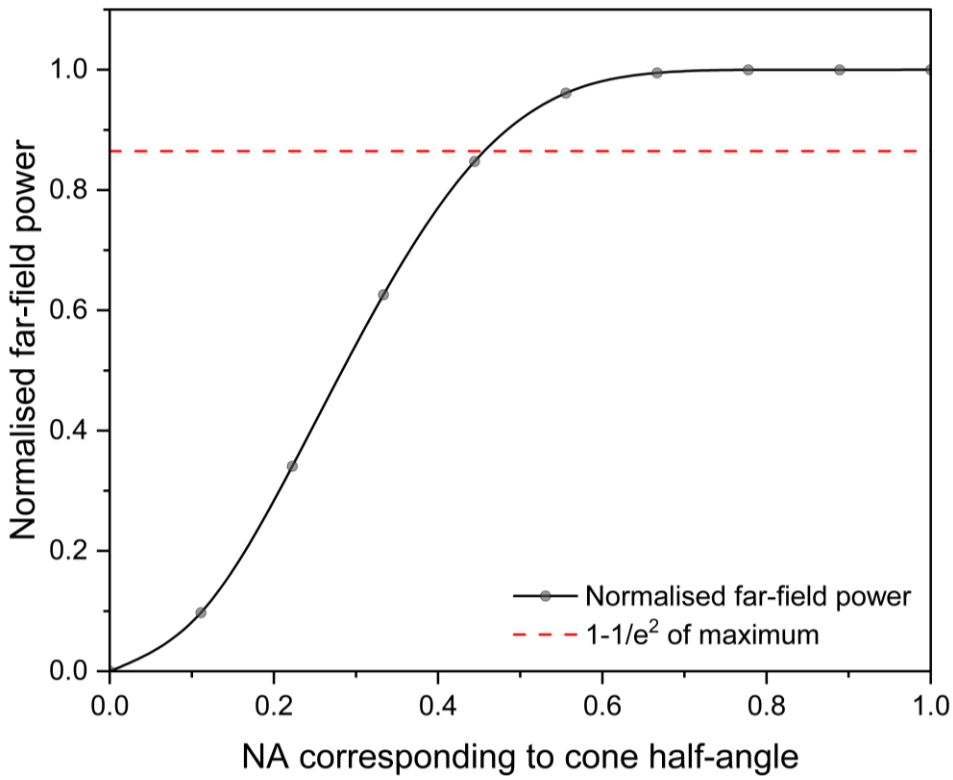

Fig. 3.8 – Power transmitted through a cone projected into the far-field above a 2.00 µm diameter micropillar with 17 (26) upper (lower) DBRs from the planar frequency-domain monitor above it, as a function of numerical aperture corresponding to the sine of the cone cross-section half-angle. The power is normalised to the maximum value, as obtained over the entire hemisphere above the monitor. A red dashed line indicates 86.5%, or $1 - 1/e^2$, of the maximum, the intersection of which with the data gives the $1/e^2$ NA, here being 0.456.

3.4 Summary and conclusion

To conclude, this chapter laid out the details of the finite-difference time-domain method utilised in several pieces of later work in this thesis. This numerical technique allows the simulation and analysis of electromagnetic fields for different materials and geometries, such as the quantum dot micropillar. The quantum dot is modelled as an electric dipole, placed in the spacer layer of the device. The volumes of the GaAs and $Al_{0.95}Ga_{0.05}As$ semiconductor layers are described by frequency-dependent refractive index data. A small section of the sample around the subject device is simulated, bound in a region with PML boundary conditions. Additional boundary conditions applied in planes of symmetry, where they exist, allow the simulation volume to be reduced, reducing the required computing resources. This chapter also described methods for analysing the resulting electric field data to derive important results such as the Purcell factor, coupling efficiency parameters, and the far-field numerical aperture.

Several assumptions are thus made. On a basic level, the target pillar is modelled as being isolated, with emissions dispersing in all directions at the absorptive simulation boundaries. It is also assumed that no absorption losses arise in the pillar itself, with the refractive index data used to describe materials lacking any imaginary components. As mentioned in the previous chapter, this component of Q factor losses is negligible for low Q micropillars like those used in this thesis. On the other hand, losses due to scattering at the sidewall semiconductor-air boundary are not simulated in this simplified model, with the simulated surfaces lacking any roughness, despite this being a significant component of Q losses. Finally, rather than many quantum dots in random positions being excited by an external laser, the system is instead driven in most cases by a single x-oriented electric dipole placed in the centre of the cavity spacer layer, unless stated otherwise. This is justified by us being primarily focused on the behaviour of the HE_{11} fundamental cavity mode, to which our quantum dots are coupled.

Chapter 4
Experimental methods

This chapter lays out the experimental methods used in laboratory work featured in the following chapters of this thesis. First the general apparatus design, a dark field microscope setup, is introduced and discussed. Afterwards, the chapter discusses experimental techniques used to obtain photoluminescence, reflectivity, and resonance fluorescence spectra, and time-resolved measurements such as the transition lifetime, single-photon purity, and the two-photon indistinguishability.

4.1 Experimental setup

The experimental work in this thesis makes use of an optical kit set up in a dark field cross-polarisation microscope configuration (Kuhlmann et al. 2013a). In this setup, the light input into the system can be easily swapped between a white light emitting diode (LED) for reflectivity measurements, and laser excitation for most other measurements. Co- and cross-polarised light can be collected separately, allowing resonance fluorescence and scattered laser light to be distinguished. A general schematic of the apparatus is shown below in Fig. 4.1.

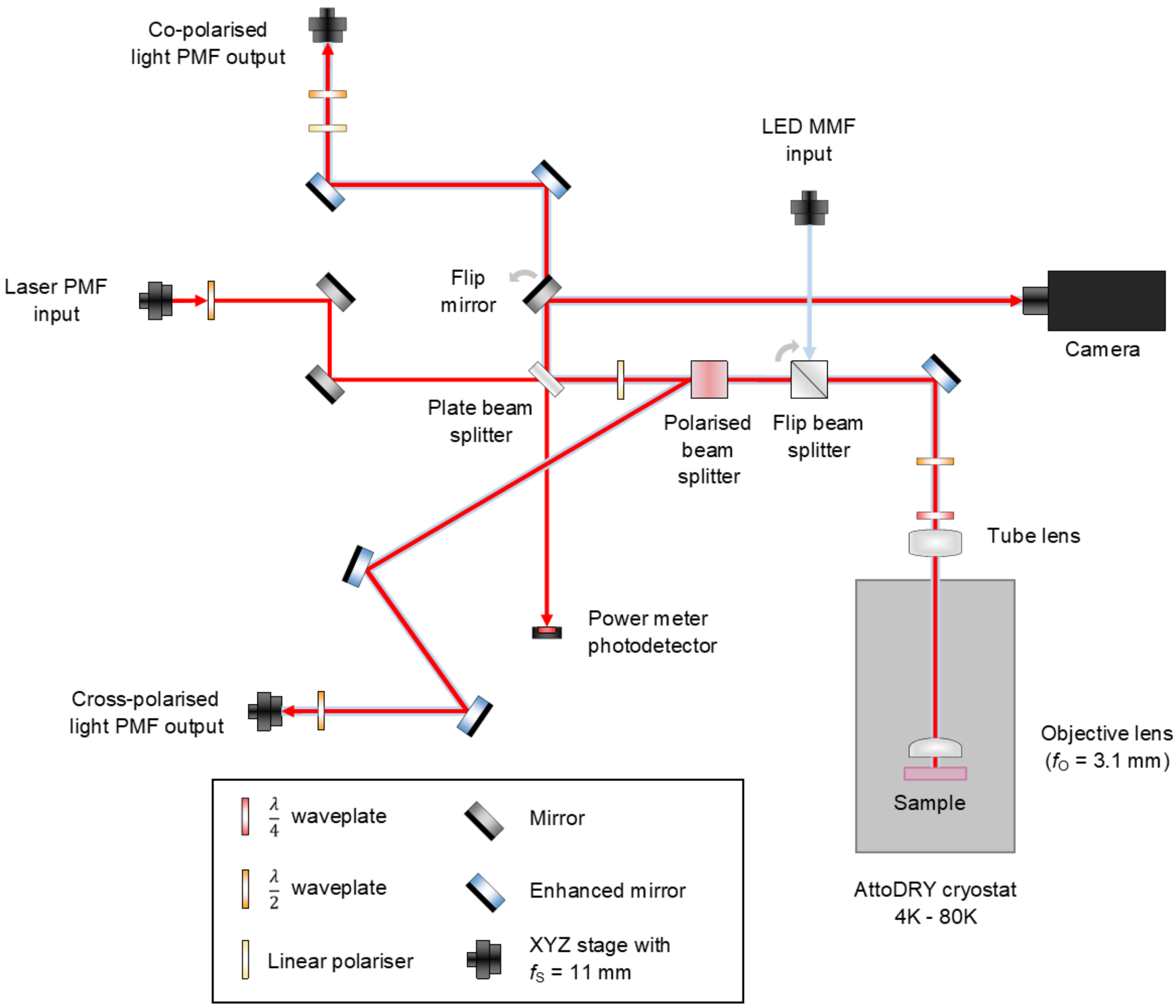

Fig. 4.1 – Diagram of the cross-polarised experimental apparatus. The sample sits below an objective lens of NA = 0.81, in a cryostat cooled to temperatures ranging from 4 K to 80 K.

A 4 x 4 mm sample chip is held on a controllable piezo-electric x-y-z translation stage in an Attocube attoDRY 1000 closed-cycle cryostat at temperatures ranging from 4 K to 80 K under normal operation, achieved using a He exchange gas and managed using a Lakeshore Model 335 cryogenic temperature controller containing resistance temperature detectors and thermocouples. The controller also provides up to 75 W of heater power, allowing sample temperatures to be changed directly during experimentation. The attoDRY also contains superconducting magnets, capable of generating a magnetic field at the sample of up to 9 T in a Faraday configuration, which can be used to change the transition energies and section rules of the QD. Under Faraday geometry, the magnetic field is parallel to the optical axis, as opposed to Voigt geometry, where the magnetic field is orthogonal to the light propagation. An optical breadboard is mounted on the cryostat, on which the input and output ports, lenses, and mirrors of the apparatus sit.

There are multiple light sources available for resonant and non-resonant excitation, reflectivity, and visibly navigating the sample. Along with the broadband white light LED source mentioned previously, also available are a PicoQuant PDL 828 Sepia II laser with an 850 nm laser diode head (LDH) capable of both picosecond pulsed and CW operation for non-resonant excitation, an M Squared SolsTiS Titanium-Sapphire CW laser with Equinox pump tuneable over 700-1000 nm, and a similarly tuneable Coherent Mira-900 Titanium-Sapphire laser with Verdi G10 laser head, capable of CW and femtosecond or picosecond pulsed operation. Each laser is delivered via an input polarisation-maintaining fibre (PMF). Three options for attenuation exist: using the direct laser power controls if available, rotating a motor controlled $\lambda/2$ waveplate to rotate the polarisation of the transmitted laser light, such that its intensity can be continuously reduced upon passing through a linear polariser, or adding neutral density filters to the laser path. To monitor the power, light is picked-off by a plate beamsplitter into a Thorlabs optical power meter. The white light may be simply added or removed using a flip beam splitter, for easy spatial navigation, and allowing quick comparison of photoluminescent spectra with cavity modes sometimes better visible in reflectivity spectra.

Directly above the sample is an objective lens of NA = 0.81 and focal length 3.1 mm, through which light is both input and collected via confocal arrangement with a tube lens above. Collection into an optical fibre serves as an effect pinhole, filtering out-of-focus light from detection, improving the contrast of collected light (Semwogerere and Weeks 2005). XYZ stages and mirrors on the breadboard allow the beam to be carefully aligned to the pinhole and coupled into each fibre. There are also $\lambda/4$ and $\lambda/2$

waveplates on rotation stages above the sample. Together, these allow the light to be polarised in any orientation of the Poincaré sphere (Poincaré 1889), which is sketched in Fig. 4.2.

There are multiple outputs for the emitted light. Cross-polarised light is split off using a polarised beam splitter (PBS). This is then collected into a PMF. The remaining co-polarised light may then be directed either to another PMF or to a camera used for navigating the sample, switchable using a flip mirror.

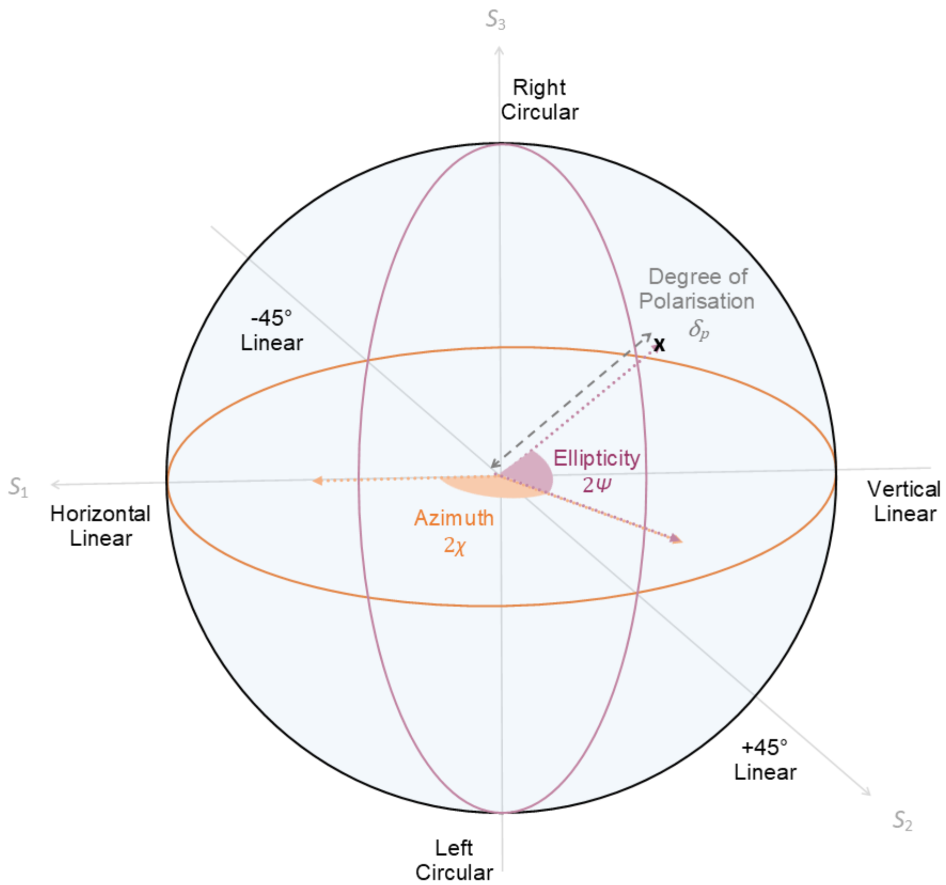

Fig. 4.2 – The Poincaré sphere, an approach for representing polarisation states using spherical coordinates. The polarisation is described by two angles, the azimuth/orientation and ellipticity, and a radius, the degree of polarisation up to a maximum of 1. S_1, S_2, and S_3 are the Stokes parameters, which form the Cartesian form of the polarisation coordinates (Collett 2003; Chipman et al. 2018).

Each fibre output can be connected to either an Andor Shamrock SR-750 spectrometer of 750 mm focal length, ID Quantique ID281 superconducting nanowire single photon detectors (SNSPDs) of timing jitter ~31 ps, or avalanche photodiodes (APDs) of 247 ps Gaussian FWHM timing jitter. For time-resolved measurements, the latter two are interfaced with a Swabian Time Tagger.

Where possible, computer-connected devices (e.g. spectrometer, rotation stages, temperature monitor) are connected to virtual instruments in a modular, universal National Instruments LabVIEW project. Where this is not implemented, such as for time-resolved measurements using the Time Tagger, they are controlled by the proprietary software. The spectrometer, for example, is primarily utilised using Andor's SOLIS spectroscopy software.

4.2 Wavelength-resolved photoluminescence, absorption and reflectivity

Using the apparatus as laid out above, the photoluminescence (PL) and white light (WL) reflectivity spectra of a cavity can be obtained. By toggling the LED flip beam splitter, and conversely locking or unlocking the laser used, it is possible to switch between laser excitation and white light.

To make certain that the light sources are focused on the sample, the laser is targeted first at a reference near-planar 'box' structure, of 20 x 20 μm square. By adjusting the height z of the stage, it is ensured the laser forms a small, clear spot, with minimal concentric fringes around it. The sample can then be aligned in x and y using the piezo stage such that the objective is aligned above the target micropillar by examining the spectrum, peak count rate, and camera feed. In the case of photoluminescence, this is done with the goal of maximising the photon count rate of the target feature. In the case of reflectivity, the magnitude of the dip of the cavity mode is maximised.

The spectrometer has grating of 600 l/mm, 1200 l/mm, or 1800 l/mm, with bandpasses ranging from 18 to 59 nm and resolutions of 0.09 to 0.03 nm. The front input, side input, and output slots can also be opened and closed, as can its shutter. Combined with changing the integration time these can be combined to obtain high quality spectra of cavity modes and transitions without saturating the charge-coupled device (CCD) detectors. Unless otherwise specified, measurements are performed using an integration time of 10 seconds.

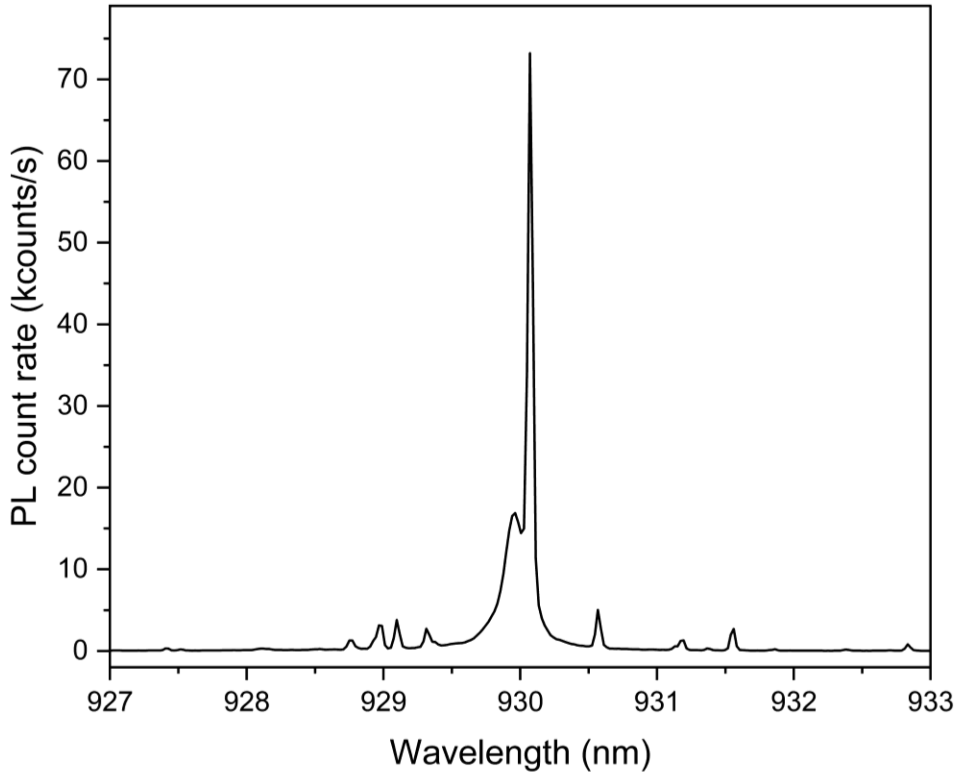

Fig. 4.3 – Example of a photoluminescence spectrum for a 2.00 μm diameter micropillar with 17 (26) upper (lower) DBR pairs, recorded using a spectrometer grating of 1200 l/mm over an integration time of 1 second. Two bright features are visible: the fundamental cavity mode of the device and a bright on-resonance, though red-sided, transition peak. The background count rate recorded by the CCD has been subtracted.

PL and WL spectra are limited in resolution by that of the spectrometer, which can be insufficient to accurately capture individual transition peaks in detail, with the resolution being much larger than an individual transition's linewidth, as in Chapter 6 of this thesis. Higher-resolution wavelength-resolved spectra can be obtained by performing a resonance fluorescence scan across the spectrum. In this method, the M Squared SolsTiS Ti-Sa laser is swept across the target wavelength range and the resulting fluorescence count rate is plotted against it, forming a high-resolution spectrum limited instead by the laser wavelength step size.

4.3 Time-resolved photoluminescence

Time-resolved measurements can be performed by filtering the micropillar emissions through the spectrometer, such that only emissions from a single transition are detected.

The Coherent Mira 900 laser in ps-pulsed mode is the primary laser used for these measurements. It has a repetition rate of 76 MHz, producing pulses of transform-limited duration (1.93 ± 0.03) ps separated by 13.2 ns

4.3.1 Transition lifetime

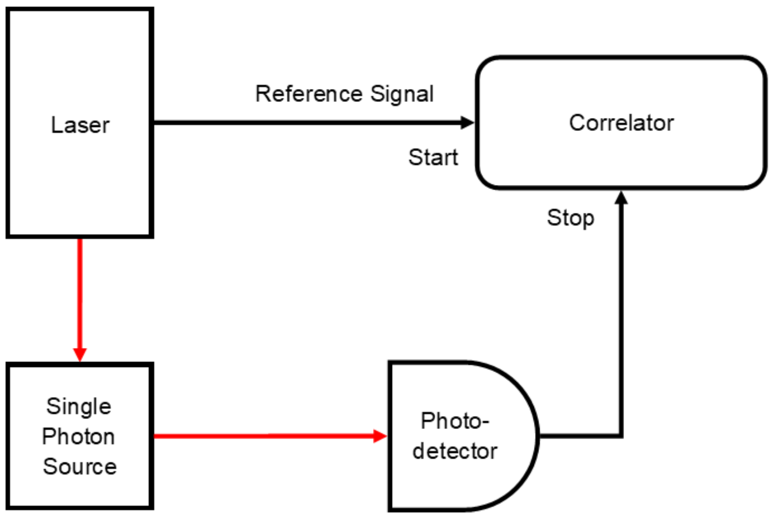

Fig. 4.4 – Configuration used to measure the radiative lifetime of a transition. The laser provides a reference start signal for the correlator, while the photodetector sends the stop signal.

The lifetimes of transitions are measured using one APD or SNSPD connected to correlation electronics, such as the Swabian Time Tagger in our setup. After the pulsed laser provides a reference ‘start’ signal synced to the output pulse, the photodetector provides a ‘stop’ signal to the correlator when it detects a photon.

The resulting detections and their corresponding time delays τ between start and stop signals are then grouped into time bins and plotted as a histogram. This effectively forms a plot of the exponentially decaying photoluminescence of a transition after each laser pulse. An example of one of these pulsed decays, obtained for a quantum dot transition of lifetime (0.118 ± 0.003) ns is shown below in Fig. 4.5.

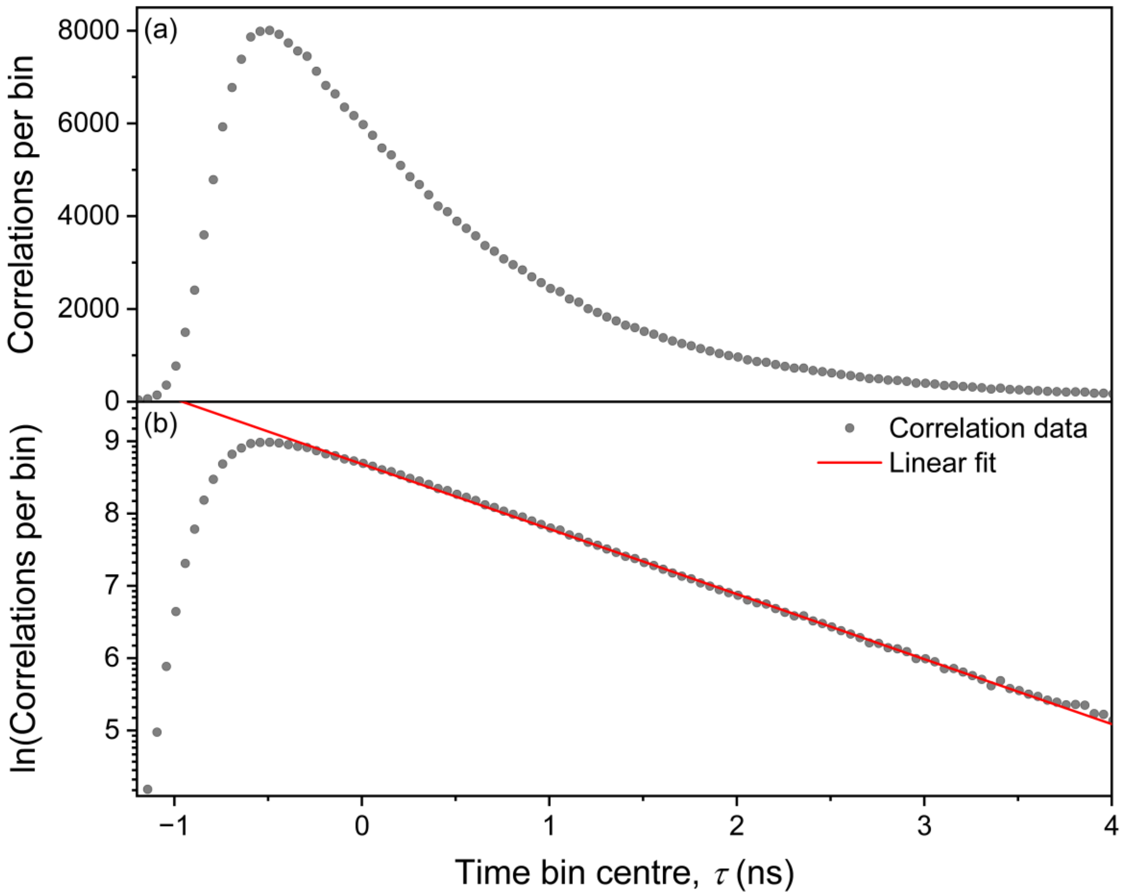

Fig. 4.5 – Example decay curve obtained for a quantum dot transition under pulsed excitation, plotted (a) on a normal scale, and (b) on a logarithmic scale, which is fitted linearly to find a radiative lifetime of (1.112 ± 0.004) ns. This data was obtained using a 76 MHz pulsed laser, a Swabian TimeTagger system, and ID Quantique APDs.

By fitting this, it is possible to extract the transition lifetime. The fitting equation for a single spontaneous decay lifetime takes the form:

$$y = A_0 e^{-\frac{\tau}{T_1}} \tag{4.1}$$

Where T_1 is the lifetime, or the time taken for the emissions to decay by a factor of $1/e$, and A_0 describes the amplitude of the decay curve. On a logarithmic scale, this thus forms a linear equation, which is easier to fit:

$$\ln(y) = \ln\left(A_0 e^{-\frac{\tau}{T_1}}\right) = -\frac{1}{T_1}\tau + \ln(A_0) \tag{4.2}$$

Such that the gradient of the fitted line is $-\frac{1}{T_1}$.

4.3.2 Second-order correlation, $g^{(2)}(t)$

The antibunching of a system, and thus its single photon purity, can be analysed by performing a Hanbury Brown and Twiss (HBT) photon coincidence experiment (Brown and Twiss 1956). A Hanbury-Brown and Twiss interferometer consists of two photon detectors capable of detecting single photons, a 50 : 50 beam splitter and correlation electronics, which are used to measure the time delay between a ‘start’ detection and a ‘stop’ detection between the two detectors (Zwiller et al. 2004). A sketch of this experiment is presented below in Fig. 4.6.

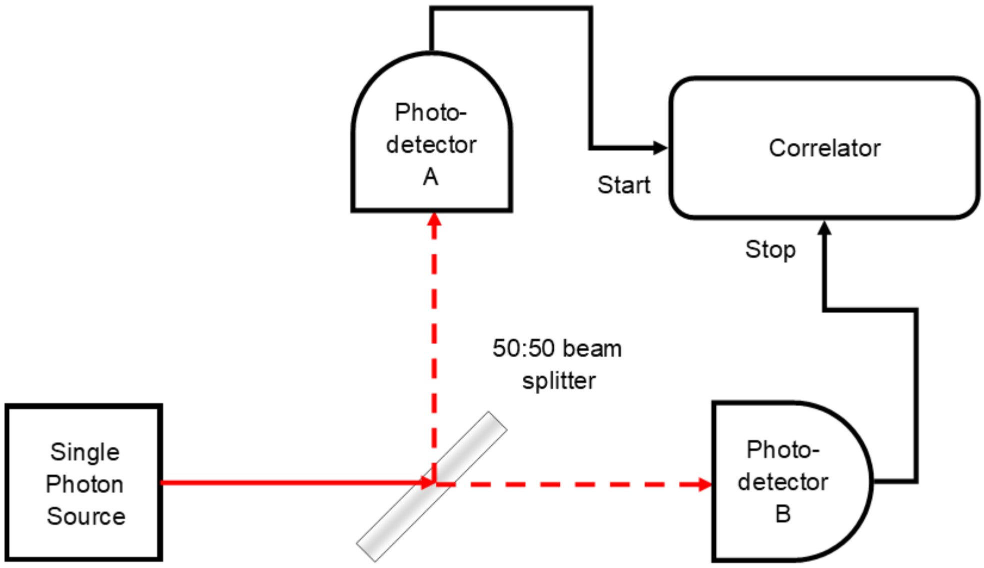

Fig. 4.6 – Configuration used in a Hanbury Brown and Twiss experiment. A 50 : 50 beam splitter sends the incoming beam towards two single-photon detectors. The detector signals are then fed into a correlator.

After many events have been recorded, the time intervals can again be collected, typically in time bins of around 10 ps width, and plotted as a second-order correlation histogram. Experimentally, uncorrelated coincidences from room lights, laser leakage, and dark counts provide a source of error.

The resulting photon correlation probability of a photon at time τ after a photon detection at time t is thus defined using normally-ordered operators (Scully and Zubairy 1997; Zwiller et al. 2004):

$$g^{(2)}(\tau) = \frac{\langle : I(t) I(t+\tau) : \rangle}{\langle I(t) \rangle \langle I(t+\tau) \rangle} \tag{4.3}$$

If time delays are measured relative to a start time of $t = 0$ on one detector, this will thus then take the form:

$$g^{(2)}(\tau) = \frac{\langle : I(0) I(\tau) : \rangle}{\langle I(0) \rangle \langle I(\tau) \rangle} \tag{4.4}$$

Coherent light would follow Poissonian statistics, producing a flat line. However, a preference for single photon emission events would produce an 'antibunching dip' around time delay $\tau = 0$, showing that two photons are unlikely to be detected simultaneously. An example plot of the predicted correlations of an ideal single-photon emitter is presented in Fig. 4.7.

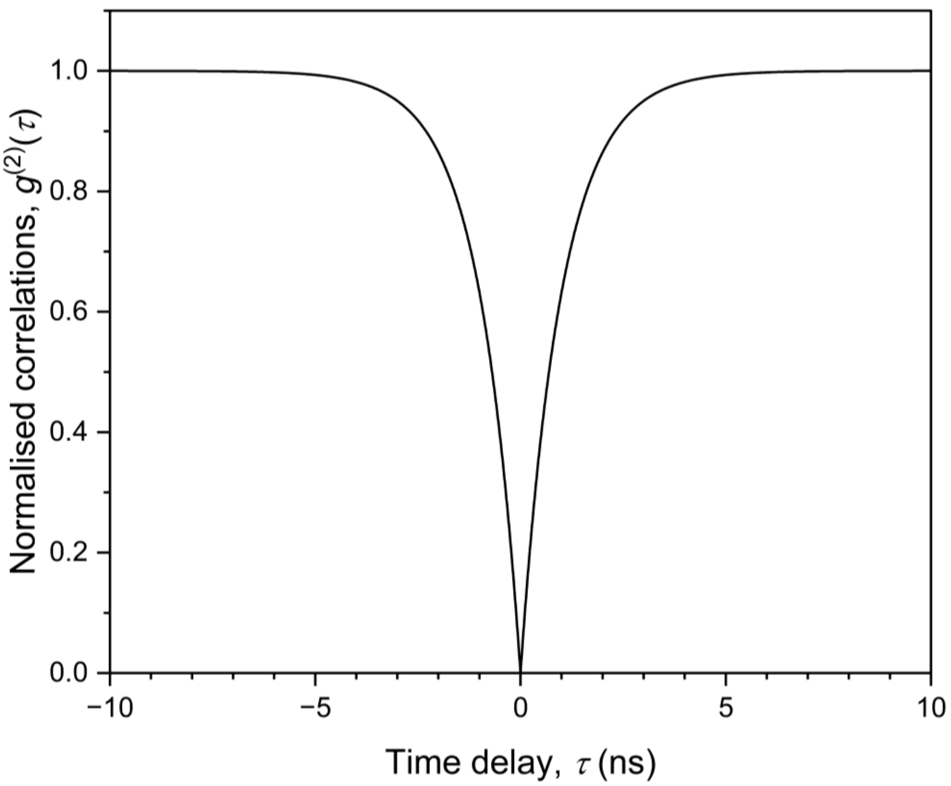

Fig. 4.7 – Example $g^{(2)}(\tau)$ function for a perfect single-photon emitter that is continuously excited, dipping to 0 at $\tau = 0$ ns.

For one single-photon source, the probability is reduced to 0 at $\tau = 0$. The use of more single-photon emitters will produce a dip down to a normalised value of $1 - (1/N_{\mathrm{e}})$, where N_e is the number of emitters. The width of the dip is related to the time taken for the emitter to decay radiatively and be excited again, such that $\tau_{\mathrm{re}} = \mathrm{FWHM}/\ln(2)$. Based on all this, the dip can be fitted to the form:

$$g^{(2)}_{\mathrm{HBT}}(\tau) = R_{\mathrm{f}}(\tau)\left[1 - e^{-|\tau|/\tau_{\mathrm{re}}}\right] \tag{4.5}$$

Where $R_{\mathrm{f}}(\tau)$ is a normalisation factor and τ_{re} is the system recycling time (Zwiller et al. 2004). Alternatively, $g^{(2)}(0)$ may be simply extracted using the ratio of the coincidence count at $\tau = 0$ to that far from $\tau = 0$.

In the case of a sub-Poissonian source under pulsed excitation, rather than a straight line there will be peaks at time internals equal to the laser repetition rate, with the peak height being similarly reduced at $\tau = 0$. An example of this for an imperfect emitter, where $g^{(2)}(0) = 4.0$ % is shown in Fig. 4.8.

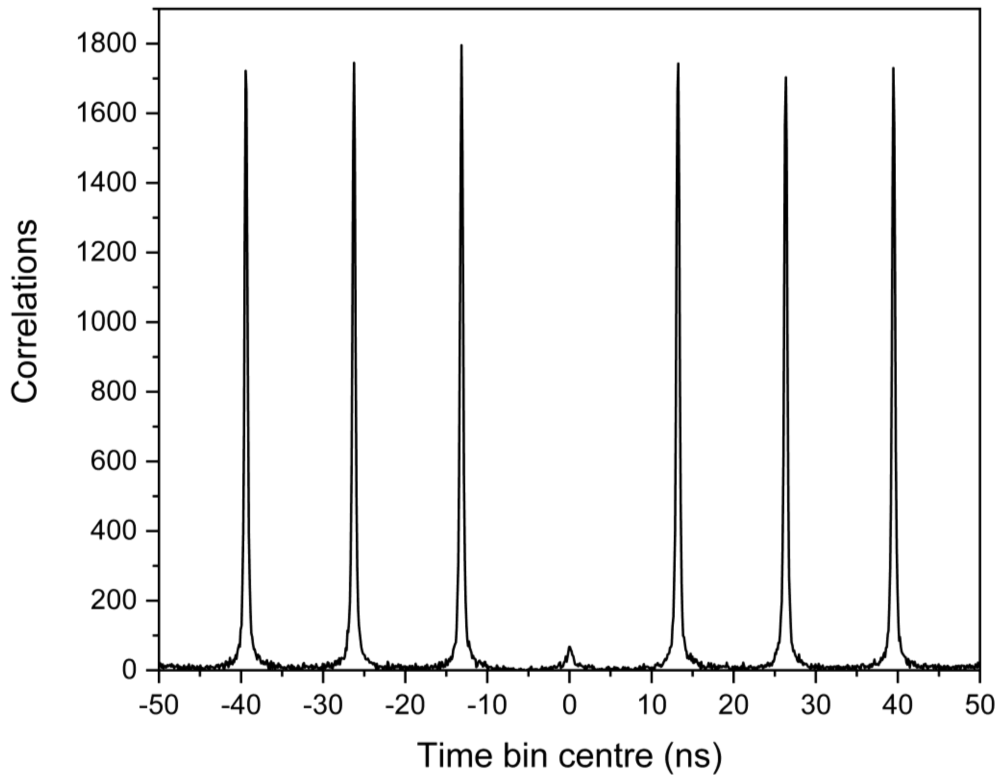

Fig. 4.8 – $g^{(2)}(\tau)$ data obtained for an imperfect single-photon emitter under pulsed excitation, recorded using avalanche photodiodes.

It is possible to relate the second-order correlation value at $\tau = 0$, $g^{(2)}(0)$ with the photon number probability distribution using the equation:

$$g^{(2)}(0) = \frac{\sum_{N_\mathrm{p}=0}^{\infty} N_\mathrm{p}\left(N_\mathrm{p}-1\right)P(N_\mathrm{p})}{\left[\sum_{N_\mathrm{p}=0}^{\infty} N_\mathrm{p}P(N_\mathrm{p})\right]^2} \tag{4.6}$$

Where N_p is the pulse photon number and $P(N_\mathrm{p})$ is the probability density corresponding to N_p. This can be expanded to:

$$g^{(2)}(0) = \frac{2P(2) + 6P(3) + 12P(4) + \cdots}{[P(1) + 2P(2) + 3P(3) + \cdots]^2} \tag{4.7}$$

$$g^{(2)}(0) = \frac{2P(2) + 6P(3) + 12P(4) + \cdots}{\overline{N}_\mathrm{p}^{\,2}} \tag{4.8}$$

Where $\overline{N}_\mathrm{p}$ is the mean photon number per pulse (Stevens 2013).

Along with anti-bunching, a HBT measurement also allows one to observe bunching in super-Poissonian sources (Sparavigna 2021), where photons are detected not simply randomly nor with a delay between detections, but instead are clustered together. Through this, a coincidence counting rate peak greater than unity can appear at $\tau = 0$, rather than a dip (Paul 1982).

4.3.3 Two-photon interference visibility

The Hong-Ou-Mandel experiment allows one to quantify the degree of indistinguishability between two photon streams by observing an absence of coincidences in the apparatus of Fig. 4.9 (Hong et al. 1987; Santori et al. 2002). Quantum mechanics makes the prediction that when identical single-photons enter a 50:50 beam splitter from opposite sides with perfectly overlapping wave packets, they must leave in the same direction (Santori et al. 2002). The probability of photons leaving in different directions is cancelled out due to destructive interference between the photon coincidences.

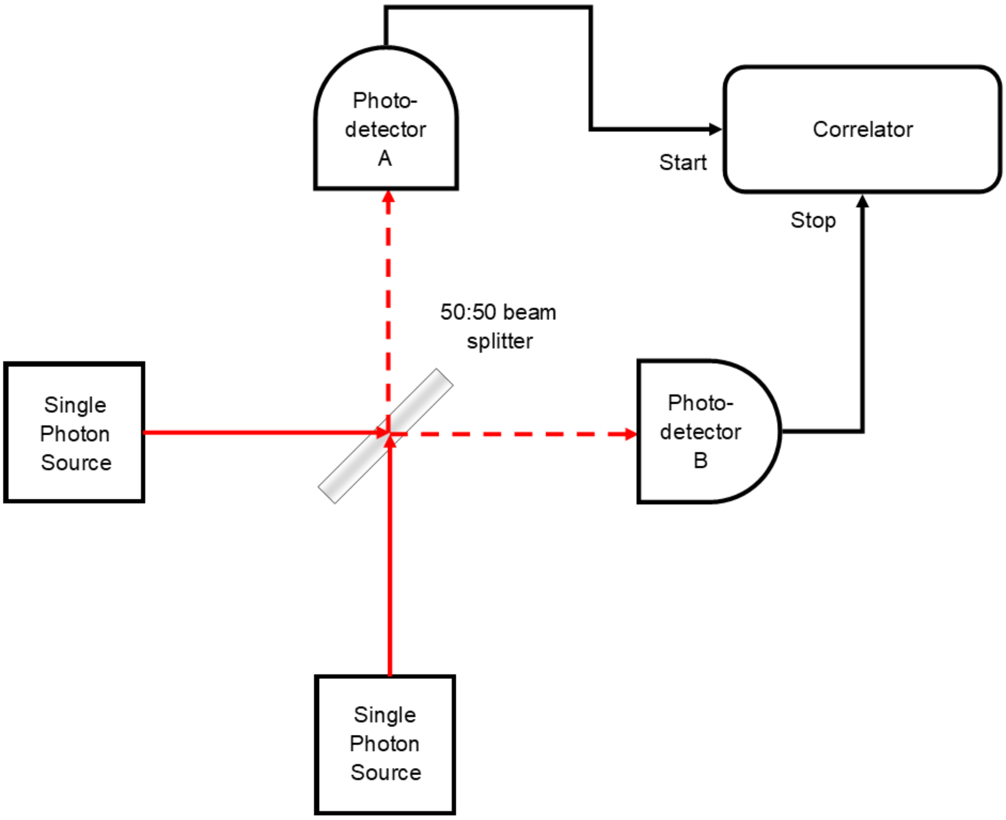

Fig. 4.9 – Configuration used in a two-photon interference experiment. A photon reaches the beam splitter from each source, where they may either be reflected to one detector, or pass through to another detector.

This may be understood by considering the state of two identical photons incident on the 50:50 beam splitter via either input mode a or b. The input state takes the form:

$$\left|\psi_{\text{input}}\right\rangle_{ab} = |1,1\rangle_{ab} = \hat{a}^{\dagger}\hat{b}^{\dagger}|0,0\rangle_{ab} \tag{4.9}$$

Here $\hat{a}^{\dagger}$ and $\hat{b}^{\dagger}$ refer to the creation operators for identical photons in either mode. $|0,0\rangle_{ab}$ and $|1,1\rangle_{ab}$ respectively are Fock states referring to both modes being empty or containing a photon.

When the state interferes with a 50:50 beam splitter, which can output into either mode c or d, it evolves following the unitary $\hat{U}_{BS}$ (Bachor and Ralph 2019), which acts on the creation operators:

$$\hat{a}^\dagger \xrightarrow{\hat{U}_{BS}} \sqrt{1/2}\,\hat{c}^\dagger + \sqrt{1/2}\,\hat{d}^\dagger \tag{4.10}$$

$$\hat{b}^\dagger \xrightarrow{\hat{U}_{BS}} \sqrt{1/2}\,\hat{c}^\dagger - \sqrt{1/2}\,\hat{d}^\dagger \tag{4.11}$$

With the probabilities of each output being equal. The change of sign arises from the unitary transformation, physically corresponding to a phase-shift of π for reflection from opposite sides of the beam splitter.

The combined state upon exiting the beam splitter into either output is thus:

$$|\psi_{\text{output}}\rangle_{cd} = \hat{U}_{BS}\left(\hat{a}^\dagger \hat{b}^\dagger |0,0\rangle_{ab}\right) \tag{4.12}$$

$$|\psi_{\text{output}}\rangle_{cd} = \left(\sqrt{1/2}\,\hat{c}^\dagger + \sqrt{1/2}\,\hat{d}^\dagger\right)\left(\sqrt{1/2}\,\hat{c}^\dagger - \sqrt{1/2}\,\hat{d}^\dagger\right)|0,0\rangle_{cd} \tag{4.13}$$

$$|\psi_{\text{output}}\rangle_{cd} = 1/2\left(\,\hat{c}^{2\dagger} + \hat{c}^\dagger \hat{d}^\dagger - \hat{d}^\dagger \hat{c}^\dagger - \hat{d}^{2\dagger}\right)|0,0\rangle_{cd} \tag{4.14}$$

There are thus four possibilities regarding the photon behaviour which exist in superposition and whose probability amplitudes are summed: both photons could be transmitted through the beam splitter, both could be reflected by the beam splitter, or one or the other can be reflected, and the other transmitted. A diagram demonstrating these interaction possibilities is shown below.

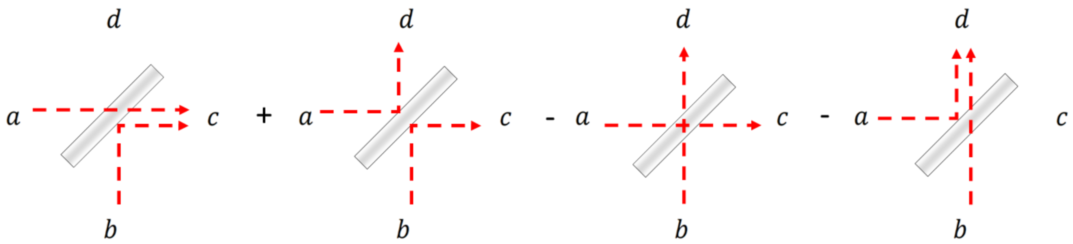

Fig. 4.10 – The four different ways for photons from two sources to interact with a beam splitter. In the case of indistinguishable photons, the middle probability states cancel out via destructive interference. This destructive interference will be degraded based on the difference between the photons' spectral profiles and their arrival times at the beam splitter.

Since the photons are identical, this means the states where the photons leave in different directions, $\hat{c}^{\dagger}\hat{d}^{\dagger}$ and $\hat{d}^{\dagger}\hat{c}^{\dagger}$ (which are equal, as $\hat{c}^{\dagger}$ and $\hat{d}^{\dagger}$ operate on different spaces and are thus commutable) are indistinguishable and thus cancel out perfectly due their opposite signs, with their superposition terms vanishing (Hong et al. 1987; Brańczyk 2017):

$$\left|\psi_{\text{output}}\right\rangle_{cd} = 1/2\left(\hat{c}^{2\dagger} - \hat{d}^{2\dagger}\right)|0,0\rangle_{cd} \tag{4.15}$$

Thus, perfectly indistinguishable photons will always arrive at a single detector simultaneously, with coincidences between the two detectors never being observed. By comparison, fully distinguishable photons will be unaffected and will have a 50:50 probability of arriving at the same detector or different ones. It is thus possible to measure the degree of indistinguishability of two photons by performing a HOM experiment and obtaining a correlation histogram for the two detectors, as in the pulsed Hanbury-Brown and Twiss experiment, which will similarly produce a reduced peak at $\tau = 0$ with an area dependent on the degree of overlap between the two wave packets, and thus their degree of indistinguishability (Santori et al. 2002).

Another method of obtaining the two simultaneous photons required for the measurement, which is used later in this in this thesis, divides the single photon emissions of the characterised device using another 50:50 beam splitter. As the photons transmitted down each path will be emitted in separate pulses, a path delay is introduced corresponding to the time difference between them $\Delta\tau$, so as to temporally align them. One beam then passes through a $\lambda/2$ waveplate, to control polarisation indistinguishability. As there will also be a dip in coincidences at $\tau = 0$ due to the limited probability of subsequent photons being sent into different beams at the first beam splitter, the indistinguishability must instead be inferred from the ratio of peak areas at $\tau = 0$ ns for co- and cross-polarised photon pairs, controlled using the half waveplate. While the prior will show a reduction from the degree of indistinguishability, the latter are fully distinguishable due to their difference in polarisation, meaning that the effects of the imperfect beam splitting can be isolated. A diagram of the configuration used for this HOM measurement is shown in Fig. 4.11:

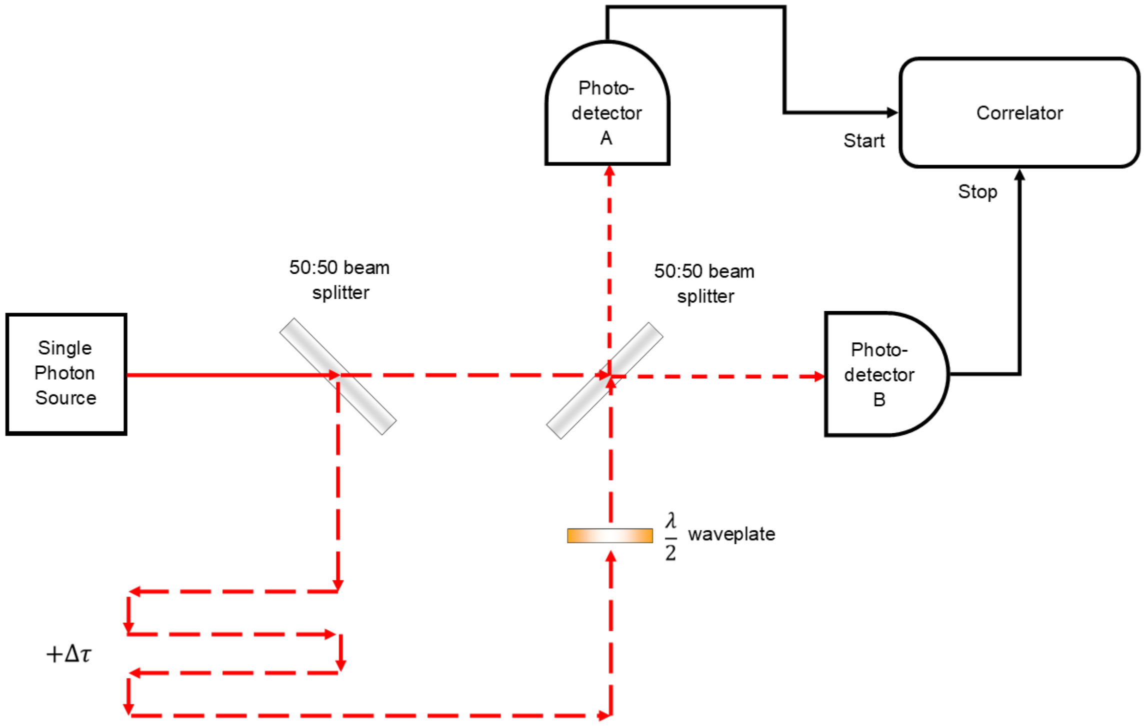

Fig. 4.11 – Alternative configuration used in a two-photon interference experiment. Photons from a single source driven with a pulsed laser are divided using a beam splitter. One beam experiences a path delay corresponding to the time between pulses, then passes through a half-waveplate to reintroduce polarisation indistinguishability before being interfered with the other beam.

Regardless of methodology, it may also be necessary to account for the probability of multiple photons being emitted from the source at once if one is not using a perfectly pure single photon source. This would cause the Hong-Ou-Mandel interference visibility to be decreased. This effect may be treated as separable noise and accounted for using the following equation to obtain the intrinsic two-photon indistinguishability M_S, using the measured V_{HOM} and $g^{(2)}(0)$, in the limit where the latter is small (Ollivier et al. 2021):

$$M_{\mathrm{S}} = \frac{V_{\mathrm{HOM}} + g^{(2)}(0)}{1 - g^{(2)}(0)} \tag{4.16}$$

4.4 Resonant Rayleigh scattering and spectral filtering

There is a need to distinguish between incoherent scattering, which produces resonance fluorescence, and coherent scattering (elastically, where a phase relationship between photons is conserved across scattering) (Konthasinghe et al. 2012). For an ideal two-level system, most light is scattered coherently via RRS (Resonant Rayleigh Scattering) when the Rabi frequency Ω (the fluctuation frequency in populations of the two atomic levels involved in a transition) is smaller than the radiative decay rate. Otherwise, scattered light is dominated by incoherent resonance fluorescence (Mollow 1969). When scattered light originates from a single two-level system, it shows anti-bunching for any value of the Rabi frequency (Cohen-Tannoudji et al. 1992).

The fraction of the total emitted light due to resonant Rayleigh scattering is given by:

$$\frac{I_{\mathrm{RRS}}}{I_{\mathrm{total}}} = \frac{T_2}{2T_1(1 + \Omega^2 T_1 T_2)} \tag{4.17}$$

Where T_1 is the radiative lifetime and $T_2 = 2\hbar/\Delta E$, where ΔE is the uncertainty in the photon energy (Bennett et al. 2016b). Below is a plot of this relationship for various values of $T_2/2T_1$, calculated with $T_1 = 1$ ns.

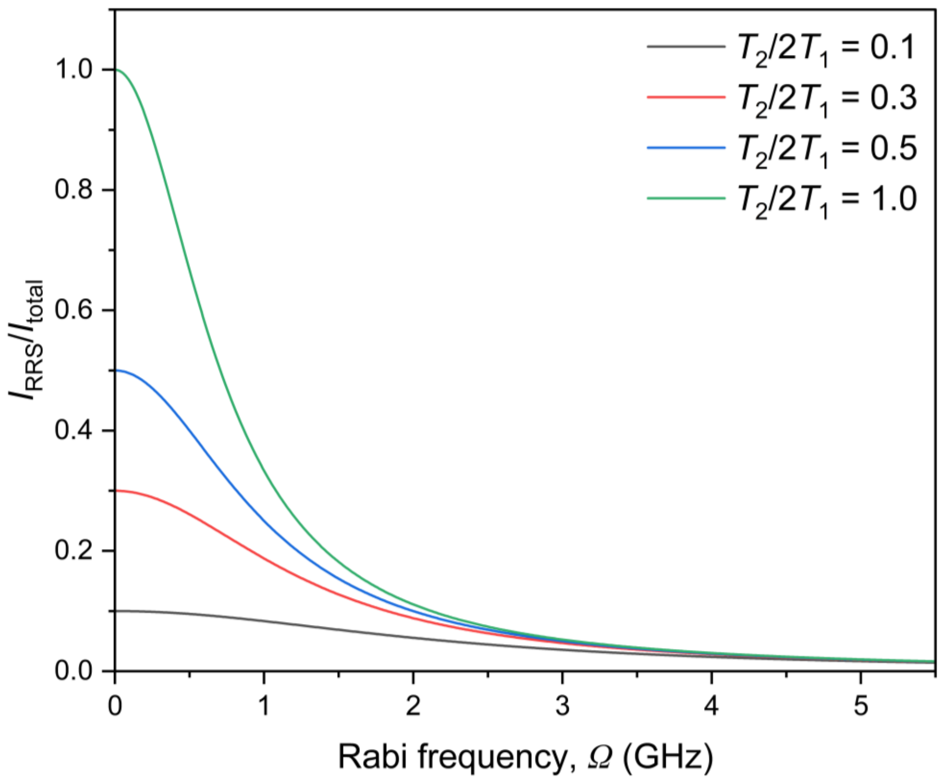

Fig. 4.12 – Relationship between the fraction of light produced by Resonant Rayleigh Scattering and Rabi frequency, for several values of $T_2/2T_1$.

The result follows a Lorentzian curve, starting at $T_2/2T_1$ at $\Omega = 0$ (though this would correspond to an emission rate of 0), then approaches 0 as the Rabi frequency tends to infinity, as RRS makes up a diminishing part of the total intensity.

Unwanted backgrounds in driving laser, transitions and phonon sidebands can also be removed using spectral filtering of resonance fluorescence, improving the measured single-photon purity and indistinguishability. However, complex behaviour is predicted as the filter bandwidths approach the linewidth of the emitter. This is due to preferential transmission of components with differing photon statistics. This regime was probed by Phillips et al (2020) using a Purcell-enhanced quantum dot. They found that changing the filter width can transform the photon statistics between antibunched, bunched or Poissonian distributions. This showed that a sub-natural linewidth cannot simultaneously be observed with strong antibunching (Phillips et al. 2020).

Chapter 5
Design and characterisation of Bragg cavity micropillars

This chapter discusses the micropillar designs used throughout this thesis and presents some initial simulation results using these designs, obtaining parameters such as the cavity mode wavelength, Purcell factor, efficiencies, numerical aperture and mode field diameter as functions of the pillar diameter. This is followed by detailing of the fabrication and processing process developed to produce samples of these devices, making use of a novel direct-write lithography-based method. The produced samples are characterised, with their resulting Q factors suggesting a high sidewall smoothness competitive with other methods. Finally, a supplementary study is included, in which the possibility of utilising remaining SiO_2 hard mask deposits as a microlens to improve coupling into single mode fibres is examined.

5.1 Design of micropillars used in this work

The work in this thesis primarily focuses on two designs of micropillars, one with a lower intrinsic quality factor of around 600, offering a broader fundamental cavity mode, and one with a higher intrinsic quality factor of around 22,500, providing a higher Purcell effect for resonant QD transitions while still having an efficient outcoupling through the top of the structure, which will decrease with the addition of more top DBRs and must be balanced with an increased Q factor.

The low Q design's broader cavity mode simplifies the process of selecting on-resonance transitions, which due to the random growth of QDs in our samples can require the testing of hundreds of devices to optimise in a high Q pillar. It also allows for less resource-intensive FDTD simulations, which play a large part of this work, as a lower Q factor reduces the required computation time. This is due to a reduction in the ringdown time of the device. These devices also show a high outcoupling efficiency, with a high proportion of light being output to a fibre, partially contributable to the increased reflection from Bragg mirrors below the cavity spacer layer. Previous authors have supplemented this by suppressing emissions into non-cavity modes (Wang et al. 2021; Ginés et al. 2022), a prospect which is examined in detail in Chapters 7 and 8. Finally, as shown in previously published work (Androvitsaneas et al. 2023) also presented later in this thesis, it has been proven that low Q devices, regardless of their reduced Purcell enhancement and brightness, can still generate highly indistinguishable photons under resonant excitation.

Meanwhile, while finding on-resonance transitions can be more difficult in high Q micropillars, the results are a lot brighter, enabling use in further experimental work. The increased Purcell factor, which is proportional to the structures Q factor, can increase the detected photon number more than tenfold, curtesy of their increased Purcell factor, which is directly proportional to the structure's Q factor (and inversely so to its effective mode volume) (Purcell 1946). Previous research has shown that devices of comparable Q factors are also particularly suitable for the generation of indistinguishable photons under pulsed resonant excitation. Specifically, an increase to the Purcell factor, and thus a reduction in the radiative lifetime of QD transitions, is expected to improve the indistinguishability of the output light (He et al. 2013; Ding et al. 2016; Somaschi et al. 2016). Finally, a high Q factor is also beneficial when it comes to characterising the side wall roughness of etched devices, as this will reduce the percentage uncertainty in the measured Q factors, and thus the losses due to scattering.

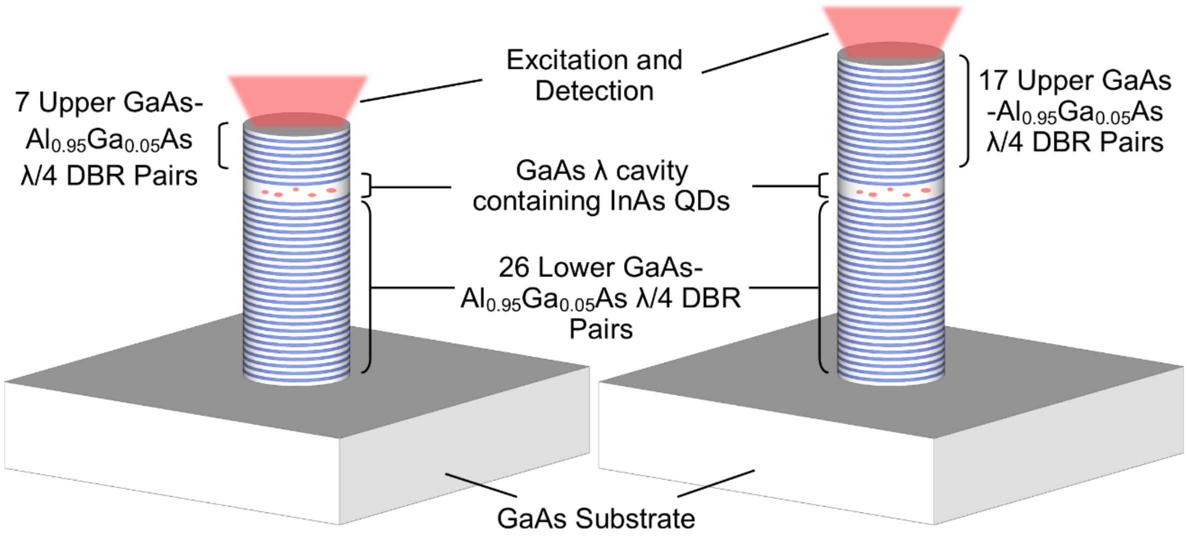

Fig. 5.1 – Labelled diagrams of low Q (left) and high Q (right) high-aspect ratio Bragg cavity micropillars.

The "low Q" ("high Q") design consists of 7 (17) upper and 26 lower pairs of alternating $\lambda/4$-thick GaAs and $Al_{0.95}Ga_{0.05}As$ Bragg mirror layers above and below a λ-thick GaAs cavity spacer layer. This spacer contains a deposited 0.483 nm thick layer of InAs, which self-assembles into quantum dots using the Stranski-Krastanov growth method, courtesy of an InAs/GaAs lattice mismatch of ~7% (Gerard 1991; Khandekar et al. 2005). For best coupling, as desired in most cases, the layer is positioned in the centre of the spacer at the electric field anti-node of the fundamental mode, while for suppressing coupling, it is positioned $\lambda/4$ lower at the field node, as discussed in Chapter 7. The epitaxial pillar structure is grown on an undoped GaAs substrate of 500 μm thickness, with crystal orientation (100). Excitation and collection are both performed through the top of the pillar.

The pillars are designed for a cavity resonance wavelength of λ = 940 nm, or a photon energy of 1.319 eV. Considering the refractive index of each material, this requires the cavity spacer layer to have a thickness of 267.856 nm, and the GaAs and $Al_{0.95}Ga_{0.05}As$ $\lambda/4$ layers 66.964 nm and 78.893 nm thickness respectively.

The theoretical quality factors Q of the unstructured planar cavities as function of top and bottom pair numbers calculated using (2.8) are shown in Fig. 5.2. The two designs studied here have Q = 613 and Q = 22540, corresponding to HE_{11} FWHMs of 1.53 and 0.04 nm, or 2.15 and 0.06 meV respectively.

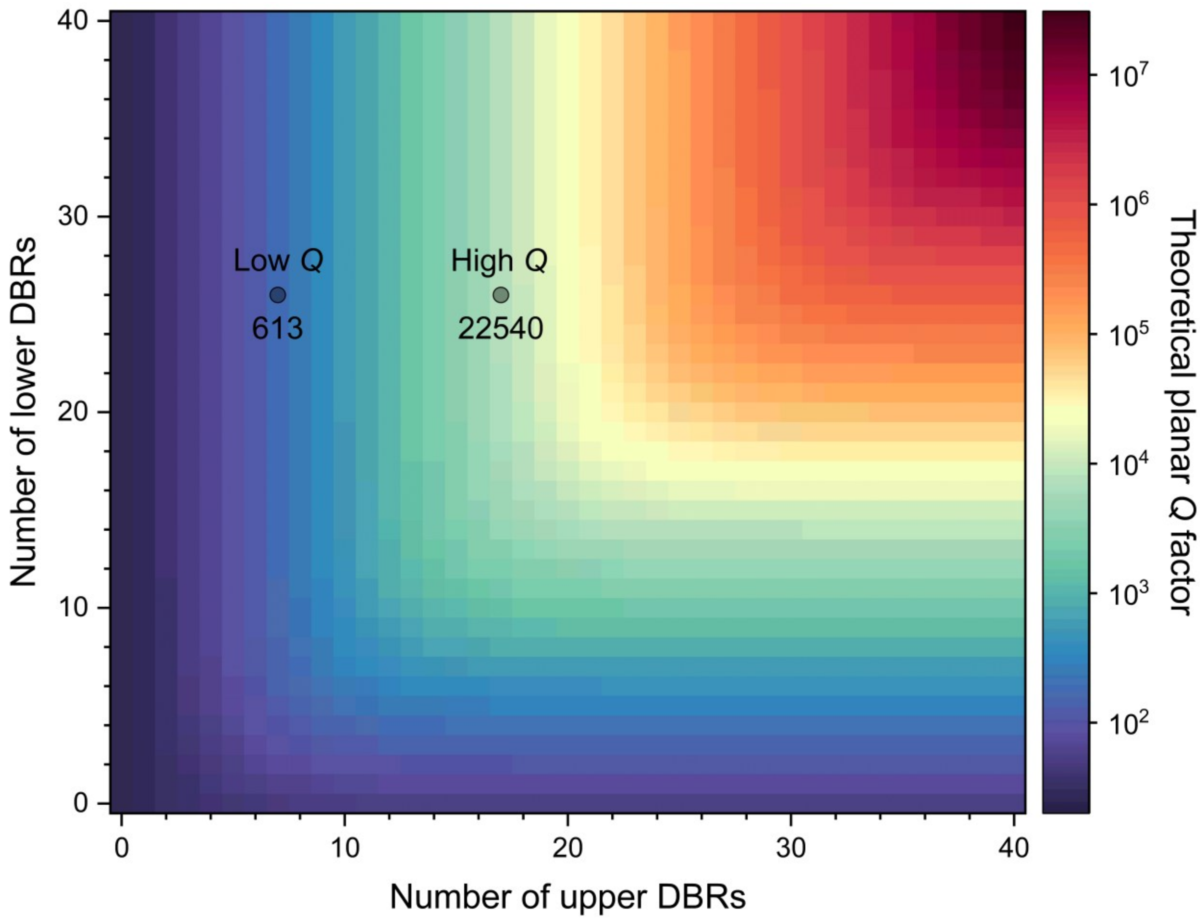

Fig. 5.2 – Theoretical quality factors of $GaAs/Al_{0.95}Ga_{0.05}As$ planar micro-cavities with a λ-thick GaAs spacer layer and different numbers of upper and lower Bragg mirror pairs, for a design wavelength of 940 nm, plotted on a logarithmic scale The quality factors of the two designs used in this thesis's work are indicated.

Real micropillar devices will have a lower quality factor than calculated here, due to losses via sidewall scattering and absorption (Reitzenstein and Forchel 2010), as discussed in section 2.2.3.

5.2 Simulation results

The two pillar designs presented here were simulated using finite-difference time-domain simulations in Lumerical FDTD, as detailed in Chapter 3.

Micropillars were modelled as per the designs above, placed on a GaAs substrate. While the substrate of the physical example has a thickness of 500 μm, the simulated substrate is only 5.5 μm thick. This overlaps the absorbing simulation boundaries, as it is assumed that reflection from within the substrate is negligible. QD emission is modelled as an electric dipole source in the central height of the cavity spacer layer, on the central axis such that the dipole is placed at $x = y = z = 0$.

For this work, the simulation volume is a rectangular cuboid with x and y dimensions of 7 μm, sufficient for simulating large diameter pillars, and a z dimension of 10 μm, with PML conditions applied at the simulation boundaries. A mesh resolution of 0.01 μm is used in each direction for the space immediately surrounding and including the pillar, overriding the automatically set mesh of the simulation to ensure the DBRs and sidewalls are modelled sufficiently precisely.

The simulations were terminated once the system energy dropped to $10^{-4.5}$ of its initial, maximum value at the excitation pulse. The simulation volume was reduced by a factor of 4 using symmetric and anti-symmetric boundary conditions were used in the two planes of symmetry at $x = 0$ and $y = 0$ to reduce computation time. If any divergences are detected, usually involving the energy of the system unexpectedly increasing exponentially due to modelling errors, the simulations end early in a failure state.

The mesh settings, system energy threshold, and simulation boundaries were initially tested using a series of convergence tests, to minimise computer workload without sacrificing accuracy of results. For example, as noted in the following section, the system energy was chosen such that the quality factor determined from the produced emission spectra closely matched the theoretical planar value (as expected, given that losses due to scattering and absorption are not simulated). Each cavity mode peak is also ensured to follow a Lorentzian distribution, with no broadening or side fringes due to remaining energy in the system, which would otherwise have such an effect when Fourier transformed. Other tests involved performing high-impact simulations with higher mesh resolutions then comparing to results with the setting lowered, and testing different simulation volumes.

5.2.1 Example – simulating 2.00 μm high Q and low Q micropillars

Fig. 5.3 shows emission spectra for both a 2.00 μm diameter high Q (a, b) and low Q (c, d) micropillar, both towards the top (through the top planar monitor) (a, c) and omnidirectional through all boundary monitors (b, d). The power is normalised to the source power for a homogenous embedding medium, so that (b) and (d) represent the Purcell factor, F_{P} of the two devices.

For a high Q pillar of this diameter, the spectra are clear of higher order modes and variation in the non-cavity mode background, which appears approximately flat other than the mode peak within the studied spectral range, allowing them to be easily fitted with Lorentzian curves with constant y-offsets to extract the proportion of emissions via coupling to the cavity mode.

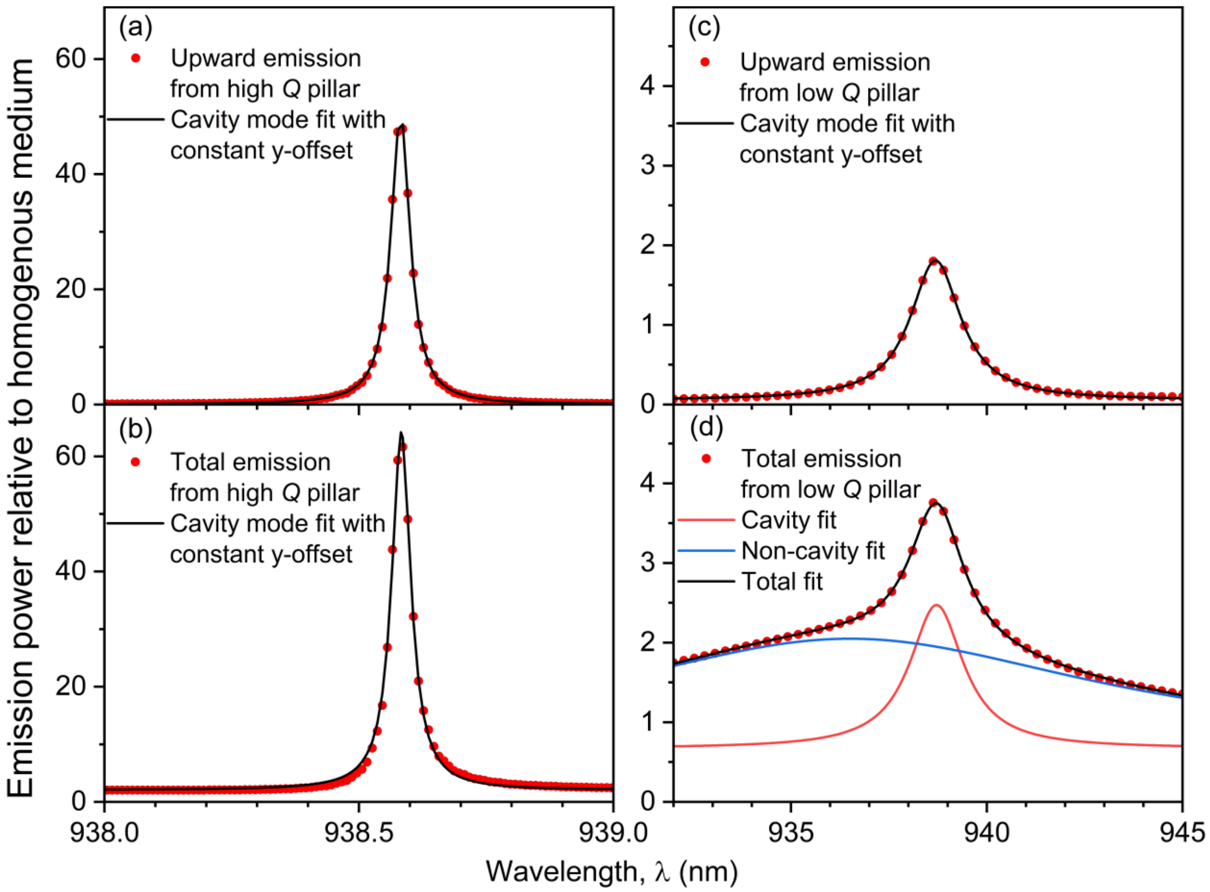

Fig. 5.3 – Simulated emission power spectrum relative to that in a homogenous medium of the local embedding refractive index (GaAs) of 2.00 µm diameter high Q (a, b) and low Q (c, d) pillars each excited by a dipole at position x = y = z = 0, polarised in the x direction, through the top boundary (a, c) and through all boundaries (b, d). The main resonance seen is the HE_{11} cavity mode and is fitted with a Lorentzian, the non-cavity modes are fitted as a constant background, or in (d) as an overlapping Lorentzian.

These fits both find the cavity mode wavelength to be λ_c = 938.58 nm and the mode FWHM $\Delta\lambda$ = 0.05 nm, with differing y-offsets of 0.02 and 2.05 respectively for (a) and (b). The quality factor $Q = \lambda_c/\Delta\lambda$ of the modelled pillar is thus determined to be 20800, some 8% below the planar value for the high Q design in the previous section. The maximum normalised emission power in all directions in (b) provides the Purcell factor at the HE_{11} mode wavelength, 64.18. By using the fitted amplitude of the total emissions via the cavity mode and dividing by F_{P}, one can determine the SE coupling factor β to be 0.968. Similarly, assuming that only the emission through the top boundary is collected in a device, one obtains an outcoupling efficiency ξ of 0.787, indicating that the majority of cavity mode emission are directed upwards.

By contrast, while (c) has an approximately constant background, allowing the HE_{11} mode to be fitted again using a Lorentzian with a constant y-offset and showing that that little of the non-cavity mode emissions are directed in the upwards direction, a non-cavity mode is very prominent in (d). This is a combined result of the reduced coupling strength of the low Q cavity mode and the broader spectrum being examined, directly due to the lower Q factor and thus FWHM. Thus, to fit the data accurately, it is also necessary to add a second Lorentzian fitting a much broader, overlapping mode peak. These components and the total fitted curve are each shown in (d).

(c) and (d) both find λ_{c} = 938.7 nm, and $\Delta\lambda$ = 1.6 and 1.7 nm respectively. The difference in these values likely arises from the differing fitting of the non-cavity mode background. (c) finds a constant y-offset of 0.05. Meanwhile, (d) finds a constant y-offset of 0.67 in combination with a fitted broad mode of λ_{L} = 936.5 nm, and $\Delta\lambda_{\mathrm{L}}$ = 15.8 nm. It also has a peak height of 1.38, or 2.05 including the y-offset, such that the non-cavity mode background in the low Q pillar at the HE_{11} mode matches that in the high Q pillar. The cavity mode and fitted non-cavity mode thus have Q factors of 561 and 59 respectively, the prior being similarly about 8% below that of a planar cavity of the same layer composition. The F_{P} obtained from the total emissions at HE_{11} mode is 3.75, while β = 0.481 and ξ = 0.468, both much lower than in the high Q pillar, due to the increased relative influence of the non-cavity modes on the Purcell factor.

Based on the non-cavity mode fits in (b) and (d), it may be noted that the non-cavity mode background for this size of micropillar of either design is approximately 2 times the emission of the source in a homogenous medium. The non-cavity mode is very broad, as seen in (d), effectively constant as a function of wavelength within the range studied in (b). These modes will be re-examined in greater detail further below and in later chapters of this thesis.

It is primarily scattering from the roughness of sidewalls that reduces the quality factor of a real device as it is confined in the x and y directions, as can be seen in (2.15), but this is not modelled within the FDTD simulations performed, resulting in a Q very close to that in the planar case for both designs.

5.2.2 HE11 wavelength as a function of pillar diameter

To perform systematic studies as function of diameter, it was opted to use the low Q pillar design, as they have a shorter emission time, curtesy of their lower planar quality factor, and thus have a lower computational cost in FDTD simulations. They not only require less simulation time, but as the cavity modes have a larger FWHM, they may be characterised with a lower density of frequency monitor peaks. Thus, a wider range of frequencies can be monitored, allowing higher order modes to be included in some of the simulations. Otherwise, the simulations are similar to the example previously presented.

Fig. 5.4 shows the HE_{11} mode wavelength as a function of pillar diameter. In each case, the spectrum was found, as in the previous section, and fitted with a Lorentzian to determine the peak wavelength.

The results were fitted with (2.6), describing cavity mode wavelengths as a function of diameter. As the HE_{11} mode is described, X_{φ,N_0} takes the form of the first zero of the zeroth order Bessel function, $X_{0,1} = 2.40483$ (Kowalski et al. 2010; Le Kien et al. 2017), as noted in Section 2.2.1.

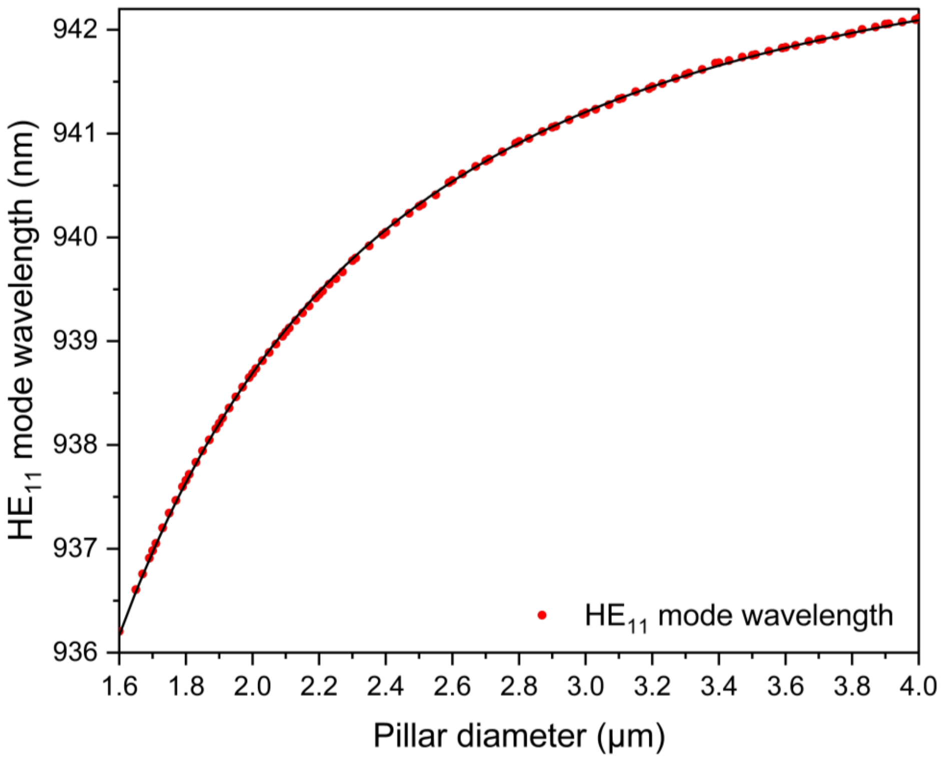

Fig. 5.4 – HE_{11} mode wavelength of the low Q 7 (26) micropillar as function of pillar diameter, from fits to FDTD simulations.

As can be seen, the resulting mode wavelengths match very well to theoretical predictions, based on the quality of the fit above, with a root mean square (RMS) error of 0.017 nm. For this low Q design, it returns fit parameters for the effective dielectric constant and planar wavelength of $\varepsilon_{\mathrm{r,eff}}$ = 13.44 ± 0.01 and λ_0 = (943.233 ± 0.004) nm respectively.

5.2.3 HE_{11} Purcell factor, emissions, and efficiencies versus pillar diameter

Using the low Q micropillar simulations with a single centred source, it is possible to determine the dependence of the Purcell factor and cavity efficiencies on the pillar diameter, determining the values for each simulation as demonstrated in Section 3.3.2.

Fig. 5.5 (a) shows the on-resonance HE_{11} Purcell factor F_{P} and its split into corresponding cavity mode emission Γ_{C} and non-cavity mode emission Γ_{L} components, as functions of diameter. Similar to F_{P}, the emissions are normalised based on the source emission in a homogenous medium Γ_0. The SE coupling efficiency β (2.20), emission directionality η (2.21), and outcoupling efficiency ξ (2.22) for each simulation were also calculated and plotted against diameter, in (b).

As can be seen, the non-cavity modes have periodic peaks in diameter within the spectral range studied, repeating every 0.28 µm. While variation in these emissions would have a limited impact on a high Q structure with a much stronger cavity enhancement, for a low Q pillar like that studied here it has a significant effect on the total Purcell factor. By comparison, the HE_{11} cavity mode coupling decreases with an inverse-square relationship with diameter, due to the increase in mode volume, which has been fitted with a dashed curve, using the equation below with fitting parameter K being found to be 7.13 µm^2:

$$\Gamma_{\mathrm{C}} = \frac{K}{d^2} \tag{5.1}$$

Meanwhile in (b), both cavity efficiencies plotted β and ξ follow very similar patterns with pillar diameter, dipping at the diameters where the non-cavity modes peak as they become a more dominant portion of the total emissions, reducing the proportion of emissions coupled to the cavity mode. They also decrease with diameter, matching the trend of the cavity mode emissions and the overall trend of F_{P}.

Also plotted in this subfigure is the emission directionality η, which approximates the overall proportion of light directed upwards. Interestingly, while showing periodic modulation, this does not appear to share the same period as the other parameters. This, combined with its changing amplitude, implies there could be two effects on the parameter with different periods, whose phases change with diameter, with the change in amplitude arising from constructive and destructive effects. Given that β and ξ are so similar, despite the prior factoring in cavity emissions in directions other than upwards, it appears to be near-exclusively the directionality of the non-cavity modes that changes with diameter, rather than the cavity mode, which is nearly entirely emitted out the top of the pillar. Similar periodic behaviour has previously been observed in results by Wang et al. (2020b) and Ginés et al. (2022).

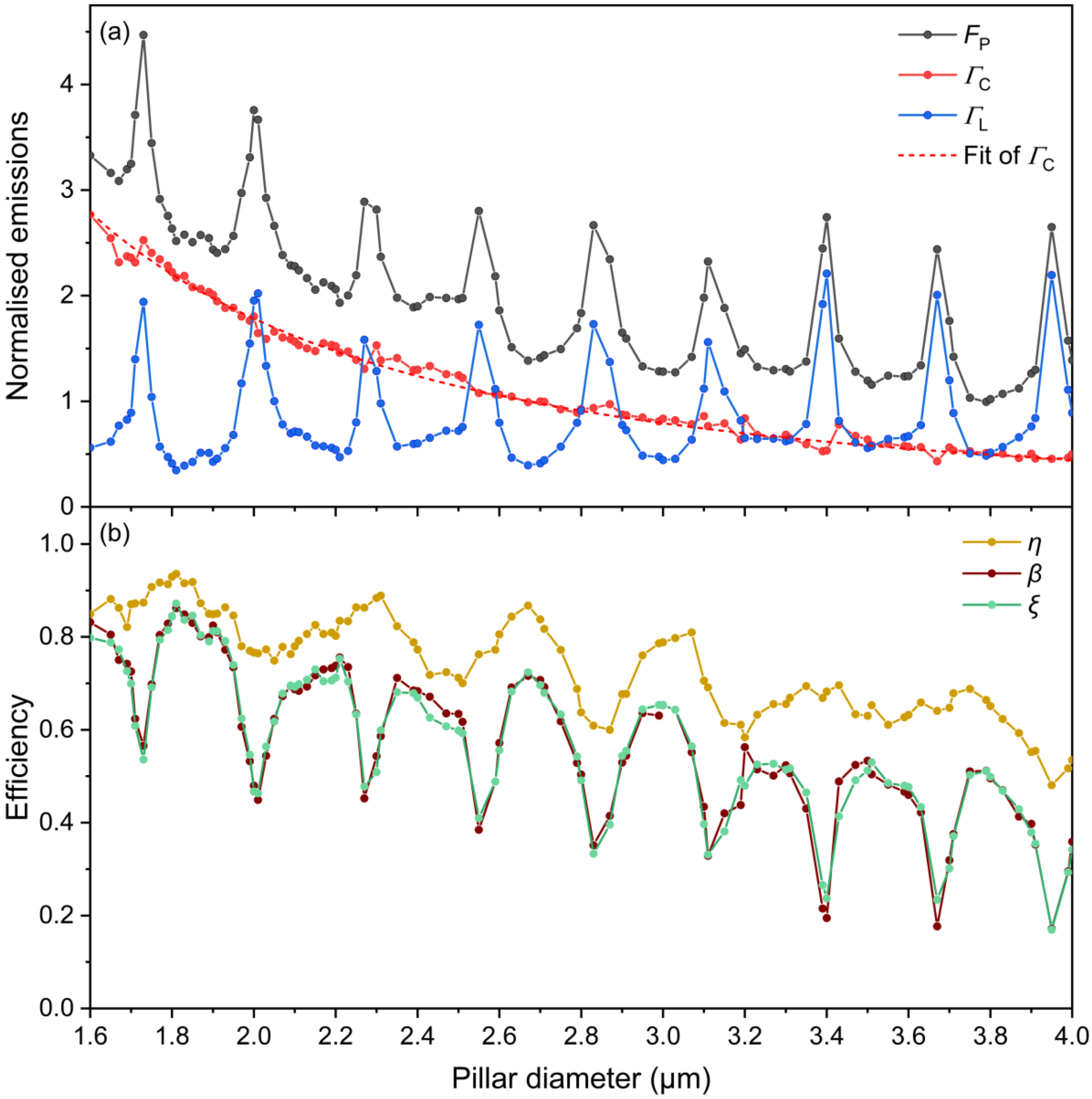

Fig. 5.5 – (a) The extracted Purcell factor F_P, cavity mode emissions Γ_C, and non-cavity mode emissions Γ_L, and (b) the cavity directionality η, SE coupling efficiency β and outcoupling efficiency ξ of a low Q micropillar as functions of pillar diameter as simulated in Lumerical FDTD. In the case of (a), all emissions are normalised based on the source emission power in a homogenous medium. The cavity mode emissions have been fitted with an inverse-square relationship as a function of diameter (dashed).

5.2.4 Far field, NA and MFD

The below figure shows an example of the far field above a 1.85 μm low Q micropillar at its HE$_{11}$ mode wavelength, normalised to the maximum value. The electric field is projected into the far field, to a radial distance of 1 metre.

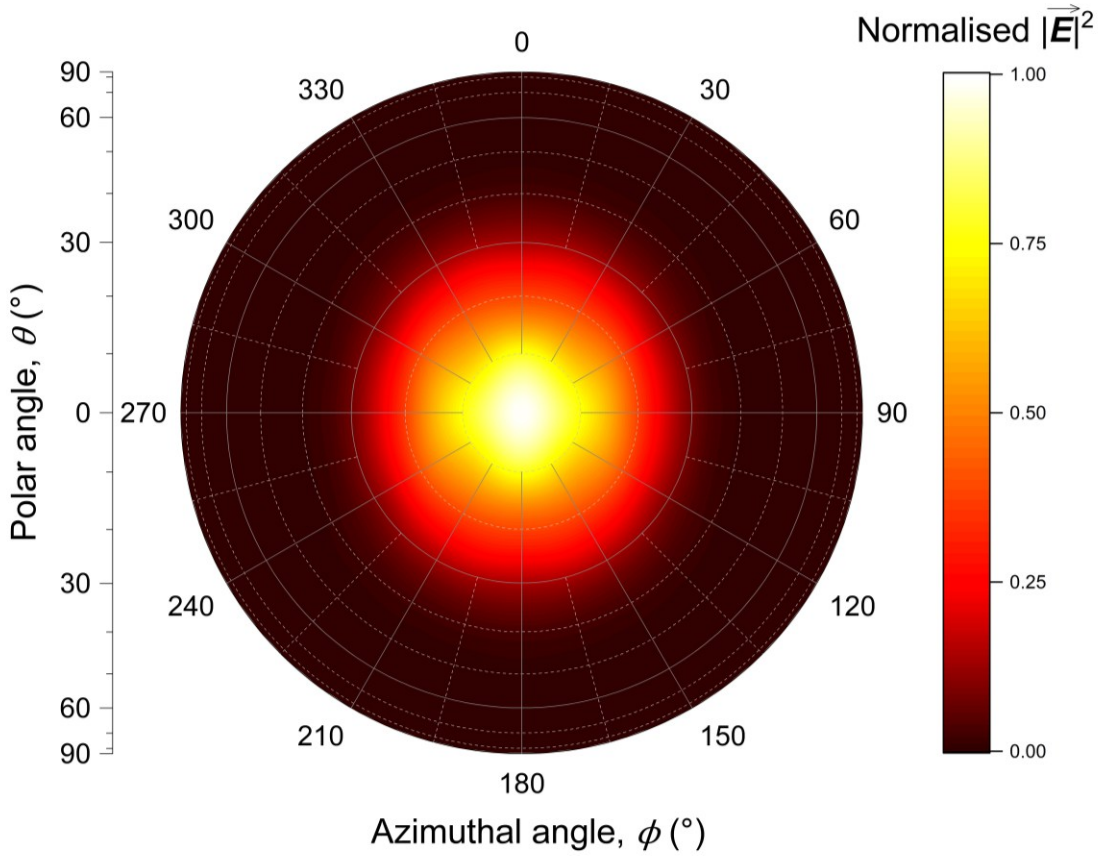

Fig. 5.6 – Far-field $|\vec{E}|^2$ plot, calculated at 1 metre distance and normalised to its maximum value, above a 1.85 μm low Q micropillar at the HE$_{11}$ mode wavelength 937.837 nm.

As may be seen, the HE$_{11}$ far field distribution largely circularly symmetrical, albeit slightly elliptical with a major axis on along the ϕ = 0 and 180° axis, corresponding in Cartesian space to the $\pm x$ directions on which the dipole is oriented.

While here, the far field takes a near-Gaussian spatial distribution, this isn't always to be expected. This can be seen by comparing with the HE$_{11}$ far field for a 2.00 μm pillar:

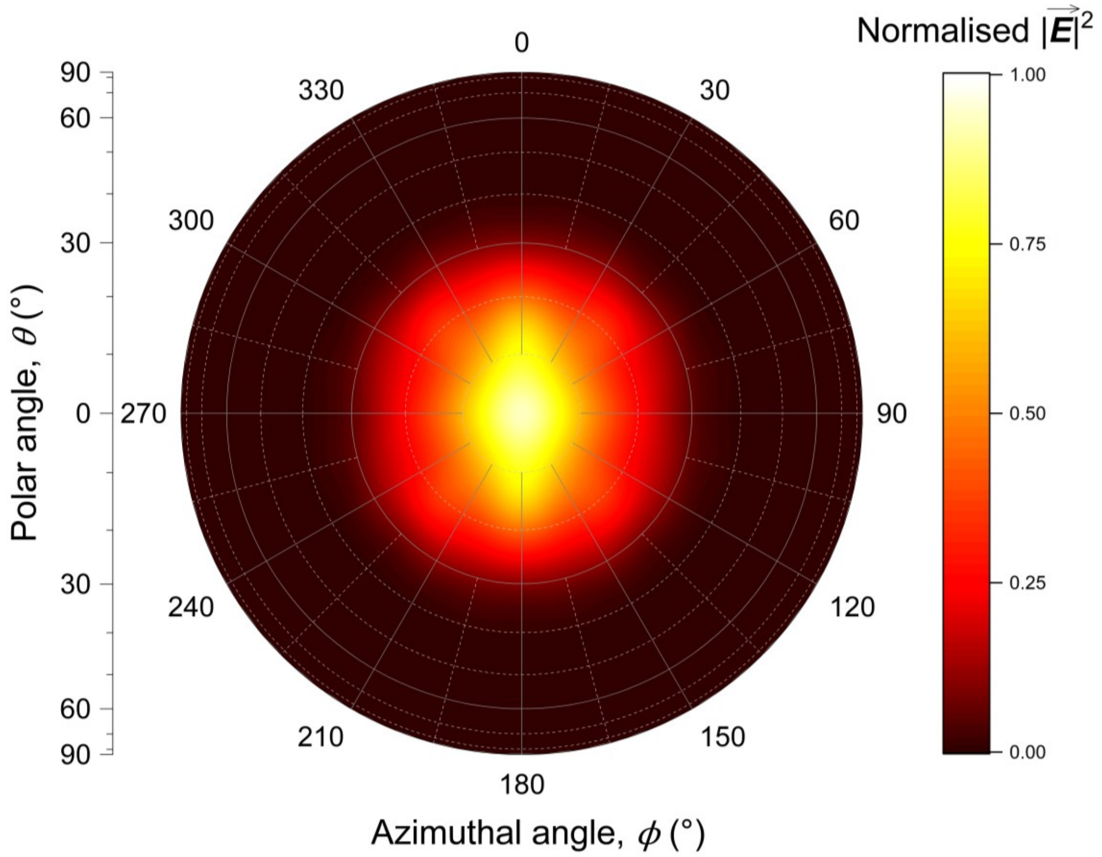

Fig. 5.7 – Far-field $|\vec{E}|^2$ plot, calculated at 1 metre distance and normalised to its maximum value, above a 2.00 μm low Q micropillar at the HE_{11} mode wavelength 938.633 nm.

This shape is the combination of two orthogonally polarised HE_{11} modes which are driven asymmetrically because of the dipole nature of the emitter used in the simulations, which doesn't emit along its axis, leading to emission power varying by azimuthal angle. There is also some increased coupling to the non-cavity modes (demonstrated in Chapter 7) which interfere with the HE_{11} mode, which show an increased influence at the cavity mode wavelength of a 1.85 μm pillar compared to a 2.00 μm pillar, as discussed in the previous section (see Fig. 5.5) contributing to the difference between the two figures.

By projecting the emissions through the top monitor into the far field like this, the $1/e^2$ NA is calculated as a function of low Q pillar diameter, using the average power transmitted vs far field angle via the method demonstrated in section 3.3.4. These results are shown in Fig. 5.8.

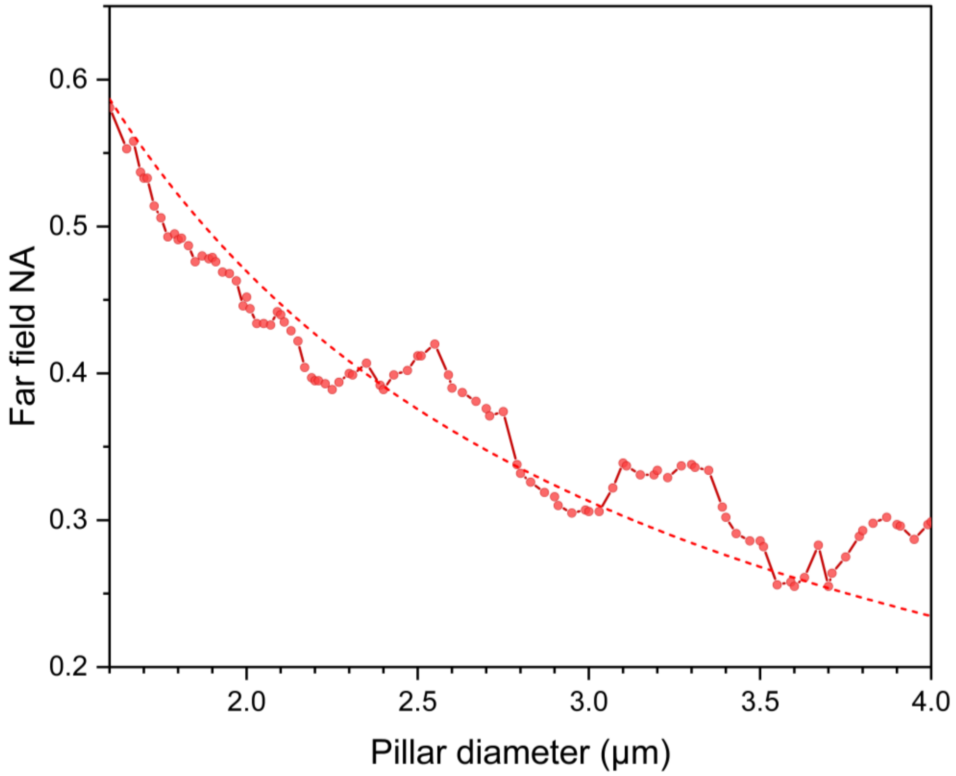

Fig. 5.8 – Far-field $1/e^2$ NA as a function of pillar diameter, calculated at the HE_{11} mode wavelength in each case. Data is fitted with a relationship inversely proportional to diameter (dashed line).

As may be seen, the numerical aperture decreases with diameter, albeit at a reduced rate at larger sizes, and is expected to follow a reciprocal decay trend. To test this, the data has been fitted with a relationship inversely proportional to the diameter of the pillar, shown as a dashed line. The fit is not perfect, with an RMS error of 0.029, and some modulation is present, increasing with diameter. While possibly related to interference across the cavity and non-cavity modes at the top surface of the pillar, this pattern does not appear to be directly related to the changing non-cavity mode emission intensity, based on its significantly larger period.

Similarly, the $1/e^2$ mode field diameter (MFD) at the top of pillar can be estimated using the mean of the x and y cross sectional electric field intensities at this height. This property is ill-defined for a micropillar, as opposed to structures like single-mode optical fibres (Artiglia et al. 1989), so is here approximated by fitting a Gaussian peak to the data, with the error in the fit providing the error bars seen in Fig. 5.10. However, as interference effects are significant in this measurement taken directly at the top of the pillar, often showing multiple peaks in the electric field at different radii from the central axis, the field profile will often not be described well with this fitting function. One of the better fit examples, for a 2.00 μm pillar is presented in Fig. 5.9.

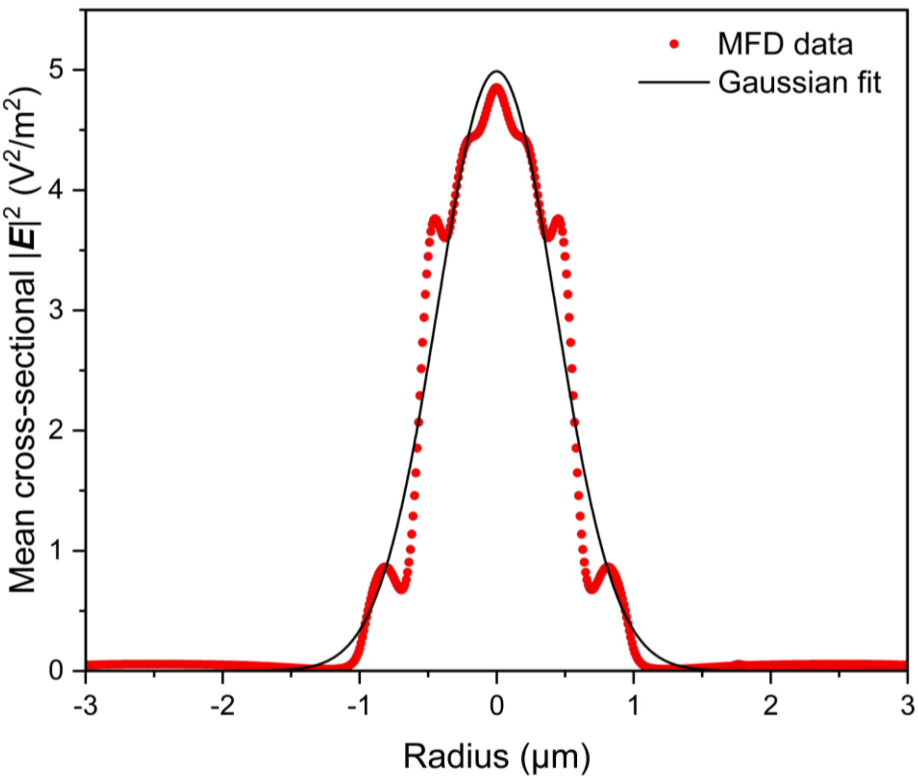

Fig. 5.9 – Example of the average cross-sectional electric field intensity of a 2.00 μm low Q micropillar, calculated at the top surface of the pillar at the HE_{11} mode wavelength.

Regardless, as other methods such as directly finding the cross-sectional diameter where the intensity drops $1/e^2$ are difficult to define when multiple peaks above this height are visible, Gaussian fits have been attempted for each diameter to estimate the overall change in total mode width, producing the plot in Fig. 5.10.

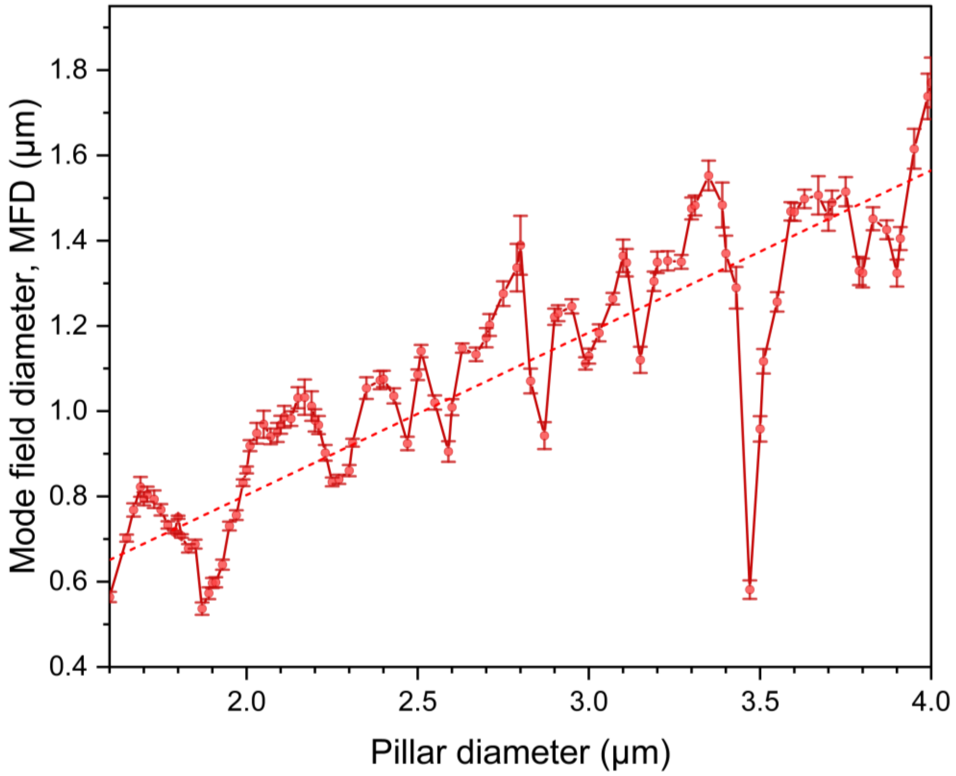

Fig. 5.10 – Estimated $1/e^2$ MFD at the top of each micropillar as a function of pillar diameter, calculated at the HE_{11} mode wavelength in each case. Error bars are plotted based on the error in the curve fitting applied to the data.

Converse to the numerical aperture, the MFD shows a gradual increase as a function of diameter, as would be expected as the confinement in the x and y directions is reduced. Within the range studied, this appears to be directly proportional to the pillar diameter. The data is fitted with a line of best fit, shown as a dashed line, returning a gradient of 0.400 ± 0.004. The MFD also shows signs of modulation, likely due to the changing near-field profile at the top of the micropillar. There is a significant dip at 3.47 µm, far exceeding other features. This is unlikely to be related to the non-cavity modes of the structure, as previous figures show that this diameter does not correlate with a non-cavity mode peak.

5.3 Characterisation of samples produced using direct-write lithography

For the experimental work in thesis, low Q and high Q samples were fabricated. This section introduces the lithography and processing methodology used to accomplish this and characterises the etch quality of the devices produced.

5.3.1 Fabrication method

We developed a novel direct-write photolithography and processing method, enabling the manufacture of high-aspect ratio micropillars in GaAs and $Al_{0.95}Ga_{0.05}As$ (Androvitsaneas et al. 2023). The full process of this is sketched in Fig. 5.12 in steps (i) to (viii).

First, the two GaAs/$Al_{0.95}Ga_{0.05}As$ samples, low Q and high Q, are grown on a 3-inch wafer (i) using molecular beam epitaxy (MBE). InAs dots are distributed with a uniform density, with only ~0.5% variation in InGaAs growth rate over the chip (ii). Measurements of calibration structures finds a density in the range of 50 to 90 QDs per square micron, however in-practise the number capable of confining charges may be lower. This is due to overgrowth and capping with GaAs potentially leading to some Indium-Gallium interdiffusion. Only a fraction of these QDs will also be in range of the HE_{11} cavity mode.

The chips are coated with a hard mask layer of 750 nm SiO_2, deposited via plasma-enhanced chemical vapour deposition (PECVD), which allows the thermal energy required for the vapour deposition to be reduced compared to other chemical vapour deposition techniques like low pressure chemical vapour deposition (LPCVD) (Snyders et al. 2023). A 2 µm layer of AZ2020 negative photoresist (Shaw et al. 1997) is then applied (iii).

The photoresist is then exposed to UV light using the MicroWriter ML3 Pro direct-write photo-lithography tool, projecting the design pattern onto the sample, consisting of 5 x 5 arrays of pillars with diameters ranging from 1.55 to 5.00 µm. This uses a 385nm

UV light source, a digital light modulator acting as a mask and computer-controlled optics, which together project the design pattern onto the photoresist (Fig. 5.11). This method is inexpensive, and as flexible as electron beam lithography, capable of a 400 nm minimum resolution that is sufficient for creating devices like those studied here, and has been shown in benchmark tests to be fast enough to pattern 14,000 devices in just 240 seconds (Durham Magneto Optics 2019), approximately two orders of magnitude faster than could be achieved with an electron beam lithography machine from the same era, though both projection lithography and e-beam tools have seen speed improvements since this work (Androvitsaneas et al. 2023).

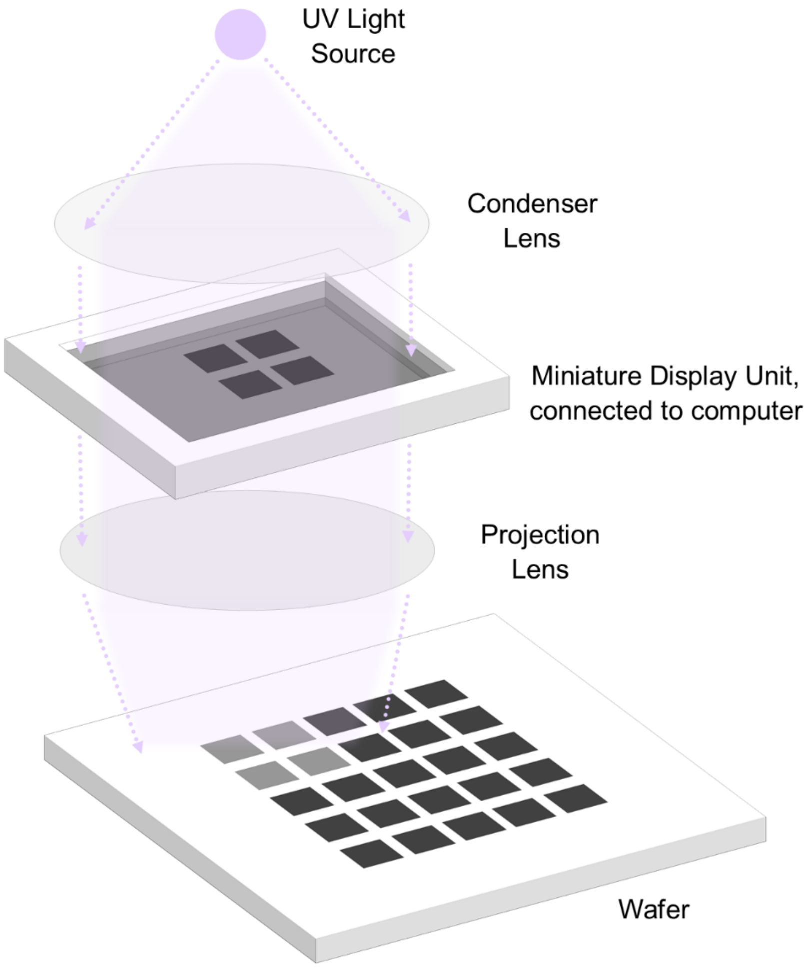

Fig. 5.11 – Diagram showing the operation of the MicroWriter direct-write photolithography tool.

After the photoresist is developed using AZ726, dissolving the unexposed pattern regions (iv), the SiO_2 hard mask is etched using a C_4F_8/O_2 ICP (v). Once this etch is complete, the photoresist is removed (vi).

The semiconductor is etched into the final micropillar shape using a $Cl_2/BCl_3/N_2$ ICP (vii), before finally the remaining hard mask on top of the devices is removed with another C_4F_8/O_2 etch (viii).

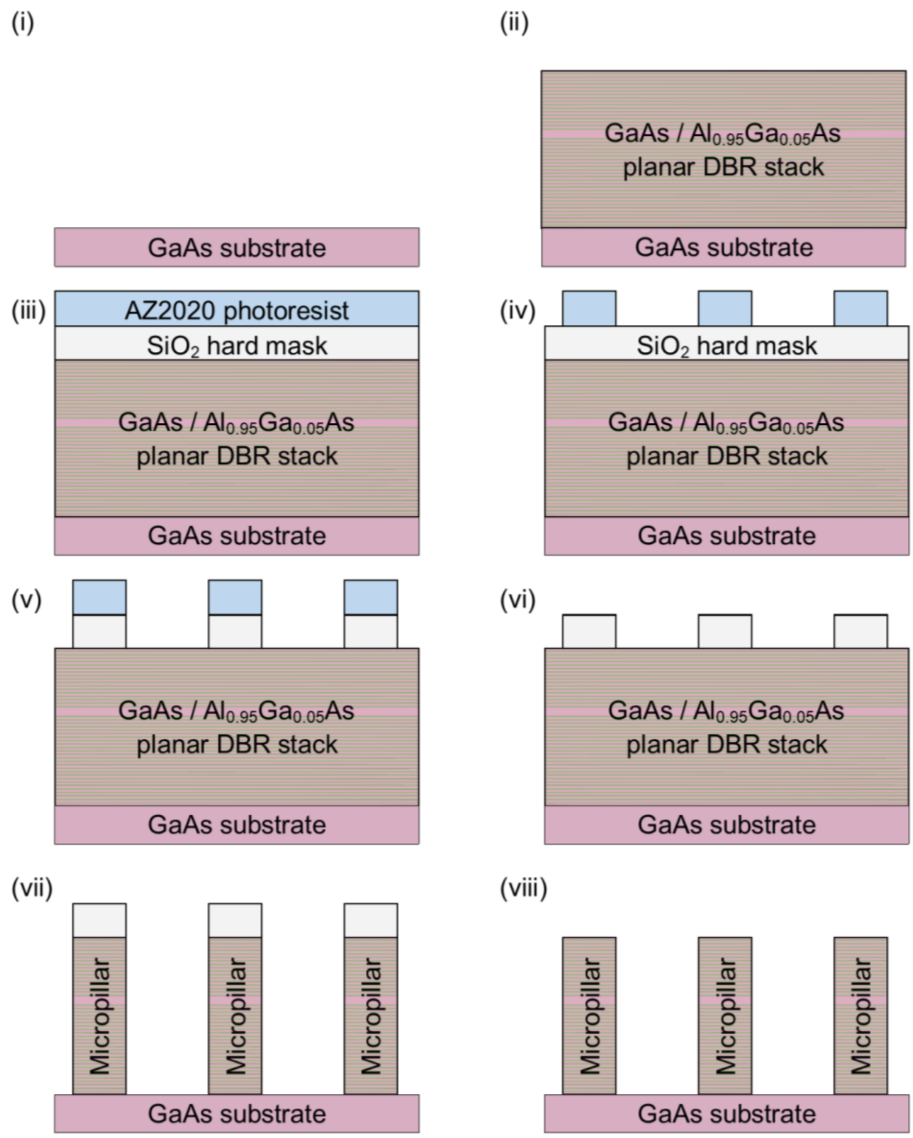

Fig. 5.12 – Step-by-step schematic of the fabrication and processing method.

By covering the pillars in a uniform 10 nm atomic layer deposition (ALD) coating of Ta_2O_5, the sample is protected against oxidation, meaning it is not necessary to store the samples in a vacuum.

Of the micropillars of diameter 2 µm and below, >99% are optically active, with only 1-2 out of 200 devices being critically damaged and showing no emission.

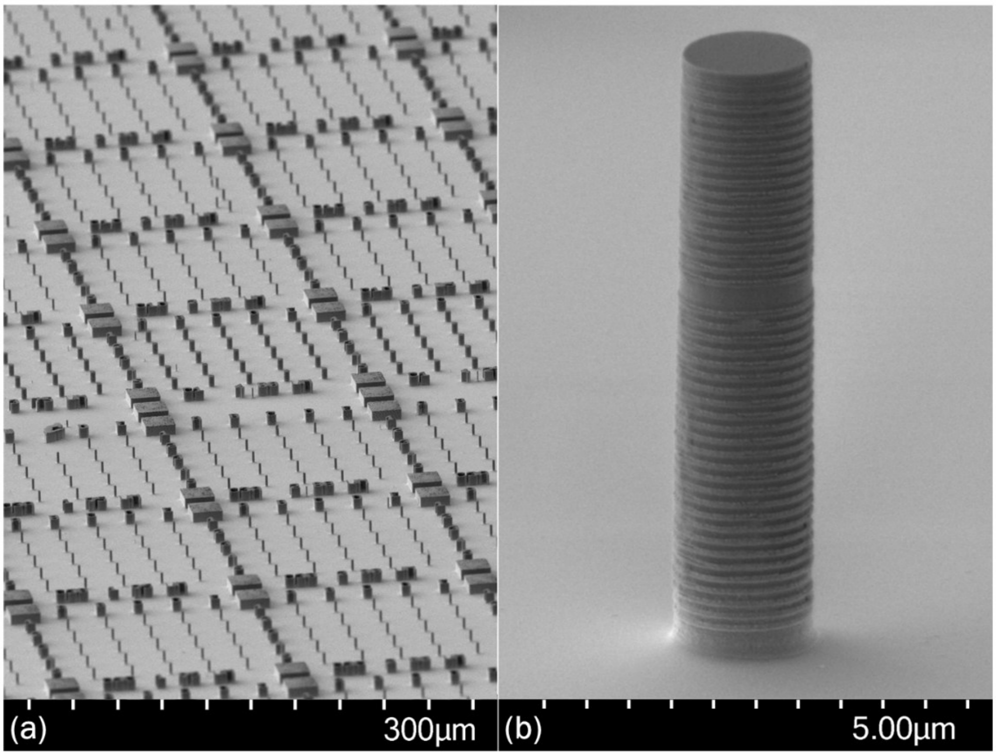

Fig. 5.13 – Scanning electron microscope images (SEMs) of the etched structures (a) over a wide area, showing a variety of difference diameters in 5 x 5 grids, and (b) close up on a high Q micropillar of 1.75 µm diameter.

In the high Q sample, 0.5% of pillars show sharp quantum dot emission lines within the narrow HE_{11} cavity mode's FWHM. By comparison, all cavities in the low Q sample have such lines within the mode width, as a combined result of a high areal density of dots and the broader cavity mode.

5.3.2 Quality factor characterisation

For a selection of high Q pillars of sizes ranging from 1.55 µm to 4.75 µm, white light reflectivity spectra of the fundamental HE_{11} mode were recorded at 4 K and 80 K. Photoluminescent spectra were also recorded at 80 K. PL measurements at 4 K were attempted, but these were dominated by bright on- and near-resonance transition lines from the quantum dots within the cavity, making an accurate extraction of the HE_{11} mode quality factor infeasible.

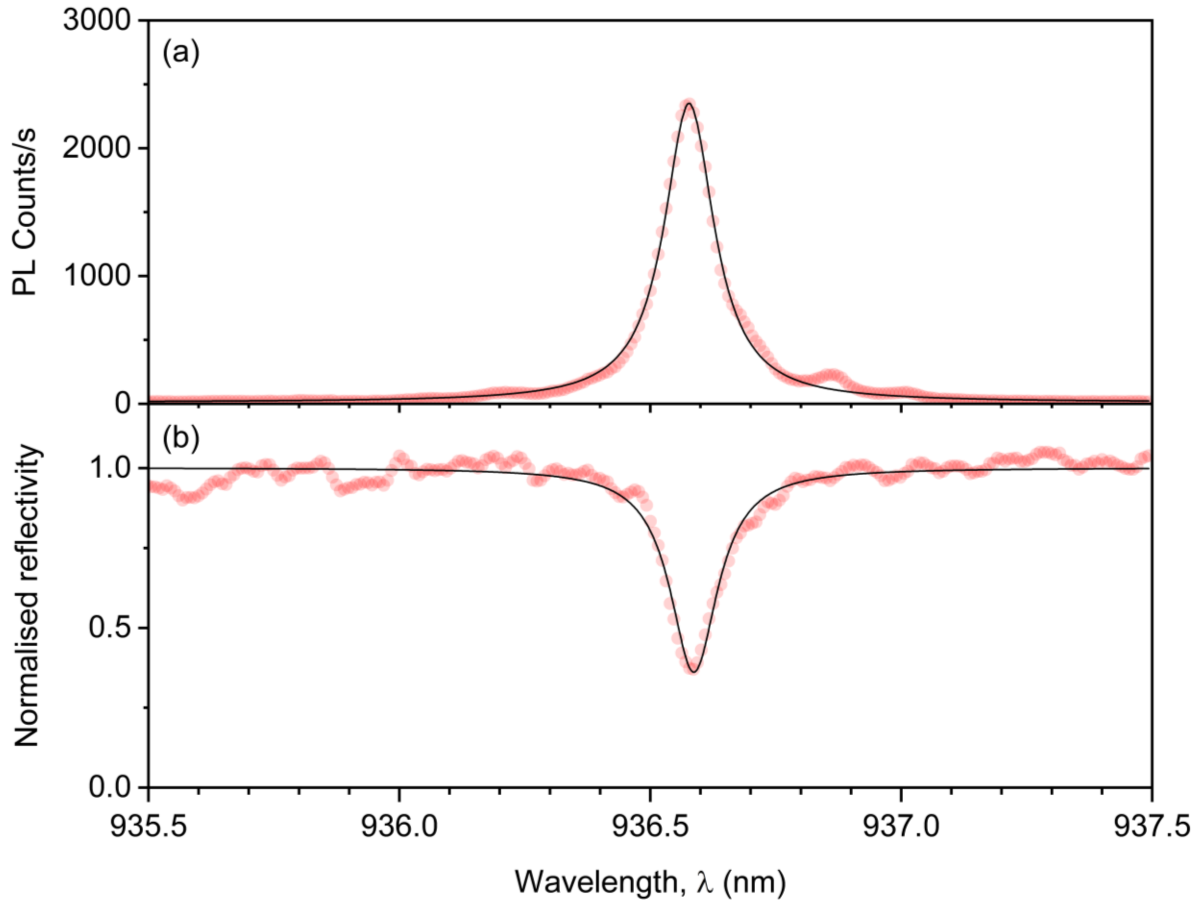

Fig. 5.14 – (a) PL and (b) WL spectra of a 3.14 µm high Q pillar at 80 K. Fitting with Lorentzian curves finds a mode wavelength of 936.58 nm and quality factors of 7740 ± 60 and 8100 ± 300 respectively.

In each spectrum, the mode was fitted with a Lorentzian to obtain its HE_{11} mode wavelength and quality factor, Q, as demonstrated in Fig. 5.14 (a) and (b).

As the actual diameters of the pillars are likely to vary from those labelled on the sample, the corrected values were determined from the fitted mode wavelength for each micropillar and its expected difference from the measured cavity mode wavelength of a near-planar square region of 200 μm width used for calibration, as calculated using (2.6). A plot of the fitted mode wavelengths vs labelled pillar diameter, which as can be seen does not perfectly fit to theoretical expectations due to the slightly incorrect diameters, is shown in Fig. 5.15.

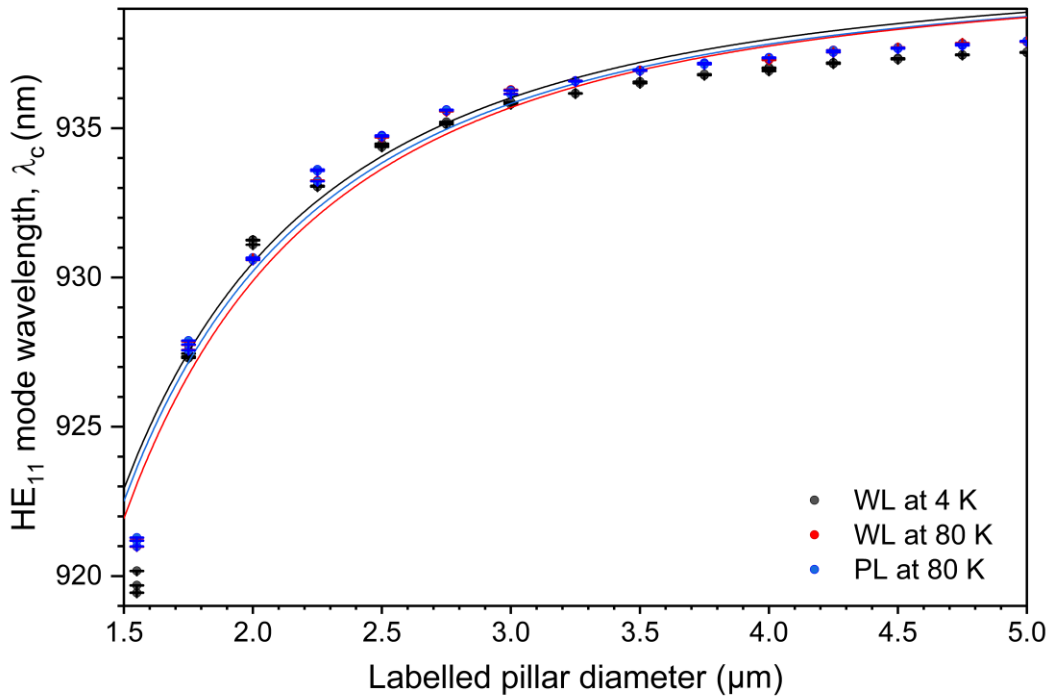

Fig. 5.15 – Fitted wavelengths for each pillar vs labelled micropillar diameter.

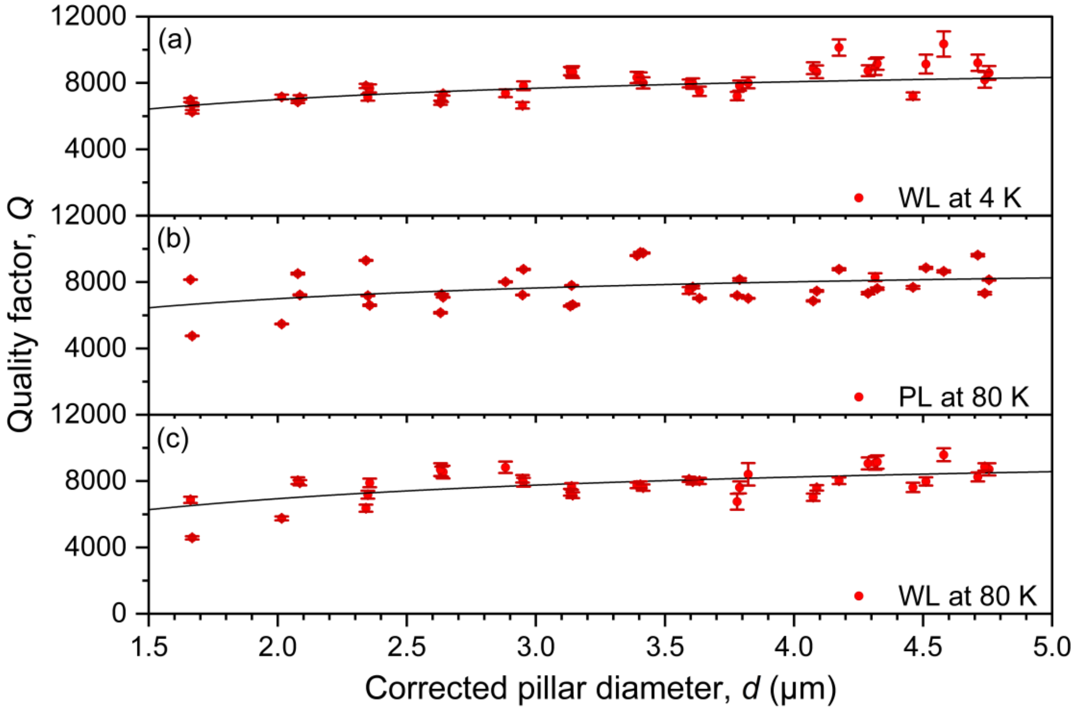

Fig. 5.16 – Quality factor vs diameter, d, for high Q pillars from (c) WL at 4 K, (d) PL at 80 K, and (e) WL at 80 K.

The extracted quality factors of each pillar were then plotted and fitted as a function of this diameter, d, corrected based on the measured wavelength, using (2.15) to obtain values of the sidewall roughness constant κ_s. Specifically, Fig. 5.16 (a-c) shows these results for WL at 4 K, PL at 80 K, and WL at 80 K respectively.

Using this method, it was found that all three datasets yield similar values for the sidewall roughness, finding κ_s to be (48 ± 9) pm, (50 ± 20) pm, and (60 ± 20) pm for the data plotted in subfigures c, d, and e respectively, each value agreeing well with one another when accounting for errors. These can be combined to find an average value of (53 ± 10) pm.

The etch smoothness is thus comparable to state-of-the-art values reported previously by other authors. A table of these results are shown below.

Table 5.1 – Etch quality results reported for papers detailing microstructure fabrication, including the patterning method and the etch chemistry used. The result by our research group is included in bold for comparison.

Paper	Patterning method	Etch chemistry	Min. reported κ_s (pm)
Reitzenstein et al. (2007)	E-beam	Ar/Cl_2 ECR[1] ICP	21 ± 5
Schneider et al. (2016)	E-beam	Ar/Cl_2 ECR ICP	68
Huber et al. (2020)	E-beam	Cl_2/Ar ICP	382
Han et al. (2022)	Direct-write	SF_6/C_4F_8 Bosch ICP	600
Androvitsaneas et al. (2023)	**Direct-write**	**Cl_2/BCl_3/N_2 ICP**	**53 ± 10**
Limame et al. (2024)	E-beam	Unstated ICP-RIE[2]	249 ± 35

As can be seen, the value of κ_s varies significantly, even with the same patterning method and etch chemistry. Regardless, the value obtained in the work presented in this chapter is competitive with some of the lower reported roughness values, such as that by Reitzenstein et al. (2007). Our method of fabrication also shows an order of magnitude improvement over previous results using maskless projection lithography.

Looking back at the data plotted in Fig. 5.16, the data points show a moderate amount of scatter. This is a combination of two sources of noise. Firstly, there is some experimental noise, as demonstrated by some of the differences between the data sets. This may be attributed to a number of causes, including wavelength tuning and strain effects in QDs from the change of temperature from 4 K to 80 K, as well as other features in the white light reflectivity and photoluminescence spectra, such as reflection fringes in the prior and quantum dot transitions in the latter, which may have affected fits.

[1] Electron Cyclotron Resonance (ECR)
[2] Reactive Ion Etching (RIE)

However, even comparing datapoints with similar Qs in each dataset there are some differences in Q attributed to individual pillars, likely due to some variation in growth and etch quality between the structures and not explainable by diameter differences, which have already been corrected for. Despite this, SEM images and the fitting above indicate that all the pillars studied show exceptional etch smoothness compared to most other fabrication methods, an excellent result given the ease of reconfiguration, low cost, and speed offered by maskless direct-write lithography.

5.4 Design study: micropillars with SiO_2 hard mask microlenses

In a supplementary piece of work (Jordan et al. 2024b), an amount of SiO_2 hard mask was deliberately left on the top of the micropillars of one sample after etching the semiconductor, with the aim of using this layer as a microlens to modify the numerical aperture for better coupling into a single mode collection fibre.

To assess the effectiveness of such an addition, further finite-difference time-domain simulations were performed of GaAs-$Al_{0.95}Ga_{0.05}As$ micropillars capped with SiO_2 microlenses of differing shapes and heights, with the aim of optimising the design and thickness of this microlens to achieve better coupling to a far field collection optic and to understand its influence on the dot's emission.

5.4.1 Dependence on lens height for truncated cone and cylindrical lenses

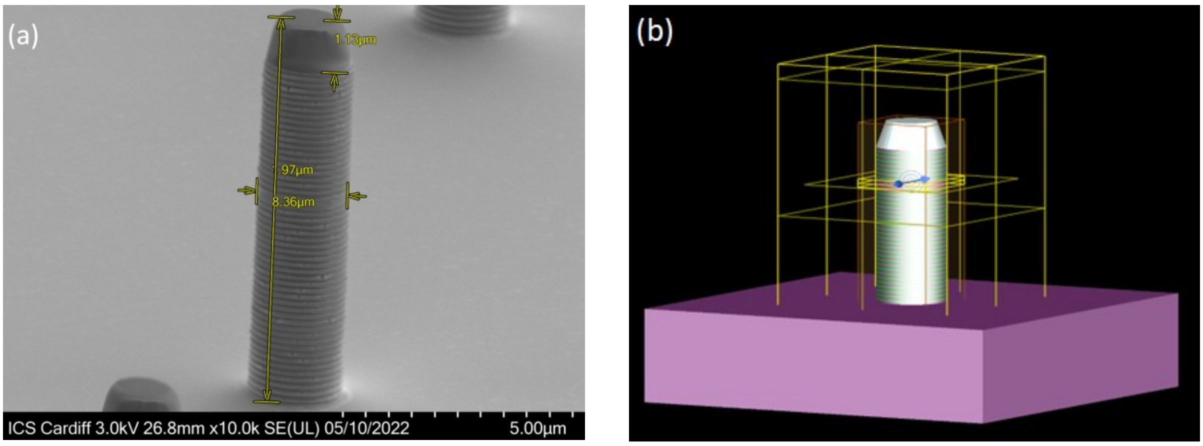

Fig. 5.17 – SEM image of a 2 μm micropillar with 20 upper and 30 lower DBR pairs with a layer of SiO_2 hard mask of about 850 nm thickness deliberately left on top (b) A model of a micropillar, this time with 7 upper and 26 lower DBR pairs, with a similar hard mask lens in Lumerical FDTD.

The FDTD simulations were performed in Lumerical FDTD, using a 1.8 μm GaAs-$Al_{0.95}Ga_{0.05}As$ low Q micropillar, capped by a SiO_2 lens modelled to have similar shape and dimensions to those observed in SEM during the development of an alternative pillar design with 20 (30) upper (lower) DBR pairs, as in Fig. 5.17. The shape of the SiO_2 layer observed is a result of recession during the plasma etch process of fabrication. While this specific example is used as a test case, the shape can change depending on the etch conditions. For example, in an ICP etcher it is possible to control the gas mix, pressure, RF (radio frequency) power, and bias. This allows one to tune the relative strengths of isotropic and anisotropic etching. The allows the profile of the etched structure to be modified, something which was observed during the optimisation of the process laid out in the previous section.

The cavities are excited as previously by a horizontal electric dipole driven with a 5.6 fs pulse covering a wavelength range of 845nm to 1060nm. This allows the exploration of how the HE_{11} mode wavelength, the quality factor Q, the Purcell factor F_{P}, the β-factor (2.20), cavity emission directionality η (2.21), outcoupling efficiency ξ (2.22), the numerical aperture and the mode field diameter vary as functions of the lens height. These relationships are studied for two designs: a truncated cone fitted to the top of the pillar with a top diameter of 0.656 µm, based directly on that seen in the physical sample, and simple cylindrical SiO_2 layer with the same diameter as the pillar.

Finally, the far field $1/e^2$ NA is calculated from the power transmitted through the top monitor projected into the far field. Meanwhile, the mode field diameter is, slightly differently to the results in the previous section, determined from the electric field cross-section 2 µm above the top DBR surface, so as to allow a consistent definition as the shape of the pillar top is modified, finding the change in mode field diameter at a fixed height above the semiconductor.

The below figure shows how these parameters vary with the height of the two lens designs. Red plots show the results for a cylindrical layer of SiO_2 with a constant diameter of 1.8 µm, matching the pillar. Blue plots show the results for a lens based on a truncated cone shape, as previously described, with a fixed top diameter of 0.656 µm.

Both sets of simulations follow similar trends. As might be expected, most of the parameters follow repeating patterns with a period of about 0.33 µm, approximately half the design wavelength in a SiO_2 medium, due to Fabry-Perot resonances set up by the reflections of the GaAs-SiO_2 and SiO_2-air interfaces.

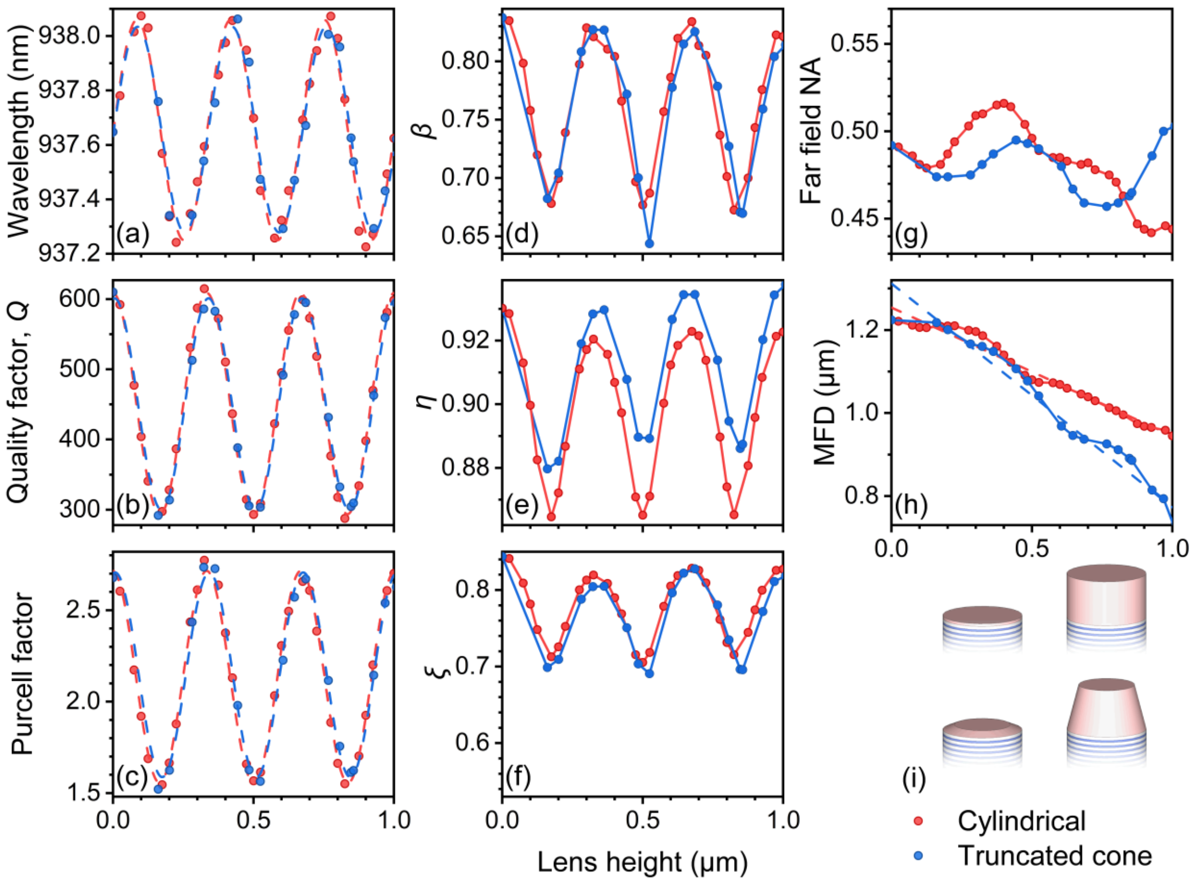

Fig. 5.18 – Simulation results as function of the height of a SiO_2 hard mask lens of either a cylindrical shape (red) or a truncated cone shape with a top diameter of 0.656 µm (blue). (a) HE_{11} mode wavelength, (b) quality factor, (c) Purcell factor (d) spontaneous emission coupling factor β, (e) cavity emission directionality η, (f) outcoupling efficiency ξ, (g) $1/e^2$ NA, and (h) HE_{11} mode field diameter. (i) shows a sketch of the two lens shapes at both a small and large height. The wavelength, quality factor, and Purcell factor have been fitted with a sinusoid. The MFD has been fitted linearly. Fits are shown as dashed lines.

We observe a sinusoidal oscillation in the fundamental mode's wavelength, varying with similar amplitudes of (0.378 ± 0.017) nm and (0.405 ± 0.015) nm about an average wavelength of 937.65 nm in panel (a) of Fig. 5.18. The quality factor Q (b) and Purcell factor (c) also follow a sinusoidal trend, albeit a quarter-wavelength out of phase with the wavelength's oscillation. In both datasets, Q oscillates between ~600 and ~300, such that odd quarter multiples of the design wavelength consistently halve the quality factor of the cavity. This is understandable considering the difference of the GaAs-air normal incidence reflectivity of about 32%, which is reduced by a quarter-wavelength SiO_2 coating to close to zero, noting that quantitative differences will arise as the cavity mode encompasses a broad range of incidence angles. As the thickness of the SiO_2 is varied, the phase difference between the reflection at the surface and the DBR mirror changes, altering the overall reflectivity and Q of the cavity. The Purcell factor similarly oscillates between about 1.6 and 2.7, as might be expected given that $F_\mathrm{P} \propto Q/V_\mathrm{m}$ (Purcell 1946), where V_m is the mode volume. The reduction in modulation factor suggests a 10% increase in the mode volume, with negligible difference between the two designs in this regard. However, a change of the emission into non-cavity modes can also contribute to this (Jordan et al. 2024a).

The β-factor (d), η (e), and ξ (f) also show similar periodic behaviour for both lens designs, though these show small deviations from a sinusoid. They have the same phase and period as Q and F_P, but may show small overall reductions in mode coupling efficiencies with the addition of a lens. Both designs follow quite similar trends, although η is slightly higher for the truncated cone lens than the cylindrical lens.

The numerical aperture (g), being 0.49 without lens, shows oscillations of some 5-10% peak to peak with lens height for both designs, and a superimposed reduction by some 10% for the cylindrical lens. By comparison, the mode field diameter (h) is significantly reduced by adding the microlens to the device, decreasing approximately linearly with lens height, which is attributed to the light guiding by the lens towards the monitor. It also shows superimposed weak oscillations decaying with height, similar to the oscillatory behaviour observed in the NA. Notably, the gradient of the linear decrease in the MFD is larger for the truncated cone shape (-0.539 ± 0.016) than for the cylindrical layer (-0.309 ± 0.010).

5.4.2 Dependence on lens top diameter

Taking one lens thickness, specifically 0.856 μm – the value from SEM measurements, I performed further simulations modifying the overall shape of the lens. This produces results as functions of the diameter of the top of the lens, ranging from a perfect cone up to a cylindrical design as studied above, extreme cases of the previously mentioned variation due to different etch conditions.

Similar patterns are observed for the wavelength, quality factor, Purcell Factor, and efficiencies (a-f), all dipping to minima around lens top diameters of 0.4 - 0.6 μm and peaking around 0.0 - 0.1 μm and 0.8 – 1.0 μm. The quality factor, F_{P}, and β are all maximised at this first peak, for a conical lens. Meanwhile, η appears to be near constant with diameter. Finally, it is notable that the cavity mode outcoupling efficiency ξ is not only maximised as the lens approaches a cylindrical shape, but significantly exceeds β, indicating that the emissions coupled to the cavity mode are effectively suppressed in the downward direction (which is included in β but excluded from ξ).

As with changing the lens thickness, the numerical aperture (g) and mode field diameter (h) are also modified as a function of the lens top diameter. The NA follows a near-linear negative trend with width, with a gradient of -0.076 ± 0.007 μm^{-1}, comparable to the overall trend seen for a micron-thick cylindrical lens. Meanwhile, the effect on the mode field diameter is not as significant as for changing the lens height, dipping by only ~0.12 μm for a truncated design. The MFD is approximately the same for both cone and cylindrical lenses.

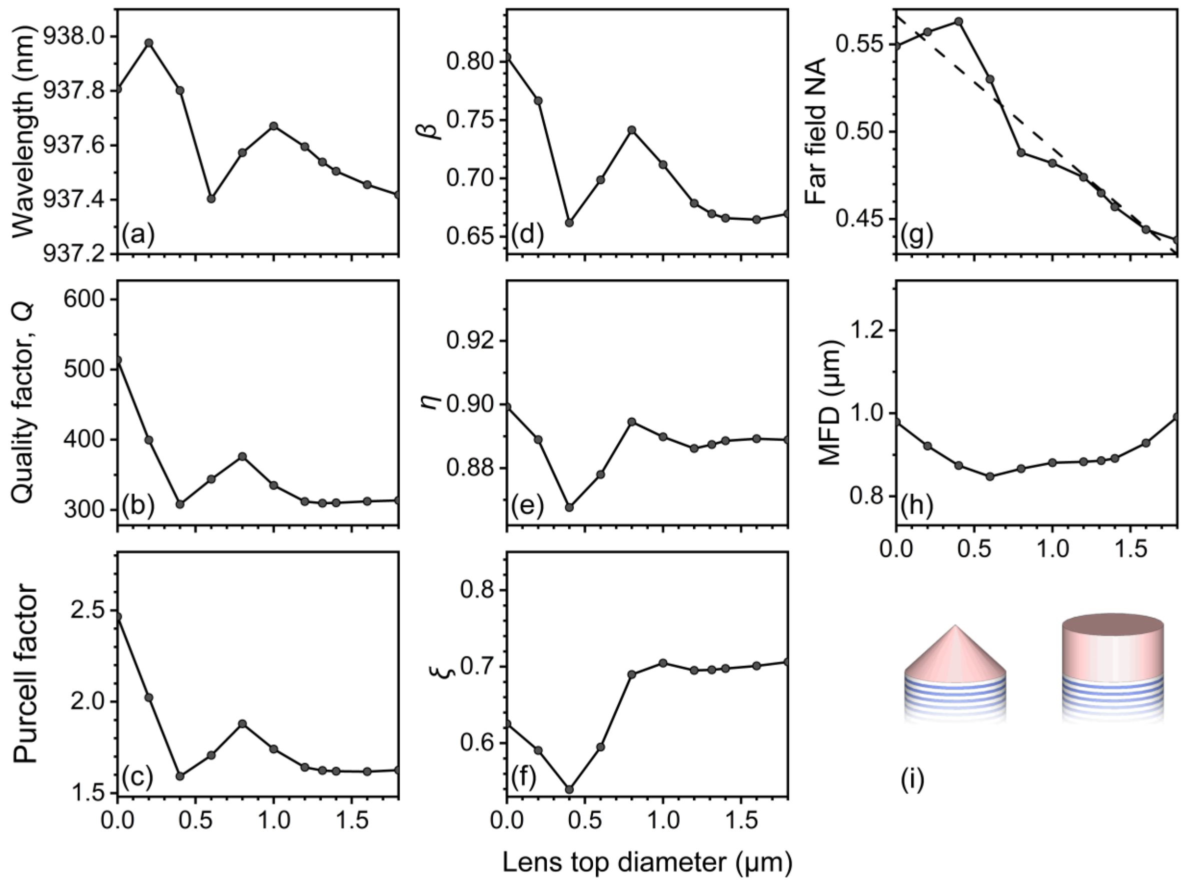

Fig. 5.19 – Simulation results as function of the height of a cylindrical SiO_2 hard mask lens. (a) HE_{11} mode wavelength, (b) quality factor, (c) Purcell factor (d) spontaneous emission coupling factor β, (e) cavity emission directionality η, (f) outcoupling efficiency ξ, (g) $1/e^2$ NA, and (h) HE_{11} mode field diameter. (i) shows a sketch of the lens shape at both a small and large top diameter. The NA has been fitted linearly (dashed).

These results, combined with those in the previous subsection, indicate that the exact behaviour of properties for different microlens shapes is quite complex and difficult to predict, given these are influenced by superposition of many modes, which will be affected by the structure differently. A larger study varying both the lens profile and thickness in different combinations would be required to find an optimal microlens design, and even then, this would likely only be reliable for a single design of micropillar.

5.5 Conclusions

This chapter introduced the two designs of micropillars used primarily in this work, a low Q and high Q design, of maximum theoretical quality factors around 600 and 20,000.

Using finite-difference time-domain simulations, which show the expected behaviour of the HE_{11} mode wavelength as a function of diameter, it was also found that the diameter of the pillar used can have a significant effect on the other properties of the device. This includes not just the resulting Purcell enhancement, but also the efficiency of cavity-mode outcoupling and the shape of the emitted light, described close to the pillar using the mode field diameter and far from it using the far field numerical aperture. Each of these parameters is modified not just by overall trends with diameter (e.g. NA decreasing as the pillar becomes closer to a planar cavity), but at specific diameters where coupling to modes other than the HE_{11} fundamental mode become more dominant. Simulating low Q pillars provides a good way to explore this, given the reduced relative strength of the primary cavity mode in the overall emission spectrum. Later work in this thesis will further explore the influence of these non-cavity modes, quantifying them further, determining their spectral width, and assessing their influence on experimental determinations of properties like the Purcell factor.

Using a direct-write projection photolithography-based process, samples were produced containing micropillars of a range of diameters. This technique is fast and cheap, and the addition of an oxide ALD removes the requirement for storage in a vacuum. Characterising these devices using photoluminescence and reflectivity spectroscopy and fitting the resulting Q factors found that the pillars showed an exceptional etch quality, with a sidewall roughness constant of around 50 pm, exceeding the state of the art. This confirms that this method is effective at producing the high aspect ratio micropillars necessary for this thesis's work.

Finally, the included design study demonstrates how the addition of a SiO_2 microlens layer could be used to tune the outgoing emission's numerical aperture and mode field diameter to better mode-match with an output single-mode fibre, with the thickness and cross-sectional profiles of the lens being key variables in accomplishing this. However, careful control of the design is required to minimise any resulting side-effects on the Purcell factor and collection efficiencies, which show their own periodic dependencies on the lens thickness, as well as modification with lens width. Future work could further examine how the top diameter of the lens affects the properties of the emitted light for different lens heights with the goal of determining optimal lens shapes for modifying the outcoupling with minimal reductions to the Purcell enhancement and other parameters. Further simulations could also examine the emission properties achievable with a high Q micropillar, to allow a direct comparison with experimental results and to test the impact of a modified pillar design on lens performance.

Chapter 6
Characterisation of quantum dots

This chapter investigates the dependence of quantum dot emission properties including resonant fluorescent scans, lifetimes, and second-order correlation $g^{(2)}(\tau)$ on power and excitation conditions, including the use of a non-resonant laser and resonant laser powers up to saturation.

Following this, the chapter returns to the low Q sample fabricated in the previous chapter using the direct-write lithography-based process (Androvitsaneas et al. 2023) and performs a series of further measurements using experiments previously laid out in this thesis to confirm and quantify the single photon source properties of the devices, culminating in finding the indistinguishability of the produced single photons using a Hong-Ou-Mandel experimental setup.

6.1 Effect of excitation power on spectral properties

In this section, an on-resonance emitter at 924.62 nm in a 1.75 μm diameter low Q micropillar, preselected from a set of ~200 pillars, was excited using different laser powers and measurements were taken. A low Q pillar design was chosen as the broader cavity mode simplified finding a QD transition sufficiently resonant with the cavity, i.e. within the HE_{11} mode's FWHM. For example, a high-aspect ratio high Q micropillar might have a quality factor of ~5000, including losses due to sidewall scattering. At the design wavelength of 940 nm, this corresponds to a mode of 0.2 nm FWHM. By contrast, a low Q micropillar with a quality factor of 400 would have a FWHM of 2.4 nm, over ten times wider and, thus, over ten times more likely to contain a transition on resonance. It has been shown in the past that low Q cavities such as these can be efficient and broadband (Androvitsaneas et al. 2016; Ginés et al. 2022).

Fig. 6.1 shows the measured photoluminescence (a) and white light reflectivity spectra for the chosen pillar, as integrated over 10 seconds, recorded using a 1200 l/mm spectrometer grating. The photoluminescence was performed using a cross-polarised setup (Kuhlmann et al. 2013a) with a Coherent Mira-900 Titanium-Sapphire laser at the resonance wavelength of 924.6 nm at 10 μW of power. The latter has been fitted with a Lorentzian curve on a linear background, finding a quality factor of 400 ± 30. While there are prominent fringes visible in the spectrum, the result of beating between the two modes of the polarising maintaining fibre used, the broad spectral width of the mode allows it to be distinguished from these patterns.

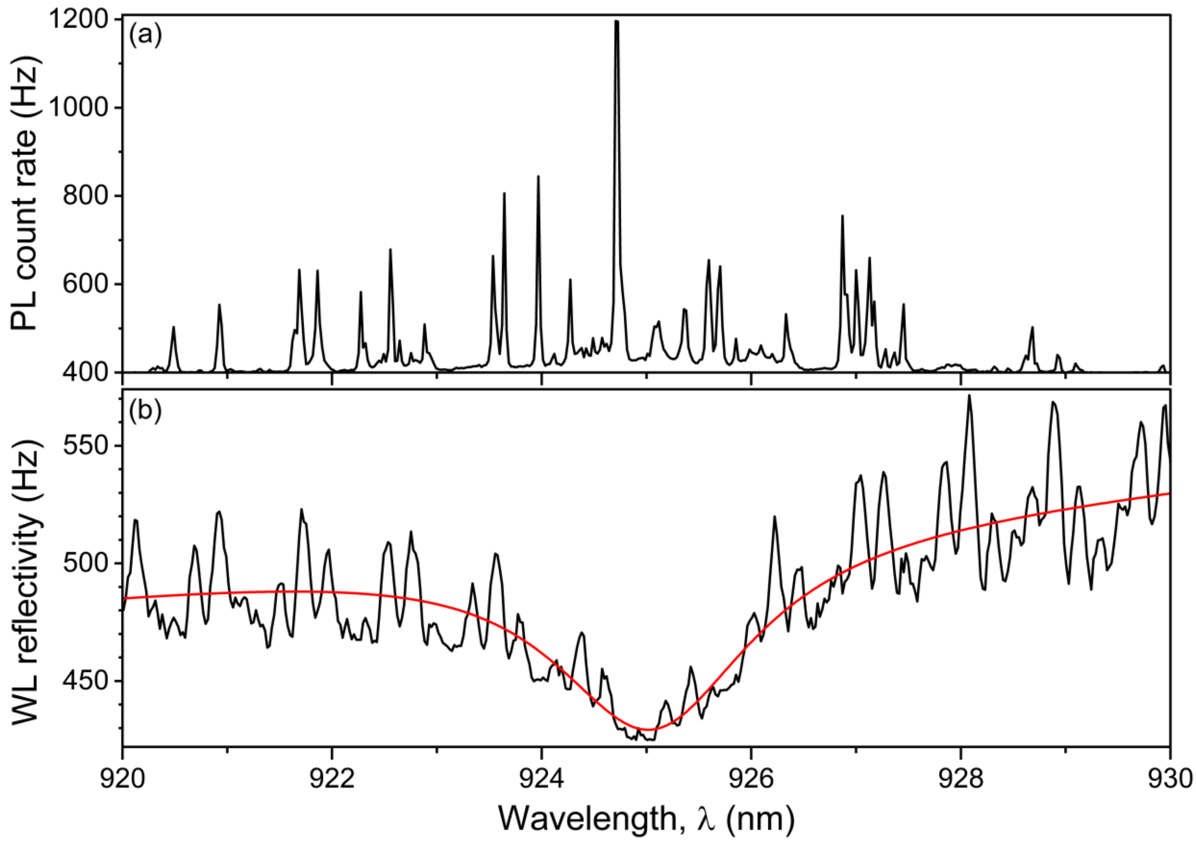

Fig. 6.1 – Photoluminescence (a) and raw white light reflectivity (b) spectra recorded over a 10 second integration time from the low Q micropillar device studied. The cavity mode dip in the white light reflectivity has been fitted with a Lorentzian with a linear background function (red).

The studied transition is visible as the brightest peak in (a): around 924.6 nm with a count rate of ~1200 Hz with background, or ~800 Hz without, largely isolated from other transition peaks, besides some possible dim features neighbouring on its blue side. As can be seen comparing the two subplots, this transition is approximately resonant with the pillar's HE_{11} cavity mode and thus will be maximally Purcell enhanced. While the transition is later seen to consist of two peaks in high resolution scans, due to fine structure splitting, they are unresolved in this spectrum. A subtle, broad peak may also be seen in the background of (a), albeit dominated in brightness by the overlapping narrow transitions – given its alignment with the mode's dip in reflectivity, this is likely phonon-assisted cavity feeding into the mode.

6.1.1 Resonance fluorescence scans at different powers, use of 850 nm laser

Fig. 6.2 (a) shows a high-resolution resonance fluorescence wavelength scan across the emitter performed using an M Squared CW laser at low powers ranging from 1.8 nW to 6.8 nW, collecting into the cross-polarised arm of our setup. A second set of data, performing the same measurements but supplementing the CW excitation with a 1 nW 850 nm CW PicoQuant laser was also recorded and plotted in Fig. 6.2 (b). In each case, scans were also performed once the transition had saturated, at 102 nW, which are shown in Fig. 6.2 (c) and (d). By supplementing with a non-resonant laser, additional charge carriers can be added to the system, reducing the significant low-frequency charge noise in the resulting emission spectrum. With these measurements, the power dependencies of both setups are probed.

While this and successive experiments were intended to be performed using diagonally polarised laser light, so as to as to excite the two transition polarisations equally, the results obtained at higher powers show this not to have been the case, with the imperfect diagonal polarisation only being caught at a later point. The data is presented regardless and the impacts of this change on the results found are discussed.

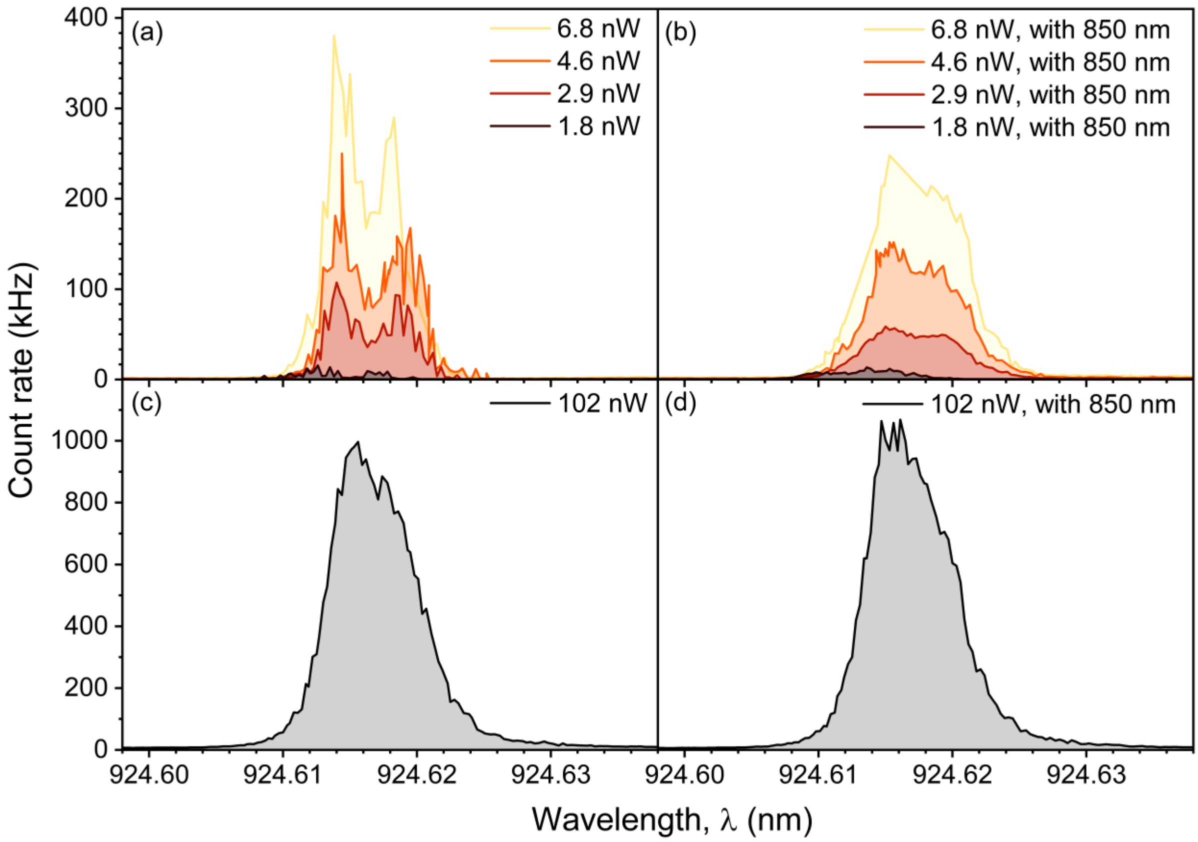

Fig. 6.2 – CW resonance fluorescence scans across transition at (a, b) several different low powers and (c, d) at a saturating power of 102 nW. (a) and (c) show results without use of a 1 nW 850 nm laser, (b) and (d) with it.

Using Gaussian curves to fit the data in Fig. 6.2 (a) and (b), where the two transitions can be resolved, obtains the parameters in Table 6.1. While a Lorentzian better fits the Fourier transformation of an exciton's exponential decay, a Gaussian is found to fit the data more closely in this case, possibly due to the large amount of intensity noise. In fitting, it is assumed in each case that the two peaks will share the same FWHM.

Table 6.1 – Parameters obtained from Gaussian fits of transitions from the high-resolution scans presented in Fig. 6.2.

Resonant laser power (nW)	Average transition wavelength (nm)	Spectral width, FWHM (pm)
Without non-resonant laser		
1.8	924.6147 ± 0.0002	2.9 ± 0.2
2.9	924.6165 ± 0.0001	3.0 ± 0.1
4.6	924.6167 ± 0.0001	3.2 ± 0.1
6.8	924.6162 ± 0.0001	2.7 ± 0.1
With non-resonant laser		
1.8	924.6127 ± 0.0001	4.4 ± 0.1
2.9	924.6172 ± 0.0001	4.8 ± 0.1
4.6	924.6175 ± 0.0001	4.5 ± 0.1
6.8	924.6174 ± 0.0001	4.9 ± 0.1

In both (a) and (b) there is a notable power-dependent redshift in emissions, observed entirely in the step from 1.8 to 2.9 nW. For (a), without a non-resonant laser, this is ~1.8 pm. For (b), it's ~4.7 pm, slightly larger. The fine structure splitting of the transition remains approximately constant, averaging (4.5 ± 0.1) pm, discounting an anomalous result for 6.8 nW in (a), seemingly due to noise. By comparison, the spectrum at 6.8 nW in (b) shows a difference between the peak wavelengths that is more consistent with the values at other powers. Finally, and most significantly, it is observed that inputting the 850 nm laser alongside the primary laser causes the spectrum to appear smoothed out, with broader peaks and reduced noise. Specifically, the peaks obtained without the non-resonant laser have an average spectral width of (2.9 ± 0.1) pm, while adding it broadens them to (4.7 ± 0.1) pm.

These effects mostly arise from local charge fluctuation in the semiconductor. As defect states close to the target quantum dot (<100 nm away) are occupied, they produce charge noise. By adding a non-resonant laser, as performed with the 850 nm laser here, this can be controlled, reducing the low frequency noise by fully occupying the defects (Houel et al. 2012). However, this also has the effect of increasing the linewidth, as high frequency noise is increased (Yılmaz et al. 2010; Kuhlmann et al. 2013b).

Occupied defects modify the local electric field which, if the defect is near the quantum dot, can induce a Stark shift in the quantum dot's resonant wavelength (Houel et al. 2012; Kuhlmann et al. 2013b), as observed here, or induce Coulomb interactions in the case of charged excitons (Engström et al. 2011). This suggests the difference in the Stark shift for the two datasets may be explained by the increased occupation of defects for the same resonant laser power, allowed by the addition of the non-resonant laser.

Similarly, fluctuations in the nuclear spins in the semiconductor will result in the (Overhauser) magnetic field also fluctuating on the order of 10 - 100 mT (Kuhlmann et al. 2013b), through the hyperfine interaction. Both this, and the charge noise, can result in fast quantum dot spin dephasing (Greilich et al. 2006; Xu et al. 2008). These fluctuations in the magnetic field may also change the linewidth of the transition, on account of linear Zeeman splitting, which has been previously discussed in this thesis, but are small enough to contribute a negligible overall shift in frequency, which increases quadratically with magnetic field strength (Walck and Reinecke 1998). Specifically, for a large Overhauser magnetic field of 100 mT and a typical InAs QD exitonic g-factor of ~3 (Nakaoka et al. 2004; Nakaoka et al. 2005), one would expect a linear energy level splitting of 17.4 μeV, or 12.0 pm. Even for this magnetic field, far exceeding anything observed in this experiment based on the splitting being larger than the spectral width of the peaks in the data presented in Fig. 6.2 and Table 6.1, one would only observe a quadratic shift of 0.08 μeV, or <0.1 pm, assuming a diamagnetic coefficient of 8 μeV/T^2. This would be in the middle of the range of values observed in our previous work utilising the Zeeman effect (Jordan et al. 2024a). Whereas the charge noise is the dominant source of low frequency noise, spin noise becomes dominant at higher frequencies (Kuhlmann et al. 2013b).

An additional possible cause of the apparent transition broadening in (b), is that non-resonant excitation in the wetting layer may cause multiple charging in QDs, producing a broad background peak, as the dots feed into the cavity mode.

At higher powers, as seen in Fig. 6.2 (c) and (d), the two peaks are now unresolved, forming a single smooth peak. The added 850 nm laser now has a negligible effect on the peak width. It also no longer masks the change in intensity with power, with the intensity now being ~1 MHz for both datasets. This would suggest that the high resonant laser power is now sufficient to occupy all the defect states, even without the non-resonant laser.

The increased linewidth can be partially explained using the previously discussed effects. However, even neglecting the presence of defects near the quantum dot, the transition will experience power broadening as the intensity increases. The QD population, and thus the fluorescence, is given by:

$$N_\infty = \frac{1}{2}\frac{\Omega^2 T_1/T_2}{\Delta\omega^2 + T_2^{-2} + \Omega^2 T_1/T_2} \tag{6.1}$$

Where Ω is the Rabi frequency, $\Delta\omega$ is the detuning of the laser from the transition frequency, T_1 is the radiative lifetime, and T_2 is the dephasing time (Flagg et al. 2009). This can thus be rearranged to find an expression for the full width at half maximum of the peak, taking the peak maximum to be at $\Delta\omega = 0$:

$$N_{\infty,peak} = \frac{1}{2}\frac{\Omega^2 T_1/T_2}{T_2^{-2} + \Omega^2 T_1/T_2} \tag{6.2}$$

$$N_{\infty,HWHM} = \frac{1}{2}N_{\infty,peak} \tag{6.3}$$

$$\Delta\omega_{HWHM} = \sqrt{T_2^{-2} + \Omega^2 T_1/T_2} \tag{6.4}$$

$$\Delta\omega_{FWHM} = 2\sqrt{T_2^{-2} + \Omega^2 T_1/T_2} = 2\sqrt{\frac{T_1}{T_2}}\sqrt{\frac{1}{T_1T_2} + \Omega^2} \tag{6.5}$$

Ω increases linearly with the square root laser power (Flagg et al. 2009) leading to an increased FWHM.

6.1.2 Photon count power dependence

Using the same dot and setup, a pulsed laser power-dependence was performed, using pulses of transform-limited duration (1.93 ± 0.03) ps separated by 13.2 ns, resonantly exciting the exciton to trigger Rabi cycling, with the emission rate oscillating when recorded by a superconducting nanowire single-photon detector (SNSPD).

In the ideal case, as the system is resonantly driven with a strong coherent laser pulse, it enters an oscillation in the two-level system between the ground state and an excitation state as a function of the time-integrated Rabi frequency Ω or 'pulse area':

$$\Theta(t) = \int_0^t \Omega(t')\,dt'\,E_p = \frac{|\vec{\boldsymbol{d}}|}{\hbar}\int_0^t E_p(t')\,dt' \tag{6.6}$$

Where E_p is the pulse envelope and $|\vec{\boldsymbol{d}}|$ is the dipole moment magnitude (Allen and Eberly 1987; Melet et al. 2008). After the system has entirely interacted with the pulse, the probability of being in the excited state $|e\rangle$ can be described with the equation:

$$P_e(t) = \frac{1}{2}(1 - \cos{(\Theta(t))} \tag{6.7}$$

Thus, when the pulse area is an odd multiple of π, $P_e(t) = 1$ and the population will be entirely within the excited state $|e\rangle$, or 'inverted'. Meanwhile, when the pulse area is an even multiple of π, $P_e(t) = 0$, and the population will be entirely within the initial ground state $|g\rangle$ (Vitanov et al. 2001). This relationship is known as the area theorem and holds while the pulse length is small compared to the lifetime (Fischer et al. 2017).

Ω is proportional to the electric field amplitude associated with the laser pulse, itself proportional to the square root of the pulsed laser power (Mandel and Wolf 1995; Flagg et al. 2009). After the short pulse, the system spontaneously decays before the next pulse. The emission intensity will be proportional to $P_1(t)$, and thus also follow a sinusoidal relationship as the square root power increases, with peak emission rates at odd multiples of π, and minima at even multiples (Kalt and Klingshirn 2024).

These results are shown in Fig. 6.3, plotting the intensity against the square root power as measured at a pick-off power monitor before the objective. A visible oscillatory trend confirms the presence of a two-level system, although only one and a half cycles are clear.

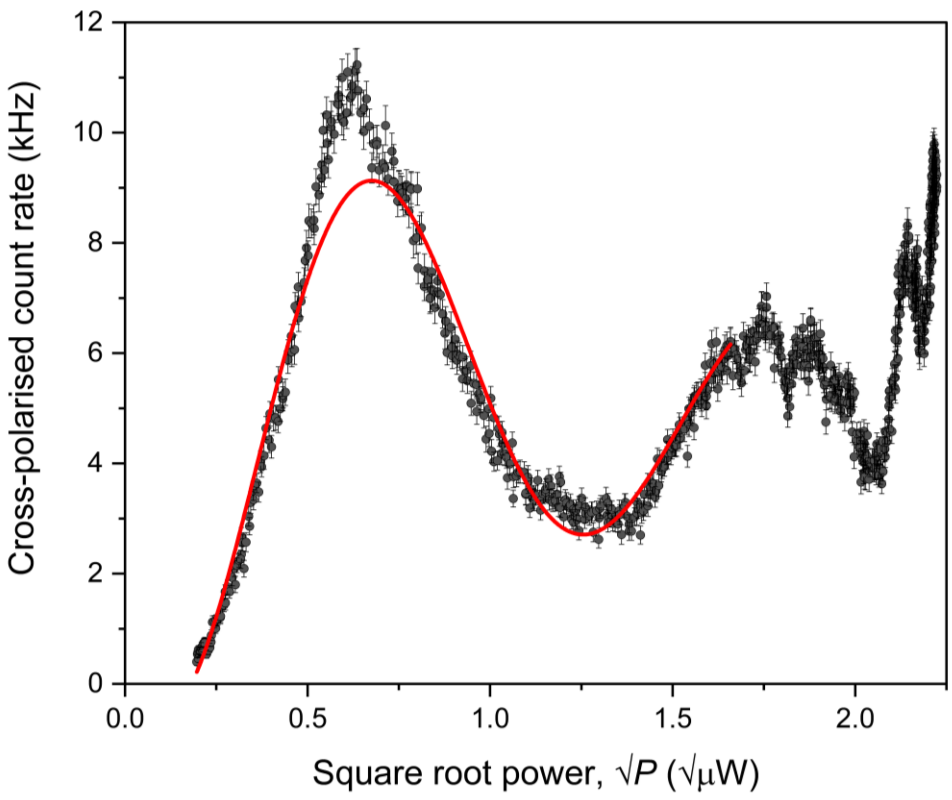

Fig. 6.3 – Square root power dependence for a neutral exciton, showing Rabi oscillations in the pulse amplitude. The data is fitted with a sinusoidal function with an exponential damping component (red).

At π-pulse excitation (i.e. the first maximum, corresponding to a pulse area of π), or a square root power of 0.636 $\sqrt{\mu W}$, thus a power of 0.797 μW, a maximum count-rate of ~11.2 kHz was recorded. The next maximum, at 3π-pulse, is significantly damped, with a maximum of only ~6.4 kHz.

The Rabi power oscillations can be fitted using a sinusoid with an exponential decay component accounting for the damping observed (Unsleber et al. 2015). The fit obtains an oscillatory period of (1.159 ± 0.006) $\sqrt{\mu W}$. Examining the literature finds this to be reasonable, albeit on the lower end of wide range of possible values on the scale of $\sqrt{\mu W}$ to $\sqrt{mW}$ (Besombes et al. 2004; Stufler et al. 2005; Melet et al. 2008; Monniello et al. 2013; Ramachandran et al. 2024). By considering the pulse area equation stated previously, one can conclude that the periodic behaviour of the system will depend on a number of parameters related to the Rabi frequency, including the transition's dipole moment and the laser pulse length / shape.

The fit is not perfect, as the change in amplitude appears more complex than the exponential decay used in the fit, sharply peaking higher than predicted. This is likely due to a combination of laser leaking through the polarisation filtering as the power increases and as the oscillations become damped.

The observed damping of Rabi oscillations can arise from various sources of decoherence. A common cause of this in sources is the presence of longitudinal acoustic (LA) phonons of the Rabi energy between the two energy levels (Ramsay et al. 2010b), which as they are emitted and absorbed leads to dephasing as a function of the Rabi frequency, and a shift in the splitting induced by phonon fluctuations (Ramsay et al. 2010a)., though this is not the case here, as only empty and full states are present, with an energy different of ~1 eV. Other possible sources of decoherence include wetting layer state interactions, common in samples produced using the Stranski-Krastanov growth method (Villas-Bôas et al. 2005; Wang et al. 2005), and multiexciton transitions (Patton et al. 2005). The high density of transition peaks in the previous scans may suggest that other transitions are responsible for the decoherence.

Instead, it is likely that the extremely fast dephasing observed here occurs due to the two energy levels not being driven equally. As may be seen in Fig. 6.2, the two transitions have different intensities, likely due to not being excited with a perfectly diagonally polarised light source. This results in two oscillatory trends which will move out of phase with each other. When they are in anti-phase to one another, they effectively destructively interfere, resulting in the rapid damping observed. This may also influence the results in the next section.

6.1.3 Power-dependent lifetimes

Recording the time-resolved emission intensity after a pulse, applied in a diagonal polarisation to the two polarisation states of the transition, allows the radiative decay of the exciton to be plotted on a logarithmic scale for multiple powers in Fig. 6.4, corresponding to pulse areas π (a), 2π (b), and 3π (c), as described in the previous section.

As can be seen in plots (b) and (c), reflection from the laser produces a bright narrow peak just before the transition’s decay curve, indicated with an arrow. This becomes brighter and thus more easily resolvable above π-pulse power, though is clearer in (b) than (c), due to the comparative reduced transition emission at the Rabi cycle minimum of 2π.

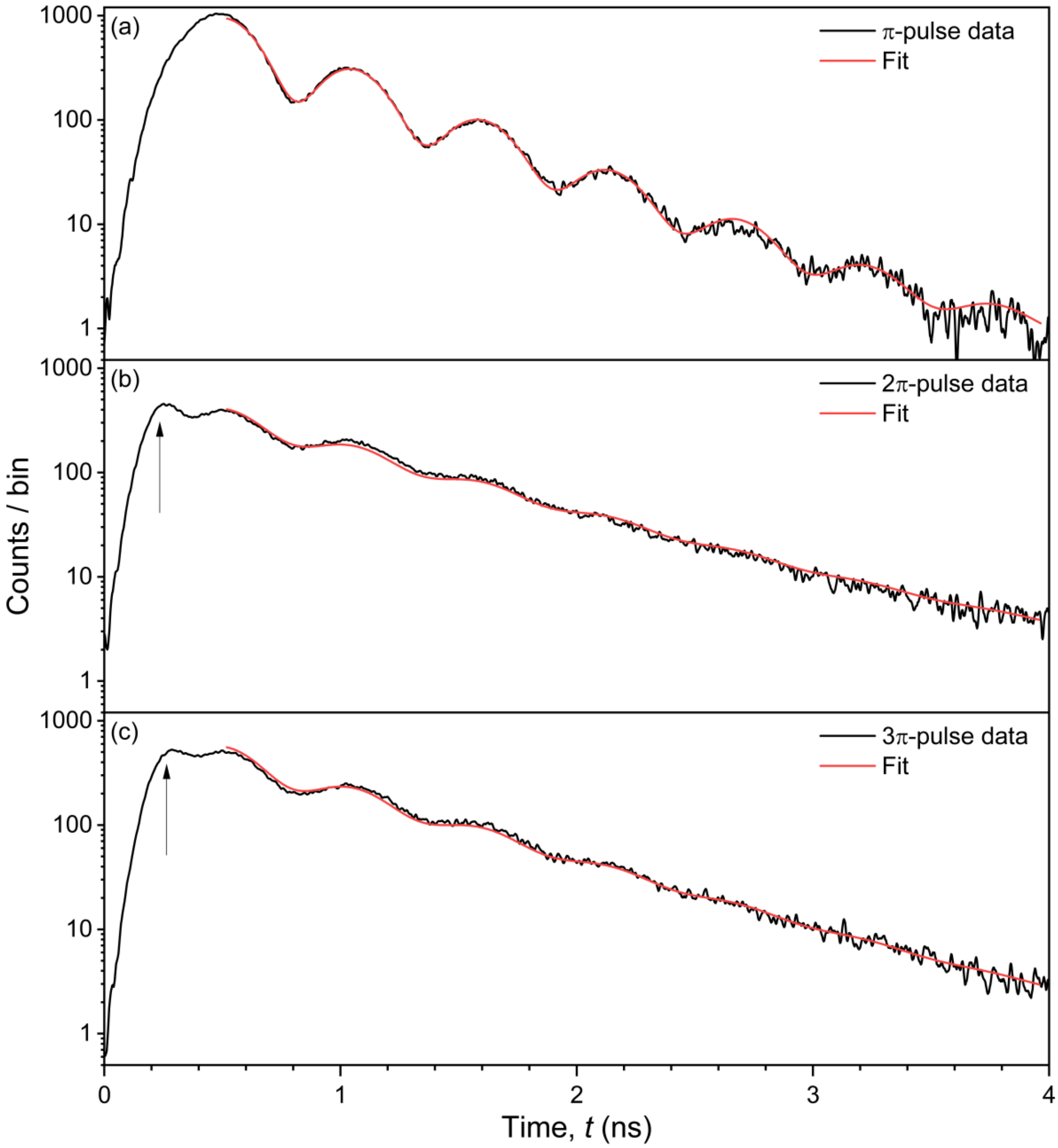

Fig. 6.4 – Time-resolved emission intensity after a single pulse on a logarithmic scale, showing the radiative lifetime of the transition, for three different powers corresponding to (a) π-pulse, (b) 2π-pulse, and (c) 3π-pulse. Clearly visible in each case is a beat in count rates. The fit of the decay, for data where the beat amplitude is larger than the count rate noise, is shown in red. In (b) and (c), an arrow shows the narrow peak arising from laser reflection.

A quantum beat is clearly visible in each subplot, revealing the fine structure splitting of the neutral exciton. Due to the diagonal polarisation of the coherent laser light, the horizontal and vertical polarisation states are both driven, albeit not equally, and interfere with one another. As the states have different energies and decay at different rates, the probability of the excited superposition will oscillate as a function of time, resulting in modulation in the radiative count rate at a period corresponding to the difference in energy between the two fine structure polarisation lines (Meier and Koch 2005; Mowbray and Skolnick 2005; Dyakonov and Khaetskii 2017). Interestingly, the beat shows a damping faster than the exponential lifetime decay in each of the datasets, most obvious in (b) and (c), visibly decreasing in amplitude even on a logarithmic scale, where the exponential decay of the lifetime is linear, suggesting rapid decoherence (Flissikowski et al. 2001). This may again be a result of the imperfect diagonal polarisation of the laser light, resulting in the phase changing over time.

The following equation describes a radiative lifetime's periodic beat and exponential decay curve:

$$y = y_0 + A_0 e^{-\frac{t}{T_1}} + A_1 e^{-\frac{t}{T_1}} sin\left(\frac{2\pi t}{w} + \varphi\right) \tag{6.8}$$

Where y_0 is the y offset, T_1 is the lifetime, A_0 describes the base amplitude of the decay curve, A_1 is the base amplitude of the sinusoidal beat, w is its time period, and φ is a phase offset. However, to account for the increased damping of the beat relative to the exponential lifetime decay, the equation has been modified to include a damping parameter, k_{damp}.

$$y = y_0 + A_0 e^{-\frac{t}{T_1}} + A_1 e^{-\frac{k_{\mathrm{damp}} t}{T_1}} sin\left(\frac{2\pi t}{w} + \varphi\right) \tag{6.9}$$

Applying fits with such an equation extracts values for the exponential time constant of (498.8 ± 1.7) ps, (713.1 ± 3.3) ps, and (639.8 ± 11.8) ps respectively. The fitted value increases as power does, despite the radiative lifetime being constant. This is possibly due to the increased laser reflection, something which is supported by the value for 2π pulse being larger than that at 3π pulse. The π-pulse lifetime can be compared with measurements from a control sample with QDs not enhanced by a cavity (discussed and studied in Chapter 7), which showed a mean radiative lifetime of (1099.1 ± 42.3) ps. Thus, the transition emission rate is predicted to be enhanced by a Purcell factor of approximately 2.20 ± 0.09. By comparison, FDTD simulations of a low Q pillar with the same diameter, as shown in the previous chapter, reveal a maximum theoretical Purcell factor of 3.16, with an overall efficiency of up to 0.79 at the collection lens above the device.

From the three data sets can also be extracted a consistent beat period of (543.7 ± 0.9) ps. This corresponds to a frequency of (1.839 ± 0.003) GHz, and thus an energy level separation of (7.605 ± 0.012) μeV, or a difference in emission wavelength of (5.24 ± 0.01) pm. While close, this doesn't agree with the average fine structure splitting extract from the spectra fitted in section 6.1.1. It's possible this is partially due to the noise in the section, as well as ambiguity from fitting overlapping functions, especially when only just resolved, as with the broader peaks obtained with a non-resonant laser.

6.1.4 Power-dependent second order correlations

Pulsed second order correlation measurements were also performed for this transition using a Hanbury Brown and Twiss setup, at powers corresponding to π/2-pulse, π-pulse, and 2π-pulse. These results are shown in Fig. 6.5. The plotted correlations are normalised using the mean fitted heights of peaks far from $\tau = 0$ ns, and the values for $g^{(2)}(0)$ are obtained from the areas under the peaks.

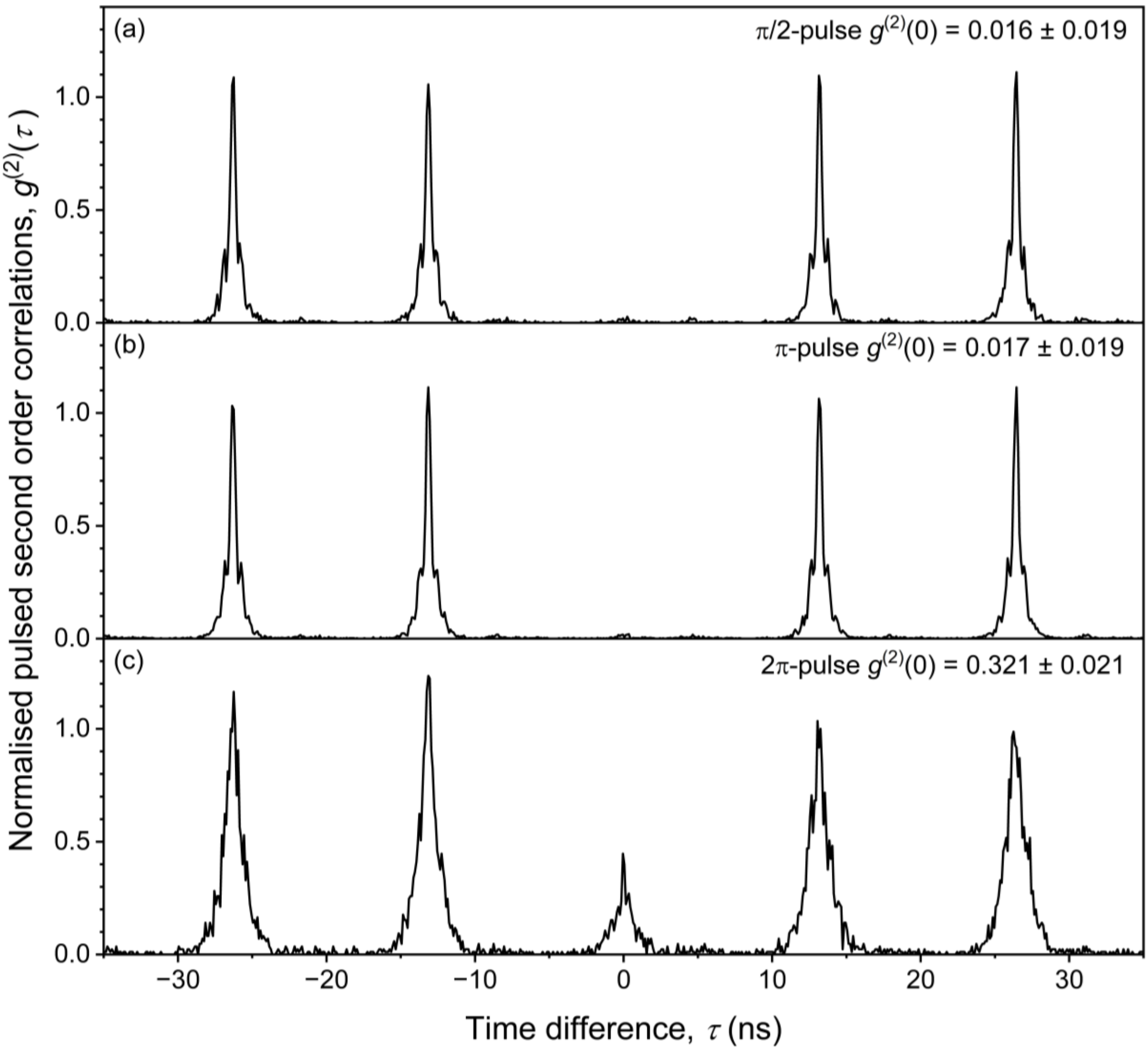

Fig. 6.5 – Second order correlation $g^{(2)}(\tau)$, produced using a pulsed laser at three different powers, corresponding to π/2-pulse, π-pulse, and 2π-pulse. The plotted correlations are normalised using the mean fitted heights of peaks at large delays.

Each of the datasets show a reduced peak at $\tau = 0$ ns, indicating antibunching, or a reduced probability of detecting photons at the two detectors at the same time, as only one photon is produced in the majority of emission events. This is because photons are spontaneously emitted by the two-level system of the quantum dot, which takes a short relaxation time to spontaneously decay from an excited energy level to the ground state, in which time it cannot emit again. Thus, fewer correlations are recorded.

As (a) and (b) show, the emitter shows a good single photon purity of (98.4 ± 1.9) %. The reduced emission rate at 2π and the increased laser reflection, as seen in the previous lifetime measurements, lead to a proportional decrease of detected emission from the quantum dot, and thus an increase in $g^{(2)}(0)$ for (c), up to 0.321 from the similar values of 0.016 and 0.017 in (a) and (b).

Specifically, between π- and 2π-pulse, the laser will be 4 times more intense, while the previous Rabi plot in Fig. 6.3 suggests the transition's emission drops by ~4 times. Thus, the intensity ratio between the laser and the transitions increases by a multiple of ~16. If the imperfect second-order correlation arises from the laser, this would suggest that its value should increase by around the same amount. Indeed, comparing the π- and 2π-pulse fitted $g^{(2)}(0)$ values finds a similar ratio of 18.9.

A second order correlation was also performed using the continuous wave laser for a range of different powers up past saturation to 112 nW, the results of which are depicted in a colour map in Fig. 6.6. The colours are chosen in such a way that data points >1 will be tinted red, and those <1 will be tinted blue.

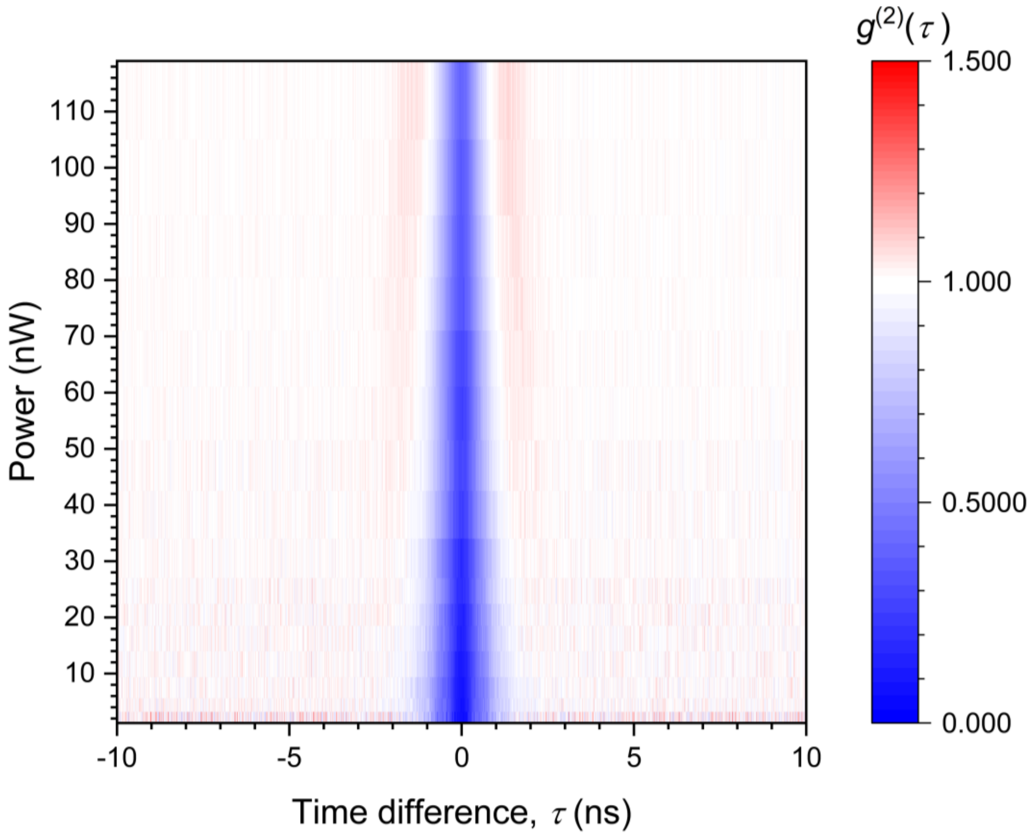

Fig. 6.6 – Second order correlations $g^{(2)}(\tau)$ vs the power of a CW laser, normalised based on correlations far from $\tau = 0$ ps. Colours are chosen such that any data points above 1 after normalisation will be visible in red.

These results show a pair of peaks greater than 1 increasing in intensity with power on either side of the central dip, physically suggesting an increased probability of detecting two photons spaced by about 2 ns. The appearance of additional oscillations on either side of $\tau = 0$ ps is due to the emitter, when in the non-linear regime, experiencing Rabi cycles to emit again after the first detection sets the system into the ground state $|0\rangle$ (Flagg et al. 2009).

This pattern can be fitted using the following equations, extended by Flagg et al. (2009) to include both pure dephasing and radiative recombination:

$$g^{(2)}(\tau) = 1 - e^{-\varpi_1|\tau|}\left[\cos(\varpi_2|\tau|) + \frac{\varpi_1}{\varpi_2}\sin(\varpi_2|\tau|)\right] \tag{6.10}$$

Where $\varpi_1 = (1/T_1 + 1/T_2)/2$ and $\varpi_2 = \sqrt{\Omega^2 + (1/T_1 + 1/T_2)^2}$. T_1 is the transition's radiative lifetime, T_2 is the dephasing time, and Ω is the Rabi frequency. This can be modified further to allow imperfect values of $g^{(2)}(0)$:

$$g^{(2)}(\tau) = 1 - \left(1 - g^{(2)}(0)\right) e^{-\varpi_1|\tau|} \left[\cos(\varpi_2|\tau|) + \frac{\varpi_1}{\varpi_2}\sin(\varpi_2|\tau|)\right] \tag{6.11}$$

Where $\left(1 - g^{(2)}(0)\right)$ acts as a scaling factor based on the single photon purity of the emitter. This version of the equation is used for the fits in this work.

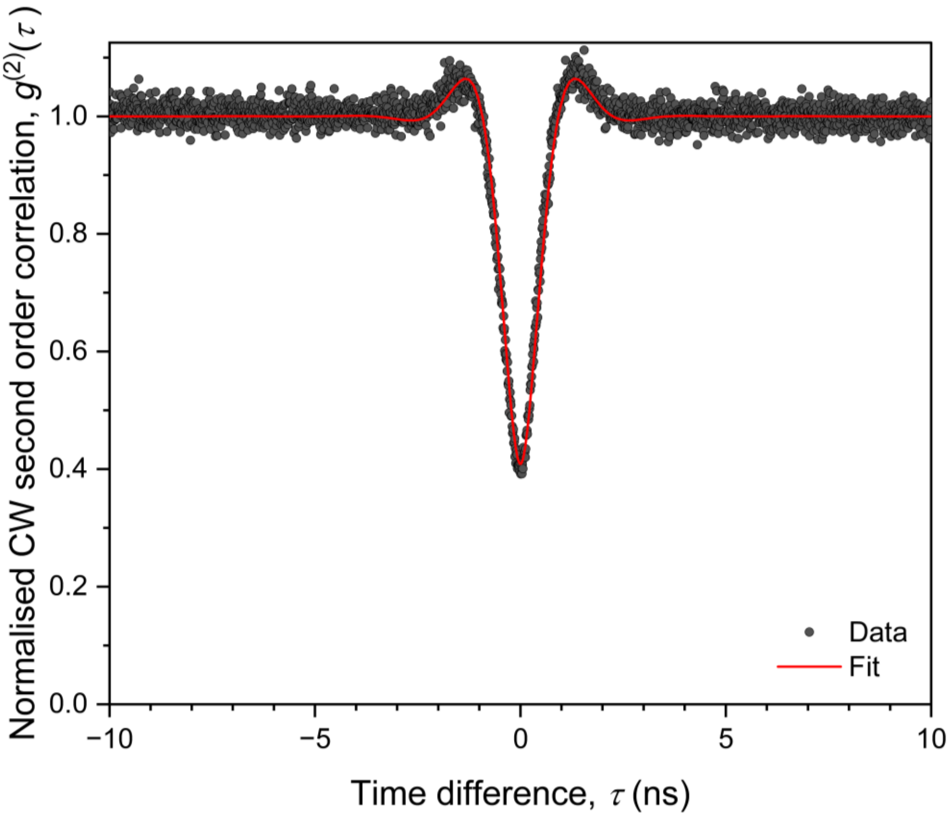

Fig. 6.7 – Second order correlation $g^{(2)}(\tau)$ produced using a CW laser at 112 nW, normalised based on correlations far from $\tau = 0$ ps. The data points have been fitted using (6.11).

An example of this is presented in Fig. 6.7, for the highest power shown in the previous figure: 112 nW. The lifetime T_1 was fixed at 498.8 ps, the value obtained at π-pulse in the previous section, which is assumed here to accurately describe the intrinsic lifetime of the transition.

The fit describes the data well, including the two peaks on either side of $\tau = 0$ ps, as well as suggesting a further cycle that isn't visible at this power within the data's noise. From this were obtained values for the dephasing time, $T_2 =$ (749.7 ± 21.2) ps, and for the Rabi frequency, $\Omega =$ 2.27 ± 0.02 GHz. The fit also serves the role of determining a value of $g^{(2)}(0)$, which here is 0.409 ± 0.003.

By fitting the data for each power, all three values are shown to increase with additional laser power. In particular, the dephasing time is originally shorter than the lifetime, but approaches a value double this ($2T_1/T_2 \approx 1.$) as emission saturates, showing that the emission is radiatively limited (Flagg et al. 2009).

The Rabi frequency is proportional to the electric field, as $\Omega = |\vec{\boldsymbol{d}}||\vec{\boldsymbol{E}}|/\hbar$, where $|\vec{\boldsymbol{d}}|$ is the quantum dot's dipole moment magnitude and $|\vec{\boldsymbol{E}}|$ is the electric-field amplitude (Berman and Malinovsky 2011), and thus is expected to be approximately proportional to the square root of the laser power (Flagg et al. 2009), similar to the trend observed here.

Finally, the second order correlation also steadily increases as the power does, albeit at a decreasing rate like with the other results, as can also be seen in the direct correlation data in Fig. 6.6. Initially, this may suggest that this effect is linked to the proportional effect of the power-dependent count rate of emitted photons saturating at high powers and the increased laser reflection, both of which were shown in previous figures. However, similar analysis by other authors suggests the cause may be an overlapping bunching effect, caused by spectral diffusion due to the occupation of defects near the quantum dot (Sallen et al. 2010; Tamariz et al. 2020), as has previously been shown to increase with power in this chapter, and which like the Rabi frequency will be dependent on the square root power, to which the resulting bunching's characteristic time would be inversely proportional (Holmes et al. 2015; Gao et al. 2019).

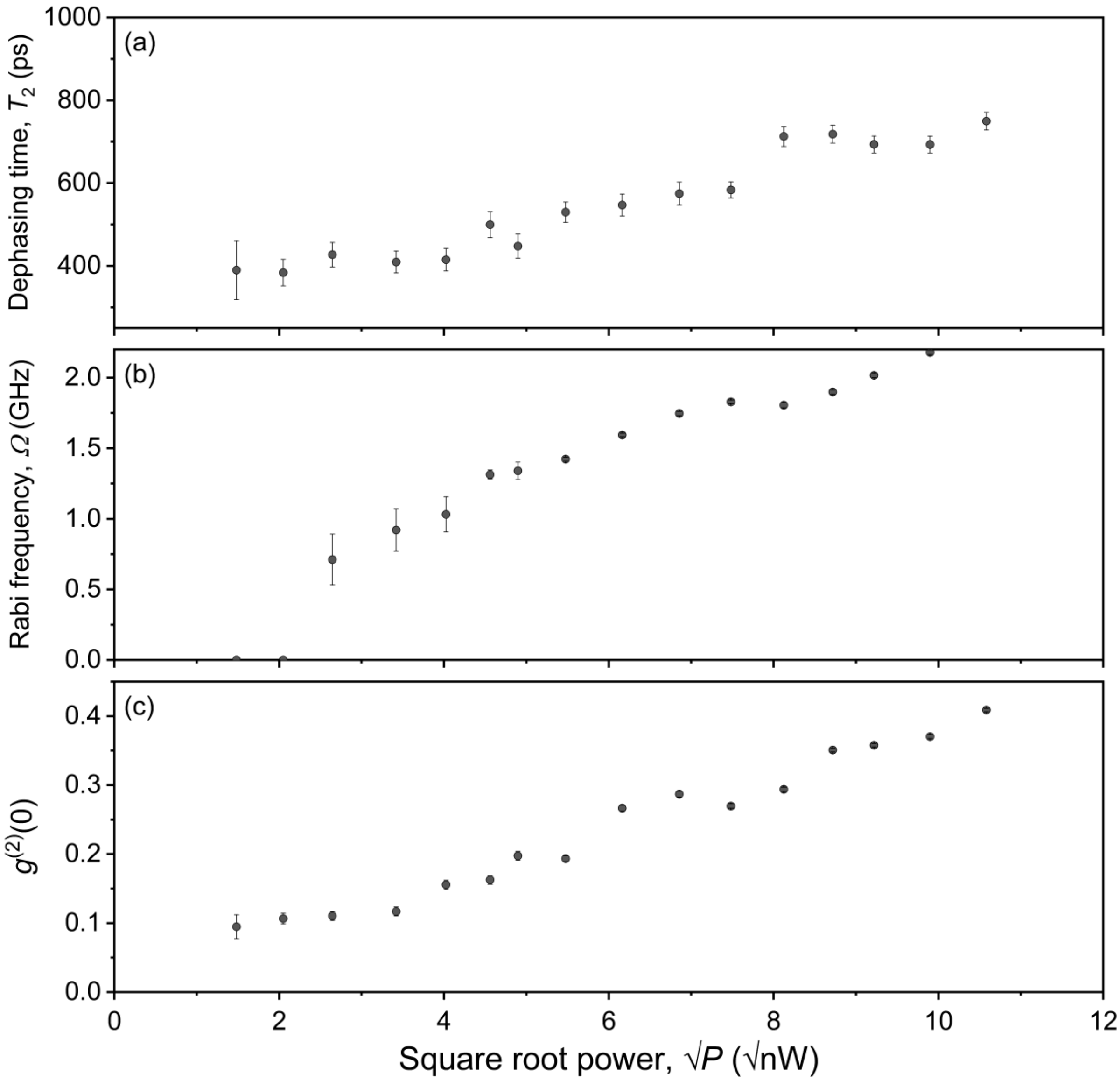

Fig. 6.8 – Values extracted from fits for (a) dephasing time T_2, (b) Rabi frequency Ω, and (c) the second order correlation at $\tau = 0$ ps, $g^{(2)}(0)$ as functions of square root power.

6.2 Confirmation of indistinguishable single-photon emission in a low Q sample

This section returns to the low Q micropillar sample produced using the direct-write lithography process described in the previous chapter and examines another micropillar to show that our devices produce single, indistinguishable photons. This is done by establishing the single photon emission properties of the device using the results discussed in the previous section, before confirming that the photons produced are indistinguishable using a Hong-Ou-Mandel experiment.

The data and results presented are obtained using a new subject than that used in the previous section: a neutral exciton from a quantum dot in a 1.7 μm diameter micropillar, resonant with the pillar's HE_{11} cavity mode. It has a quality factor of 440 ± 30.

6.2.1 Resonance fluorescence scan showing fine structure splitting

A high-resolution resonance fluorescence scan across the exciton using a CW laser at 31 nW, shown in Fig. 6.9, confirms the fine structure splitting. Two peaks are visible, with fitted wavelengths of (925.11981 ± 0.00002) nm and (925.12728 ± 0.00002) nm, for a difference of (7.47 ± 0.03) pm, or an energy splitting of (10.82 ± 0.04) μeV. Unlike previously in Fig. 6.2, they are now equally driven by a diagonally polarised laser, resulting in very similar count rates for the two peaks.

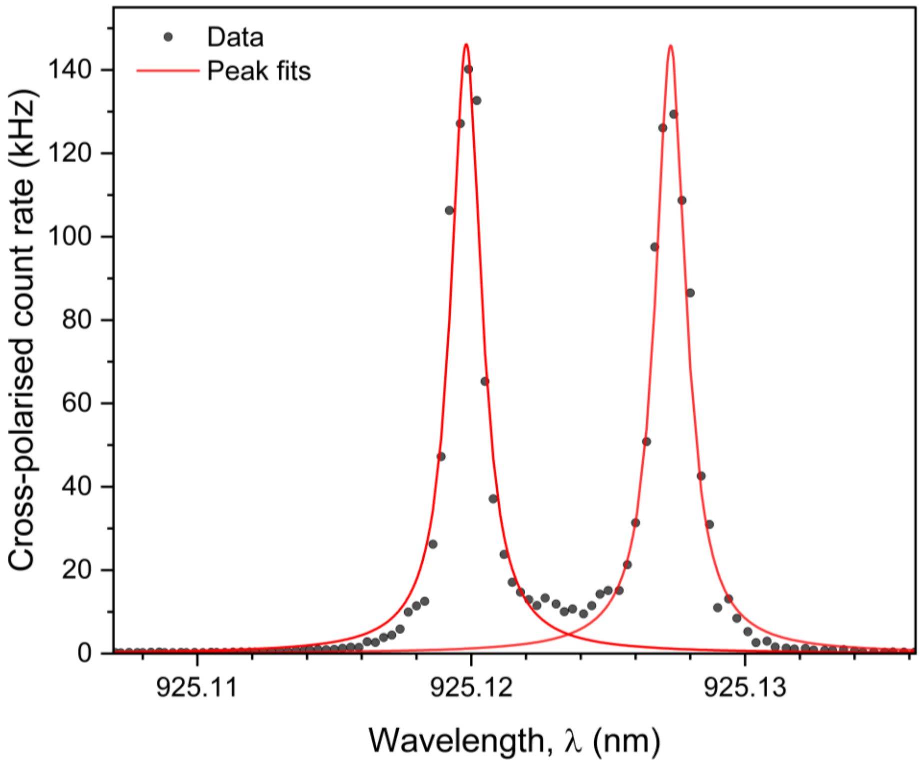

Fig. 6.9 – CW laser resonance fluorescence scan showing a high-resolution spectrum of another exciton, revealing its fine structure splitting. Each polarisation is equally driven by a diagonally polarised laser. Each peak is fitted with a Lorentzian, shown in red.

Also in contrast to the results presented in the previous section, the fine structure splitting is a lot wider, suggesting the quantum dot associated with the transition might be more anisotropic. The spectrum is also less noisy, suggesting there are far fewer nearby defects. This is also reflected in the spectral width: (1.35 ± 0.03) pm, approximately 3x narrower than the peaks of the previously studied transition. Combined with the lack of noise, this supports the idea that defect-caused magnetic field fluctuations could have influenced the breadth of the emission lines studied in section 6.1.1.

6.2.2 Rabi oscillations in power dependence

Again resonantly exciting the exciton using a cross-polarised setup (Kuhlmann et al. 2013a), varying the pulsed laser power under the same parameters produces a Rabi oscillation, observed in this case to repeat over several cycles. This is plotted in Fig. 6.10, against the square root power as measured at a pick-off power monitor before the objective. Though the data is discontinuous at around 2 $\sqrt{\mu W}$, this is merely due to a split in the two ranges of power accessed using a neutral density filter.

The clear periodic trend, with a fitted period of (1.825 ± 0.006) $\sqrt{\mu W}$, confirms the two-level system of the neutral exciton. This is on a similar scale to the timescale in the previous section. Given both experiments were performed with the same pulsed laser, the small difference between the two values likely arises from variation in the magnitude of the transitions' dipole moments.

The limited damping of the Rabi oscillations in this data suggests the sources of decoherence in this device are weaker. This could be linked to the reduced charge noise in this device, as well as the lower uncertainty in the emission energy. However, based on the hypothesis raised in the previous attempt, it is likely that this is instead a result of the two energy levels now being equally driven, and thus remaining in phase with each other longer, reducing any destructive interference driven damping.

The axis of the oscillations visibly appears to change as the square root power is increased. To allow a fit, the exponentially decaying sinusoid was applied on top of a quadratic background. Physically, this can be partially attributed to the increase in laser reflection as the power increases, as discussed previously. However, unlike the previous pulsed power dependence, where the laser quickly overwhelmed the dampened oscillations, the effect is more gradual with a slower overall increase in count rate at higher laser powers, suggesting less laser reflection is picked up by the detector.

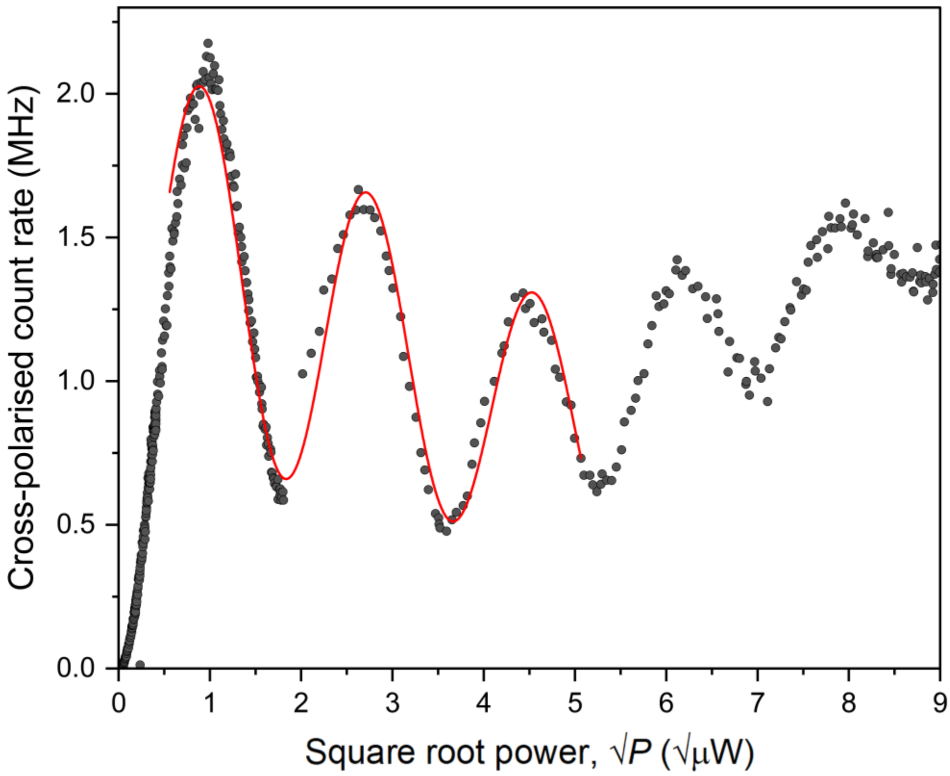

Fig. 6.10 – Square root power dependence for a neutral exciton, showing Rabi oscillations in the pulse amplitude. The data is fitted with a sinusoidal function with an exponential damping component (red).

At π-pulse excitation, or a square root power of 0.969 $\sqrt{\mu W}$ (and thus a power of 0.984 μW), a maximum count-rate of ~2.2 MHz is recorded by the SNSPD. This is equivalent to a first lens brightness of 64%.

6.2.3 Lifetime and beat

Similarly, the radiative lifetime was also measured for this emitter at π-pulse and plotted on a log scale in Fig. 6.11. A beat is clearly visible, emerging from the fine structure splitting of the transition.

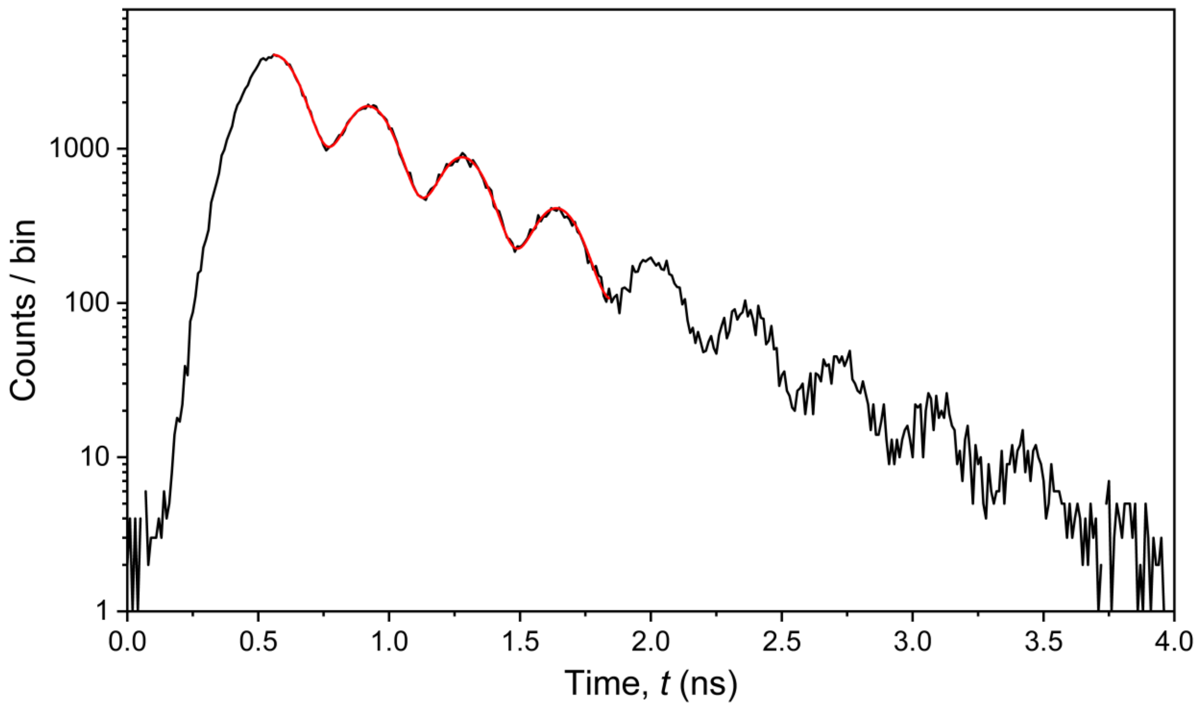

Fig. 6.11 – Logarithmic plot of the time-resolved emission intensity after a single pulse, showing the radiative lifetime of the transition. Clearly visible is a beat in count rates. The fit of the decay, for data where the beat amplitude is larger than the count rate noise, is shown in red.

This is again fitted with an exponentially decaying sinusoidal as in (6.7) (with no additional damping term in this case) returning a lifetime of (470.5 ± 4.2) ps, similar to that observed in the previous device. Again, comparing with a control sample not enhanced by a cavity in which the quantum dots are placed at a node in the spacer electric field, the transition is estimated to be enhanced by a Purcell factor of 2.34 ± 0.09.

Also obtained is a beat period w of (359.8 ± 0.8) ps. This is shorter than that observed in the previous section's transition, with the higher frequency corresponding to a greater fine structure splitting. Specifically, this beat period corresponds to an energy level separation of (11.494 ± 0.026) μeV, or a difference in emission wavelength of (7.93 ± 0.01) pm. This is slightly larger than the value obtained from the resonance fluorescence scan of (7.47 ± 0.03) pm.

Unlike before, the amplitude is reduced consistently on a logarithmic scale, suggesting that the effect that caused it to dampen at an increased rate is not present in this sample. Again, this may be attributable to the improved diagonal polarisation of the resonant laser.

6.2.4 Second order correlation $g^{(2)}(\tau)$ and single-photon purity

A Hanbury Brown and Twiss measurement was also performed to obtain the second order correlation measurement $g^{(2)}(\tau)$, which is shown in Fig. 6.12. This provides a measurement of the single photon purity when the system undergoes a full population inversion under π-pulse (0.984 μW) excitation.

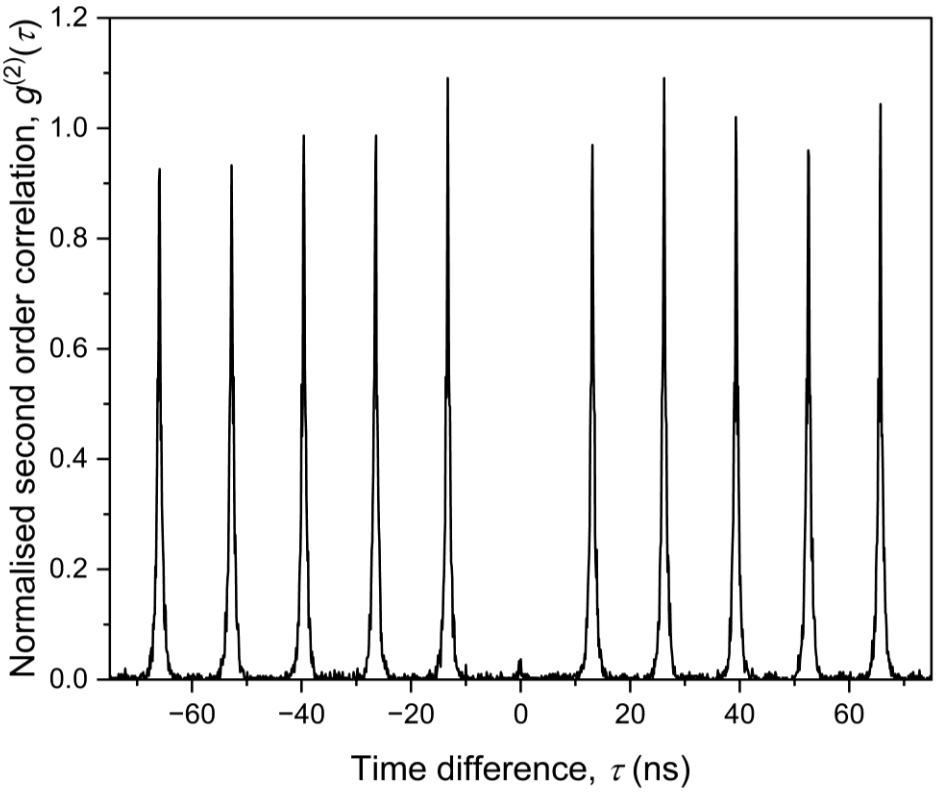

Fig. 6.12 – Second order correlation $g^{(2)}(\tau)$, produced using a pulsed laser at π-pulse power (0.984 μW). The plotted correlations are normalised using the mean fitted heights of peaks at large delays.

Fitting the area under the peak at $\tau = 0$ ns, and normalising based on the mean area of peaks far from this point at large delays, obtains a $g^{(2)}(0)$ value of 0.027 ± 0.004, or a near-unity single photon purity of (97.3 ± 0.4) %, comparable to values reported by other authors (Ding et al. 2016; Somaschi et al. 2016; Wang et al. 2019a; Tomm et al. 2021). The single photon purity is similar to that obtained with the previously studied transition, though slightly lower.

6.2.5 Hong-Ou-Mandel (HOM) interference visibility

Using the same conditions, two photons emitted in sequence from our quantum dot in pulses 13.2 ns apart are interfered using a Hong-Ou-Mandel experimental setup. The interferometer used for this measurement had a first-order visibility 0.950 ± 0.002, which was determined using a narrowband (<1 MHz) single frequency laser at approximately the same wavelength as the exciton studied.

As laid out previously in this thesis, the Hong-Ou-Mandel experiment utilises and demonstrates the Bose-Einstein statistical properties of photons. As two fully indistinguishable photons enter a 50:50 beam splitter in opposite directions, their wave packets overlap perfectly, and they will either destructively or constructively interfere with one another. This means they must exit the beam splitter in the same direction (Santori et al. 2002). Thus, one would expect a decrease in the simultaneous correlation count between two detectors at each exit of the beam splitter. This experiment is diagrammed and discussed further in section 4.3.3.

In this case, the two photons were obtained by first splitting the single-photon emission with a prior 50:50 beam splitter and directing half the photons emitted by the device through a path delay corresponding to the time difference between pulses to temporally align them. A half waveplate is used to introduce and control polarisation indistinguishability. Using this, two correlation measurements were obtained and plotted in Fig. 6.13, for cross-polarised photons (a) and co-polarised photons (b). The prior, with the input photons fully distinguishable by their polarisation, will not interfere, though will show a decrease near $\tau = 0$ ns due to the limited probability of subsequent photons being transmitted/reflected in different directions by the first beam splitter. Meanwhile co-polarised photons, while also showing this probabilistic decrease near zero, should also entirely destructively appear at 0 ns, in the case of a perfect source of indistinguishable photons. The degree of visibility can thus be calculated by finding the ratio of peak areas at $\tau = 0$ ns for the two datasets, which will also discount the beam splitter effects.

By doing this, one obtains a raw two-photon interference visibility V_{raw} of (88.9 ± 0.6) %. Scaled based on interferometer visibility, this is then corrected to V_{corr} = (93.6 ± 0.7) %.

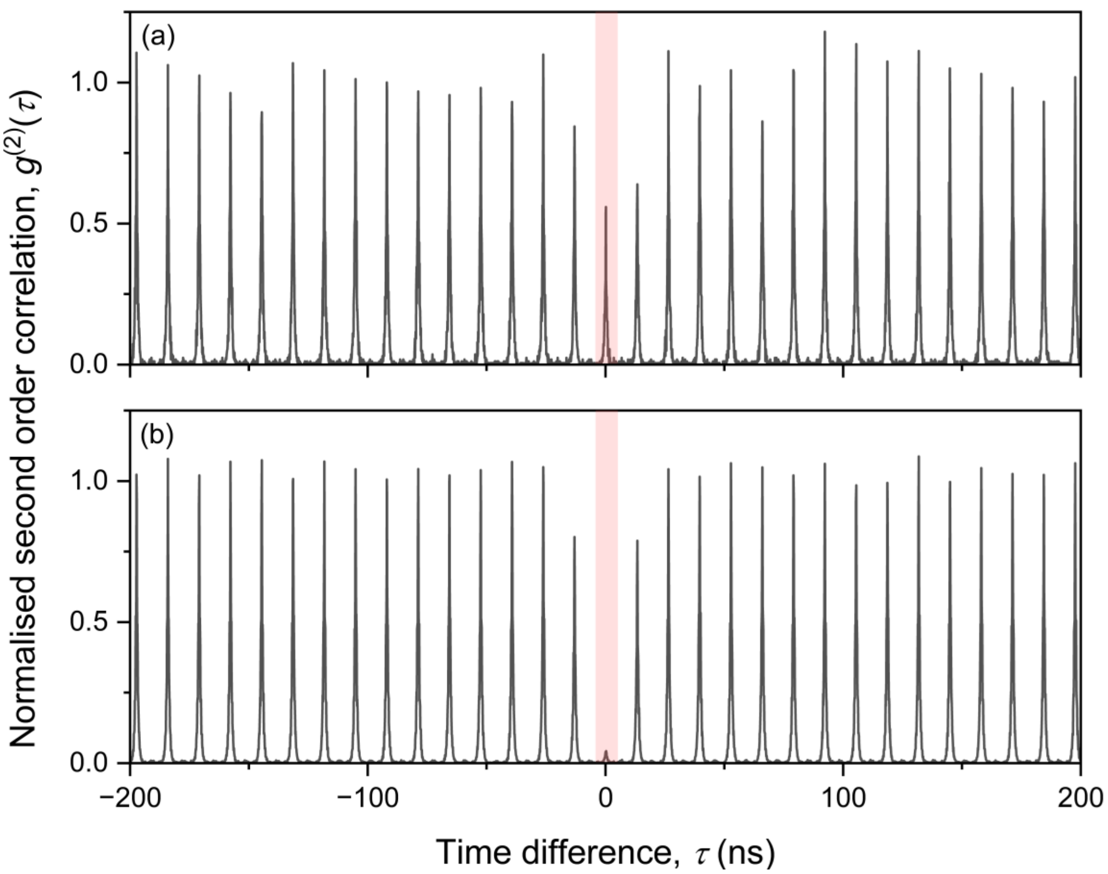

Fig. 6.13 – Hong-Ou-Mandel interference results for (a) cross-polarised and (b) co-polarised photons emitted by a quantum dot. The correlations are normalised using the mean area fitted under peaks at large delays. The red shaded rectangles indicate the regions where fitted areas are used to determine the interference visibility.

With an imperfect single photon source, whether exciton or trion based, Hong-Ou-Mandel visibility is reduced regardless of the intrinsic photon indistinguishability. In both cases, the multiphoton component can be treated as separable and distinguishable noise and thus the sub-unity single photon purity $1 - g^{(2)}(0)$ may be accounted for by using equation (4.16), which applies in the limit of low $g^{(2)}(0)$ (Ollivier et al. 2021). By doing this, a value is obtained for the source's inherent two-photon indistinguishability M_S of (99.0 ± 1.0) %.

Even using a pillar with a low quality factor, as done here, this near-unity value is comparable to previous reported visibilities obtained using more strongly Purcell-enhanced QDs (Ding et al. 2016; Somaschi et al. 2016; Wang et al. 2019a; Tomm et al. 2021). This further demonstrates the quality of the samples produced by the direct write lithography method described in the previous chapter, as well as the effectiveness of the additional oxide ALD in protecting the semiconductor from damage due to exposure to an ambient environment.

The lifetime, dephasing time, and indistinguishability are all linked by the equation (Bylander et al. 2003; Kambs and Becher 2018):

$$M_S = \frac{T_2}{2T_1} \tag{6.12}$$

Thus, the dephasing time T_2 of this device can be estimated to be around (931.6 ± 12.6) ps. This is notably significantly larger than the values obtained from the fits of CW second-order correlations using the previous transition, though the different excitation conditions mean these values aren't truly comparable. This lines up with the slower loss of coherence observed when comparing the power-dependent Rabi oscillations for each transition.

6.2.6 Summary of results from low Q sample

Finally, several other quantum dot transitions in the low Q sample, pre-selected to show bright emission peaks clear of surrounding features under non-resonant excitation, were also examined. Table 6.2 shows performance metrics from these sources, demonstrating the repeatability of results on a single fabricated chip. As before, the indistinguishability is corrected based upon the interferometer visibility and the limited single-photon purity.

Table 6.2 – A summary of different performance metrics for five sources. This additional data was recorded by Dr. Petros Androvitsaneas, Dr. Rachel Clark, and Miguel Alvarez Perez.

Transition wavelength, λ (nm)	**Rate under π-pulse excitation (MHz)**	**Radiative lifetime (ps)**	**Second order correlation, $g^{(2)}(0)$**	**Indistinguishability**
925.12	2.2	471	0.027	0.941
925.35	2.1	474	0.021	0.968
924.62	1.6	449	0.028	0.954
925.91	1.5	545	0.066	0.981
925.35	0.9	471	0.044	0.964

Together, these results confirm that the direct-write lithography-based method outlined in the previous chapter is indeed capable of producing high-performing quantum dot micropillar single-photon sources, even using a low quality factor design.

These results are competitive with single-photon sources reported by other authors such as Wang et al. (2017) and Tomm et al. (2021), as discussed and tabulated in Chapter 2.

6.3 Conclusions

This chapter obtains several important quantum dot emission properties for quantum dots in low Q pillars using well-known methods like the Hanbury Brown and Twiss and Hong-Ou-Mandel experiments and studies their dependence on excitation conditions and laser power. A number of common effects are demonstrated and discussed, including charge noise, power broadening, and dephasing due to imperfectly diagonally polarised laser light.

It is also confirmed, thus, that the devices produced using the direct-write method laid out in the previous chapter are capable of reproducibly generating indistinguishable single photons, with near unity single photon purity and HOM visibility even with a lower quality factor. However, the exact performance of different devices will vary, owing to the effects and differences discussed, such as the heavy presence of defects in the first dot studied, which likely lead to broader linewidths, noise, and faster decoherence times, or the higher anisotropy of the second, resulting in a larger fine structure splitting and thus more rapid Rabi oscillations. Different experimental conditions, such as changes to the polarisation scheme as seen here, will also have an impact, meaning further work may be required to offer a better like-for-like comparison between two similar devices.

Chapter 7

Influence of non-cavity modes on Purcell factor and collection efficiency

In this chapter, I quantify how key metrics of pillar microcavity devices characterising the interaction of localised exitonic transitions with the confined photonic modes, including the Purcell factor, spontaneous emissions coupling factor β, and collection efficiency ξ, are modified by the non-cavity modes which exist in such devices. This is achieved by comparing collection rates and emission lifetimes for physical samples with dots at different positions in the electric field of the cavity spacer layer. It is also shown that the zero-phonon line and the off-resonant phonon-assisted emission into the cavity mode HE_{11}, which can have a detrimental effect on the emission's single photon purity, is completely suppressed when dots are positioned at the electric field node.

7.1 Introduction to Purcell factor determination

Numerical design of solid-state single photon sources generally focuses on localised 'cavity' modes with high quality factors. These modes facilitate efficient photon collection due to their clear initial decay and finite physical extent, allowing them to be well approximated within a small solvable simulation volume, and thus in a practical run-time. However, simulations are less able to predict non-cavity (often called 'leaky') modes, which are spectrally broad, overlapping, and are difficult to extract from numerical FDTD and FEM simulations. Understanding the role these non-cavity modes fill is important for a complete understanding of photon source behaviour, as they provide alternative radiative decay channels, and thus are also important in the general experimental determination of the effective Purcell enhancement in microresonators and other devices.

Here the effects of a pillar's non-cavity modes are investigated, computationally and experimentally comparing a pair of nominally identical micropillar samples, differing only in that one has QDs located at an electric field anti-node where Purcell-enhanced emission into HE_{11} dominates, and the second has QDs at a node, where coupling into HE_{11} is suppressed and coupling into non-cavity modes dominates. This was motivated by discussions of how random distributed quantum dots will result in different coupling strengths to the cavity electric field, while non-cavity modes are less impacted. Thus, by comparing the emission of QD transitions as the height of the source is varied and the local electric field strength is suppressed to various degrees, the proportion of emission that is collected from non-cavity modes can be quantified. Furthermore, individual cavities with a small number of well-resolved transitions are studied to investigate cavity-feeding - the phonon-assisted emission into HE_{11}. Finally, single transitions are magnetically detuned across the cavity mode using a $\vec{\boldsymbol{B}}$-field in Faraday geometry, taking advantage of diamagnetic shift and Zeeman effects, to determine the change in decay time arising from the Purcell effect.

7.2 Simulations of micropillars with dipole sources of different z-positions

First, 1.85 μm diameter circularly cylindrical GaAs-$Al_{0.95}Ga_{0.05}As$ micropillars were simulated in ANSYS Lumerical FDTD, as shown in Fig. 7.1 (a). As in previous work in this thesis, the micropillar consists of a 267.9 nm GaAs λ spacer layer, with DBRs of 17 $\lambda/4$ alternating GaAs and $Al_{0.95}Ga_{0.05}As$ pairs above and 26 pairs below the spacer, all standing on a planar GaAs substrate. QD emission is modelled as an electric dipole source on the central axis of the micropillar $x = y = 0$, oriented in plane along the x-axis. The height of the dipole (z) is varied from the bottom to the top of the GaAs spacer layer across multiple simulations to probe the electric field nodes and antinodes of the HE_{11} cavity mode as sketched in Fig. 7.1 (b). To simulate the spectral response, the dipole is driven with a Gaussian pulse with 5.6 fs full width at half maximum, covering a spectral range from 840 nm to 1070 nm, injecting a total spectral average power of 3.79 fW.

The simulation volume has x and y dimensions of 5.5 μm and a z dimension of 10 μm, with PML conditions applied at the simulation boundaries. Each surface of the simulation volume is covered by a planar frequency-domain field monitor to record the electric field and directional transmission of power through the plane. Fitting the spectrally resolved power through the top surface monitor reveals an HE_{11} quality factor of ~21600, consistent with analytical models (Schubert 2018). Additional planar field monitors normal to each dimension x, y, and z intersect at the pillar's centre at the origin. The simulations were allowed to run until the system energy dropped to 10^{-6} of its initial value, at which point it automatically stopped. Symmetric and anti-symmetric boundary conditions were used in the two vertical planes of symmetry through the pillar to reduce computation time.

The electric field amplitude profiles at the HE_{11} mode energy of 1.322 eV, or a wavelength of 937.827 nm, on the y = 0 (x-z) and x = 0 (y-z) planes are shown in Fig. 7.1 (c-f). For a dipole at the anti-node of the electric field (z = 0), the distribution on the plane y = 0 parallel to the dipole reveals a dominant component of emission in the vertical direction (Fig. 7.1 (c)). The distribution on the plane x = 0, orthogonal to the dipole (Fig. 7.1 (d)) also shows a strong degree of emission in the vertical direction, along with some guiding in the horizontal direction at the spacer layer, which will not be collected by an optic above the sample. This is a result of stronger coupling to the non-cavity modes, something not seen on the plane parallel to the dipole, as it does not emit along its axis. Conversely, when the dipole is placed at the lower node of the cavity electric field (Fig. 7.1(e) and Fig. 7.1(f)), at one quarter of the spacer height (z = -0.067 μm), the field intensity is not enhanced and guided modes of high radial quantum number are dominant. A large fraction of the light is seen to escape downward into the high index substrate. As with a dipole placed at the anti-node, there is a stronger degree of emission in directions perpendicular to the dipole axis, although it is focused toward the upper half of the micropillar.

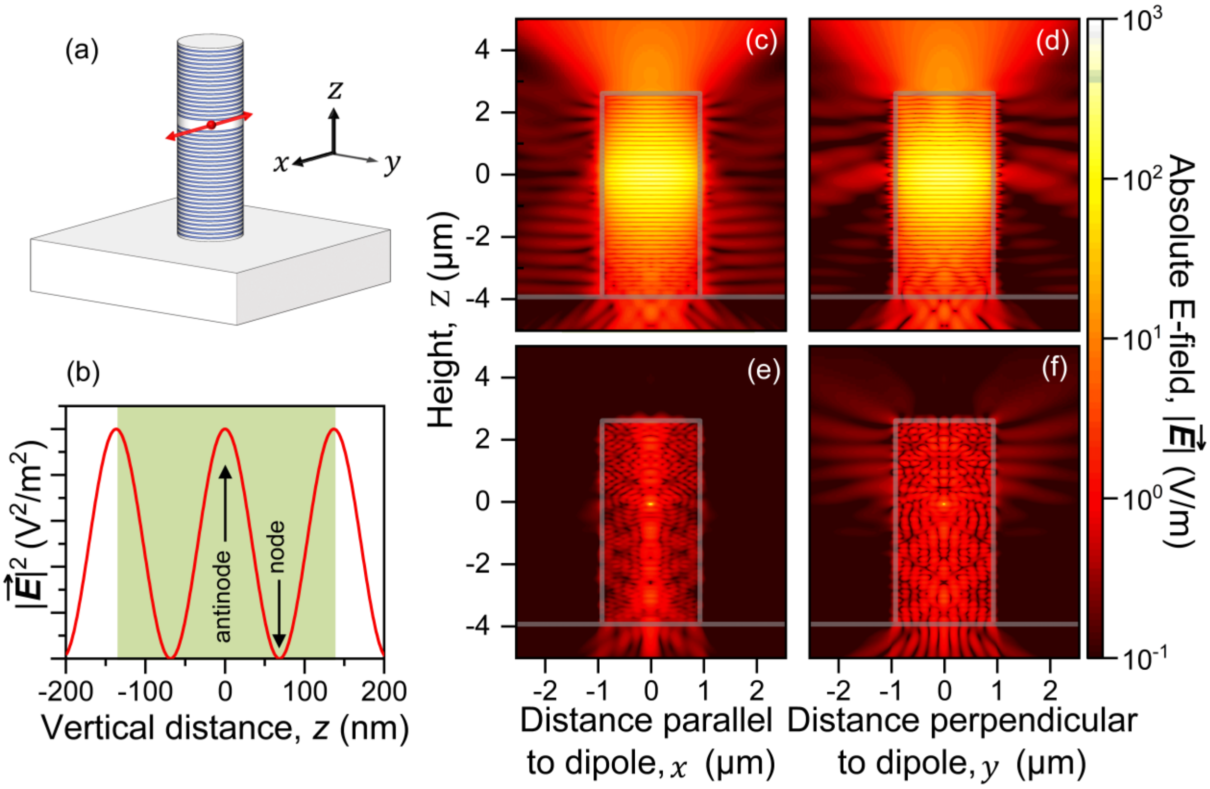

Fig. 7.1 – (a) Diagram of the simulation geometry containing a GaAs-$Al_{0.95}Ga_{0.05}As$ micropillar with 17 (26) upper (lower) DBR pairs on a GaAs substrate, excited by a dipole orientated along the x-axis (red). (b) Sketch of the standing wave in the cavity mode electric field intensity in the GaAs spacer layer (green), bordered by $Al_{0.95}Ga_{0.05}As$ DBR layers. (c-f) Absolute electric field $|\vec{E}|$ cross-sectional profiles for a 1.85 μm micropillar (grey outline) at the HE_{11} mode wavelength of 937.827 nm. (c,d) for a dipole at the anti-node position in the center of the spacer layer: (c) on the y = 0 plane (x-z), parallel to the dipole and (d) on the x = 0 plane (y-z), perpendicular to the dipole. (e,f) as (c,d), but for a dipole at the lower node.

Fig. 7.2 shows the total emitted power around the pillar in the simulation, as functions of both energy and the dipole source height z. It is plotted on a logarithmic colour scale, so both bright and dim features are visible. The bright band at 1.322 eV is the

HE_{11} mode, which can be seen to change in strength in a periodic pattern. There also is a secondary broadband dim pattern in the background, which does not remain constant with z, out of phase with the cavity mode oscillation. This is a result of variation in the non-cavity mode density of states.

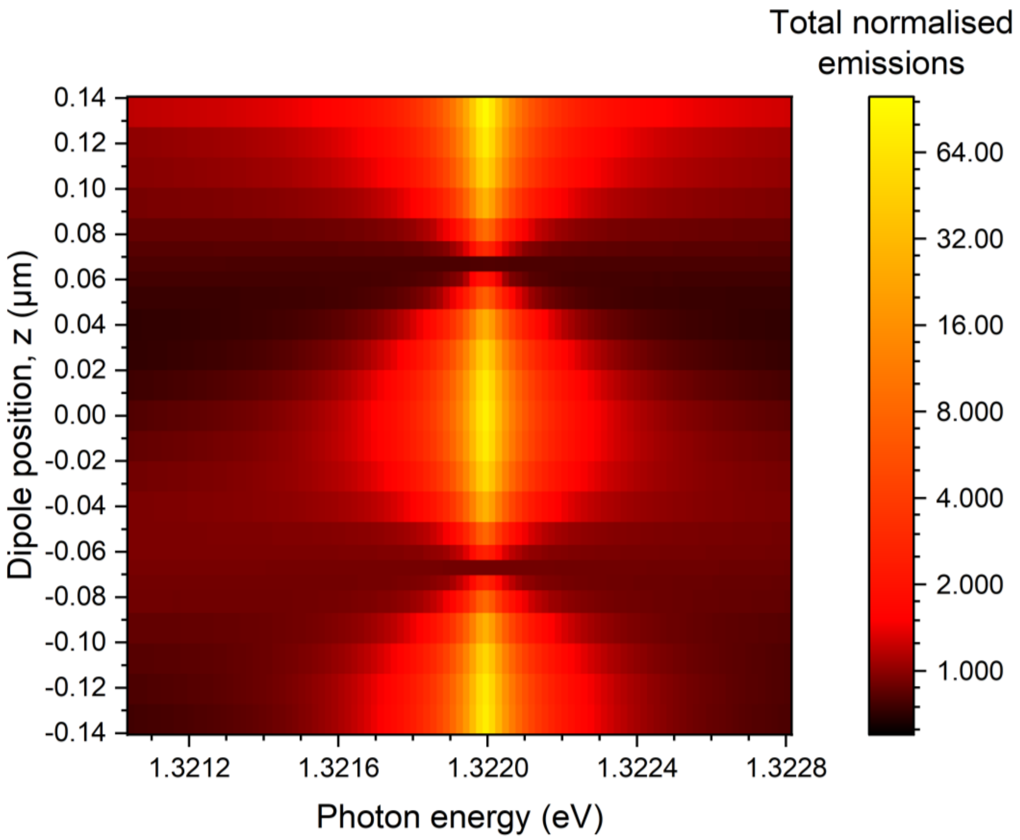

Fig. 7.2 F– Logarithmic colour map of the total emitted power recorded in all directions in each simulation, normalised to the power emitted by the source in a homogenous medium, as a function of photon energy and the height of the dipole source z in a 1.85 μm micropillar.

As the non-cavity modes are too broad to fully capture in the results here, data was also recorded at the same planar frequency-domain monitor positions over a much broader spectral range of 1.16 to 1.48 eV, or 836.5 to 1072.6 nm, albeit at a lower resolution of 2.2 meV, which corresponds to approximately 1.2 to 2.0 nm per pixel (varying due to the frequency-spacing). This is shown in Fig. 7.3, revealing the broad, complex spectrum of non-cavity modes. Also visible are bright narrow bands (for example, around 1.4 eV) corresponding to the higher-order modes also coupled with the emissions of the dipole on the central axis of the micropillar. While there is significant variety in the shape of the non-cavity mode bands, they appear to generally be 10 meV or larger in width, far greater than the high Q cavity modes seen here. If these modes were characterised in the same way as the HE_{11} mode has been in previous work, they would have Q factors of <150.

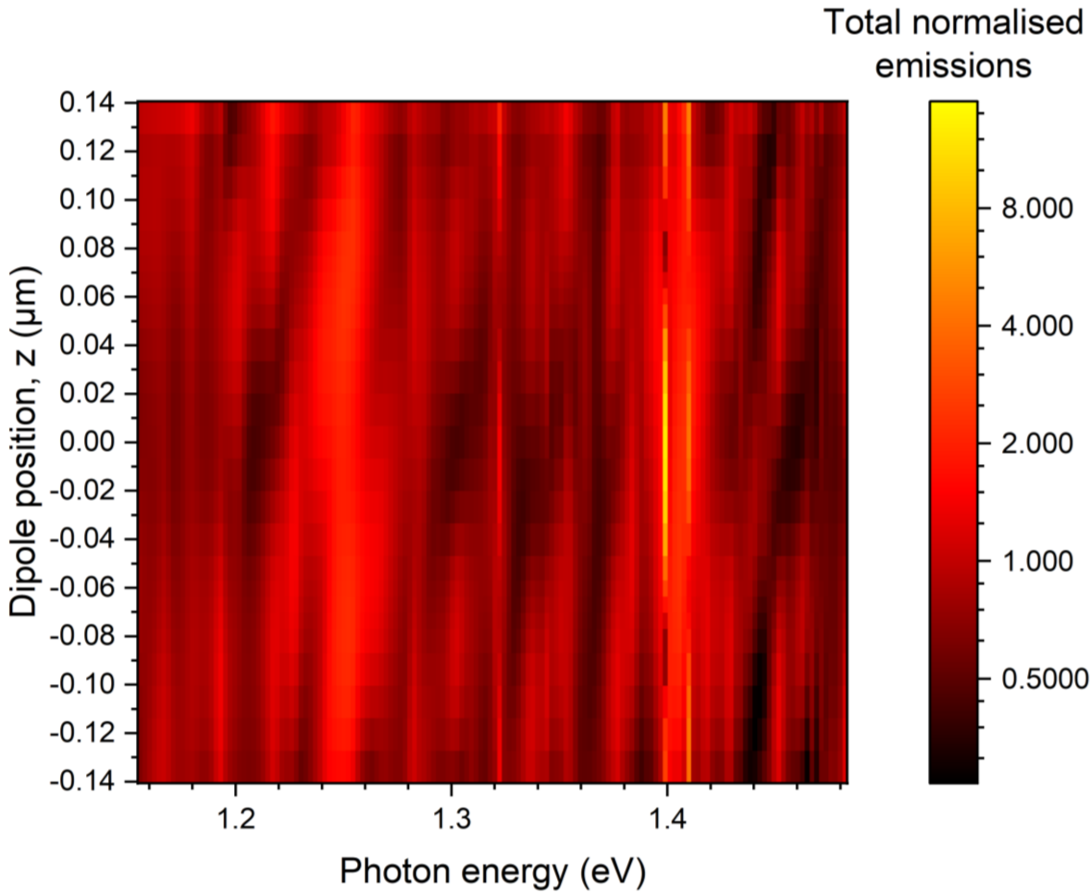

Fig. 7.3 – Logarithmic colour map of the total transmitted power spectrum recorded in all directions in each simulation, normalised to the power emitted by the source in a homogenous medium, as a function of the height of the dipole source z in a 1.85 µm micropillar. This data is recorded at a lower spectral resolution, but over a broader spectrum than Fig. 7.2.

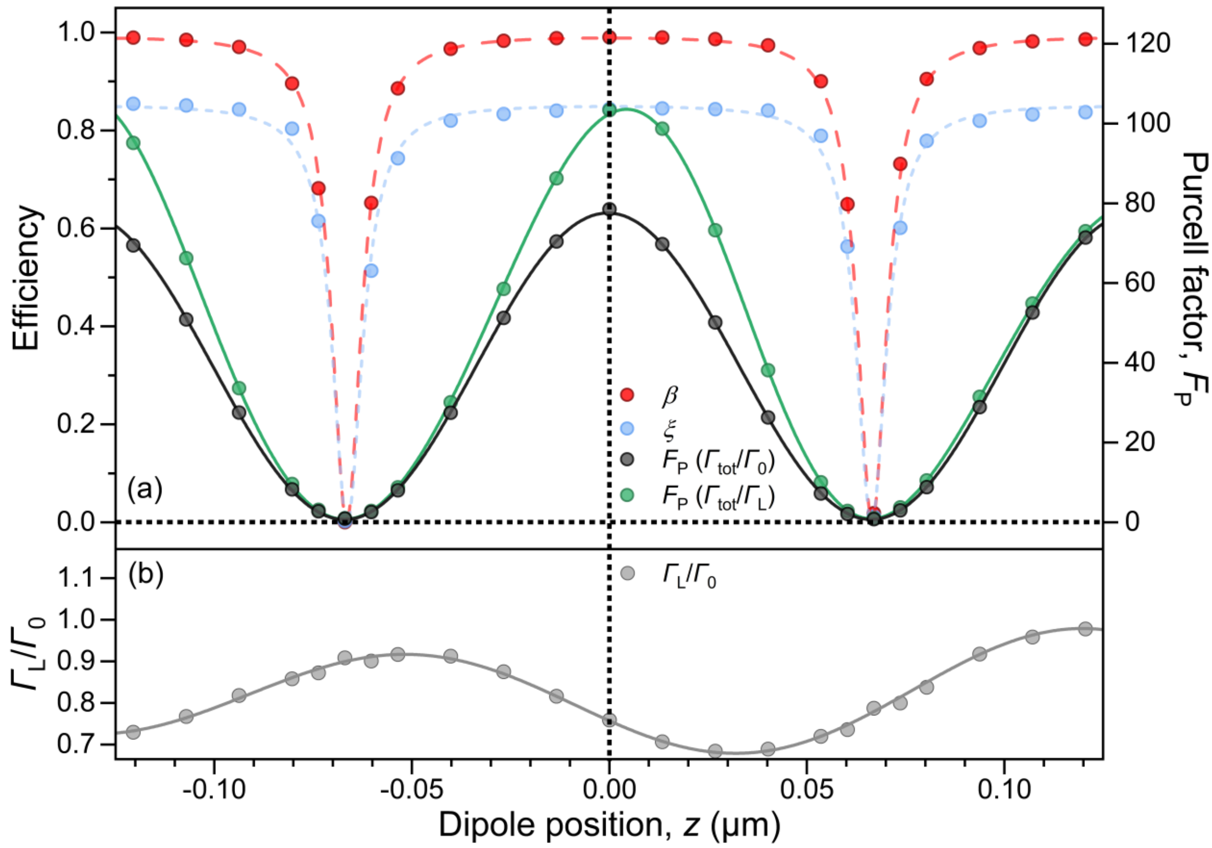

Fig. 7.4 – Simulation results showing how (a) the spontaneous-emission coupling factor β (red) and outcoupling efficiency ξ (blue), the Purcell factor F_{P} calculated both as a ratio of the total decay rates to that in a homogenous medium $\Gamma_{\mathrm{tot}}/\Gamma_0$ (black), and as a ratio to the non-cavity modes decay rate $\Gamma_{\mathrm{tot}}/\Gamma_{\mathrm{L}}$ (green), and (b) the ratio of non-cavity modes decay rate to the decay rate in a homogenous medium $\Gamma_{\mathrm{L}}/\Gamma_0$ (grey) vary with the height of the dipole source z in a 1.85 µm micropillar.

Fig. 7.4 (a) shows the calculated spontaneous-emission coupling factor β, outcoupling efficiency ξ, and Purcell factor F_{P}, calculated both as a ratio of the total decay rates to that in a homogenous medium $\Gamma_{\mathrm{tot}}/\Gamma_0$, and as a ratio to the non-cavity modes decay rate $\Gamma_{\mathrm{tot}}/\Gamma_{\mathrm{L}}$, as functions of the dipole source position z within the spacer, relative to the centre of the cavity. β was calculated using (3.26) based on the energy-resolved total transmission through the surrounding closed box of planar monitors, as plotted in Fig. 7.2, isolating the HE_{11} mode from the spectrally broad non-cavity-mode emission background by fitting the resulting spectrum using a Lorentzian function, so as to isolate cavity mode emissions regardless of direction. This obtains a value of β = 0.989 when the dipole is at the anti-nodes in the bottom, middle, and top of the spacer, and drops as far as β = 5 × 10^{-4} when the dipole approaches the nodes (z = ±0.067 μm). This has also been fitted with a simple equation based on (3.26) to provide the fitted curve:

$$\beta = \frac{\Gamma_{\mathrm{C}_0} \cos^2\left(\frac{2\pi z}{L_{\mathrm{cav}}}\right)}{\Gamma_{\mathrm{L}} + \Gamma_{\mathrm{C}_0} \cos^2\left(\frac{2\pi z}{L_{\mathrm{cav}}}\right)} \tag{7.1}$$

Where Γ_{C_0} is the maximum cavity mode decay rate, as obtained at the central antinode z = 0 μm, Γ_{L} is the non-cavity mode decay rate, and L_{cav} is the total thickness of the cavity spacer layer. This equation assumes the cavity mode emission drops to 0 at nodes while the decay rate via cavity modes is sinusoidal as a function of z, as implied by F_{P}. As may be seen, the data is found to closely match this prediction.

The outcoupling efficiency ξ is determined similarly to β, but instead specifically using the ratio of the energy-resolved emission through the top planar monitor, Γ_{out}, again isolating the HE_{11} mode from the background using a Lorentzian function, to the total emissions in all directions as per (3.28). Examples of such fits to extract the total and directional cavity mode emissions for these calculations can be found in Chapter 5 in Fig. 5.3. The results are then fitted with an equation similar to (7.1), similarly assuming that Γ_{out} is sinusoidal with z and decreases to 0 at the cavity's nodes:

$$\xi = \frac{\Gamma_{\mathrm{out}} \cos^2\left(\frac{2\pi z}{L_{\mathrm{cav}}}\right)}{\Gamma_{\mathrm{L}} + \Gamma_{\mathrm{C}_0} \cos^2\left(\frac{2\pi z}{L_{\mathrm{cav}}}\right)} \tag{7.2}$$

ξ follows the predicted trend well and behaves similarly to β, reaching 0.849 at the anti-nodes and falling to 3 × 10^{-6} at the nodes, showing that emission upward via the cavity mode is nearly entirely suppressed.

F_{P} was also calculated from the total power emitted in all directions at the HE_{11} mode energy, normalised to the dipole source power in a homogenous medium of the local refractive index (black) and normalised to Γ_{L} (green). As methods of determining the Purcell factor that compare the emission rates of transitions on- and off-resonance with the cavity mode often assume that $\Gamma_{\mathrm{L}} = \Gamma_0$, they will regularly present their determined Purcell factor as being equal to $\Gamma_{\mathrm{tot}}/\Gamma_0$, when actually they will have calculated $\Gamma_{\mathrm{tot}}/\Gamma_{\mathrm{L}}$, which as seen can take on radically different values depending on the proportion of emissions via non-cavity modes. For values of $\Gamma_{\mathrm{L}}/\Gamma_0$ less than 1, as seen here, this results in a systematic overestimate of F_{P}, as generally defined.

$\Gamma_{\mathrm{tot}}/\Gamma_0$ closely follows a sinusoidal pattern, as fitted, peaking at F_{P} ~ 78 at anti-node positions. Conversely, it falls to 0.91 at the lower node, indicating some suppression of radiative emission at the mode wavelength at these source heights, as shown also in Fig. 7.4 (b). Meanwhile, $\Gamma_{\mathrm{tot}}/\Gamma_{\mathrm{L}}$ follows a similar near-periodic pattern, but peaks now at 104, at a z position of +0.004 μm, due to the variation in $\Gamma_{\mathrm{L}}/\Gamma_0$. The plotted curve is calculated similarly from a ratio of the previous sinusoidal fit of $\Gamma_{\mathrm{tot}}/\Gamma_0$ and the fit of $\Gamma_{\mathrm{L}}/\Gamma_0$ presented in (b). It should be noted that the FDTD simulations do not simulate rough sidewalls on the cavities, which have been reported (Gerard et al. 1996; Reitzenstein and Forchel 2010; Androvitsaneas et al. 2023) to dominate losses for cavity diameters below 2.5 μm, suppressing Q and decreasing F_{P} towards unity.

Fig. 7.4 (b) shows the emission via non-cavity modes relative to the emission in a homogenous medium, $\Gamma_{\mathrm{L}}/\Gamma_0$, calculated from F_{P} and β as a function of z. This also shows a near-sinusoidal pattern but with lower contrast, a different phase and longer period than the variation in F_{P} shown in Fig. 7.4 (a). This variation in non-cavity modes is expected to be a result of the semiconductor-air interfaces. The difference in period clearly shows that the cavity mode has no direct influence on the non-cavity modes and there is no conservation in LDOS at a given frequency. It is noted that despite common assumptions, $\Gamma_{\mathrm{L}}/\Gamma_0$ is below unity at all heights, being 0.76 at position z = 0. As the non-cavity modes are different to the cavity mode HE_{11}, observing a different periodicity in Fig. 7.4 (b) is expected. Specifically, higher-order guided modes of the extended cylindrical pillar, outside the stop band of the Bragg mirrors due to their in-plane wavevector, are reflected at the top GaAs-air interface. Due to the high index contrast, the reflection is strong, creating a standing wave pattern, which leaks to the GaAs substrate. As the emission seen here is a result of a superposition of the decay rates from multiple non-cavity modes, the data is fitted with two summed sinusoids to approximate the relationship with z observed. This returns two wave components of wavelengths (0.17 ± 0.01) µm and (0.24 ± 0.15) µm, with corresponding amplitudes of (0.13 ± 0.05) and (0.04 ± 0.04), oscillating about an offset of (0.82 ± 0.01) times the emission in a homogenous medium.

7.3 Experimental study of samples with quantum dot layers at an antinode and at a node

The following experimental work studies samples with emitters at different heights, nominally identical to the simulated structures. Using direct-write projection photolithography, two samples grown on 3-inch wafers by molecular beam epitaxy were etched into cylindrical micropillars of a range of sizes (Androvitsaneas et al. 2023), although here we focus on those of 1.85 µm diameter, as simulated. Sample A contains InAs QDs at the mid-point of the cavity spacer, at a cavity mode anti-node. Conversely, sample B contains InAs QDs at one-quarter of the spacer height, at a node of the cavity mode. The cavity mode energy, measured via white light reflectivity for a planar structure at room temperature, varies between the samples by 0.73%. Therefore, the following data is plotted against energy relative to the cavity mode determined from white light reflectivity spectra at 4 K.

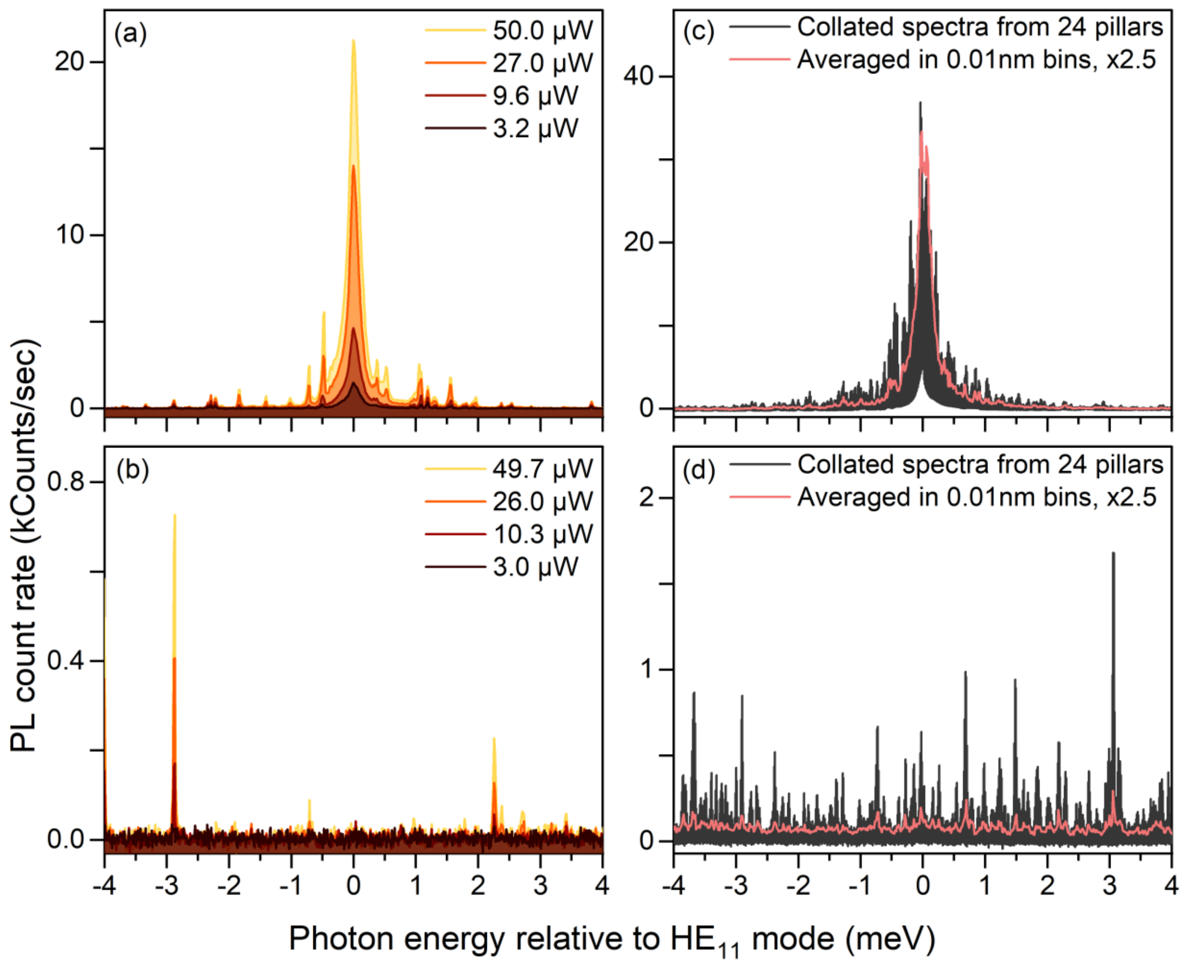

Fig. 7.5 – PL spectra integrated over 10 s at varying powers for 1.85 μm pillars without transitions resonant with the HE_{11} mode in (a) Sample A and (b) Sample B. Averaged spectra from twenty-four 1.85 μm pillars at low power in (c) sample A and (d) sample B. Spectra are plotted as functions of the photon energy relative to the HE_{11} mode energy of each pillar, as determined via white-light reflectivity measurements.

Photoluminescence spectra under 850 nm CW laser excitation, using a PicoQuant PDL 828 Sepia II laser, were recorded from single micropillars using a confocal arrangement with an objective lens of numerical aperture NA = 0.81. Exemplary cavities, shown in Fig. 7.5 (a) and (b) were selected to show no sharp transitions near the HE_{11} cavity mode at 4 K and 50 μW excitation power. Sample A displays an emission peak at the HE_{11} mode energy, as if driven by a spectrally broad internal light source in the cavity, such that the intensity at the mode energy is a factor of 418 ± 48 greater than when far from the mode. This “cavity feeding” is the result of cavity-enhanced phonon-assisted emission by spectrally detuned transitions within the cavity (Hohenester et al. 2009; Hohenester 2010b). The intensity at the energy of the mode increases and saturates at higher powers, as the zero-phonon transitions also do. Conversely, when sample B is exposed to identical excitation conditions there is no visible mode at the energy where the mode is observed under white-light reflectivity, confirming that positioning the dots at a node suppresses the cavity-enhanced phonon-assisted emission. This is consistent with the simulations in Fig. 7.1 and Fig. 7.4 for a dipole at the node. The ratio of intensities at the mode energy for the two cavities is 764 ± 70, suggesting that even if emission is reaching the collection optic via the non-cavity modes, it does not display any spectral structure within the 35 nm range acquired with the spectrometer, and is strongly suppressed relative to photon collection via the HE_{11} mode in Sample A.

It is non-trivial to compare two individual cavities in any experiment where the x-y position of the dot, its intrinsic internal decay rate Γ_0, and photo-physics, are unknown. It was also necessary, therefore, to probe a set of twenty-four neighbouring micropillars of ~1.85 μm diameter under identical conditions, at 4 K under 50 μW power 850 nm CW excitation. As the HE_{11} mode will vary slightly between pillars, in each case the spectrum is offset by the mode energy determined from a Lorentzian-fitted white-light reflectivity measurement to produce, in Fig. 7.5 (c) and Fig. 7.5 (d), plots of the mean spectrum. In sample A, we see a clear enhancement in intensity as the transitions near the mode become much brighter. It is thus possible to estimate a Q factor of ~5000 in PL, and an enhancement of the photon collection by a factor of 560 ± 150 over the transitions spectrally detuned from the mode. Conversely, in sample B, there is no enhancement at the mode energy; the transitions’ brightness displays no trend with energy, regardless of proximity of the cavity mode. The intensity at the mode energy is a factor of 395 ± 5 below the comparable value in sample A. The absence of the cavity mode in the spectra of sample B is consistent with the simulations performed, which suggest only a small fraction of light collected via the cavity mode ξ. Any light that is collected may have been scattered from imperfections in the pillar sidewalls, explaining the lack of spectral features.

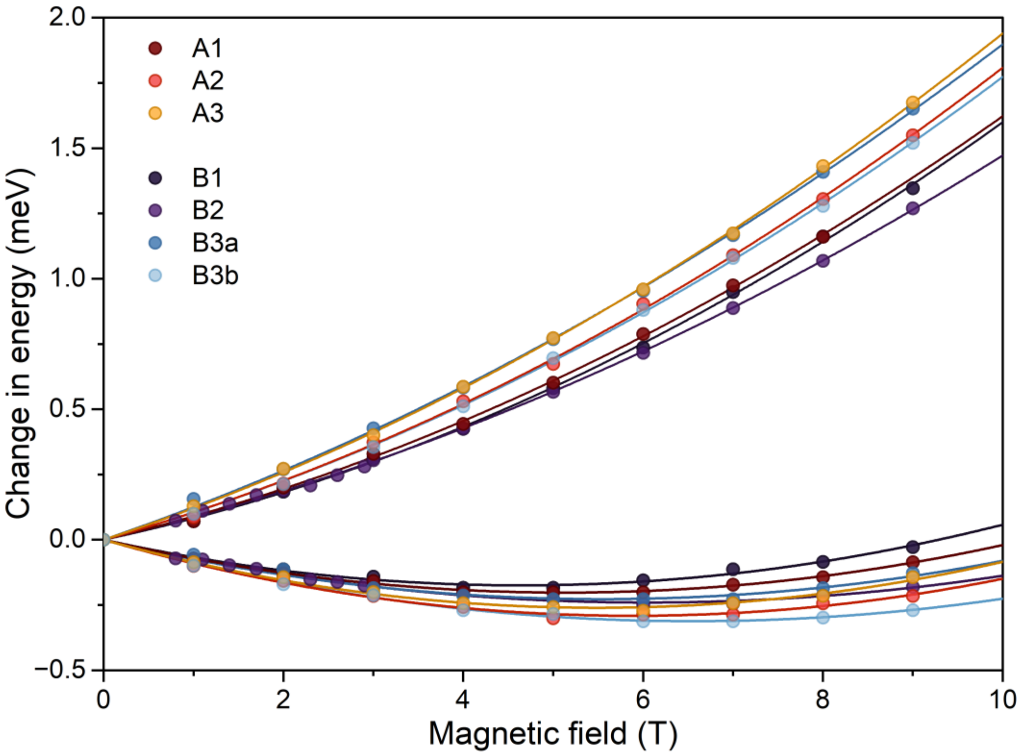

Fig. 7.6 – Dependence of the transitions' energy as function of magnetic field, applied in a Faraday geometry. The data points have been fitted with a function describing the Zeeman splitting and quadratic diamagnetic shift.

Finally, it was sought to tune a single QD transition relative to the cavity mode to evaluate these device's Purcell factors and compare the behaviour of the two pillar designs as a function of detuning from the resonance. While other methods exist to accomplish this (see Section 2.2.4), such as temperature tuning (Munsch et al. 2009; Engel et al. 2023), this was here achieved by varying the strength of a magnetic field. Measurements were taken under a magnetic field $\vec{\boldsymbol{B}}$ ranging from 0 T to 9 T applied along the z-axis in Faraday geometry, making sure at each point to re-optimise to sample stage position to counter any movement due to the applied magnetic field. The induced Zeeman effect and diamagnetic response tunes the transition energy to different positions relative to the cavity mode, as shown in Fig. 7.6. It is assumed that the magnetic field does not modify the Γ_{L} and Γ_0 emission rates. A 76 MHz pulsed laser, a Swabian TimeTagger system, and ID Quantique APDs of 247 ps Gaussian FWHM timing jitter were used to record the decay time of each transition at a time-averaged power of 14.4 μW, where the transition is substantially below saturation, plotted as functions of the detuning from the HE_{11} cavity mode. The data was collected from pre-selected bright, isolated transitions less than 1 nm in the wavelength above the cavity resonance at a magnetic flux density of $|\vec{\boldsymbol{B}}|$ = 0 T. Most transitions studied are in separate micropillars, except B3a and B3b, which are from different transitions in the same micropillar.

The Zeeman energy splitting increases linearly as expected, consistent with excitonic *g*-factors between 2.639 and 3.525, as would be expected for InAs QDs of this type (Nakaoka et al. 2004; Nakaoka et al. 2005). There is also a quadratic diamagnetic blueshift with coefficients ranging from 6.67 to 9.66 μeV/T^2.

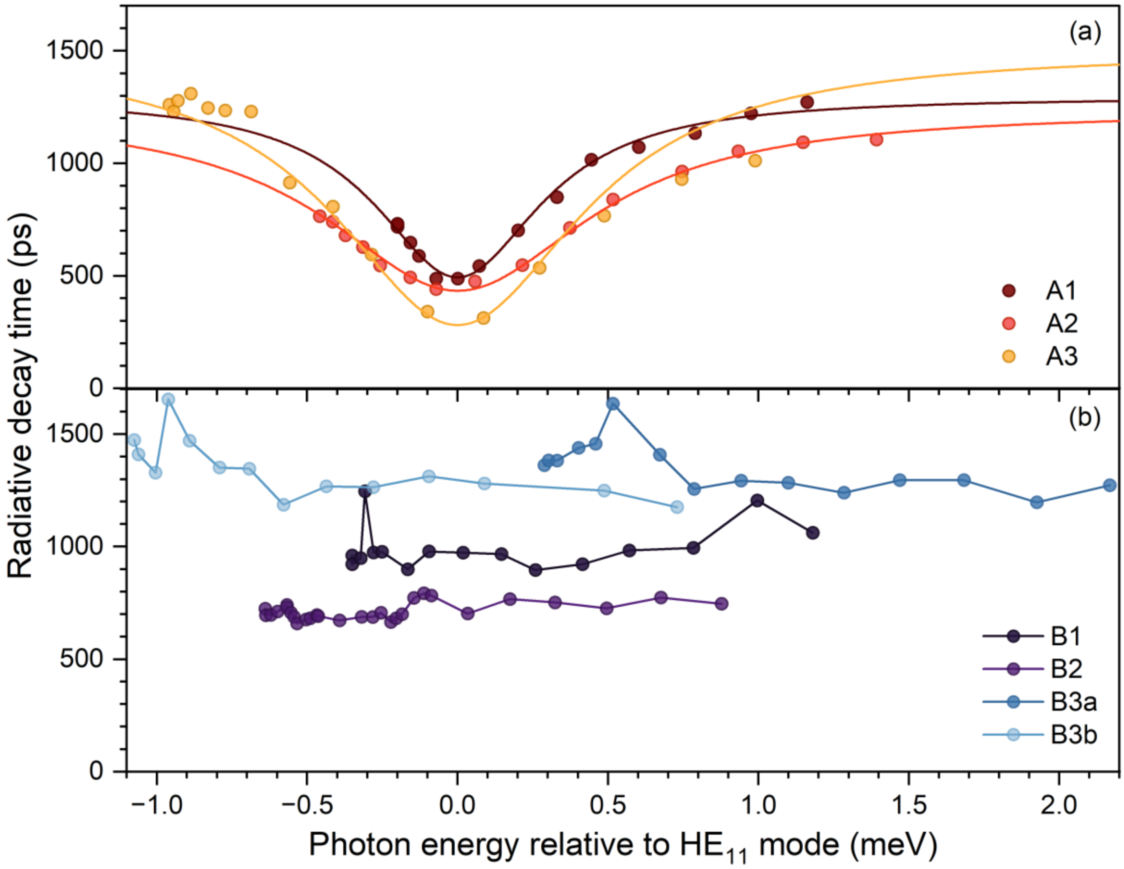

Fig. 7.7 – Radiative decay time as a function of transition-mode detuning via magnetic field tuning in Faraday geometry for (a) sample A and (b) B. Different transitions are indicated in different colors, as labeled.

In sample A (Fig. 7.7 (a)) one can observe a clear reduction of the decay time for transitions resonant with the cavity mode, consistent with Purcell enhancement. The data has been fitted with a Lorentzian curve, which matches the data closely in most cases, but some asymmetric deviation far from the mode is observed for A3. The ratio of the lifetime at large detunings to the minimum lifetime, for transitions A1, A2 and A3, is 2.53 ± 0.05, 3.80 ± 0.09, and 5.02 ± 0.69 respectively. While the Purcell factor can be estimated using this ratio, this assumes that the lifetime at large detunings determined by Γ_L is comparable to that in an infinite homogenous medium. Given the non-cavity mode results obtained from the previous FDTD simulations, F_P as defined in (2.19) will actually be a factor of approximately $\Gamma_\mathrm{L}/\Gamma_0$ = 0.76 lower than these ratios:

1.92 ± 0.04, 2.89 ± 0.07, and 3.82 ± 0.52 respectively. Corresponding β values of 0.72 ± 0.02, 0.79 ± 0.04, and 0.83 ± 0.16 can thus also be found using (2.20).

In contrast, for sample B (Fig. 7.7 (b)) there does not appear to be any cavity-mode-dependent enhancement or suppression of the lifetime of a quantum dot transition, confirming that the coupling of the transition to the cavity mode is strongly suppressed. The minimal variation in lifetime with detuning also confirms the LDOS given by the total of the non-cavity modes is spectrally flat over the tuning range of a few meV, too small when compared to the broad spectral results seen in Fig. 7.3. In practical terms it will be hard to engineer a sample with the several hundred nm wavelength variation required to experimentally probe wide-band spectral structure of the non-cavity modes, which is broader than the stopband of the mirrors. The reduced density of states at this location in the cavity, Γ_L/Γ_0= 0.91 found in the simulations (Fig. 7.4 (b)), implies a small Purcell suppression of radiative decay for all these transitions. It may also be noted that B2, and to a lesser extent B1, both show a reduced lifetime compared to both transitions in B3 and the transitions in A when tuned out of resonance. The cause of this isn't immediately clear but may be related to a difference in the quantum dots themselves, as possible causes like temperature were well controlled during this work. It has been shown that the radiative lifetime of a quantum dot depends on its shape and size (de Mello Donegá et al. 2006; Johansen et al. 2008; Ji and Song 2023) though this would imply, due to the differences in confinement, the transition would have a radically different emission energy and/or significant fine-structure splitting. Alternatively, while B2 and B1 should not be affected by the cavity mode, there may be differences in their interactions with the non-cavity modes of the devices, possibly due to being displaced at different positions from the central axis of the pillar, though it is doubtful that this would have such a large impact on the radiative lifetime. Finally, it has also been reported that surface defects can have an effect on the lifetime (Cheng et al. 2017), which may be the most likely cause of this difference.

F_P and β are lower than predicted, which can be attributed to the differences between the ideal case modelled and a real quantum dot in a micropillar. Firstly, the quality factors of the micropillars studied experimentally are significantly lower than those simulated, which may be attributed to the roughness of the sidewalls. This roughness can be quantified by a single value that benchmarks how cavity loss is affected by scattering, known as the sidewall loss coefficient, previously shown to be approximately κ_s= 50 ± 20 pm in these samples (Androvitsaneas et al. 2023). This effect is particularly strong for micropillars of small diameters. Assuming roughness leaves the mode volume of the micropillar unchanged, one might thus expect a proportional decrease in F_P, based on (2.19). The 1.85 μm micropillars in each sample displayed Q factors of approximately 5000 under white light reflectivity and photoluminescence, as seen in Fig. 7.5, a factor of about 4 below the simulated value, which reduces the maximum F_P to 18. Secondly, as mentioned above, the QDs observed may not be located on the central axis of the pillar, unlike those simulated. In fact, there will typically be several QDs distributed at different positions within the QD growth layer, the brightest of which is chosen for study. Assuming a uniform density of QDs over the cross-sectional area of the pillar, we can estimate a median radial displacement of 0.654 μm. Simulations of 1.85 μm pillars with dipole sources displaced from x = y = 0 indicate that the Purcell factor decreases rapidly with displacement from the centre of the micropillar in a Gaussian-like pattern, such that one might expect the median F_P to be further reduced to 5.8. A slightly larger radial displacement of > 0.7 μm would be sufficient to reduce F_P to the experimentally observed values.

7.4 Conclusions

In the cavity that has been considered here, the local density of states of the non-cavity modes results in $\Gamma_\mathrm{L}/\Gamma_0$ = 0.68-0.98 as the dipole position is varied along z. This implies the common experimental practice of tuning transitions relative to the cavity mode systematically overestimates the Purcell factor, because the system moves from an enhanced decay rate on resonance to suppression of emission at large detuning.

Using a sample with emitters at a node in the cavity mode, it is confirmed experimentally that the non-cavity modes are spectrally broad relative to the limited tuning range accessible, reporting no modification of a transition's emission rate and brightness as a function of energy relative to the cavity mode, in contrast to conventional cavities where the intensity is strongly detuning dependent. This is consistent with simulations, which additionally reveal a reduced fraction of emission in the upward direction at the node.

Future work may focus on the design of cavities with modified mirrors, spacer and diameter that result in a reduced $\Gamma_{\mathrm{L}}/\Gamma_0$ over an increased volume in the cavity, to increase F_{P} and β for a larger number of dots.

This study underlines the importance of a proper understanding of the interplay between cavity and non-cavity modes in experimental determination of the Purcell factor, which has implications for the characterisation of photon sources in all nanostructured systems including nano-lasers, photonic crystals, open cavities, nano-antennae, and integrated photonics.

In the following chapter of this thesis, further simulations are performed in order to understand and model the broadband structure of the non-cavity modes' LDOS.

Chapter 8
Modelling non-cavity modes using a micropillar without Bragg reflectors

Following on from the work in the previous chapter, the non-cavity modes of a micropillar are studied in greater detail, with the goal of identifying their origin and better understanding their dependence on properties like the pillar's diameter and source position. It is shown that these modes arise primarily from the overall pillar profile of the semiconductor stack, rather than from reflections between mirror layers.

This chapter presents a toolset for modelling and studying these often-disregarded decay channels: simulating a pillar of uniform refractive index, lacking any Bragg reflectors, so as to reproduce these modes without any cavity resonances.

8.1 Behaviour of non-cavity modes at the HE_{11} wavelength as a function of pillar diameter

As demonstrated and discussed in the previous work, despite the common assumption that a decay rate detuned from a mode, Γ_L, is comparable to that of an emitter in a homogenous medium, Γ_0, the rate may vary considerably depending on properties such as diameter and the placement of emitters within the subject device.

It is possible to extract the Purcell factor, cavity mode emissions, and non-cavity mode emissions at the HE_{11} resonance wavelength from the total emission spectrum of the micropillar. Specifically, the Purcell factor will be equal to the total emissions normalised by the dipole source power. The proportion of emissions via the cavity mode can then be isolated from this data using a Lorentzian fit (an example of which is shown in Chapter 5). Meanwhile, the proportion of emissions from non-cavity modes at the mode wavelength will be effectively equal to the y-offset determined by the fit. By repeating this for different sizes of pillar, the behaviour of each component as a function of pillar diameter can be determined, as observed in Fig. 5.5 in Chapter 5.

Unlike the HE_{11} cavity mode, where the emission enhancement drops gradually at a decreasing rate with diameter due to the reduced mode volume (and thus, a decreased vacuum field to couple to (Khitrova et al. 2006)), the non-cavity modes peak periodically with diameter, with a period of approximately 0.278 μm (~0.0758 μm in GaAs), suggesting some resonant behaviour with the pillar sidewalls. In a low Q pillar, as studied here, these can have a significant impact on the total Purcell factor, even dominating over the HE_{11} emissions. This is less likely in a high Q pillar, where the cavity mode emissions will be further enhanced. This will also affect the efficiencies β and ξ, which are minimised when emission into the non-cavity modes peaks, due to the reduced relative proportion of emissions via the cavity mode.

It was also shown in the previous chapter that the non-cavity modes are also somewhat dependent on source height, following a sinusoidal pattern similar to the HE_{11} mode, with a larger wavelength than the cavity spacer layer and out-of-phase with its fundamental nodes and anti-nodes.

This method is somewhat flawed however, in that it is entirely analytical and dependent on accurately fitting the cavity mode(s). In the work presented in this chapter, a new simulated device design is used that can approximate the behaviour of a micropillar with the cavity resonance removed, so that further information can be derived about the origin of these modes.

8.2 FDTD model of a uniform micropillar

Further simulations were performed in Lumerical FDTD. Instead of constructing a model of a low Q or high Q micropillar as previously shown in this thesis, it is replaced with a cylindrical pillar of a single frequency-dependent refractive index, of the same height as a low Q pillar, here thereafter referred to as a “uniform” micropillar to distinguish it from a “cavity” micropillar. Like before, this is stood on a GaAs substrate layer, and excited by an electric dipole oriented in the x direction, placed in a position corresponding to the electric anti-node at the centre of a cavity micropillar’s spacer layer. It may be noted that only modes with a non-zero component at the source position will be driven, so some modes will not be seen, in the same way some higher order cavity modes cannot be seen without a cylindrically asymmetric distribution of sources. A box of planar monitors surrounds the uniform pillar, identical to the previous work. It was hypothesised that by eliminating the spacer layer and the Purcell enhancing DBRs, while keeping a refractive index approximating that of the pillar, it would be possible to reproduce the non-cavity modes without the cavity resonances, in a similar way to placing a source at a node, as presented in the previous chapter.

Different ‘averaged’ refractive index models were used in attempting to best simulate the pillar without the influence of the cavity modes. Primarily this involved either using a weighted mean index (accounting for the additional GaAs cavity spacer layer), or an index based on the weighted mean dielectric constant. For the sake of this work, these models disregarded any imaginary parts of the refractive index.

Each one of these was compared with the diameter-dependent spectra of a normal low Q cavity micropillar. While all showed some visible resemblance, it was the “weighted mean index”, which is related to the optical path length along the longitudinal axis of the pillar, that proved best able to reproduce the non-cavity modes. It is thus those results that are presented here.

Accounting for the relative volumes for GaAs and $Al_{0.95}Ga_{0.05}As$ in the structure, the weighted mean refractive index was thus calculated using (8.1), where K_{cav} is the number of wavelengths in the GaAs cavity spacer layer, M_{A} and M_{G} are the number of $Al_{0.95}Ga_{0.05}As$ and GaAs $\lambda/4$ DBRs respectively, n_{A} and n_{G} are the corresponding refractive indices of the two materials, and L_{A} and L_{G} are the thicknesses of the corresponding DBR layers.:

$$n_{\mathrm{mean}}(\lambda) = \frac{M_{\mathrm{A}} n_{\mathrm{A}} L_{\mathrm{A}} + (M_{\mathrm{G}} + 4M_{\mathrm{C}}) n_{\mathrm{G}} L_{\mathrm{G}}}{M_{\mathrm{A}} L_{\mathrm{A}} + (M_{\mathrm{G}} + 4M_{\mathrm{C}}) L_{\mathrm{G}}} \tag{8.1}$$

Given the 7 upper and 26 lower λ/4 mirror pairs of different thickness for each material in a low Q cavity pillar and the λ-thick spacer, there are thus effectively 33 total quarter-wavelength layers of $Al_{0.95}Ga_{0.05}As$, and 37 (with the cavity spacer) of GaAs, such that the weighted mean index can be written:

$$n_{\mathrm{mean}}(\lambda) = \frac{33 n_{\mathrm{A}} L_{\mathrm{A}} + 37 n_{\mathrm{G}} L_{\mathrm{G}}}{33 L_{\mathrm{A}} + 37 L_{\mathrm{G}}} \tag{8.2}$$

As the DBRs are designed to have a thickness equal to a quarter of the design wavelength λ in each index, each can thus be replaced:

$$L = \frac{\lambda}{4n} \tag{8.3}$$

The $\lambda/4$ cancels out on the numerator and denominator, and (8.2) simplifies to:

$$n_{\mathrm{mean}}(\lambda) = \frac{70}{\frac{33}{n_{\mathrm{A}}} + \frac{37}{n_{\mathrm{G}}}} = \frac{70 n_{\mathrm{A}} n_{\mathrm{G}}}{33 n_{\mathrm{G}} + 37 n_{\mathrm{A}}} \tag{8.4}$$

After interpolating the refractive index datasets from Lumerical for each material to the same wavelength scale, this calculation was performed for each data point to produce a mean refractive index dataset with dispersion. This is plotted against wavelength in Fig. 8.1 (a), along with the indices for $Al_{0.95}Ga_{0.05}As$ and GaAs for comparison. (b) shows a sketch of the uniform pillar, substrate and dipole source, with directions indicated:

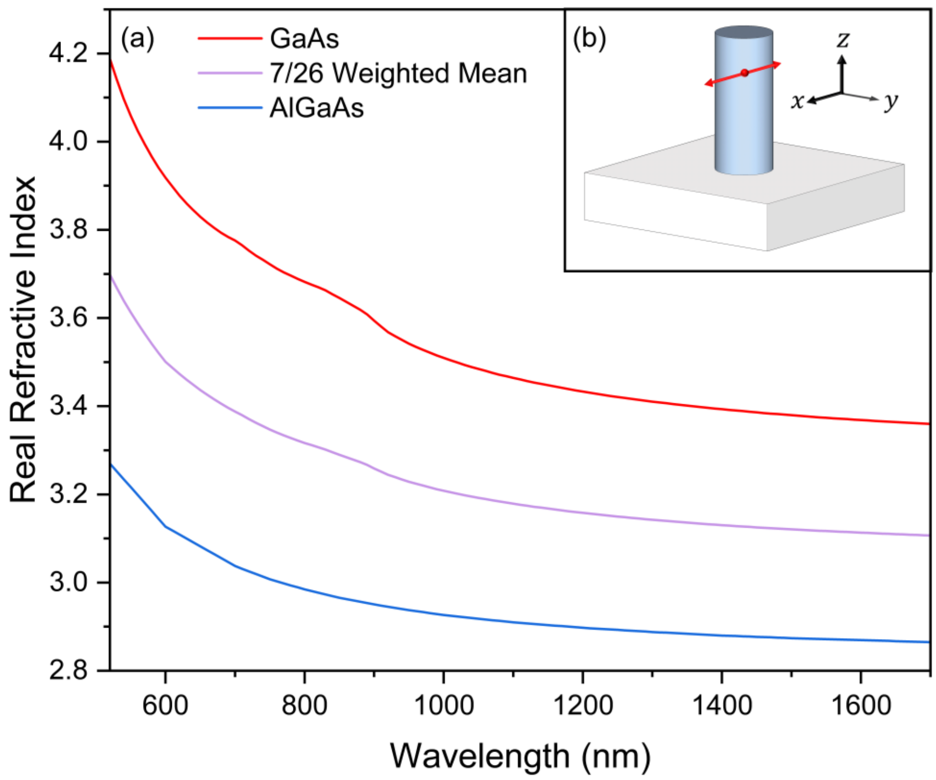

Fig. 8.1 – (a) Dispersion plot showing the refractive indices of GaAs, $Al_{0.95}Ga_{0.05}As$, and the weighted mean of the two as functions of wavelength. (b) Diagram of a uniform micropillar on GaAs substrate consisting of a material emulating the mean of GaAs and $Al_{0.95}Ga_{0.05}As$'s refractive indices, excited by a dipole pulse in the same position as in previously studied pillars.

8.3 Comparison with typical micropillar cavities

With the goal of this work being to reproduce the sum of non-cavity modes observed, each run of simulations was compared against similar results using a normal low Q cavity micropillar, comparing the non-cavity mode background of their emissions to the new spectra.

As was shown in previous work, the non-cavity modes are spectrally broad. For this reason, the spectra were taken over a range of a couple hundred nm (albeit at a lower resolution, due to computing limitations), rather than a small wavelength space near the HE_{11} mode.

Given light may be emitted from the device in different directions, as shown previously in this thesis, the light transmitted through the planar monitors around the pillar was summed in three different ways: the total emission through the top and bottom monitors (in the $\pm z$ directions), through which the cavity mode would primarily emit in a typical device, through side monitors (in the $\pm x$ and $\pm y$ directions), and the total emissions in all directions. These are normalised in each case to the dipole source power, making this final dataset equivalent to the Purcell factor. While these 'directional emissions' are approximate, as wide-angle emissions from the top surface may pass through a side monitor and vice versa, they are a useful tool for breaking down the behaviour of these lesser studied modes.

8.3.1 Diameter dependence

The simplest place to start was by studying how the non-cavity modes evolve as the micropillar diameter increases, an expansion of the results presented in Fig. 5.5, such that a wider spectrum can be studied rather than just the emissions at the HE_{11} wavelength. The modes change rapidly, so the results focus on a range of diameters in the primary band of interest of this project, from 1.75 to 2.25 μm. These results are plotted on colourmaps in Fig. 8.2, where (a, b, c) show results from a low Q cavity pillar, while (d, e, f) show results from a uniform pillar of mean refractive index. The electric dipole source is placed at a position corresponding to the central spacer electric field anti-node in the low Q cavity micropillar, $x = y = z = 0$, in both types of pillar,

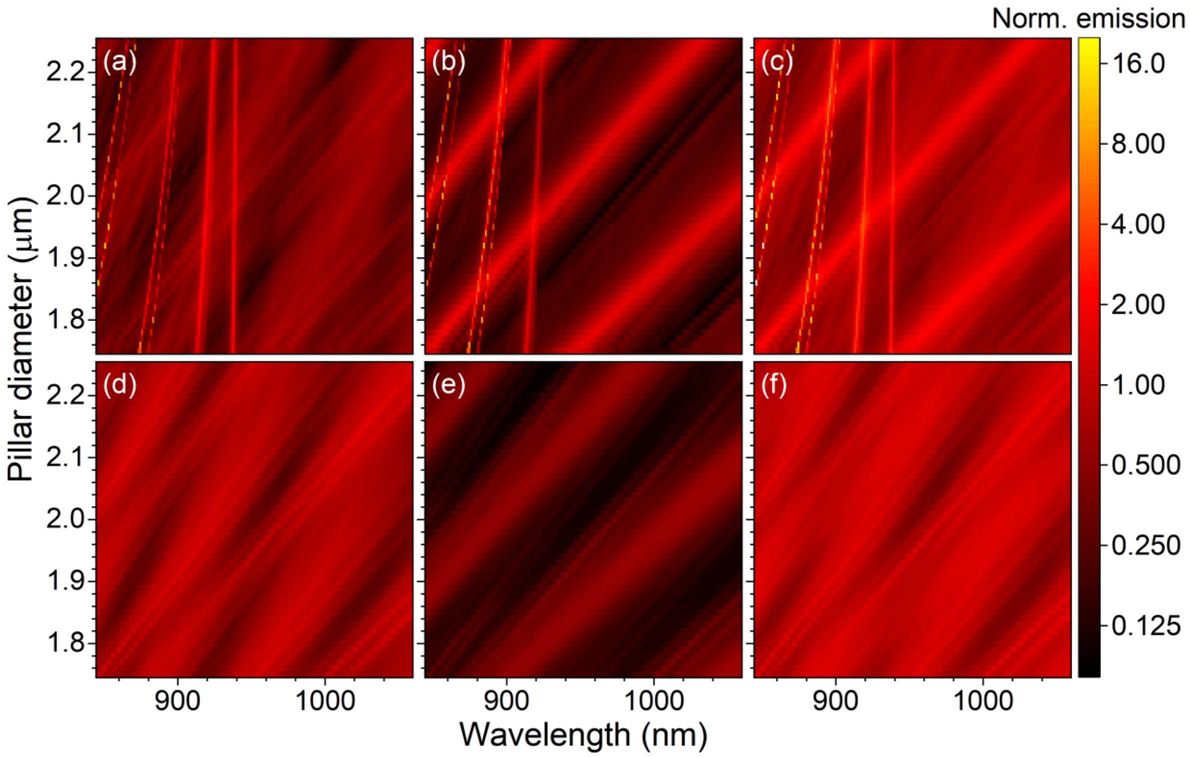

Fig. 8.2 – Colourmap showing the emission intensity in the vertical (a, d) and horizontal (b, e) directions, as well as the total emissions or Purcell factor (c, f) as a function of pillar diameter for both (a, b, c) a low Q cavity micropillar and (d, e, f) a uniform micropillar. All subplots are plotted on a single colour scale.

Disregarding the HE_{11} and higher order modes, visible as steep narrow streaks on the top row of plots from the low Q cavity micropillar, some notable similarities exist between the two simulation models. In particular, the evenly periodic peaks observed previously increase in wavelength rapidly with an increase in diameter, at a rate of ~0.4 nm in wavelength per nm diameter, forming bold diagonal lines. These are most clear in (b) and (e), where they dominate the spectrum, with emissions about an order of magnitude greater than any other features. While reproduced closely by the uniform pillar, with similar gradients, the resonances are spaced further apart, in a different phase. They are spaced ~118.9 nm apart in wavelength, or ~0.291 μm apart in diameter, as opposed to ~120.6 nm and 0.278 μm respectively in (b). These show peak emission rates ~3x higher than those in (e), but also have a Q factor of ~20, as opposed to the ~40 observed in the uniform pillar.

Similar behaviour is visible in the light emitted vertically, where the emission colour map consists primarily of a superposition of two diagonal patterns crossing one another with different gradients. The periodicities of the lines are well-reproduced by the uniform pillar, as are their phases. In contrast to the resonances in (b) and (e), the non-cavity modes are ~50% brighter in (d) as opposed to (a).

All these modes are therefore similarly dependent on the pillar diameter. By contrast, the similarity between the two models suggests the presence, or lack thereof, of DBRs have a minimal impact in combination with this change.

8.3.2 Source height dependence

Next, a similar test to that in the previous chapter was performed, with the dipole source's height z being varied through the thickness of the cavity spacer layer, or where it would have been in the case of the uniform pillar. As before, this is done using pillars of 1.85 μm diameter. These results are presented similarly in Fig. 8.3.

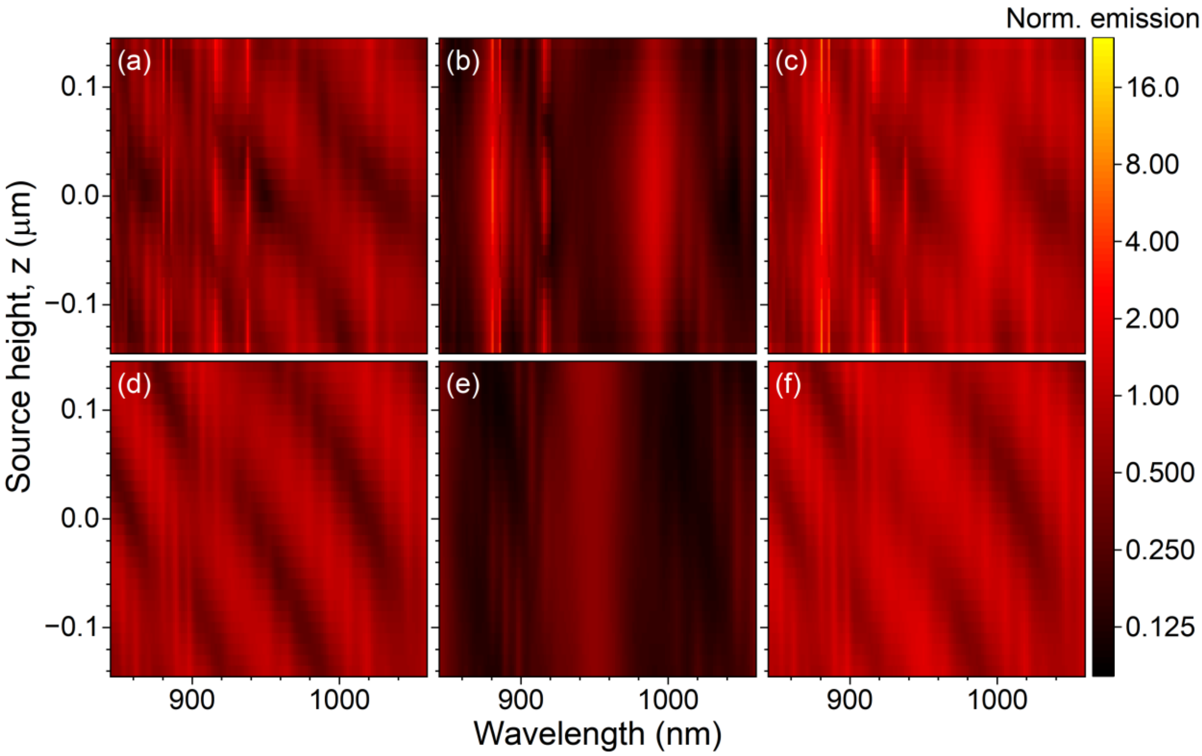

Fig. 8.3 – Colourmap showing the emission intensity in the vertical (a, d) and horizontal (b, e) directions, as well as the total emissions or Purcell factor (c, f) as a function of dipole source height z for both (a, b, c) a low Q cavity micropillar and (d, e, f) a uniform micropillar. Both pillars are 1.85 µm in diameter. All subplots are plotted on a single colour scale.

The uniform pillar again does a fair job at reproducing the non-cavity mode behaviour of the cavity micropillars. The 'vertical-dominant' non-cavity modes decrease in wavelength with z at similar rates in both the cavity (a) and uniform (d) pillars, and show similar periods, though the phase of these patterns differ at this diameter. This may also just be an apparent effect caused by the superposition between numerous non-cavity modes at different phases. Indeed, in both cases, there are discrete bright resonances that pass-through nodes and antinodes as the dipole height is changed with a period greater than that seen for cavity modes, similar to the cavity and non-cavity mode behaviour seen in Chapter 7.

Meanwhile, the ‘side-dominant’ modes that produced the bold diagonal lines observed in the previous section are unaffected by the change in dipole height in both datasets, as may be most clearly seen in (b) and (e), though the plots aren’t identical due to the mode wavelengths again being in a different phase at this pillar size between the two types of pillars.

8.3.3 Effects of changing pillar height with GaAs cap

Finally, the mode volumes of the pillars were modified by adding a layer of GaAs of various thicknesses on top, similar to the work previously shown in this thesis adding SiO_2 microlenses to pillars. This will also modify the relative position of the source, which will be fixed in its usual central position, compared to the full micropillar volume. These results are presented in Fig. 8.4.

The results resemble those in the previous section – something to be expected given the similar changes in source position. Again, the uniform pillar largely reproduces the non-cavity modes of the low Q device, albeit with significant differences in their phases and brightnesses.

The side-dominant modes again are unchanged by the additional layer, with near constant wavelength and brightness regardless of its thickness.

Meanwhile, the non-cavity resonances dominant in (a) and (d) again progress diagonally, although now the wavelength increases as the GaAs layer thickness increases. This is likely due to the effect of the dipole source being further from the top of the pillar, where a reflection at the GaAs/air interface occurs. The apparent Q and gradient of these lines is similar between the two models in these results. Discrete, individual modes moving through nodes and anti-nodes are still visible in both datasets. These modes, as well as the cavity modes in (a, b, c), form curving streaks in this figure, unlike in Fig. 8.3, an effect caused by the compounding of the moving relative source height and the change in the mode volume.

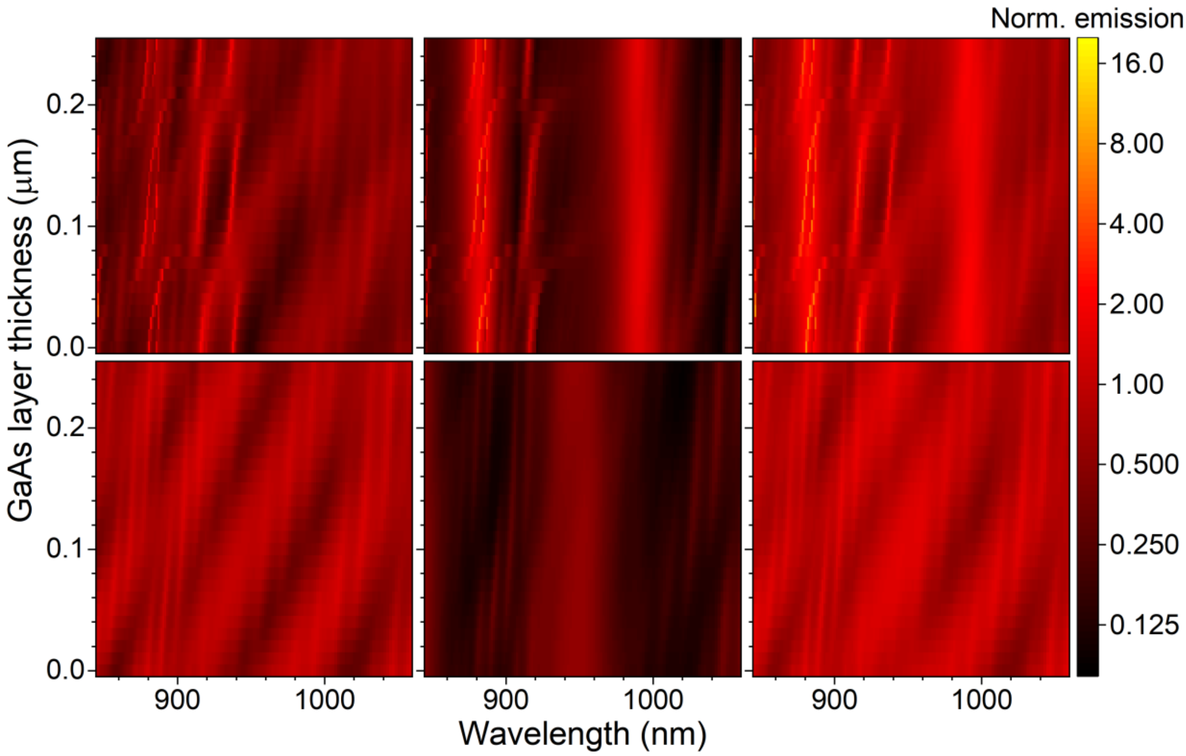

Fig. 8.4 – Colourmap showing the emission intensity in the vertical (a, d) and horizontal (b, e) directions, as well as the total emissions or Purcell factor (c, f) as a function of the GaAs layer thickness for both (a, b, c) a low Q cavity micropillar and (d, e, f) a 1.85 μm uniform micropillar. All subplots are plotted on a single colour scale.

8.3.4 Absolute electric field side profiles

Finally, similar to Fig. 7.1 in the previous chapter, the absolute electric field profile taken as a cross-section through the pillars at the HE_{11} wavelength was recorded, comparing the y = 0 μm (x-z) and x = 0 μm (y-z) planes, parallel and perpendicular to the dipole axis respectively, for a 1.85 μm diameter low Q 'anti-node-excited' cavity micropillar (dipole at z = 0 μm), a 'node-excited' cavity micropillar (dipole at z = -0.067 μm), and the uniform pillar (dipole at z = 0 μm). This was performed with the goal of examining how the spatial distributions of emissions compare. These results are presented in Fig. 8.5.

Similar emission patterns are seen in the two structures. In both cases the non-cavity modes emit strongly through the sides and bottom of the pillar, with more light being emitted in the plane perpendicular to the dipole than that parallel to it. This is in contrast to the cavity-coupled light in (a) and (b), which is emitted primarily in the vertical, upwards direction, towards where an optic would be placed above the sample.

On a more precise level, it can be seen that both the cavity and uniform pillars form similar patterns in- and outside of the pillar. For example, similar ‘zig-zagging’ bright spots can be seen inside the structure, most visible in (d) and (f), in the perpendicular plane. Parallel, both (b) and (e) show the electric field is most intense on the central axis on the pillar, due to the dipole not emitted along its own axis, though a weaker version of the previous pattern is still visible. Even without the presence of DBRs, similar horizontal bands of electric field intensity can be seen emitted out of the sides of the pillar, due to the constructive and destructive interference.

The modes in the uniform pillar may be expected to correspond to the waveguide modes of a cylindrical fibre with different radial quantum numbers, resulting in a concentration of energy near the centre of the pillar where the emitter is placed. The mode electric fields then interfere destructively at further distances from this point. The modulation seen on the central, longitudinal axis of the micropillar results from different values of the effective mode propagation index or phase constant, $\beta_{\mathrm{HE}_{11}}$, causing the interference of the mode to change from constructive near the source, to partially destructive for larger path differences. Meanwhile, the fine interference fringes of the modes arise from total internal reflection at the top boundary of the pillar.

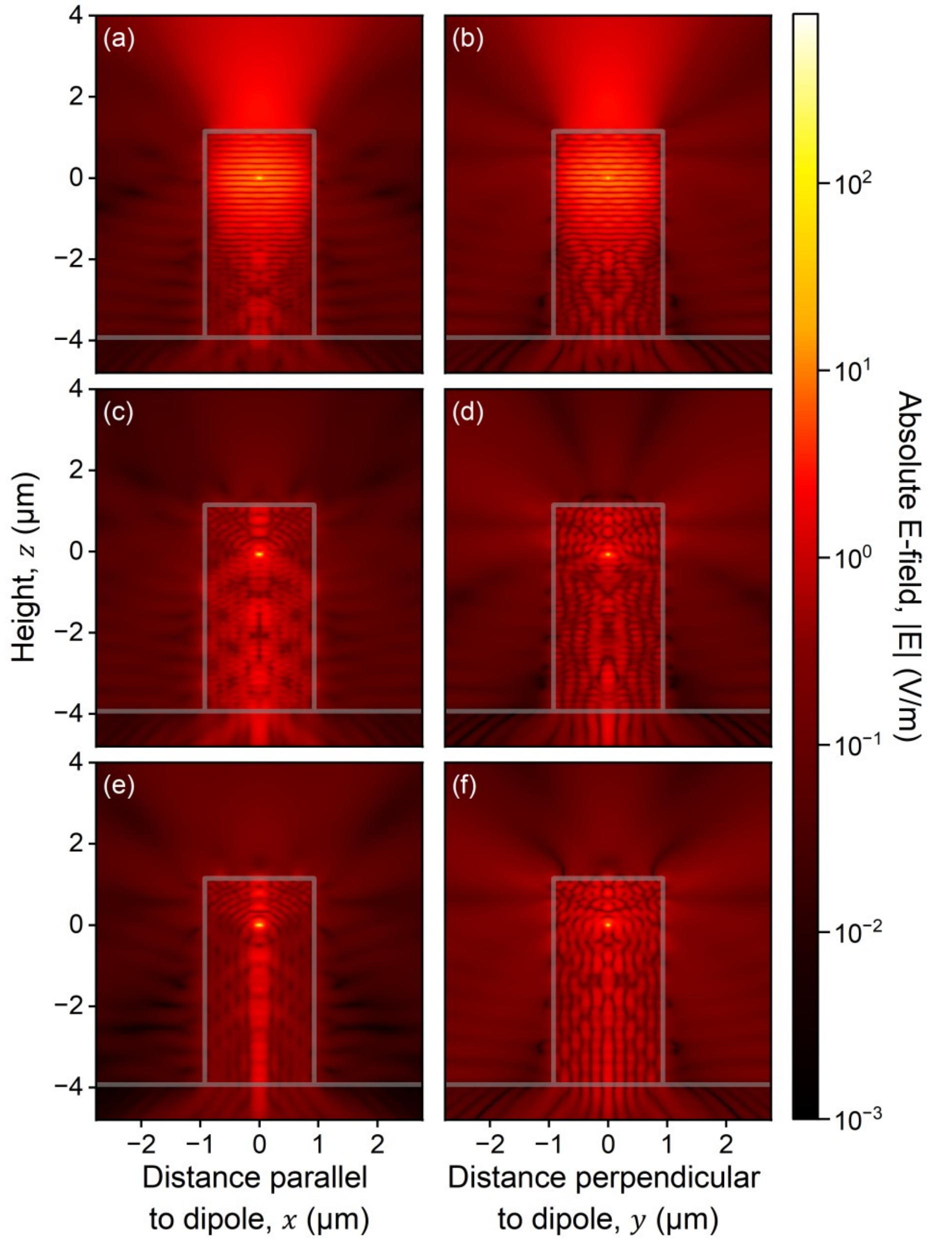

Fig. 8.5 – Absolute electric field $|\vec{E}|$ cross-sectional profiles for 1.85 μm micropillars (grey) at the HE_{11} mode wavelength of 937.827 nm for a low Q cavity micropillar excited by a dipole at the anti-node (z = 0 μm) in the centre of the spacer layer (a) on the y = 0 plane (x-z), parallel to the dipole and (b) on the x = 0 plane (y-z), perpendicular to it. (c, d) and (e, f) as (a, b), but for a low Q cavity micropillar with a dipole at the lower node (z = -0.067 μm) and for a uniform micropillar with a dipole at z = 0 μm respectively.

8.4 Analysis and conclusions

Overall, the model using a uniform micropillar consisting of a material with a refractive index that is the wavelength-dependent mean of GaAs and $Al_{0.95}Ga_{0.05}As$'s indices, weighted by the wavelength-volume of each material, provides a good approximation of the non-cavity modes of a low Q cavity micropillar of the same height and diameter. Major features of the non-cavity mode spectrum are reproduced, including the periodic bright broad bands observed in previous simulations. These, and other features, also show similar dependencies on wavelength, source position, and mode volume regardless of the model used. The spatial emission pattern is also similar, producing cross-sectional electric field profiles as shown in Chapter 7.

The similar behaviour across both the uniform and cavity pillars supports the idea that the non-cavity modes are similar to the waveguide modes in a cylindrical fibre, resulting in similar features, such as the concentration in the centre of the pillar where the emitter is placed in Fig. 8.5.

While the model is largely successful in reproducing similar non-cavity mode features to those seen in an ordinary cavity pillar, there are a few remaining differences. For example, the diameter-dependent phases of periodic features may not match up, most obvious in cases like Fig. 8.3, where only a single pillar size is examined. Meanwhile, while features are reproduced between the two structures, the brightness of these features can differ, though this can be largely attributed to the fact that there are alternative emission channels available in the cavity micropillar, whereas the dipole can only emit into the non-cavity modes in the uniform pillar. Separating the light emitted based on its spatial direction keeps these features visible and allows them to be validated, even as dimmer features may be overwhelmed when they are combined in the total emission / Purcell factor spectrum, which shows a similar average intensity in both models.

It could also be that some differences in brightness are attributable to the presence, or lack thereof, of the cavity spacer layer and $\lambda/4$ DBR layers having an impact on the non-cavity modes' LDOS, and the directional emission of light in the pillar. For example, the addition of layers may cause light that is totally internally reflected to be directed towards the pillar sides, rather than vertically, resulting in the emissions in that direction being stronger with the cavity structures than without. While Fig. 8.5, provides evidence against this, with light being emitted very similarly in a normal cavity micropillar where cavity emission is suppressed and in a uniform micropillar, it should be remembered that it only provides a snapshot of emissions at a single wavelength, and may not resemble the emission patterns at other points in the non-cavity mode spectrum.

One might also suspect that changes to the dipole source's height, which in this work was kept identical across the two pillars, could play a part in the relative phases and brightness differences of the modes observed, if it is located differently in the total mode volume of the uniform pillar structure. Sections 8.3.2 and 8.3.3 appear to partially debunk this, however, as the brightest non-cavity mode peaks in (b) and (e) appear to be unaffected. However, some other features do undergo changes in phase as the source height changes.

In conclusion, while some questions remain, the fact that the non-cavity mode features are reproduced by the uniform pillar model strongly hints at them originating from the pillar profile shared between the structures, rather than the presence of DBRs. Many of these modes are highly dependent on the diameter of the micropillar, changing at a rate far exceeding that seen in cavity modes within the chosen wavelength range, with the confinement provided by the etched cylinder seemingly being strongly connected. This suggests they might correspond to a high radial quantum number. The brightest of these modes, peaks seen in previous work which are here shown to be emitted primarily through the sidewalls of the pillar (b, e), also seem to be unaffected by the vertical placement z of the dipole source, unlike some of the discrete modes forming the non-cavity background, with intensities about an order of magnitude lower.

Given the similarity of its results, modelling non-cavity modes using a uniform pillar offers multiple advantages for use in future studies. Firstly, it can be utilised to predict optimal designs of a pillar microcavity based on the periodicity of non-cavity modes in wavelength and diameter, offering particular advantages for low Q micropillars where these modes have a greater influence on the total emissions of the device and its efficiencies. FDTD simulations can also be run within a much shorter computing time compared to a cavity micropillar, for which the resources required will increase with the Q factor of the design. It may even be possible to increase this advantage, with the model being potentially suitable for calculating an analytical solution for the non-cavity mode spectrum using an eigenmode solver, with the potential to offer further insights into the nature of these modes.

Future work may seek to improve the phase-matching of periodic features using an improved refractive index model, possibly utilising some method of integrating the energy density of emitted light over the different volumes of GaAs and $Al_{0.95}Ga_{0.05}As$, rather than weighting based on the physical cavity mode-volume of each layer. Further studies could also examine the dependence of modes on other changes. For example, as noted earlier, this work only concerns itself with modes that may be excited by a centralised dipole source, as has been largely kept constant throughout this thesis, with a few exceptions. However, this discards any modes with zero field components at the source position. This has previously been seen for higher order cavity modes like HE_{31} or EH_{01}, and is likely to apply to other modes too.

Chapter 9
Concluding Remarks

This thesis examined the use of self-assembled InAs quantum dots embedded in $GaAs/Al_{0.95}Ga_{0.05}As$ semiconductor pillar microcavities, a promising platform for the efficient generation of indistinguishable single photons for use in quantum applications including quantum computing. By embedding the emitter in a cavity, the spontaneous emission rate of the QDs are enhanced via the Purcell effect and the direction coupling of emissions into a collection fibre is improved.

Two designs of micropillar, configured for a low- or high-quality factor, were studied both computationally, using finite-difference time-domain methods, and experimentally. The high-aspect ratio pillars used in lab work were produced using a novel direct-write lithography-based fabrication process capable of deep sidewall etches as determined using photoluminescence and reflectivity based spectroscopic characterisation, with a fitted sidewall roughness coefficient of ~50 pm, competitive with previous results. Further simulations also suggested that a SiO_2 microlens layer could be used to tune the outgoing emission's numerical aperture and mode field diameter to improve mode-matching with an output single-mode fibre, though the shape of the lens would require careful optimisation and control to be beneficial.

The two-level single photon source properties were confirmed by observing Rabi oscillations in power dependence data, low $\tau = 0$ second-order correlation counts, and high Hong-Ou-Mandel interference visibilities, even when using devices of a low quality factor. Also observed were the dependence of photoluminescence spectra, lifetimes, and single photon purity on power, demonstrating and discussing common effects such as charge noise and power broadening.

By exciting a pillar with emitters at different heights within the cavity electric field, with placement at an electric field node completely suppressing the HE_{11} mode, a theoretically predicted broad background spectrum of ‘leaky’ non-cavity modes was confirmed, with negligible modification of a transitions emission rate over photon energies accessible by turning a transition using the Zeeman effect. By magnetically detuning single transitions, device Purcell factors were extracted by comparing pulse excitation lifetimes. Simulations also found that $\Gamma_{\mathrm{L}}/\Gamma_0$ varies between 0.68 and 0.98 as the dipole height is varied along z, which had to be accounted for when experimentally determining the Purcell factor.

Simulating a pillar of a uniform refractive index averaging those of GaAs and $Al_{0.95}Ga_{0.05}As$, without distributed Bragg reflectors, allowed the non-cavity mode spectrum to be modelled, reproducing it and offering new insights into the pillar shape’s influence on its optical properties, which can inform the design of more efficient cavity devices. These non-cavity modes originate predominantly from the etched pillar profile, rather than from DBRs and are heavily dependent on the diameter of the micropillar, suggesting they correspond to a high radial quantum number. Modes in the spectrum show some differing behaviour, including a dependence, or lack thereof, on the vertical placement of the dipole source as observed in previous studies.

9.1 Impact of this work

Overall, the research presented in this thesis takes key steps to push the optimisation of quantum dot micropillar systems in two main aspects. First is the result showing that fabrication processes like ours utilising direct-write lithography for patterning, as opposed to the more common electron-beam lithography, can offer state-of-the-art level smooth etching of the deep sidewalls of micropillars and similar semiconductor devices reducing the impact of scattering on the Q factor – the dominant source of such losses in small pillars. The resulting devices, even with low Q designs, are shown to be capable of producing single photons with near-unity indistinguishability and purity. Meanwhile, this process is fast and inexpensive, with the use of a digital modulator instead of a physical mask accelerating the design iteration process and offering faster development and testing of new cavity designs to increase efficiency. Such designs could include modifications such as the SiO_2 lenses concept studied in the same chapter, although more computational optimisation would be required first. The addition of an oxide ALD also serves to simplify the storage, allowing samples to be stored in ambient conditions for months at a time without degradation of Q or quantum properties. Finally, given that finding micropillars containing bright on-resonance transitions is a key challenge is research like that performed here, the demonstration that even low Q devices are capable of producing indistinguishable single photons opens up the possibility of increasing the yield of usable micropillars in a sample in future experiments, courtesy of a wider cavity mode peak, albeit with reduced Purcell enhancement.

The research presented in Chapter 7 and Chapter 8 is one of the few examples of such to take a closer look at the behaviour of non-cavity modes in micropillars. Notably, by showing that decay via the non-cavity modes may vary significantly from that in a homogenous medium, taking values anywhere between 0.35 and 2.21 times this rate in the range studied, peaking periodically as a function of diameter every 0.28 μm. Given that Purcell factor characterisation often uses this decay rate as a baseline for determining the enhancement at a cavity mode, this result makes it clear that researchers may often be systematically overestimating or underestimating the value of F_{P} for their devices. The inconsistency of this methodology risks hampering the development of brighter and more efficient single photon sources. On the other hand, these results also offer another method by which the photon source behaviour may be optimised, with some manipulation of the mode coupling efficiency and Purcell factor of the device being capable simply by choosing a design wavelength corresponding to an optimal value of Γ_{L}. These studies thus demonstate the importance of properly understanding how cavity and non-cavity modes interact and can impact the characterisation of photon sources in all nanostructured systems.

The chapters also offer new frameworks allowing for further study of these modes, whether by positioning emitters at a node in the cavity electric field to fully supress cavity-coupled emissions, which can also be compared with normal cavity micropillars to estimate their Purcell factors, or by eliminating a cavity all together and instead modelling the isolated non-cavity mode behaviour using a pillar of uniform refractive index. FDTD simulations using the latter also require much less in the way of the computational resources, simplifying theoretical study, and possibly even being suitable for calculating an analytical solution for the non-cavity mode spectrum using an eigenmode solver, which could offer further understanding of the nature these modes beyond the insights already obtained in this work.

9.2 Suggestions for future work

Purcell-enhanced quantum dots in micropillars are a well-researched system for generating indistinguishable single photons with a lot of promise for producing the flying qubits required for quantum applications, though work continues on maximising the internal and outcoupling efficiencies of these devices without sacrificing the quantum properties of the output light. The following are three potential directions for further research, building on the results obtained in this thesis.

9.2.1 Deterministic placement of quantum dots in micropillar cavities

Given the strong dependence of coupling strength on quantum dot placement, future work could focus on improving the alignment of positions of the quantum dots and micropillars to increase the yield of bright, active devices. This could be achieved either by mapping the locations of QDs prior to processing and etching pillars around them, possibly using a maskless method like direct-write lithography (Dousse et al. 2008), or by deliberately positioning arrays of QDs to match the design pattern, as has been recently demonstrated by Große et al. (2020). This could potentially allow a yield of usable devices approaching 100%, offering accelerated development and deployment.

This could also allow one to procedurally design pillars on a dot-by-dot basis to maximise the coupling strength, such as by etching to a diameter such that the cavity mode is perfectly resonant with a quantum dot transition, using the well-known relationship between micropillar diameter and mode cavity energies given in (2.5) (Heuser et al. 2018; Androvitsaneas et al. 2023). Such precise control of quantum dot/micropillar positioning and fabrication could also open the door to optimising microlens top structures for improved output fibre coupling (Jordan et al. 2024b), as briefly discussed in Chapter 5.

9.2.2 Designs optimising non-cavity modes in micropillars

Another open research possibility following the work in this thesis is to continue studying the behaviour of non-cavity modes with the goal of minimising their influence and maximising the SE coupling efficiency, and mode outcoupling efficiency, optimising the coupling of light from the quantum dot micropillar system into a single mode fibre. Chapter 5, Chapter 7 and Chapter 8 show that these modes are strongly dependent on properties such as the pillar diameter and source position, meaning these could be manipulated to minimise the non-cavitry mode emission rate, which in Fig. 5.5 is seen to vary between as low as 0.35 and as high as 2.21 times the emission rate in a homogenous medium, peaking periodically as a function of diameter every 0.28 μm within the range studied. Each minimum corresponds in the emission rate corresponds to a peak in the coupling efficiencies of the micropillar. Future work may thus focus on the design of cavities with modified mirror and spacer thickness and diameters which result in a reduced Γ_L/Γ_0 over an increased volume in the cavity, to increase coupling strength for greater numbers of dots.

This could potentially be combined with some of the suggested fabrication procedures suggested in the previous section. For example, while the grown quantum dot density could potentially be reduced in cases where they can be definitely placed in the centres of etched micropillars (by control of either the dot placement or the pillar placement), it may be necessary to maintain a density high enough to allow a choice between QDs resonant with pillar diameters corresponding to minimised non-cavity mode emission rates.

9.2.3 Efficient frequency conversion of near-infrared single photons

While this thesis has demonstrated the ability to generate near-infrared indistinguishable single photons using quantum dot micropillars, this emission band is not optimal for usage in quantum applications, which generally favour telecom frequencies (anywhere from 179 to 238 THz, commonly C-band, ~193 THZ (Paschotta 2008)) so as to take advantage of pre-existing developments of modern optical networking and communication for long-distance operations (Yu et al. 2023), such as providing the flying qubits required of quantum computing (DiVincenzo 2000). Purcell-enhanced quantum dots (Reitzenstein and Forchel 2010), tend in general to emit in the near-infrared range (Wang et al. 2019b; Tomm et al. 2021; Androvitsaneas et al. 2023), as in this thesis, although there has been progress in producing telecom band quantum dots in recent years (Olbrich et al. 2017; Zeuner et al. 2021; Wells et al. 2023). Between this and the long term goal of constructing a quantum internet (Walmsley and Nunn 2016), which would have to coherently convert between a wide range of different frequency components, it is desirable to develop efficient methods of photonic frequency conversion that preserves quantum properties capable of transduction of frequency differences over at least 125 THz – far beyond what's feasible using the Zeeman effect and Stark shifts.

This may be achieved through the development of quantum frequency conversion (QFC) methods, which allow the frequency of a quantum light field to be altered while preserving its non-Gaussian correlation statistics (Huang and Kumar 1992; Baune et al. 2014). This may itself be divided into 'upconversion', in which input light can be combined with a seed laser to produce a third optical field at a frequency equal to the sum of frequencies of the two via sum-frequency generation (SFG), thus reciprocally reducing the wavelength (Boyd and Kleinman 1968), and 'downconversion', similarly achieved with difference-frequency generation (DFG) in which the output wave similarly corresponds to the difference of the input frequencies (Inaba and Hidaka 1969; Suhara et al. 2003a; Zaske et al. 2012):

$$f_{\mathrm{in}} + f_{\mathrm{seed}} = f_{\mathrm{up}} \tag{9.1}$$

$$f_{\mathrm{in}} - f_{\mathrm{seed}} = f_{\mathrm{down}} \tag{9.2}$$

One possible approach for future study is using periodically poled Lithium Niobate (PPLN) waveguides, second-harmonic generation (SHG) devices which exploit quasi-phase-matched (QPM) second order nonlinear interactions (Suhara et al. 2003b). These are one of the most popular implementations of both SFG and DFG, offering spectral shifts in the hundreds of nm at efficiencies conistently greater than >70% while preserving pre-conversion indistinguishabilities and single photon purities (Rakher et al. 2010; Ikuta et al. 2011; Zaske et al. 2012; Kuo et al. 2013; Dréau et al. 2018; Xie et al. 2019; Morrison et al. 2021).

An alternative approach is Bragg-scattering four-wave mixing, a third-order process, via microrings (Sohler et al. 2009; Singh et al. 2019; Liu et al. 2021) or photonic crystal fibres (McKinstrie et al. 2005; McGuinness et al. 2010; Murphy et al. 2024). This approach is typically utilised for conversions on small scales of up to 20 nm, but shows potential for being extended to the hundreds of nm conversions required for quantum dot to telecom fibre interfacing. Four-wave mixing has seen steady improvements, now offering up to 80% potential internal conversion efficiency (Singh et al. 2019; Murphy et al. 2024). This is the approach, utlising photonic crystal fibres, our research group has begun researching, in collaboration with the University of Bath.

Bibliography

Abbas, A. et al. 2023. Quantum optimization: Potential, challenges, and the path forward. *arXiv preprint arXiv:2312.02279*,

Abramczyk, H. 2005. *Introduction to laser spectroscopy*. Elsevier.

Acernese, F. et al. 2019. Increasing the astrophysical reach of the advanced virgo detector via the application of squeezed vacuum states of light. *Physical Review Letters* 123(23), p. 231108.

Aharonov, D. and Ben-Or, M. eds. 1997. *Fault-tolerant quantum computation with constant error*. *Proceedings of the twenty-ninth annual ACM symposium on Theory of computing.*

Akimoto, O. and Hasegawa, H. 1967. Interband optical transitions in extremely anisotropic semiconductors. II. Coexistence of exciton and the Landau levels. *Journal of the Physical Society of Japan* 22(1), pp. 181-191.

Al-Jashaam, F. L. M. 2020. *The development of micropillars and two-dimensional nanocavities that incorporate an organic semiconductor thin film.* University of Sheffield.

Alivisatos, A. P. 1996a. Perspectives on the physical chemistry of semiconductor nanocrystals. *The Journal of Physical Chemistry* 100(31), pp. 13226-13239.

Alivisatos, A. P. 1996b. Semiconductor clusters, nanocrystals, and quantum dots. *Science* 271(5251), pp. 933-937.

Allen, L. and Eberly, J. H. 1987. *Optical resonance and two-level atoms*. Courier Corporation.

Aminian, A. and Rahmat-Samii, Y. 2006. Spectral FDTD: A novel technique for the analysis of oblique incident plane wave on periodic structures. *IEEE Transactions on antennas and propagation* 54(6), pp. 1818-1825.

Anderson, P. W. 1987. The resonating valence bond state in La2CuO4 and superconductivity. *Science* 235(4793), pp. 1196-1198.

Androvitsaneas, P. et al. 2023. Direct-write projection lithography of quantum dot micropillar single photon sources. *Applied Physics Letters* 123(9), p. 094001.

Androvitsaneas, P. et al. 2019. Efficient quantum photonic phase shift in a low Q-factor regime. *ACS Photonics* 6(2), pp. 429-435.

Androvitsaneas, P. et al. 2016. Charged quantum dot micropillar system for deterministic light-matter interactions. *Physical Review B* 93(24), p. 241409.

ANSYS. 2019a. *Adjusting the projection distance in far field projections*. Available at: https://optics.ansys.com/hc/en-us/articles/360034914833-Adjusting-the-projection-distance-in-far-field-projections [Accessed: 31 Aug 2024].

ANSYS. 2019b. *Finite Difference Time Domain (FDTD) solver introduction*. Available at: https://optics.ansys.com/hc/en-us/articles/360034914633-Finite-Difference-Time-Domain-FDTD-solver-introduction [Accessed: 4 Feb 2024].

ANSYS. 2019c. *Integrating power in far field projections*. Available at: https://optics.ansys.com/hc/en-us/articles/360034914813-Integrating-power-in-far-field-projections [Accessed: 31 Aug 2024].

ANSYS. 2019d. *Material Database in FDTD and MODE*. Available at: https://optics.ansys.com/hc/en-us/articles/360034394614-Material-Database-in-FDTD-and-MODE [Accessed: 11 Feb 2024].

ANSYS. 2019e. *PML boundary conditions in FDTD and MODE*. Available at: https://optics.ansys.com/hc/en-us/articles/360034382674-PML-boundary-conditions-in-FDTD-and-MODE [Accessed: 10 Feb 2024].

ANSYS. 2019f. *Soft sources*. Available at: https://optics.ansys.com/hc/en-us/articles/4412892727955-Soft-sources [Accessed: 11 Feb 2024].

ANSYS. 2019g. *Symmetric and anti-symmetric BCs in FDTD and MODE* Available at: https://optics.ansys.com/hc/en-us/articles/360034382694-Symmetric-and-anti-symmetric-BCs-in-FDTD-and-MODE [Accessed: 10 Feb 2024].

ANSYS. 2019h. *transmission - Script command*. Available at: https://optics.ansys.com/hc/en-us/articles/360034405354-transmission-Script-command [Accessed: 31 Aug 2024].

Appel, M. H. et al. 2022. Entangling a hole spin with a time-bin photon: a waveguide approach for quantum dot sources of multiphoton entanglement. *Physical Review Letters* 128(23), p. 233602.

Arakawa, Y. and Holmes, M. J. 2020. Progress in quantum-dot single photon sources for quantum information technologies: A broad spectrum overview. *Applied Physics Reviews* 7(2),

Arthur, J. R. 2002. Molecular beam epitaxy. *Surface science* 500(1-3), pp. 189-217.

Artiglia, M. et al. 1989. Mode field diameter measurements in single-mode optical fibers. *Journal of Lightwave Technology* 7(8), pp. 1139-1152.

Asano, T. et al. 2006. Analysis of the experimental Q factors (~ 1 million) of photonic crystal nanocavities. *Optics express* 14(5), pp. 1996-2002.

Ashoori, R. 1996. Electrons in artificial atoms. *Nature* 379(6564), pp. 413-419.

Aslam, N. et al. 2023. Quantum sensors for biomedical applications. *Nature Reviews Physics* 5(3), pp. 157-169.

Bachor, H.-A. and Ralph, T. C. 2019. *A guide to experiments in quantum optics*. John Wiley & Sons.

Banin, U. et al. 1999. Identification of atomic-like electronic states in indium arsenide nanocrystal quantum dots. *Nature* 400(6744), pp. 542-544.

Barnes, W. et al. 2002. Solid-state single photon sources: light collection strategies. *The European Physical Journal D-Atomic, Molecular, Optical and Plasma Physics* 18, pp. 197-210.

Barth, M. et al. 1992. A near and far-field projection algorithm for finite-difference time-domain codes. *Journal of Electromagnetic Waves and Applications* 6(1-4), pp. 5-18.

Baune, C. et al. 2014. Quantum non-Gaussianity of frequency up-converted single photons. *Optics express* 22(19), pp. 22808-22816.

Bennett, A. et al. 2016a. A semiconductor photon-sorter. *Nature Nanotechnology* 11(10), p. 857. doi: 10.1038/nnano.2016.113

Bennett, A. J. et al. 2016b. Cavity-enhanced coherent light scattering from a quantum dot. *Science Advances* 2(4), p. e1501256. doi: 10.1126/sciadv.1501256

Bennett, C. H. and Brassard, G. 1984. Proceedings of the IEEE International Conference on Computers, Systems and Signal Processing. IEEE New York.

Bera, D. et al. 2010. Quantum dots and their multimodal applications: a review. *Materials* 3(4), pp. 2260-2345.

Berenger, J.-P. 1994. A perfectly matched layer for the absorption of electromagnetic waves. *Journal of computational physics* 114(2), pp. 185-200.

Berkovits, R. 1995. Broadening of quantum-dot energy levels due to short-range elastic scatterers. *Physical Review B* 51(7), p. 4653.

Berman, P. R. and Malinovsky, V. S. 2011. *Principles of laser spectroscopy and quantum optics*. Princeton University Press.

Besombes, L. et al. 2004. Polarization-dependent Rabi oscillations in single InGaAs quantum dots. *Semiconductor science and technology* 19(4), p. S148.

Björk, G. et al. 1993. Spontaneous-emission coupling factor and mode characteristics of planar dielectric microcavity lasers. *Physical Review A* 47(5), p. 4451.

Booker, K. et al. 2020. Deep, vertical etching for GaAs using inductively coupled plasma/reactive ion etching. *Journal of Vacuum Science & Technology B* 38(1),

Born, M. and Wolf, E. 2013. *Principles of optics: electromagnetic theory of propagation, interference and diffraction of light*. Elsevier.

Bouarissa, N. and Boucenna, M. 2008. Band parameters for AlAs, InAs and their ternary mixed crystals. *Physica Scripta* 79(1), p. 015701.

Boyd, G. and Kleinman, D. 1968. Parametric interaction of focused Gaussian light beams. *Journal of Applied Physics* 39(8), pp. 3597-3639.

Brańczyk, A. M. 2017. Hong-ou-mandel interference. *arXiv preprint arXiv:1711.00080*,

Braunstein, S. L. and Van Loock, P. 2005. Quantum information with continuous variables. *Reviews of Modern Physics* 77(2), pp. 513-577.

Bravyi, S. et al. 2024. High-threshold and low-overhead fault-tolerant quantum memory. *Nature* 627(8005), pp. 778-782.

Brench, C. E. and Ramahi, O. M. eds. 1998. *Source selection criteria for FDTD models*. *1998 IEEE EMC Symposium. International Symposium on Electromagnetic Compatibility. Symposium Record (Cat. No. 98CH36253).* IEEE.

Brod, D. J. et al. 2019. Photonic implementation of boson sampling: a review. *Advanced Photonics* 1(3), pp. 034001-034001.

Brooks, M. 2023. Quantum computers: what are they good for? *Nature* 617(7962), pp. S1-S3.

Brown, K. L. et al. 2010. Using quantum computers for quantum simulation. *Entropy* 12(11), pp. 2268-2307.

Brown, R. H. and Twiss, R. Q. 1956. Correlation between photons in two coherent beams of light. *Nature* 177(4497), pp. 27-29.

Brus, L. 1986. Electronic wave functions in semiconductor clusters: experiment and theory. *The Journal of Physical Chemistry* 90(12), pp. 2555-2560.

Bruzewicz, C. D. et al. 2019. Trapped-ion quantum computing: Progress and challenges. *Applied Physics Reviews* 6(2), Brylinski, J.-L. and Brylinski, R. 2002. Universal quantum gates.*Mathematics of quantum computation*. Chapman and Hall/CRC, pp. 117-134.

Buchanan, W. J. 1996. *Analysis of electromagnetic wave propogation using 3D finite-difference time-domain methods with parallel processing.*

Buechler, D. N. et al. 1995. Modeling sources in the FDTD formulation and their use in quantifying source and boundary condition errors. *IEEE Transactions on Microwave Theory and Techniques* 43(4), pp. 810-814.

Busch, P. 2002. The time-energy uncertainty relation.*Time in quantum mechanics*. Springer, pp. 69-98.

Bylander, J. et al. 2003. Interference and correlation of two independent photons. *The European Physical Journal D-Atomic, Molecular, Optical and Plasma Physics* 22, pp. 295-301.

Cabello, A. 2000. Quantum key distribution without alternative measurements. *Physical Review A* 61(5), p. 052312.

Cangellaris, A. et al. 1993. A hybrid spectral/FDTD method for the electromagnetic analysis of guided waves in periodic structures. *IEEE microwave and guided wave letters* 3(10), pp. 375-377.

Celuch-Marcysiak, M. and Gwarek, W. K. 1995. Spatially looped algorithms for time-domain analysis of periodic structures. *IEEE Transactions on Microwave Theory and Techniques* 43(4), pp. 860-865.

Chan, C. T. et al. 1995. Order-N spectral method for electromagnetic waves. *Physical Review B* 51(23), p. 16635.

Chason, E. et al. 1997. Ion beams in silicon processing and characterization. *Journal of Applied Physics* 81(10), pp. 6513-6561.

Chauvin, N. et al. 2009. Controlling the charge environment of single quantum dots in a photonic-crystal cavity. *Physical Review B—Condensed Matter and Materials Physics* 80(24), p. 241306.

Cheng, C. et al. 2017. Photoluminescence lifetime and absorption spectrum of PbS nanocrystal quantum dots. *Journal of Luminescence* 188, pp. 252-257.

Chew, W. C. and Weedon, W. H. 1994. A 3D perfectly matched medium from modified Maxwell's equations with stretched coordinates. *Microwave and optical technology letters* 7(13), pp. 599-604.

Chipman, R. et al. 2018. *Polarized light and optical systems*. CRC press.

Claudon, J. et al. 2010. A highly efficient single-photon source based on a quantum dot in a photonic nanowire. *Nature Photonics* 4(3), pp. 174-177.

Cohen-Tannoudji, C. et al. 1992. Atom-Photon Interactions: Basic Processes and Applications John Wiley and Sons. *New York*,

Collett, E. 2003. *Polarized light in fiber optics*. SPIE Press.

Colocci, M. et al. 1999. Controlled tuning of the radiative lifetime in InAs self-assembled quantum dots through vertical ordering. *Applied Physics Letters* 74(4), pp. 564-566.

Connor, F. R. 1972. *Wave transmission*. London: Edward Arnold.

Costen, F. et al. 2009. Comparison of FDTD hard source with FDTD soft source and accuracy assessment in Debye media. *IEEE Transactions on antennas and propagation* 57(7), pp. 2014-2022.

Cozzolino, D. et al. 2019. High-Dimensional Quantum Communication: Benefits, Progress, and Future Challenges. *Advanced Quantum Technologies* 2(12), p. 1900038.

Crawford, S. E. et al. 2021. Quantum sensing for energy applications: Review and perspective. *Advanced Quantum Technologies* 4(8), p. 2100049.

Curto, A. G. et al. 2010. Unidirectional emission of a quantum dot coupled to a nanoantenna. *Science* 329(5994), pp. 930-933.

de-Leon, S. B.-T. and Laikhtman, B. 2002. The spin structure of quasi–two-dimensional biexcitons in quantum wells. *Europhysics Letters* 59(5), p. 728.

De Broglie, L. 1924. *Recherches sur la théorie des quanta.* Migration-université en cours d'affectation.

de Mello Donegá, C. et al. 2006. Size-and temperature-dependence of exciton lifetimes in CdSe quantum dots. *Physical Review B—Condensed Matter and Materials Physics* 74(8), p. 085320.

Degen, C. L. et al. 2017. Quantum sensing. *Reviews of Modern Physics* 89(3), p. 035002.

Delbecq, M. et al. 2014. Full control of quadruple quantum dot circuit charge states in the single electron regime. *Applied Physics Letters* 104(18), p. 183111.

Denning, E. V. et al. 2019. Phonon effects in quantum dot single-photon sources. *Optical Materials Express* 10(1), pp. 222-239.

Dieleman, C. D. et al. 2020. Universal direct patterning of colloidal quantum dots by (extreme) ultraviolet and electron beam lithography. *Nanoscale* 12(20), pp. 11306-11316.

Ding, X. et al. 2016. On-demand single photons with high extraction efficiency and near-unity indistinguishability from a resonantly driven quantum dot in a micropillar. *Physical Review Letters* 116(2), p. 020401. doi: 10.1103/PhysRevLett.116.020401

DiVincenzo, D. P. 2000. The physical implementation of quantum computation. *Fortschritte der Physik: Progress of Physics* 48(9-11), pp. 771-783.

DiVincenzo, D. P. and Loss, D. 1998. Quantum information is physical. *Superlattices and Microstructures* 23(3-4), pp. 419-432.

DiVincenzo, D. P. and Loss, D. 1999. Quantum computers and quantum coherence. *Journal of Magnetism and Magnetic Materials* 200(1-3), pp. 202-218.

Dousse, A. et al. 2008. Controlled light-matter coupling for a single quantum dot embedded in a pillar microcavity using far-field optical lithography. *Physical Review Letters* 101(26), p. 267404.

Dousse, A. et al. 2010. Ultrabright source of entangled photon pairs. *Nature* 466(7303), pp. 217-220.

Dowling, J. P. and Milburn, G. J. 2003. Quantum technology: the second quantum revolution. *Philosophical Transactions of the Royal Society of London. Series A: Mathematical, Physical and Engineering Sciences* 361(1809), pp. 1655-1674.

Dréau, A. et al. 2018. Quantum frequency conversion of single photons from a nitrogen-vacancy center in diamond to telecommunication wavelengths. *Physical Review Applied* 9(6), p. 064031.

Dresselhaus, M. S. 2001. Solid state physics part ii optical properties of solids. *Lecture Notes (Massachusetts Institute of Technology, Cambridge, MA)* 17, pp. 15-16.

Durham Magneto Optics. 2019. *MicroWriter ML® 3 Pro Specification*. Available at: https://www.durhammagnetooptics.com/wp-content/uploads/2024/01/MicroWriter-ML3-Pro-v6.pdf [Accessed: 21 Feb 2024].

Dyakonov, M. I. and Khaetskii, A. 2017. *Spin physics in semiconductors*. Springer.

Dyson, F. J. and Derbes, D. 2011. *Advanced quantum mechanics*. World Scientific.

Edmonds, A. R. 1970. The theory of the quadratic Zeeman effect. *Le Journal de Physique Colloques* 31(C4), pp. C4-71-C74-74.

Edvinsson, T. 2018. Optical quantum confinement and photocatalytic properties in two-, one- and zero-dimensional nanostructures. *Royal society open science* 5(9), p. 180387.

Engel, L. et al. 2023. Purcell enhanced single-photon emission from a quantum dot coupled to a truncated Gaussian microcavity. *Applied Physics Letters* 122(4), p. 043503.

Englund, D. et al. 2005. Controlling the spontaneous emission rate of single quantum dots in a two-dimensional photonic crystal. *Physical Review Letters* 95(1), p. 013904.

Engström, O. et al. eds. 2011. *Coulomb interaction between InAs/GaAs quantum dots and adjacent impurities*. *AIP Conference Proceedings-American Institute of Physics.*

Fermi, E. 1950. *Nuclear physics: a course given by Enrico Fermi at the University of Chicago*. University of Chicago press.

Feynman, R. P. 1982. Simulating physics with computers. *Int. J. Theor. Phys* 21(6/7),

Fischer, K. A. et al. 2017. Pulsed rabi oscillations in quantum two-level systems: beyond the area theorem. *Quantum Science and Technology* 3(1), p. 014006.

Flagg, E. B. et al. 2009. Resonantly driven coherent oscillations in a solid-state quantum emitter. *Nature Physics* 5(3), pp. 203-207.

Flissikowski, T. et al. 2001. Photon beats from a single semiconductor quantum dot. *Physical Review Letters* 86(14), p. 3172.

Florian, M. et al. 2013. Phonon-mediated off-resonant coupling effects in semiconductor quantum-dot lasers. *New Journal of Physics* 15(3), p. 035019.

Fölsch, S. et al. 2014. Quantum dots with single-atom precision. *Nature Nanotechnology* 9(7), pp. 505-508.

Foteinopoulou, S. et al. 2003. Refraction in media with a negative refractive index. *Physical Review Letters* 90(10), p. 107402.

Fox, A. M. 2006a. *Quantum optics: an introduction*. Oxford University Press.

Fox, M. 2006b. *Quantum optics: an introduction*. OUP Oxford.

Gao, K. et al. 2019. Spectral diffusion time scales in InGaN/GaN quantum dots. *Applied Physics Letters* 114(11),

García de Arquer, F. P. et al. 2021. Semiconductor quantum dots: Technological progress and future challenges. *Science* 373(6555), p. eaaz8541.

Gayral, B. et al. 1998. Optical study of GaAs/AlAs pillar microcavities with elliptical cross section. *Applied Physics Letters* 72(12), pp. 1421-1423.

Gedney, S. D. and Zhao, B. 2009. An auxiliary differential equation formulation for the complex-frequency shifted PML. *IEEE Transactions on antennas and propagation* 58(3), pp. 838-847.

Georgescu, I. 2020. The DiVincenzo criteria 20 years on. *Nature Reviews Physics* 2(12), pp. 666-666.

Gerard, J.-M. 1991. Highly Strained InAs/GaAs Short Period Superlattices.*Condensed Systems of Low Dimensionality*. Springer, pp. 533-546.

Gérard, J.-M. et al. 1998. Enhanced spontaneous emission by quantum boxes in a monolithic optical microcavity. *Physical Review Letters* 81(5), p. 1110.

Gerard, J. et al. 1996. Quantum boxes as active probes for photonic microstructures: The pillar microcavity case. *Applied Physics Letters* 69(4), pp. 449-451.

Gershenfeld, N. A. and Chuang, I. L. 1997. Bulk spin-resonance quantum computation. *Science* 275(5298), pp. 350-356.

Ginés, L. et al. 2022. High extraction efficiency source of photon pairs based on a quantum dot embedded in a broadband micropillar cavity. *Physical Review Letters* 129(3), p. 033601.

Girvin, S. M. and Yang, K. 2019. *Modern condensed matter physics*. Cambridge University Press.

Glauber, R. J. 1963. Coherent and incoherent states of the radiation field. *Physical Review* 131(6), p. 2766.

Gong, Y.-X. et al. 2010. Linear optical quantum computation with imperfect entangled photon-pair sources and inefficient non–photon-number-resolving detectors. *Physical Review A—Atomic, Molecular, and Optical Physics* 81(5), p. 052303.

Gonzalez Garcia, S. et al. 2000. A time-domain near-to far-field transformation for FDTD in two dimensions. *Microwave and optical technology letters* 27(6), pp. 427-432.

Gray, R. M. and Goodman, J. W. 2012. *Fourier transforms: an introduction for engineers*. Springer Science & Business Media.

Greilich, A. et al. 2006. Mode locking of electron spin coherences in singly charged quantum dots. *Science* 313(5785), pp. 341-345.

Große, J. et al. 2020. Development of site-controlled quantum dot arrays acting as scalable sources of indistinguishable photons. *APL Photonics* 5(9),

Han, H. et al. 2022. Fabrication and characterization of on-chip silicon spherical-like microcavities with high Q-factors. *Chinese Optics Letters* 20(11), p. 111301.

Harms, P. et al. 1994. Implementation of the periodic boundary condition in the finite-difference time-domain algorithm for FSS structures. *IEEE Transactions on antennas and propagation* 42(9), pp. 1317-1324.

Haus, J. W. 2016. *Fundamentals and applications of nanophotonics*. Woodhead Publishing.

He, Y.-M. et al. 2013. On-demand semiconductor single-photon source with near-unity indistinguishability. *Nature Nanotechnology* 8(3), pp. 213-217.

He, Y.-M. et al. 2018. Polarized indistinguishable single photons from a quantum dot in an elliptical micropillar. *arXiv preprint arXiv:1809.10992*,

Hecht, E. 2002. *Optics, 5e*. Pearson Education India.

Hecht, J. 2015. *Understanding fiber optics*. Jeff Hecht.

Heitz, R. et al. 1996. Multiphonon-relaxation processes in self-organized InAs/GaAs quantum dots. *Applied Physics Letters* 68(3), pp. 361-363.

Heitz, R. et al. 1997. Energy relaxation by multiphonon processes in InAs/GaAs quantum dots. *Physical Review B* 56(16), p. 10435.

Hennessy, K. et al. 2006. Tuning photonic nanocavities by atomic force microscope nano-oxidation. *Applied Physics Letters* 89(4), p. 041118.

Heuser, T. et al. 2018. Fabrication of dense diameter-tuned quantum dot micropillar arrays for applications in photonic information processing. *APL Photonics* 3(11), p. 116103.

Hjort, M. et al. 2013. Direct imaging of atomic scale structure and electronic properties of GaAs wurtzite and zinc blende nanowire surfaces. *Nano letters* 13(9), pp. 4492-4498.

Hohenester, U. 2010a. Cavity quantum electrodynamics with semiconductor quantum dots: Role of phonon-assisted cavity feeding. *Physical Review B—Condensed Matter and Materials Physics* 81(15), p. 155303.

Hohenester, U. 2010b. Cavity quantum electrodynamics with semiconductor quantum dots: Role of phonon-assisted cavity feeding. *Physical Review B* 81(15), p. 155303.

Hohenester, U. et al. 2009. Phonon-assisted transitions from quantum dot excitons to cavity photons. *Physical Review B* 80(20), p. 201311(R).

Holmes, M. et al. 2015. Spectral diffusion and its influence on the emission linewidths of site-controlled GaN nanowire quantum dots. *Physical Review B* 92(11), p. 115447.

Hong, C.-K. et al. 1987. Measurement of subpicosecond time intervals between two photons by interference. *Physical Review Letters* 59(18), p. 2044.

Houel, J. et al. 2012. Probing single-charge fluctuations at a GaAs/AlAs interface using laser spectroscopy on a nearby InGaAs quantum dot. *Physical Review Letters* 108(10), p. 107401.

Huang, H.-L. et al. 2020. Superconducting quantum computing: a review. *Science China Information Sciences* 63, pp. 1-32.

Huang, J. and Kumar, P. 1992. Observation of quantum frequency conversion. *Physical Review Letters* 68(14), p. 2153.

Huang, Y.-z. 2021. *Microcavity Semiconductor Lasers: Principles, Design, and Applications*. John Wiley & Sons.

Huber, T. et al. 2020. Filter-free single-photon quantum dot resonance fluorescence in an integrated cavity-waveguide device. *Optica* 7(5), pp. 380-385.

Iikawa, F. et al. 2004. Optical properties of type-I and II quantum dots. *Brazilian journal of physics* 34, pp. 555-559.

Ikezawa, M. et al. 2006. Biexciton binding energy in parabolic GaAs quantum dots. *Physical Review B—Condensed Matter and Materials Physics* 73(12), p. 125321.

Ikuta, R. et al. 2011. Wide-band quantum interface for visible-to-telecommunication wavelength conversion. *Nature Communications* 2(1), p. 537.

Inaba, H. and Hidaka, T. 1969. Difference Frequency Generation due to Multiple Photon Process in a Resonant Quantum System during the Laser Action. *Nature* 224, pp. 57-59.

Jacak, L. et al. 2013. *Quantum dots*. Springer Science & Business Media.

Jackson, J. D. 2021. *Classical electrodynamics*. John Wiley & Sons.

Jenkins, F. and Segre, E. 1939. The quadratic Zeeman effect. *Physical Review* 55(1), p. 52.

Jennewein, T. et al. 2011. Single-photon device requirements for operating linear optics quantum computing outside the post-selection basis. *Journal of Modern Optics* 58(3-4), pp. 276-287.

Ji, Z. and Song, Z. 2023. Exciton radiative lifetime in CdSe quantum dots. *Journal of Semiconductors* 44(3), p. 032702.

Johansen, J. et al. 2008. Size dependence of the wavefunction of self-assembled InAs quantum dots from time-resolved optical measurements. *Physical Review B—Condensed Matter and Materials Physics* 77(7), p. 073303.

Johnson, T. H. et al. 2014. What is a quantum simulator? *EPJ Quantum Technology* 1, pp. 1-12.

Jordan, M. et al. 2024a. Probing Purcell enhancement and photon collection efficiency of InAs quantum dots at nodes of the cavity electric field. *Physical Review Research* 6(2), p. L022004.

Jordan, M. et al. eds. 2024b. *Quantum dot micropillar cavities with SiO2 hard mask microlenses*. *Photonic and Phononic Properties of Engineered Nanostructures XIV.* SPIE.

Jordan, S. P. et al. 2012. Quantum algorithms for quantum field theories. *Science* 336(6085), pp. 1130-1133.

Kalt, H. and Klingshirn, C. F. 2024. *Semiconductor Optics: Dynamics, high-excitation effects, and basics of applications*. Springer Nature.

Kambs, B. and Becher, C. 2018. Limitations on the indistinguishability of photons from remote solid state sources. *New Journal of Physics* 20(11), p. 115003.

Karl, M. et al. 2009. Dependencies of micro-pillar cavity quality factors calculated with finite element methods. *Optics express* 17(2), pp. 1144-1158.

Kaufman, A. 2015. Laser-cooling atoms to indistinguishability: Atomic Hong-Ou-Mandel interference and entanglement through spin-exchange. *PhDT*,

Khandekar, A. et al. 2005. InAs growth and development of defect microstructure on GaAs. *Journal of Crystal Growth* 275(1-2), pp. e1067-e1071.

Khitrova, G. et al. 2006. Vacuum Rabi splitting in semiconductors. *Nature Physics* 2(2), pp. 81-90.

Kira, M. and Koch, S. W. 2011. *Semiconductor quantum optics*. Cambridge University Press.

Klimov, P. V. et al. 2024. Optimizing quantum gates towards the scale of logical qubits. *Nature Communications* 15(1), p. 2442.

Knill, E. et al. 2000. Efficient linear optics quantum computation. *arXiv preprint quant-ph/0006088*,

Knill, E. et al. 2001. A scheme for efficient quantum computation with linear optics. *Nature* 409(6816), pp. 46-52.

Kogon, A. J. and Sarris, C. D. 2020. FDTD modeling of periodic structures: A review. *arXiv preprint arXiv:2007.05091*, Kok, P. et al. 2007. Linear optical quantum computing with photonic qubits. *Reviews of Modern Physics* 79(1), p. 135.

Konthasinghe, K. et al. 2012. Coherent versus incoherent light scattering from a quantum dot. *Physical Review B* 85(23), p. 235315.

Kowalski, E. J. et al. 2010. Linearly polarized modes of a corrugated metallic waveguide. *IEEE Transactions on Microwave Theory and Techniques* 58(11), pp. 2772-2780.

Kox, A. J. 1997. The discovery of the electron: II. The Zeeman effect. *European journal of physics* 18(3), p. 139.

Kuhlmann, A. V. et al. 2013a. A dark-field microscope for background-free detection of resonance fluorescence from single semiconductor quantum dots operating in a set-and-forget mode. *Review of scientific instruments* 84(7),

Kuhlmann, A. V. et al. 2013b. Charge noise and spin noise in a semiconductor quantum device. *Nature Physics* 9(9), pp. 570-575.

Kuo, P. S. et al. 2013. Reducing noise in single-photon-level frequency conversion. *Optics letters* 38(8), pp. 1310-1312.

Lal, N. et al. 2022. Indistinguishable photons. *AVS Quantum Science* 4(2),

Lang, C. et al. 2013. Correlations, indistinguishability and entanglement in Hong–Ou–Mandel experiments at microwave frequencies. *Nature Physics* 9(6), pp. 345-348.

LaPierre, R. 2021. DiVincenzo Criteria.*Introduction to Quantum Computing*. Cham: Springer International Publishing, pp. 241-244.

Lawrie, B. J. et al. 2019. Quantum sensing with squeezed light. *ACS Photonics* 6(6), pp. 1307-1318.

Le Kien, F. et al. 2017. Higher-order modes of vacuum-clad ultrathin optical fibers. *Physical Review A* 96(2), p. 023835.

Lee, J. et al. 2019. A quantum dot as a source of time-bin entangled multi-photon states. *Quantum Science and Technology* 4(2), p. 025011.

Lewenstein, M. et al. 2012. *Ultracold Atoms in Optical Lattices: Simulating quantum many-body systems*. OUP Oxford.

Li, D. et al. 2016. Phase sensitivity at the Heisenberg limit in an SU (1, 1) interferometer via parity detection. *Physical Review A* 94(6), p. 063840.

Limame, I. et al. 2024. Diameter-dependent whispering gallery mode lasing effects in quantum dot micropillar cavities. *Optics express* 32(18), pp. 31819-31829.

Liu, J. et al. 2021. Tunable frequency matching for efficient four-wave-mixing Bragg scattering in microrings. *Optics express* 29(22), pp. 36038-36047.

Liu, S. et al. 2017. A deterministic quantum dot micropillar single photon source with> 65% extraction efficiency based on fluorescence imaging method. *Scientific Reports* 7(1), p. 13986.

Lloyd, S. 1996. Universal quantum simulators. *Science* 273(5278), pp. 1073-1078.

Loudon, R. 1976. Photon bunching and antibunching. *Physics Bulletin* 27(1), p. 21.

Macleod, H. A. 2017. *Thin-film optical filters*. CRC press.

Mandel, L. and Wolf, E. 1995. *Optical coherence and quantum optics*. Cambridge university press.

Maxwell, J. C. 1865. VIII. A dynamical theory of the electromagnetic field. *Philosophical transactions of the Royal Society of London* (155), pp. 459-512.

McCoy, D. E. et al. 2021. Finite-difference time-domain (FDTD) optical simulations: a primer for the life sciences and bio-inspired engineering. *Micron* 151, p. 103160.

McGuinness, H. J. et al. 2010. Quantum frequency translation of single-photon states in a photonic crystal fiber. *Physical Review Letters* 105(9), p. 093604.

McKinstrie, C. et al. 2005. Translation of quantum states by four-wave mixing in fibers. *Optics express* 13(22), pp. 9131-9142.

Meier, T. and Koch, S. 2005. COHERENT TRANSIENTS| Foundations of Coherent Transients in Semiconductors.

Mekis, A. et al. 1999. Absorbing boundary conditions for FDTD simulations of photonic crystal waveguides. *IEEE microwave and guided wave letters* 9(12), pp. 502-504.

Melet, R. et al. 2008. Resonant excitonic emission of a single quantum dot in the Rabi regime. *Physical Review B* 78(7), p. 073301.

Mermillod, Q. et al. 2016. Dynamics of excitons in individual InAs quantum dots revealed in four-wave mixing spectroscopy. *Optica* 3(4), pp. 377-384.

Michler, P. et al. 2000a. Quantum correlation among photons from a single quantum dot at room temperature. *Nature* 406(6799), pp. 968-970.

Michler, P. et al. 2000b. A quantum dot single-photon turnstile device. *Science* 290(5500), pp. 2282-2285.

Moller, K. 2007. *OPTICS Learning by Computing, with Examples Using Mathcad®, Matlab®, Mathematica®, and Maple®: With 308 Illustrations*. Springer.

Mollow, B. 1969. Power spectrum of light scattered by two-level systems. *Physical Review* 188(5),

Monniello, L. et al. 2013. Excitation-induced dephasing in a resonantly driven InAs/GaAs quantum dot. *Physical Review Letters* 111(2), p. 026403.

Moreau, E. et al. 2001. Single-mode solid-state single photon source based on isolated quantum dots in pillar microcavities. *Applied Physics Letters* 79(18), pp. 2865-2867.

Morreau, A. and Muljarov, E. 2019. Phonon-induced dephasing in quantum-dot–cavity QED. *Physical Review B* 100(11), p. 115309.

Morrison, C. L. et al. 2021. A bright source of telecom single photons based on quantum frequency conversion. *Applied Physics Letters* 118(17), p. 174003.

Morrison, J. 2020. *Modern Physics with Modern Computational Methods*. Academic Press.

Mowbray, D. and Skolnick, M. 2005. New physics and devices based on self-assembled semiconductor quantum dots. *Journal of Physics D: Applied Physics* 38(13), p. 2059.

Muljarov, E. et al. 2005. Phonon-induced exciton dephasing in quantum dot molecules. *Physical Review Letters* 95(17), p. 177405.

Muljarov, E. A. and Langbein, W. 2016. Exact mode volume and Purcell factor of open optical systems. *Physical Review B* 94(23), p. 235438.

Muller, A. et al. 2007. Resonance fluorescence from a coherently driven semiconductor quantum dot in a cavity. *Physical Review Letters* 99(18), p. 187402.

Munsch, M. et al. 2009. Continuous-wave versus time-resolved measurements of Purcell factors for quantum dots in semiconductor microcavities. *Physical Review B* 80(11), p. 115312.

Murphy, L. R. et al. 2024. Tunable frequency conversion in doped photonic crystal fiber pumped near degeneracy. *arXiv preprint arXiv:2407.09266*,

Nakaoka, T. et al. 2004. Size, shape, and strain dependence of the g factor in self-assembled In (Ga) As quantum dots. *Physical Review B* 70(23), p. 235337.

Nakaoka, T. et al. 2005. Tuning of g-factor in self-assembled In (Ga) As quantum dots through strain engineering. *Physical Review B* 71(20), p. 205301.

Nick Vamivakas, A. et al. 2009. Spin-resolved quantum-dot resonance fluorescence. *Nature Physics* 5(3), pp. 198-202.

Nielsen, M. A. and Chuang, I. L. 2010. *Quantum computation and quantum information*. Cambridge university press.

Nowak, A. et al. 2014. Deterministic and electrically tunable bright single-photon source. *Nature Communications* 5(1), p. 3240.

O'Brien, J. L. et al. 2009. Photonic quantum technologies. *Nature Photonics* 3(12), pp. 687-695.

Olbrich, F. et al. 2017. Polarization-entangled photons from an InGaAs-based quantum dot emitting in the telecom C-band. *Applied Physics Letters* 111(13), p. 133106.

Ollivier, H. et al. 2021. Hong-Ou-Mandel interference with imperfect single photon sources. *Physical Review Letters* 126(6), p. 063602.

Ourjoumtsev, A. et al. 2006. Generating optical Schrödinger kittens for quantum information processing. *Science* 312(5770), pp. 83-86.

Özakın, M. B. and Aksoy, S. eds. 2017. *Numerical calculation of magnetic dipole fields by three-dimensional QS-FDTD method. 2017 Progress In Electromagnetics Research Symposium-Spring (PIERS).* IEEE.

Palik, E. D. 1998. *Handbook of optical constants of solids*. Academic press.

Parker, E. H. C. 1985. *The technology and physics of molecular beam epitaxy*. Plenum Press.

Paschotta, R. 2008. Optical fiber communications. *RP-Photonics Encyclopedia*,

Paschotta, R. 2019. Coherent states. *Encyclopedia of Laser Physics and Technology*,

Paskov, P. et al. 2000. Auger processes in InAs self-assembled quantum dots. *Physica E: Low-dimensional Systems and Nanostructures* 6(1-4), pp. 440-443.

Patton, B. et al. 2005. Coherent control and polarization readout of individual excitonic states. *Physical Review Letters* 95(26), p. 266401.

Pauli, W. 1925. Über den Zusammenhang des Abschlusses der Elektronengruppen im Atom mit der Komplexstruktur der Spektren. *Zeitschrift für Physik* 31(1), pp. 765-783.

Pearton, S. et al. 2000. A review of dry etching of GaN and related materials. *Materials Research Society Internet Journal of Nitride Semiconductor Research* 5(1), p. e11.

Peirce, C. S. 1880. A Boolean algebra with one constant. *Collected Papers of Charles Sanders Peirce* 4, pp. 12-20.

Phillips, C. L. et al. 2020. Photon statistics of filtered resonance fluorescence. *Physical Review Letters* 125(4), p. 043603.

Poincaré, H. 1889. *Théorie mathématique de la lumière II.: Nouvelles études sur la diffraction.--Théorie de la dispersion de Helmholtz. Leçons professées pendant le premier semestre 1891-1892*. G. Carré.

Poynting, J. H. 1884. XV. On the transfer of energy in the electromagnetic field. *Philosophical transactions of the Royal Society of London* (175), pp. 343-361.

Prescott, D. T. 1997. Reflection analysis of FDTD boundary conditions. I. Time-space absorbing boundaries. *IEEE Transactions on Microwave Theory and Techniques* 45(8), pp. 1162-1170.

Prugovecki, E. 1982. *Quantum mechanics in Hilbert space*. Academic Press.

Puangmali, T. et al. 2010. Monotonic evolution of the optical properties in the transition from three-to quasi-two-dimensional quantum confinement in InAs nanorods. *The Journal of Physical Chemistry C* 114(15), pp. 6901-6908.

Purcell, E. 1946. Spontaneous emission probabilities at radio frequencies. *Physical Review* 69(11), pp. 681-681.

Rabouw, F. T. and de Mello Donega, C. 2017. Excited-state dynamics in colloidal semiconductor nanocrystals. *Photoactive Semiconductor Nanocrystal Quantum Dots: Fundamentals and Applications*, pp. 1-30.

Rakher, M. T. et al. 2010. Quantum transduction of telecommunications-band single photons from a quantum dot by frequency upconversion. *Nature Photonics* 4(11), pp. 786-791.

Ramachandran, A. et al. 2024. Robust parallel laser driving of quantum dots for multiplexing of quantum light sources. *Scientific Reports* 14(1), p. 5356.

Ramsay, A. et al. 2010a. Phonon-induced Rabi-frequency renormalization of optically driven single InGaAs/GaAs quantum dots. *Physical Review Letters* 105(17), p. 177402.

Ramsay, A. et al. 2010b. Damping of exciton Rabi rotations by acoustic phonons in optically excited InGaAs/GaAs quantum dots. *Physical Review Letters* 104(1), p. 017402.

Reed, M. et al. 1988. Observation of discrete electronic states in a zero-dimensional semiconductor nanostructure. *Physical Review Letters* 60(6), p. 535.

Reiss, P. et al. 2016. Synthesis of semiconductor nanocrystals, focusing on nontoxic and earth-abundant materials. *Chemical reviews* 116(18), pp. 10731-10819.

Reitzenstein, S. and Forchel, A. 2010. Quantum dot micropillars. *Journal of Physics D: Applied Physics* 43(3), p. 033001.

Reitzenstein, S. et al. 2007. AlAs⁄GaAs micropillar cavities with quality factors exceeding 150.000. *Applied Physics Letters* 90(25),

Rivera, T. et al. 1999. Optical losses in plasma-etched AlGaAs microresonators using reflection spectroscopy. *Applied Physics Letters* 74(7), pp. 911-913.

Rizvi, M. and Vetri, J. L. eds. 1994. *ESD source modeling in FDTD*. *Proceedings of IEEE Symposium on Electromagnetic Compatibility.* IEEE.

Roden, J. A. and Gedney, S. D. 2000. Convolution PML (CPML): An efficient FDTD implementation of the CFS–PML for arbitrary media. *Microwave and optical technology letters* 27(5), pp. 334-339.

Roy, C. and Hughes, S. 2011. Influence of electron–acoustic-phonon scattering on intensity power broadening in a coherently driven quantum-dot–cavity system. *Physical Review X* 1(2), p. 021009.

Rudno-Rudziński, W. et al. 2021. Magneto-optical characterization of trions in symmetric InP-Based quantum dots for quantum communication applications. *Materials* 14(4), p. 942.

Safwan, S. and El–Meshed, N. 2015. Excitons and Trions in Semiconductor Quantum Dots.*Quantum Dots-Theory and Applications*. IntechOpen.

Sallen, G. et al. 2010. Subnanosecond spectral diffusion measurement using photon correlation. *Nature Photonics* 4(10), pp. 696-699.

Salter, C. et al. 2010. An entangled-light-emitting diode. *Nature* 465(7298), pp. 594-597.

Santori, C. et al. 2002. Indistinguishable photons from a single-photon device. *Nature* 419(6907), pp. 594-597.

Sapienza, L. et al. 2010. Cavity quantum electrodynamics with Anderson-localized modes. *Science* 327(5971), pp. 1352-1355.

Schiff, L. and Snyder, H. 1939. Theory of the quadratic Zeeman effect. *Physical Review* 55(1), p. 59.

Schneider, C. et al. 2016. Quantum dot micropillar cavities with quality factors exceeding 250,000. *Applied Physics B* 122, pp. 1-6.

Schneider, C. et al. 2012. In (Ga) As/GaAs site-controlled quantum dots with tailored morphology and high optical quality. Wiley Online Library.

Schneider, J. B. 2010. Understanding the finite-difference time-domain method. *School of electrical engineering and computer science Washington State University* 28,

Schubert, E. F. 2018. *Light-emitting diodes*. New York: E. Fred Schubert.

Schumacher, B. 1995. Quantum coding. *Physical Review A* 51(4), p. 2738.

Scully, M. O. and Zubairy, M. S. 1997. *Quantum optics*. Cambridge university press.

Seguin, R. et al. 2005. Size-dependent fine-structure splitting in self-organized InAs/GaAs quantum dots. *Physical Review Letters* 95(25), p. 257402.

Semwogerere, D. and Weeks, E. R. 2005. Confocal microscopy. *Encyclopedia of biomaterials and biomedical engineering* 23, pp. 1-10.

Senellart, P. et al. 2017. High-performance semiconductor quantum-dot single-photon sources. *Nature Nanotechnology* 12(11), p. 1026.

Shan, G.-C. et al. 2014. Single photon sources with single semiconductor quantum dots. *Frontiers of Physics* 9, pp. 170-193.

Shaw, J. M. et al. 1997. Negative photoresists for optical lithography. *IBM journal of Research and Development* 41(1.2), pp. 81-94.

Sheffer, H. M. 1913. A set of five independent postulates for Boolean algebras, with application to logical constants. *Transactions of the American mathematical society* 14(4), pp. 481-488.

Shor, P. W. 1994. Proceedings of the 35th Annual Symposium on Foundations of Computer Science. *IEE Computer Society Press, Santa Fe, NM*,

Shor, P. W. 1995. Scheme for reducing decoherence in quantum computer memory. *Physical Review A* 52(4), p. R2493.

Shor, P. W. ed. 1996. *Fault-tolerant quantum computation*. *Proceedings of 37th conference on foundations of computer science.* IEEE.

Silbey, R. J. et al. 2022. *Physical chemistry*. John Wiley & Sons.

Simpson, J. J. 2009. Current and future applications of 3-D global earth-ionosphere models based on the full-vector Maxwell's equations FDTD method. *Surveys in Geophysics* 30, pp. 105-130.

Singh, A. et al. 2019. Quantum frequency conversion of a quantum dot single-photon source on a nanophotonic chip. *Optica* 6(5), pp. 563-569.

Slusher, R. et al. 1993. Threshold characteristics of semiconductor microdisk lasers. *Applied Physics Letters* 63(10), pp. 1310-1312.

Smith III, T. et al. 1988. Electronic spectroscopy of zero-dimensional systems. *Physical Review B* 38(3), p. 2172.

Snyders, R. et al. 2023. Foundations of plasma enhanced chemical vapor deposition of functional coatings. *Plasma Sources Science and Technology*,

Sohler, W. et al. eds. 2009. *Wavelength conversion and optical signal processing in PPLN waveguides*. *2009 Asia Communications and Photonics conference and Exhibition (ACP).*

Somaschi, N. et al. 2016. Near-optimal single-photon sources in the solid state. *Nature Photonics* 10(5), pp. 340-345.

Someya, T. et al. 1995. Laterally squeezed excitonic wave function in quantum wires. *Physical Review Letters* 74(18), p. 3664.

Sparavigna, A. C. 2021. Poissonian Distributions in Physics: Counting Electrons and Photons.

Steane, A. M. 1996. Error correcting codes in quantum theory. *Physical Review Letters* 77(5), p. 793.

Steinhoff, A. et al. 2012. Treatment of carrier scattering in quantum dots beyond the Boltzmann equation. *Physical Review B—Condensed Matter and Materials Physics* 85(20), p. 205144.

Stevens, M. J. 2013. Photon statistics, measurements, and measurements tools.*Experimental Methods in the Physical Sciences*. Vol. 45. Elsevier, pp. 25-68.

Stier, A. V. et al. 2016. Exciton diamagnetic shifts and valley Zeeman effects in monolayer WS2 and MoS2 to 65 Tesla. *Nature Communications* 7(1), p. 10643.

Strangfeld, A. et al. 2023. Quantum sensing for Earth observation at the European Space Agency: latest developments, challenges, and future prospects. *Sensors, Systems, and Next-Generation Satellites XXVII* 12729, pp. 56-62.

Stranski, I. N. and Krastanow, L. 1938. Abhandlungen der mathematisch-naturwissenschaftlichen klasse IIb. *Akademie der Wissenschaften Wien* 146, pp. 797-810.

Stufler, S. et al. 2005. Quantum optical properties of a single In x Ga 1− x As− Ga As quantum dot two-level system. *Physical Review B* 72(12), p. 121301.

Suhara, T. et al. 2003a. Difference-Frequency Generation Devices. *Waveguide Nonlinear-Optic Devices*, pp. 237-270.

Suhara, T. et al. 2003b. Second-Harmonic Generation Devices. *Waveguide Nonlinear-Optic Devices*, pp. 193-236.

Sullivan, D. M. 2013. *Electromagnetic simulation using the FDTD method*. John Wiley & Sons.

Sun, S. et al. 2018. A single-photon switch and transistor enabled by a solid-state quantum memory. *Science* 361(6397), pp. 57-60.

Taflove, A. 1980. Application of the finite-difference time-domain method to sinusoidal steady-state electromagnetic-penetration problems. *IEEE Transactions on electromagnetic compatibility* (3), pp. 191-202.

Taflove, A. et al. 2005. Computational electromagnetics: the finite-difference time-domain method. *The Electrical Engineering Handbook* 3(629-670), p. 15.

Taflove, A. et al. 2013. *Advances in FDTD computational electrodynamics: photonics and nanotechnology*. Artech house.

Tamariz, S. et al. 2020. Toward bright and pure single photon emitters at 300 K based on GaN quantum dots on silicon. *ACS Photonics* 7(6), pp. 1515-1522.

Tan, T. and Potter, M. 2010. FDTD discrete planewave (FDTD-DPW) formulation for a perfectly matched source in TFSF simulations. *IEEE Transactions on antennas and propagation* 58(8), pp. 2641-2648.

Tan, W. et al. 2006. Fundamental optical properties of materials I. *Optical properties of condensed matter and applications* 6, p. 1.

Teixeira, F. et al. 2023. Finite-difference time-domain methods. *Nature Reviews Methods Primers* 3(1), p. 75.

Tischler, J. et al. 2002. Fine structure of trions and excitons in single GaAs quantum dots. *Physical Review B* 66(8), p. 081310.

Tomm, N. et al. 2021. A bright and fast source of coherent single photons. *Nature Nanotechnology* 16(4), pp. 399-403.

Turchette, Q. A. et al. 1995. Measurement of conditional phase shifts for quantum logic. *Physical Review Letters* 75(25), p. 4710.

Turner, G. M. and Christodoulou, C. 1999. FDTD analysis of phased array antennas. *IEEE Transactions on antennas and propagation* 47(4), pp. 661-667.

Unsleber, S. et al. 2015. Deterministic generation of bright single resonance fluorescence photons from a Purcell-enhanced quantum dot-micropillar system. *Optics express* 23(26), pp. 32977-32985.

Uppu, R. et al. 2021. Quantum-dot-based deterministic photon–emitter interfaces for scalable photonic quantum technology. *Nature Nanotechnology* 16(12), pp. 1308-1317.

Vahala, K. J. 2003. Optical microcavities. *Nature* 424(6950), pp. 839-846.

Van Kesteren, H. et al. 1990. Fine structure of excitons in type-II GaAs/AlAs quantum wells. *Physical Review B* 41(8), p. 5283.

Van Venrooij, N. et al. 2024. Fine structure splitting cancellation in highly asymmetric InAs/InP droplet epitaxy quantum dots. *Physical Review B* 109(20), p. L201405.

Vandersypen, L. M. and Chuang, I. L. 2004. NMR techniques for quantum control and computation. *Reviews of Modern Physics* 76(4), pp. 1037-1069.

Varnava, M. et al. 2008. How Good Must Single Photon Sources and Detectors Be<? format?> for Efficient Linear Optical Quantum Computation? *Physical Review Letters* 100(6), p. 060502.

Vasudevan, D. et al. 2015. Core–shell quantum dots: Properties and applications. *Journal of Alloys and Compounds* 636, pp. 395-404.

Villas-Bôas, J. et al. 2005. Damping of coherent oscillations in a quantum dot photodiode. *Physica E: Low-dimensional Systems and Nanostructures* 26(1-4), pp. 337-341.

Viola, L. and Lloyd, S. 1998. Dynamical suppression of decoherence in two-state quantum systems. *Physical Review A* 58(4), p. 2733.

Vitanov, N. et al. 2001. Coherent manipulation of atoms molecules by sequential laser pulses.*Advances in atomic, molecular, and optical physics*. Vol. 46. Elsevier, pp. 55-190.

Vonk, S. J. et al. 2021. Biexciton binding energy and line width of single quantum dots at room temperature. *Nano letters* 21(13), pp. 5760-5766.

VonNeumann, J. and Richtmyer, R. D. 1950. A method for the numerical calculation of hydrodynamic shocks. *Journal of Applied Physics* 21(3), pp. 232-237.

Walck, S. and Reinecke, T. 1998. Exciton diamagnetic shift in semiconductor nanostructures. *Physical Review B* 57(15), p. 9088.

Walls, D. F. 1983. Squeezed states of light. *Nature* 306(5939), pp. 141-146.

Walmsley, I. A. and Nunn, J. 2016. Building quantum networks. *Physical Review Applied* 6(4), p. 040001.

Wang, B.-Y. et al. 2020a. Micropillar single-photon source design for simultaneous near-unity efficiency and indistinguishability. *Physical Review B* 102(12), p. 125301.

Wang, B.-Y. et al. eds. 2020b. *A micropillar single-photon source design numerically optimized for high efficiency and high indistinguishability*. *Quantum 2.0.* Optica Publishing Group.

Wang, B.-Y. et al. 2021. Suppression of background emission for efficient single-photon generation in micropillar cavities. *Applied Physics Letters* 118(11),

Wang, H. et al. 2019a. Towards optimal single-photon sources from polarized microcavities. *Nature Photonics* 13(11), pp. 770-775.

Wang, H. et al. 2017. High-efficiency multiphoton boson sampling. *Nature Photonics* 11(6), pp. 361-365. doi: 10.1038/nphoton.2017.63

Wang, H. et al. 2019b. Boson sampling with 20 input photons and a 60-mode interferometer in a 1 0 14-dimensional hilbert space. *Physical Review Letters* 123(25), p. 250503.

Wang, Q. et al. 2005. Decoherence processes during optical manipulation of excitonic qubits in semiconductor quantum dots. *Physical Review B—Condensed Matter and Materials Physics* 72(3), p. 035306.

Warren, C. et al. 2016. gprMax: Open source software to simulate electromagnetic wave propagation for Ground Penetrating Radar. *Computer Physics Communications* 209, pp. 163-170.

Weiss, D. S. and Saffman, M. 2017. Quantum computing with neutral atoms. *Physics Today* 70(7), pp. 44-50.

Wells, L. et al. 2023. Coherent light scattering from a telecom C-band quantum dot. *Nature Communications* 14(1), p. 8371.

Xiao, L. et al. 2004. Photon statistics measurement by use of single photon detection. *Chinese Science Bulletin* 49(9), pp. 875-878.

Xie, Z. et al. 2019. Efficient C-band single-photon upconversion with chip-scale Ti-indiffused pp-LiNbO 3 waveguides. *Applied Optics* 58(22), pp. 5910-5915.

Xu, X. et al. 2008. Coherent population trapping of an electron spin in a single negatively charged quantum dot. *Nature Physics* 4(9), pp. 692-695.

Yang, F. et al. 2007. A simple and efficient FDTD/PBC algorithm for scattering analysis of periodic structures. *Radio Science* 42(04), pp. 1-9.

Yang, J. et al. 2020. Strain tunable quantum dot based non-classical photon sources. *Journal of Semiconductors* 41(1), p. 011901.

Yee, K. 1966. Numerical solution of initial boundary value problems involving Maxwell's equations in isotropic media. *IEEE Transactions on antennas and propagation* 14(3), pp. 302-307.

Yılmaz, S. et al. 2010. Quantum-dot-spin single-photon interface. *Physical Review Letters* 105(3), p. 033601.

Yu, Y. et al. 2023. Telecom-band quantum dot technologies for long-distance quantum networks. *Nature Nanotechnology* 18(12), pp. 1389-1400.

Yuan, Z. et al. 2002. Electrically driven single-photon source. *Science* 295(5552), pp. 102-105.

Zaske, S. et al. 2012. Visible-to-telecom quantum frequency conversion of light from a single quantum emitter. *Physical Review Letters* 109(14), p. 147404.

Zeuner, K. D. et al. 2021. On-demand generation of entangled photon pairs in the telecom C-band with InAs quantum dots. *ACS Photonics* 8(8), pp. 2337-2344.

Zhang, H. et al. 2021. Effects of the intramode-group coupling induced by the elliptical deformation of orbital angular momentum fibers. *IEEE Photonics Journal* 14(1), pp. 1-9.

Zhang, Y.-S. et al. 2001. Quantum key distribution via quantum encryption. *Physical Review A* 64(2), p. 024302.

Zhou, Y.-J. et al. 2011. Efficient simulations of periodic structures with oblique incidence using direct spectral FDTD method. *Progress In Electromagnetics Research M* 17, pp. 101-111.

Zwiller, V. et al. 2004. Quantum optics with single quantum dot devices. *New Journal of Physics* 6(1), p. 96.